

## **INFORMATION TO USERS**

**This manuscript has been reproduced from the microfilm master. UMI films the text directly from the original or copy submitted. Thus, some thesis and dissertation copies are in typewriter face, while others may be from any type of computer printer.**

**The quality of this reproduction is dependent upon the quality of the copy submitted. Broken or indistinct print, colored or poor quality illustrations and photographs, print bleedthrough, substandard margins, and improper alignment can adversely affect reproduction.**

**In the unlikely event that the author did not send UMI a complete manuscript and there are missing pages, these will be noted. Also, if unauthorized copyright material had to be removed, a note will indicate the deletion.**

**Oversize materials (e.g., maps, drawings, charts) are reproduced by sectioning the original, beginning at the upper left-hand corner and continuing from left to right in equal sections with small overlaps. Each original is also photographed in one exposure and is included in reduced form at the back of the book.**

**Photographs included in the original manuscript have been reproduced xerographically in this copy. Higher quality 6" x 9" black and white photographic prints are available for any photographs or illustrations appearing in this copy for an additional charge. Contact UMI directly to order.**

# **UMI**

**A Bell & Howell Information Company  
300 North Zeeb Road, Ann Arbor MI 48106-1346 USA  
313/761-4700 800/521-0600**



University of Alberta

**Dynamic Analysis of Rotor-Bearing Systems  
Using Three-Dimensional Solid Finite Elements**

by

**John Junyao Yu**



A thesis submitted to the Faculty of Graduate Studies and Research in partial fulfilment  
of the requirements for the degree of Doctor of Philosophy

Department of Mechanical Engineering

Edmonton, Alberta

Fall 1997



**National Library  
of Canada**

**Acquisitions and  
Bibliographic Services**

**395 Wellington Street  
Ottawa ON K1A 0N4  
Canada**

**Bibliothèque nationale  
du Canada**

**Acquisitions et  
services bibliographiques**

**395, rue Wellington  
Ottawa ON K1A 0N4  
Canada**

*Your file Votre référence*

*Our file Notre référence*

**The author has granted a non-exclusive licence allowing the National Library of Canada to reproduce, loan, distribute or sell copies of this thesis in microform, paper or electronic formats.**

**The author retains ownership of the copyright in this thesis. Neither the thesis nor substantial extracts from it may be printed or otherwise reproduced without the author's permission.**

**L'auteur a accordé une licence non exclusive permettant à la Bibliothèque nationale du Canada de reproduire, prêter, distribuer ou vendre des copies de cette thèse sous la forme de microfiche/film, de reproduction sur papier ou sur format électronique.**

**L'auteur conserve la propriété du droit d'auteur qui protège cette thèse. Ni la thèse ni des extraits substantiels de celle-ci ne doivent être imprimés ou autrement reproduits sans son autorisation.**

0-612-23097-X

University of Alberta

Library Release Form

Name of Author:

**John Junyao Yu**

Title of Thesis:

**Dynamic Analysis of Rotor-Bearing  
Systems Using Three-Dimensional  
Solid Finite Elements**

Degree:

**Doctor of Philosophy**

Year this Degree Granted:

**1997**

Permission is hereby granted to the University of Alberta Library to reproduce single copies of this thesis and to lend or sell such copies for private, scholarly, or scientific research purposes only.

The author reserves all other publication and other rights in association with the copyright in the thesis, and except as hereinbefore provided, neither the thesis nor any substantial portion thereof may be printed or otherwise reproduced in any material form whatever without the author's prior written permission.



---

John Junyao Yu

543 Michener Park

Edmonton, Alberta

Canada T6H 4M5

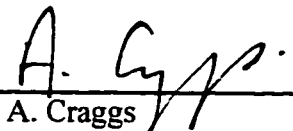
Date:

Sept. 25, 1997

University of Alberta

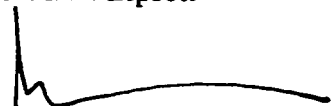
Faculty of Graduate Studies and Research

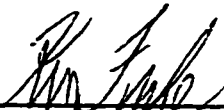
The undersigned certify that they have read, and recommend to the faculty of Graduate Studies and Research for acceptance, a thesis entitled **Dynamic Analysis of Rotor-Bearing Systems Using Three-Dimensional Solid Finite Elements** submitted by **John Junyao Yu** in partial fulfillment of the requirements for the degree of **Doctor of Philosophy**.

  
Dr. A. Craggs

  
Dr. A. Mioduchowski

  
Dr. A.W. Lipsett

  
Dr. A.E. Elwi

  
Dr. K.R. Fyfe

  
Dr. S.G. Hutton

Date: Sep 25th, 1997

*Dedicated to my little daughter Lulu*

## **Abstract**

Using Hamilton's principle, the finite element equations for both non rotating and rotating shafts are given, so that not only bending but also torsional, axial and other possible modes in a 3-D domain can be analysed simultaneously through the corresponding developed codes. The computed frequencies of bending-like 3-D modes are in very good agreement with those measured. Use of a rotating frame of reference gives a clear view of the shaft whirl as a result of bending vibration. Forward and backward whirls in this frame are found to be able to exist simultaneously along the shaft, which is reported for the first time. Resonant whirl frequencies or natural frequencies of rotating shafts can be determined with respect to the rotating or fixed frame. Critical speeds and unbalance response can also be consistently evaluated using the 3-D modelling. For this chain-like structure, reduction procedures such as the developed transfer matrix method based on finite element models and dynamic reduction method, can be implemented without any loss of accuracy. A distributed fluid/shaft interaction model has been given for rotor-bearing analysis in accordance with the 3-D shaft model. Distributed damping effects on the peak forced response frequency have also been discussed. Good agreement with some results from the ABAQUS software, testing and analytical solutions of uniform beams shows the validity of the written codes which are used throughout the research.



## **Acknowledgements**

I would like to thank my supervisors, Dr. A. Craggs and Dr. A. Mioduchowski, and the other members of my supervisory committee, Dr. A.W. Lipsett and Dr. A.E. Elwi for their advice, guidance and encouragement during the entire course of this work. I would also like to thank the Department of Mechanical Engineering for its support throughout my Ph.D. studies, and the Department of Civil Engineering for the use of ABAQUS software.

My thanks are also given to the Natural Sciences and Engineering Council of Canada for its financial support through operating grants held by Dr. A. Craggs and Dr. A. Mioduchowski, and to the University of Alberta for the Ph.D. Dissertation Fellowship.

Finally I wish to emphasize my gratitude to my wife Lucy for her support and encouragement throughout this endeavour.

# Contents

## Chapter 1

<b>Introduction</b>	<b>1</b>
1.1 A Brief History .....	1
1.2 Modeling of Rotors .....	3
1.2.1 Model types .....	3
1.2.2 Computational Techniques .....	7
1.3 Modeling of Hydrodynamic Forces .....	10
1.4 Objective of the Thesis and Main Contribution .....	12
1.5 Scope of the Thesis .....	13

## Chapter 2

<b>Modelling of Hollow Shafts with 3-D Solid Finite Elements</b>	<b>17</b>
2.1 Finite Element Formulation .....	18
2.1.1 Superelements and Basic Elements .....	18
2.1.2 Potential energy .....	21
2.1.3 Kinetic Energy .....	24
2.1.4 Equation of Motion .....	25
2.2 Use of Different Interpolations .....	27
2.2.1 Isoparametric Elements .....	27
2.2.2 Subparametric Elements .....	29
2.2.3 Comparison .....	32
2.3 Results .....	33
2.3.1 Comparison with Beam Solutions .....	34
2.3.2 Comparison with Measured results .....	35

2.4	Boundary Conditions .....	39
2.5	Discussions .....	41
 <b>Chapter 3</b>		
	<b>Modelling of Non-Axisymmetric Shafts</b>	<b>41</b>
3.1	Mass Imbalance Modelling .....	43
3.2	Non-circular Cross Section Modelling .....	52
3.3	Discussions .....	55
 <b>Chapter 4</b>		
	<b>Rotating Shaft Modelling</b>	<b>56</b>
4.1	Dynamic Modelling .....	57
4.1.1	Reference Frames and Kinematics .....	58
4.1.2	Kinetic Energy .....	58
4.1.3	Potential Energy .....	59
4.2	Finite Element Formulation .....	59
4.3	Equation of Motion .....	63
4.4	Discussions .....	65
 <b>Chapter 5</b>		
	<b>Motion of Rotating Shaft</b>	<b>67</b>
5.1	Shaft Whirl .....	68
5.1.1	Definition of Whirl in Rotating Frame .....	68
5.1.2	Forced Responses in Rotating Frame .....	70
5.1.3	Resonant Whirl Frequencies .....	78
5.2	Critical Speeds and Unbalance Response .....	89
5.2.1	Definition and Determination of Critical Speeds .....	89
5.2.2	Effects of Mass Imbalance on Response .....	92
5.3	Discussions .....	95

## Chapter 6

<b>Eigenvalues and Reduction Procedures</b>	<b>98</b>
6.1 General Eigenvalue Analysis	99
6.1.1 Generalized Eigenvalue Problem	99
6.1.2 Gyroscopic Effects on Stability	102
6.1.3 Damped Natural Frequencies	103
6.2 TMM Based on FE Models	107
6.2.1 Transfer Matrix Formulation Based on FE Models	108
6.2.2 Application and Discussion	113
6.3 Dynamic Reduction	118
6.3.1 Dynamic Matrix and Force Vector Reduction	119
6.3.2 Condensation of Elements Having Intermediate Nodes	123
6.3.3 Boundary Conditions	125
6.3.4 Implication of Solution	126

## Chapter 7

<b>Fluid/Shaft Interaction</b>	<b>128</b>
7.1 Relationship of Dynamic Coefficients between Fixed and Rotating Frames	129
7.2 Lubrication Equations in Rotating Frame	133
7.2.1 General Equations	134
7.2.2 Application of the Lubrication Equation	141
7.3 Pressure Distribution Calculation Using FEA	147
7.3.1 Equation in Rotating Frame for Eccentric Rotor	147
7.3.2 Equation in Rotating Frame for Centered Rotor	152
7.3.3 Perturbation Equations for Centered Rotor	154
7.4 Distributed Shaft Surface Forces in Accordance With 3-D FE Model	166
7.5 Numerical Examples	171
7.5.1 Unbalance Response of the Rotor-Bearing System	171
7.5.2 Damping Effects on the Rotor-Bearing System	174
7.6 Discussions	178

<b>Chapter 8</b>	
<b>Conclusions and Suggestions for Further Research</b>	<b>180</b>
8.1 Conclusions .....	180
8.2 Further Work .....	186
<b>References</b>	<b>188</b>
<b>Appendix A</b>	
<b>Matrix Coefficients</b>	<b>200</b>
A.1 Coefficients of Transformation .....	200
A.2 Constitutive Matrix .....	201
<b>Appendix B</b>	
<b>Synopsis of Developed Software</b>	<b>202</b>
<b>Appendix C</b>	
<b>Use of ABAQUS Code</b>	<b>204</b>
C.1 ABAQUS Input File .....	204
C.2 Results .....	207

## List of Tables

Table 2.1	Convergence of natural frequencies (Hz) using isoparametric elements. Percent deviation from frequencies with 24-superelement in parentheses . . . . .	29
Table 2.2	Convergence of natural frequencies (Hz) using subparametric elements. Percent deviation from frequencies with 16-superelement in parentheses . . . . .	32
Table 2.3	Comparison of natural frequencies (Hz) between isoparametric and subparametric element approaches . . . . .	33
Table 2.4	Bending frequencies of <i>slender</i> beam (length=8m) using three different approaches . . . . .	34
Table 2.5	Bending frequencies of <i>short</i> beam (length=0.8m) using three different approaches . . . . .	35
Table 2.6	Free-free natural frequencies (Hz) of tapered shaft with 8 and 12 superelements for a uniform and a tapered section, respectively. Percent error from measured frequencies in parentheses . . . . .	38
Table 2.7	Free-free natural frequencies of tapered shaft for torsional and axial modes with 8 and 12 superelements for a uniform and a tapered section, respectively. . . . .	38
Table 2.8	Effects of different “simply supported” models on the natural frequencies for the shaft shown in Figure 2.2 with a length of 0.8 m . . .	40
Table 2.9	Effects of different “simply supported” models on the natural frequencies for the shaft shown in Figure 2.2 with a length of 1.2 m . . . . .	40

Table 3.1	Effect of elliptic cross sections on the natural frequencies of bending modes .....	53
Table 3.2	Effect of elliptic cross sections on the natural frequencies of torsional modes .....	54
Table 3.3	Effect of elliptic cross sections on the natural frequencies of axial modes .....	54
Table 5.1	Resonant forward and backward whirl frequencies (Hz) for $\Omega=15000$ RPM (in parentheses is the percent difference from closed form solutions of rotating Timoshenko beams from Zu and Han (1992) with shear coefficient of 0.6202) .....	79
Table 5.2	Critical speeds of the rotating shaft .....	90
Table 5.3	Resonant whirl frequencies corresponding to <i>vibrating modes</i> in the rotating frame when the rotational speed reaches $\Omega = 764$ cyc/sec .....	91
Table 5.4	First order resonant whirl frequencies corresponding to <i>vibrating modes</i> in the rotating frame for the rotational speed just below and above $\Omega = 764$ cyc/sec .....	91
Table 6.1	$\omega_i$ shift from $\omega_n$ as non-proportional damping increase .....	106
Table 6.2	Natural Frequencies Of Simply Supported Beam .....	114
Table 7.1	Maximum values of $p_{u_i}$ with $L/D$ using FEA .....	161
Table 7.2	Fluid film elemental local coordinates matching shaft solid elemental local coordinate .....	170
Table 7.3	One-point and multiple-point damping effects on the forced response .....	176

## List of Figures

Figure 2.1	Shaft modelling with 3-D solid elements. (a) shaft element or superelement, and (b) basic continuum element .....	19
Figure 2.2	Free-free steel hollow shaft .....	28
Figure 2.3	Tapered hollow shaft .....	36
Figure 2.4	Symmetric displacement components in axisymmetric elements. (a) transverse displacements, and (b) axial displacements .....	37
Figure 2.5	Deformed circular line of a cross section. (a) $u_r^{(1)} \neq u_\theta^{(1)}$ , and (b) $u_r^{(1)} = u_\theta^{(1)}$ .....	37
Figure 2.6	“Simply supported” boundary conditions for 3-D solid continuum shaft model. Zero transverse displacements to (a) all the nodes in x and y directions, and (b) only one node in the bending direction, on the outside surface of the shaft end .....	39
Figure 3.1	Mass imbalance modelled with varying density .....	44
Figure 3.2	x-z plane bending frequency vs. mass imbalance. Coupled bending-axial modes appear for $e \neq 0$ . $\omega_0$ denotes frequency for $e=0$ and R stands for the exterior diameter of the shaft .....	47
Figure 3.3	x-y plane bending frequency vs. mass imbalance. Coupled bending-torsional modes appear for $e \neq 0$ . $\omega_0$ denotes frequency for $e=0$ and R stands for the exterior diameter of the shaft .....	48
Figure 3.4	Torsional frequency vs. mass imbalance. Coupled torsional-bending modes appear for $e \neq 0$ . $\omega_0$ denotes frequency for $e=0$ and R stands for the exterior diameter of the shaft .....	49



Figure 3.5	Axial frequency vs. mass imbalance. Coupled axial-bending modes appear for $e \neq 0$ . $\omega_0$ denotes frequency for $e=0$ and $R$ stands for the exterior diameter of the shaft . . . . .	50
Figure 3.6	Resultant inertial forces in a region over a length $\Delta z$ where $e \neq 0$ contributing to another mode type. (a) bending-axial, (b) bending-torsional, (c) torsional-bending, and (d) axial-bending. ( $F e^{i\omega t}$ stands for exciting forces causing a dominant mode, $F_A$ , $F_T$ , and $F_B$ denote resultant inertial forces causing a minor axial, torsional, and bending mode, respectively.) . . . . .	51
Figure 3.7	Elliptic cross sections compared with circular cross sections . . . . .	52
Figure 4.1	Reference frames and particle positions in shaft . . . . .	57
Figure 5.1	Shaft whirl in rotating frame . . . . .	68
Figure 5.2	Forced response when an exciting force with an amplitude of 1 kN and a frequency of 495 Hz was applied to the left end in x-direction in the rotating frame ( $\Omega= 1570.8$ rad/sec). (a) transverse displacement responses vs. axial distance, and (b) trajectories of transverse displacements for various cross sections from the left to the right end of the shaft . . . . .	71
Figure 5.3	Forced response when exciting forces with an amplitude of 1 kN and a frequency of 495 Hz were applied to the two ends in x-direction in the rotating frame ( $\Omega= 1570.8$ rad/sec). (a) transverse displacement responses vs. axial distance, and (b) trajectories of transverse displacements for various cross sections from the left to the right end of the shaft . . . . .	73
Figure 5.4	Resonance response when an exciting force with an amplitude of 1 kN and a frequency of 505 Hz was applied to the left end in x-direction in the rotating frame ( $\Omega= 1570.8$ rad/sec). (a) transverse	

	displacement responses vs. axial distance, and (b) trajectories of transverse displacements for various cross sections from the left to the right end of the shaft. Shaft whirl in rotating frame .....	74
Figure 5.5	Forced response when an exciting force with an amplitude of 1 kN and a frequency of 930 Hz was applied to the left end in x-direction in the rotating frame ( $\Omega= 1570.8$ rad/sec). (a) transverse displacement responses vs. axial distance, and (b) trajectories of transverse displacements for various cross sections from the left to the right end of the shaft .....	76
Figure 5.6	Resonance response when an exciting force with an amplitude of 1 kN and a frequency of 979.6 Hz was applied to the left end in x-direction in the rotating frame ( $\Omega= 1570.8$ rad/sec). (a) transverse displacement responses vs. axial distance, and (b) trajectories of transverse displacements for various cross sections from the left to the right end of the shaft .....	77
Figure 5.7	Comparison of transverse mode shapes vs. shaft distance between resonant forward and backward whirling cases ( $\Omega=15000$ RPM, $\omega_F=505$ Hz and $\omega_B=980$ Hz in rotating frame) .....	80
Figure 5.8	Comparison of transverse mode shapes vs. axial distance between resonant forward whirling and non-rotating cases ( $\Omega=15000$ RPM, $\omega_F= 505$ Hz in rotating frame and $\omega_N= 744$ Hz) .....	80
Figure 5.9	Comparison of transverse mode shapes vs. axial distance between backward whirl and non-rotating case ( $\Omega= 15000$ RPM, $\omega_B= 980$ Hz in rotating frame and $\omega_N= 744$ Hz ) .....	81
Figure 5.10	Variation of resonant forward whirl frequencies in the rotating frame with the shaft speed .....	84
Figure 5.11	Variation of resonant backward whirl frequencies in the rotating frame with the shaft speed .....	85
Figure 5.12	Variation of resonant shaft whirl frequencies in the fixed frame with the shaft speed .....	86

Figure 5.13	Comparison of resonant forward whirl frequencies between the 3-D solid finite element and the Timoshenko beam approaches . . . . .	87
Figure 5.14	Comparison of resonant backward whirl frequencies between the 3-D solid finite element and the Timoshenko beam approaches . . . . .	88
Figure 5.15	“A” distribution of mass imbalance . . . . .	93
Figure 5.16	Resonant unbalance response due to $e(z)$ in Figure 5.15 at 1st critical speed 764 cyc/sec. (Qualitatively showing severely bowed shape being excited, not the case in a real system due to its damping and nonlinearity) . . . . .	93
Figure 5.17	Non-resonant unbalance response due to $e(z)$ in Figure 5.15 at 2nd critical speed (1959 cyc/sec) . . . . .	93
Figure 5.18	“B” distribution of mass imbalance . . . . .	94
Figure 5.19	Non-resonant unbalance response due to $e(z)$ in Figure 5.18 at 1st critical speed (764 cyc/sec) . . . . .	94
Figure 5.20	Resonant unbalance response due to $e(z)$ in Figure 5.18 at 2nd critical speed 1959 cyc/sec. (Qualitatively showing severely bowed shape being excited, not the case in a real system due to its damping and nonlinearity) . . . . .	94
Figure 6.1	The discretized finite element model . . . . .	108
Figure 6.2	The condensation process for identical elements . . . . .	112
Figure 6.3	A simply supported beam . . . . .	113
Figure 6.4	The configuration of the rotor-bearing system . . . . .	115
Figure 6.5	The unbalance response of the rotating shaft with bearings . . . . .	117
Figure 6.6	Chain assembled elements/superelements . . . . .	120
Figure 6.7	New reduced system consisting of $k$ elements/superelements . . . . .	122
Figure 6.8	Elements having intermediate nodal variables. (a) beams element with intermediate nodes “✿”, (b) continuum elements with intermediate nodes “✿”, and (c) general elements with intermediate nodal variables . . . . .	124

Figure 7.1	Bearing force in the fixed and rotating reference frames .....	130
Figure 7.2	Fluid-film in a rotating frame .....	134
Figure 7.3	Application of Eq.(7.32) in prescribed coordinates .....	140
Figure 7.4	Circumferential coordinate parallel to the bearing surface .....	142
Figure 7.5	Circumferential coordinate parallel to the rotor surface .....	145
Figure 7.6	Perturbation in rotating frame around eccentric rotor centre O .....	148
Figure 7.7	Diagram of finite element meshes for solving Eq.(7.65) .....	154
Figure 7.8	Distribution of $p_{,u} (= \frac{\partial p}{\partial u})$ over the rotating shaft surface with fluid .....	162
Figure 7.9	Distribution of $p_{,v} (= \frac{\partial p}{\partial v})$ over the rotating shaft surface with fluid .....	163
Figure 7.10	Distribution of $p_{,u} (= \frac{\partial p}{\partial u})$ over the rotating shaft surface with fluid .....	164
Figure 7.11	Distribution of $p_{,v} (= \frac{\partial p}{\partial v})$ over the rotating shaft surface with fluid .....	165
Figure 7.12	Fluid pressure acting on the surface of a shaft solid element. (a)in the global coordinate, and (b) in the local coordinate .....	166
Figure 7.13	Fluid film elements located on the surface of a shaft solid element ...	169
Figure 7.14	A shaft supported by bearings .....	171
Figure 7.15	Unbalance response varying with shaft speed $\Omega$ in rotating frame ....	173
Figure 7.16.	Amplitude-frequency response .....	176
Figure 7.17	Phase-frequency response .....	176
Figure 7.18	One-point and multiple-point (equivalent of distributed one) damping models. (a)one-point, (b)three-point, and (c) nine-point .....	177

Figure C.1	1st bending mode with natural frequency 744 Hz (744 Hz using the author's code) .....	208
Figure C.2	2nd bending mode with natural frequency 1874 Hz (1875 Hz using the author's code) .....	209
Figure C.3	3rd bending mode with natural frequency 3304 Hz (3307 Hz using the author's code) .....	210
Figure C.4	4th bending mode with natural frequency 4887 Hz (4892 Hz using the author's code) .....	211
Figure C.5	5th bending mode with natural frequency 6538 Hz (6548 Hz using the author's code) .....	212
Figure C.6	1st torsional mode with natural frequency 1963 Hz (1963 Hz using the author's code) .....	213
Figure C.7	2nd torsional mode with natural frequency 3926 Hz (3925 Hz using the author's code) .....	214
Figure C.8	3rd torsional mode with natural frequency 5888 Hz (5888 Hz using the author's code) .....	215
Figure C.9	1st axial mode with natural frequency 3161 Hz (3162 Hz using the author's code) .....	216
Figure C.10	2nd axial mode with natural frequency 6301 Hz (6304 Hz using the author's code) .....	217

# Nomenclature

## Chapter 2

- $x, y, z$  global coordinates in Cartesian form
- $r, \theta, z$  cylindrical coordinates
- $\xi, \eta, \zeta$  local coordinates in Cartesian form
- $[T]$  coefficients of transformation
- $u, v, w$  displacement in  $x, y,$  and  $z$  directions
- $\{h\}$  polynomial vector in terms of  $\xi, \eta$
- $\{g\}$  polynomial vector in terms of  $\xi, \eta, \zeta$
- $\{g_u\}, \{g_v\}, \{g_w\}$  polynomial vector to form  $u, v, w$
- $[T_u], [T_v], [T_w]$  coefficients of transformation to form  $u, v, w$
- $[T]$  coefficient of transformation to form a transverse displacement function in which slope nodal variables are involved, dependent on the real geometry of individual elements
- $[J]$  Jacobian matrix
- $\{\epsilon\}$  strain matrix
- $\{P_l\}, \{P_g\}$  partial derivative vector with respect to local and global coordinates
- $[G]$  partial derivative matrix of local polynomial interpolations with respect to local coordinates
- $[T^*]$  matrix composed of three inverse submatrices  $[T_u]^{-1}, [T_v]^{-1}, [T_w]^{-1}$
- $[J^*]$  matrix composed of three identical inverse submatrices  $[J]^{-1}$
- $[B]$  Boolean matrix
- $[A]$  defined as multiplication of  $[B], [J^*]$  and  $[G]$
- $V$  potential energy

- $[D]$  Hooke matrix of elastic coefficients
- $r$  particle position after deformation
- $i, j, k$  unit vectors along  $x, y, z$
- $T$  kinetic energy
- $[m_u], [m_v], [m_w]$  element mass matrix components
- $L$  defined as  $T - V$
- $\{U\}$  composed of all the nodal displacement variables for each element
- $\{F\}$  generalized nodal forces
- $[M], [K]$  element mass and stiffness matrices
- $\{f\}$  internal generalized force vector
- $[M]^{(\text{sup})}, [K]^{(\text{sup})}$  mass and stiffness matrices for a superelement
- $[M]_i^{(e)}, [K]_i^{(e)}$  element mass and stiffness matrices within a superelement
- $[M]^{(i)}, [K]^{(i)}$   $[M]_i^{(e)}, [K]_i^{(e)}$  expanded to the order of a superelement matrix
- $\{\beta_1\}, \{\beta_2\}, \{\beta_3\}$  polynomial coefficient vector for  $u, v, w$
- $J_{31}^*, J_{32}^*, J_{33}^*$  three elements in the last row of  $[J]^{-1}$
- $\{g^*\}$  polynomial vector for slope  $\frac{\partial u}{\partial z}$  or  $\frac{\partial v}{\partial z}$

### Chapter 3

- $\rho$  mass density
- $\Delta\rho$  mass density increment
- $l$  distance of half ring mass centre measured from the shaft axis
- $R_1$  interior radius of the shaft
- $R_2$  exterior radius of the shaft
- $L$  shaft length
- $e$  mass eccentricity of the concerned shaft
- $\dot{\omega}_0$  natural frequency for  $e = 0$
- $\omega$  natural frequency for  $e \neq 0$

- $\Delta R$  amount increased or decreased in x or y direction to form an elliptic cross section
- $\omega_n$  natural torsional frequency using the classical formula,  $n = 1, 2, \dots$
- $G$  shear modulus

#### **Chapter 4**

- $\Omega$  rotational speed of the shaft
- $OXYZ$  fixed frame or inertial frame of reference
- $Oxyz$  rotating frame of reference
- $u$  particle displacement vector in the rotating frame
- $i, j, k$  unit vector in x, y, z direction of the rotating frame
- $x$  particle position vector before deformation
- $r$  particle position vector after deformation
- $P_0$  particle position before deformation
- $P$  particle position after deformation
- $V$  potential energy
- $T$  kinetic energy
- $T_i$  kinetic energy components,  $i=1, 2, \dots, 6$
- $\{U\}$  nodal displacement variables including slopes along the shaft axis
- $\{N_x\}, \{N_y\}$  vector involving rigid body centrifugal forces
- $[I]$  matrix involving the inertial forces caused by Coriolis acceleration due to elastic deformation
- $\{R_x\}, \{R_y\}$  vector involving the inertial forces caused by Coriolis acceleration due to the coupling of rigid and elastic displacements
- $[m_t]$  submatrix of the element mass matrix with respect to the transverse motion, rotary inertia is included due to the introduction of slope nodal variables



- $[G(\Omega)]$  gyroscopic matrix varying with  $\Omega$
- $[K_r(\Omega)]$  dynamic stiffness varying with  $\Omega$
- $\{N(\Omega)\}$  rigid body centrifugal force vector

### Chapter 5

- $u, v$  complex displacement in x, y direction
- $A, B$  amplitude of u, v
- $\omega$  forcing frequency or whirl frequency
- $\varphi_u, \varphi_v$  phase angle of u, v
- $\theta$  whirl angle relative to the x-axis
- $\omega_{rot}$  whirl frequency in rotating frame
- $\omega_{fix}$  whirl frequency in fixed frame
- $\Omega$  shaft speed, assumed to be “+”
- $\omega_B$  backward whirl frequency
- $\omega_F$  forward whirl frequency
- $\omega_N$  non-rotating natural frequency

### Chapter 6

- $M, C, K$   $n \times n$  mass, gyroscopic/damping, stiffness matrices, respectively
- $U$   $n \times 1$  vector of displacements or generalized coordinates
- $U_0$  amplitude of  $U$
- $A, B$  square matrices ( $2n \times 2n$ )
- $x$  eigenvector ( $2n \times 1$ )
- $x_0$  amplitude of  $x$  ( $2n \times 1$ )
- $\lambda$  eigenvalue
- $G$  gyroscopic matrix
- $\xi$  damping ratio

- $\omega_n$  natural frequency of the SDOF system
- $\omega_d$  damped natural frequency of the SDOF system
- $\lambda_i$   $i$ th complex frequency of the damped MDOF system
- $\alpha_i, \beta_i$  real and imaginary parts of  $\lambda_i$
- $\omega_i$  amplitude of the  $\lambda_i$ ,  $\omega_i = (\alpha_i^2 + \beta_i^2)^{1/2}$
- $\xi_i$  defined as  $-\alpha_i/\omega_i$
- $m_{j\flat}, c_{j\flat}, k_{j\flat}$  submatrix of mass, damping and stiffness matrix, respectively
- $q_{\flat}, q_{i+1}$  displacement vector
- $q_{\flat}, q_2$  amplitude of  $q_{\flat}, q_{i+1}$
- $f_{\flat}, f_{i+1}$  internal generalized force vectors
- $f_{\flat}, f_2$  amplitude of  $f_{\flat}, f_{i+1}$
- $F_{\flat}, F_{i+1}$  external generalized force vectors
- $F_1, F_2$  amplitude of  $F_{\flat}, F_{i+1}$
- $[T]_i$  transfer matrix
- $T_{ij}$  submatrix of  $[T]_i$
- $D(\omega)$  dynamic matrix
- $D_{ij}$  submatrix of  $D(\omega)$
- $\eta(x), \zeta(x)$  mass imbalance distribution along the beam
- $[M], [N]$  translational and rotary mass matrix, respectively
- $[K_b], [C_b]$  bearing stiffness and damping matrix, respectively
- $\{Q_c\}, \{Q_s\}$  unbalance force vectors
- $\{f_r\}$  internal forces
- $\{p\}$  complex response
- $\{q\}$  real response
- <sup>(e)</sup> superscript used to denote an element,  $e = 1, 2, \dots$
- $l, m, r$  Subscript used to denote left, middle, and right side of the element/superelement

- $D^*$  reduced dynamic matrix for the condensed region
- $F_l^*, F_k^*$  reduced force vectors at the two ends of the condensed region
- $U_l, U_k$  displacement amplitude vectors at the two ends of the region

## Chapter 7

- $F_x, F_y$  bearing force in fixed frame
- $[K], [C]$  stiffness and damping matrices of the bearing in fixed frame
- $F_{x^r}, F_{y^r}$  bearing force in rotating frame
- $[K_r], [C_r]$  stiffness and damping matrices of the bearing in rotating frame
- $[T]$  coordinate transformation matrix
- $c, s$  representing  $\cos(\Omega t)$  and  $\sin(\Omega t)$
- $V$  fluid velocity vector
- $\omega$  angular velocity of the reference frame
- $p$  fluid pressure or dynamic pressure
- $\rho$  fluid density
- $a_e$  acceleration at reference frame (rotating frame)
- $\Omega$  shaft speed
- $U_1, V_1$  velocity components at  $y = y_1$
- $U_2, V_2$  velocity components at  $y = y_2$
- $R$  radius of the shaft or rotor
- $\nu$  fluid kinetic viscosity
- $\mu$  fluid absolute viscosity
- $u, v, w$  fluid velocity components or shaft displacement components
- $C_r$  bearing clearance
- $Re$  Reynolds number
- $H$  fluid film thickness
- $\Delta x, \Delta y, \Delta \dot{x}, \Delta \dot{y}$  rotor displacement and velocity perturbation

- $e$  rotor eccentricity relative to the bearing centre
- $\theta$  circumferential angle with respect to the x-axis
- $\psi$  determined by shaft displacement perturbation
- $e_0$  rotor eccentricity radius relative to the bearing centre in the steady-state position
- $\phi_0$  rotor eccentricity angle relative to the bearing centre in the steady-state position
- $H_0$  fluid film thickness in the steady-state position
- $p_0$  steady-state magnitude of pressure
- $\{N_e\}, \{N(s,z)\}$  shape functions to form fluid/shaft interface elements
- $[H], [A], [B]$  coefficient matrices to form fluid/shaft interface elements
  - $s$  subscript used to denote the fluid/shaft interaction system
- $[R]$  coefficient matrix relating nodal forces to nodal pressure variables
  - $\phi$  standing for  $p_u, p_v$ , etc.
  - $s$  circumferential coordinate ( $= R \theta$ )
- $E(s)$  standing the right-hand side terms in Eq.(7.64)
- $\{Q\}$  “load” vector for dynamic pressure increment due to perturbation
- $L_s, L_z$  element lengths along  $s$  and  $z$  directions
  - $L$  bearing length (fluid/shaft interaction length)
- $[K_f], [C_f]$  distributed fluid/shaft interaction stiffness and damping matrices
  - $C$  damping coefficient

# Chapter 1

## Introduction

Rotating machinery is employed widely for power transmission throughout the industrialized world. Its applications can be found in power plants, petrochemical facilities, airplanes, marine propulsion systems, automobiles, machine tools, etc. In order to ensure safe design and reliable operation, many scientists and engineers have been engaged in the area of study called rotordynamics. The current trend toward higher speeds and lighter structures reinforces the importance of more accurate modelling of rotor-bearing systems. This thesis uses three-dimensional (3-D) solid finite elements to simulate the dynamic response of the system.

### 1.1 A Brief History

The first published paper in the area of rotordynamics was presented by Rankine (1869). When deriving equations in a rotating frame, Rankine forgot to include Coriolis acceleration and thus made erroneous conclusions which confused engineers for half a century. Later Jeffcott (1919) proposed a flexible rotor model to analyse the response of high speed rotating shafts to mass imbalance. Named after this English dynamicist, the Jeffcott rotor model consists of an unbalanced flat disk located at the mid-span of a uniform, massless, flexible shaft, which is simply supported at its ends by rigid frictionless bearings. For a simple rotating machine, this simplified modelling might be acceptable. The analysis

based on the Jeffcott model has correctly introduced the concepts of rotor critical speeds and synchronous motion due to mass imbalance. These are fundamental in rotordynamics and even today they still can be effectively used to analyse complicated problems qualitatively to a certain extent.

It is noted that the Jeffcott model is basically a particle or point-mass representation. In order to reflect the rigid-body character of flexible rotating equipment, Stodola (1927) and Green (1948) used a rigid-body model to include the effects of rotary inertia and gyroscopic coupling. When a rigid disk is not located at the mid-span of a shaft, use of the Stodola-Green model is an appropriate approach. The Stodola-Green model led to the development of multi-body lumped-parameter models.

Early rotating machinery was designed to operate below the first critical speed. One could usually obtain reliable operation by ensuring that the highest operational speed would be below the first natural frequency of the shaft. It follows that most of the early papers were concerned with predicting first critical speeds and with balancing shafts for sub-critical operations. In fact, there were few publications in the area of rotordynamics before the 1960's.

Modern rotating machinery, however, often must operate at very high speeds, far above the first critical, under high load and with light shafts. These performance requirements have required rotordynamicists to treat a greater range of problems and phenomena in the past few decades. As noted in references (Eshleman, 1984; Goodwin, 1991; Sankar, 1991), more and more papers have been published each year on the subject of rotordynamics. There have been many books published in this field (Dimarogonas and Paipetis, 1983; Rao, 1983; Vance, 1988; Goodwin, 1989; Childs, 1993) as well. Topics such as unbalanced response (Gupta et al., 1993; Yu and Craggs, 1995a), balancing (Craggs, 1986; Ehrich, 1990), stability (Ehrich, 1991; Muszynska and Grant, 1991; Taylor, 1993), hydrodynamics of bearings (Lund, 1987; Rouvas and Childs, 1993), cracked shafts (Nelson and Nataraj, 1986; Papadopoulos and Dimarogonas, 1992), torsional vibrations (Schwibinger and Nordmann, 1990; Yu, 1991 and 1994), coupled vibrations (Diken and Tadjbakhsh, 1989;

Muszynska et al., 1993), and health monitoring (Bently, 1986; Laws and Muszynska, 1987) are all of practical interest to the researchers and engineers of modern rotating machinery.

Reliable dynamic modelling is the foundation of the subject of rotordynamics. If a simplified Jeffcott model were still being used to simulate the response of today's complicated rotor-bearing systems, one would not be able to determine gyroscopic effects on the natural frequencies of the system. To study the dynamic characteristics or simulate the response of a rotor-bearing system, an appropriate modelling technique and an efficient solution method are essential for problems to be properly examined. Fortunately, the development of powerful computers has greatly accelerated the progress of accurately modelling procedures.

## **1.2 Modelling of Rotors**

In rotating machinery, rotors or shafts are the main functional components. The dynamic response depends considerably on the geometry and properties of the rotor, which in the sense of dynamics have corresponding inertial, elastic, gyroscopic and damping forces. The work of shaft modelling involves the selection of model types and computational techniques, both being closely related.

### **1.2.1 Model Types**

Generally speaking, there exist two classes of models: lumped-parameter and continuous (distributed-parameter). An approach using lumped-parameter models is more convenient for computational processes. From the physical point of view, however, the most accurate model is to be a continuous one. Though few closed form solutions can be found for continuous models, the finite element technique makes continuous models discrete and yields convergent solutions.

In a lumped-parameter model, a shaft is simplified as a collection of several rigid bodies connected by massless springs. Rigid bodies may involve a lumped mass, a diametral

mass moment and a polar mass moment of inertia, depending on what kind of vibrational behaviour is examined. Likewise, springs may include bending, torsional, and axial stiffness.

The Jeffcott rotor is the simplest lumped-parameter model when bending vibration is examined. A point mass is lumped at its mid-span and no mass moment of inertia is considered. If a rotor is relatively rigid compared to the attached bearing supports, the effective mass is the total mass of the rotor and the effective stiffness is the stiffness of all the bearings. If a rotor is relatively flexible compared to the bearing stiffness, the effective stiffness is determined by the bending stiffness of the rotor. In this case, since the mass near the bearings does not vibrate as much as that near the mid-span, only a portion of the total mass is regarded as the effective mass. The motion can be considered in two orthogonal directions and thus a whirl orbit can be computed.

If higher vibration frequencies are of interest for a rotor, additional discrete lumped rigid bodies must be added. When bending behaviour is examined, rigid bodies consist of point masses and diametral and polar mass moments of inertias. The effective stiffness can be determined by applying simple Euler beam theory to a massless shaft section. Timoshenko beam theory (Timoshenko, 1921, 1922, 1955) can be used to include shear deformation as well. For torsional vibration analysis, one or more lumped disks with polar mass moments of inertias, are connected by massless torsional springs. Likewise, for axial vibration analysis, several point mass blocks are connected by massless tensional springs.

The purpose for lumping the parameters is to describe the dynamics of each rigid body mathematically by ordinary differential equations, thus avoiding the more difficult partial differential equations required for a physically continuous rotor. The ordinary differential equations can be derived from Newton's laws, or from Lagrange's equations.

The second approach is to model a rotor as a continuous system. In reality, there may not be any valid reason to assume that the lumped masses cannot deform and that the connecting springs have no mass. In fact, every material portion of the rotor possesses both mass and elasticity and, moreover, these properties may vary from point to point.

Due to the configuration of the rotor, continuous bar theory has often been employed



to formulate the equations of motion in terms of one spatial variable along its neutral axis and time. The cross-sectional areas, diametral and polar moments of inertias may vary along the axial direction. Therefore this is a spatially one-dimensional problem, in which the properties such as mass and elasticity distribution, and the response, of the rotor, are the functions of its axial distance. When bending vibration is analysed, the bar is usually called the *beam* in which transverse displacements and their slopes are of interest. For torsional and axial vibrations, twist angles of cross sections and axial displacements are examined, respectively.

There are three main types of beam models, i.e., the Euler beam (or the Euler-Bernoulli beam), the Rayleigh beam and the Timoshenko beam. For the Euler beam, neither shear nor rotatory inertia is taken into account, though they do exist in reality. When the cross-sectional dimensions are small compared with the length of the beam, the Euler beam is a good approximation. For a rotating shaft (a spinning beam), however, this approximation may result in erroneous conclusions. What particularizes the bending vibrations of rotors, are the gyroscopic moments which do not appear in non-rotating shafts. Gyroscopic moments are proportional to the rotatory inertias of the rotating shafts. Depending on the rotational speed, gyroscopic moments can have a considerable influence on the natural frequencies and critical speeds of rotors (Dimentberg, 1961; Loewy and Piarulli, 1969). If the Euler beam theory is applied to a rotating shaft, one might conclude that forward and backward whirl frequencies would be the same in magnitude. For the Rayleigh beam, the shear effect is neglected while the rotatory inertia is included. The Timoshenko beam theory, in which both the shear deformation and the rotatory inertia effects are included, has been used widely in rotating shafts (Choi et al., 1992). For a uniform beam, using the Timoshenko beam theory will generally yield more accurate natural frequencies and responses than either the Euler or the Rayleigh beam model.

There are, however, some limitations on the use of Timoshenko beam theory. It is generally understood that the Timoshenko beam theory may only be adequate for the calculation of first few natural frequencies of thick beams with a shear correction factor of

around 5/6 (Senthilnathan and Lee, 1992). Senthilnathan and Lee (1992) also found that the Timoshenko beam theory is not adequate in the computation of stress in a vibrating beam. Moreover, it is well known that beam or bar theory is based on the assumption that its plane sections remain plane during the deformation. This assumption is violated for tapered beams (Vest and Darlow, 1990). The reason is that the Timoshenko beam theory is merely the simplification of a three-dimensional continuum into a one-dimensional bar. Cowper (1966) investigated the accuracy of the Timoshenko beam theory for dynamic analysis, and using an exact elasticity approach, found that some terms were neglected. Therefore, in order to describe the real phenomena accurately, one must refine the assumptions and conceive a continuous mathematical model. Obviously, the best model is the three-dimensional elasticity model.

The theory of elasticity (Love, 1927; Timoshenko and Goodier, 1951) can be applied to this model. It is worthwhile to note that in the dynamics of elastic bodies there exist two model types: the classical case and the Cosserat type (Teodorescu, 1975). For the classical case, only stresses and volume forces appear, and the motion of a particle is characterized by three linear velocities; while for the Cosserat type, there are additional couple-stresses and volume moments, and the motion of a particle is therefore characterized by six parameters including three angular velocities. The classical case is commonly used in the theory of elasticity.

The three displacements  $u$ ,  $v$ , and  $w$  satisfying the equations of motion at each point of the rotor body, are functions of three space variables  $x$ ,  $y$ , and  $z$ , and time  $t$ . Here the displacements  $u(x, y, z, t)$ ,  $v(x, y, z, t)$ , and  $w(x, y, z, t)$  play the role of coordinates and  $x$ ,  $y$ , and  $z$  are space variables. Each of the variables  $x$ ,  $y$ , and  $z$  can take any value within the region occupied by the system, so the system has an infinite number of degrees of freedom (Meirovitch, 1967). The equations of motion in terms of displacements are called Navier's equations. In most cases, it is impossible to find their closed form solution which satisfies the boundary conditions. It is the finite element technique that makes a solution possible.

## 1.2.2 Computational Techniques

To obtain an effective solution, one must apply an appropriate computational technique to implement a model. For a lumped-parameter model, one can employ the transfer matrix method (TMM) or the modal analysis method. For a continuous model (distributed-parameter model), there are three approaches. The first one is the analytical method which sometimes may yield a closed form solution. The second one is the assumed mode method. The third one is the finite element method (FEM), the most extensively used computational technique in engineering. Sometimes numerical integration in a time domain might be utilized to acquire the transient or nonlinear response of the rotor with either lumped or distributed parameter model.

In the TMM, a relationship is established between a set of unknowns on the two ends of the rotor section. The equation for the whole system is available by multiplying the successive matrix expressions for connected elements. In the conventional TMM approach, a lumped-parameter model is often employed, such that both the mass and inertia properties are lumped at discrete points which are considered to be connected by massless elastic members. Myklestad (1944) and Prohl (1945) developed this transfer matrix formulation to calculate the critical speeds of rotors. Lund and Orcutt (1967) employed the TMM to compute the unbalance response of a rotor. Rao et al. (1987) used the TMM for transient analysis of rotor systems. Inagaki (1987) used the TMM to include the foundation flexibility of rotor-bearing systems. The TMM was the most commonly used technique for lumped-parameter models with multiple lumped masses.

Although convenient for both modelling and computational processes, the conventional TMM is inconsistent and therefore gives poor results. As is well known, using the TMM based on lumped mass models will not yield natural frequencies which converge from above to the true values as the number of lumped mass is increased. The consistent FEM, however, has this characteristic, and thus can yield more satisfactory solutions. Yu and Craggs (1995a) developed a transfer matrix technique based on finite element formulations. In this way, the finite element solution can be obtained using the TMM technique with small

matrix operations.

Modal analysis can be applied to the developed equations of vibrational motion of the whole system, thus giving both natural frequencies and forced response (Meirovitch, 1967; 1975a). In both lumped and distributed parameter models of a rotor, the stiffness matrix is not diagonal. Using modal analysis, a set of simultaneous ordinary differential equations can be uncoupled to obtain solutions. Sometimes gyroscopic terms are neglected, and proportional or small damping is assumed to facilitate the modal analysis of the rotor. There are some methods to include gyroscopic and damping terms (Hablani and Shrivastava, 1977; Meirovitch, 1975b). The concept of modal analysis is often applied to rotor balancing as well.

For a continuous model, a closed form solution using an analytical approach would be ideal. When beam theory is applied to a uniform cross-sectional rotor, some researchers have obtained closed form solutions of critical speeds, natural frequencies and normal modes (Eshleman and Eubanks, 1969; Huang, 1961; Zu and Han, 1992). However, no closed form beam solution for a tapered or nonuniform cross-sectional rotor has been found. When three-dimensional elasticity theory is employed to model a rotor, the equations of motion become Navier's equations. In this case, an analytical approach is much more complicated. The solution form, if any, depends considerably on the boundary conditions. It is worth noting that the one-dimensional elastic wave propagation theory can be applied to torsional problems of a continuous rotor shaft (Mioduchowski and Faulkner, 1986; Mioduchowski, 1995; Bogacz, et al.). Formulation of the problems along with initial and time-dependent boundary conditions yields a set of ordinary differential equations which can be solved numerically (Mioduchowski, 1990) to give transient angular velocities and strains or elastic moments in any cross-section of the shaft. For bending problems, however, wave analysis is much more complicated and thus is seldom employed.

The assumed-mode method (Meirovitch, 1967), based on the Rayleigh-Ritz method, can be applied to a continuous system. The method does not involve any discretization of the system configuration. Instead, a solution is composed of a linear combination of admissible

---

functions, which are functions of the spatial coordinates, multiplied by time-dependent generalized coordinates. The admissible functions must satisfy the boundary conditions. The accuracy of the method considerably depends on the selection of the admissible functions. Shiau and Hwang (1989; 1993) have used this approach for the dynamic analysis of rotor-bearing systems.

The FEM, an engineering tool of wide applicability (Zienkiewicz, 1971), can be successfully employed to model a continuous rotor. Unlike the assumed-mode method, the FEM allows one to assume appropriate displacement functions in terms of coordinates for individual elements instead of the whole rotor. The expressions of potential and kinetic energy for each element can be established without involving any change of distributed physical parameters. Using Lagrange's equation or Hamilton's principle yields the equation of motion in matrix form for each element. The system matrix representation is obtained by assembling element matrices at appropriate entries dictated by the connectivity. The solutions can be determined at all nodal points. Since the individual element matrices reflect the real properties of distributed parameters involved in their formulation, the FEM technique results in better solutions than the lumped parameter approach.

Ruhl and Booker (1972) first employed the FEM for the dynamic analysis of distributed parameter turborotor systems. Since the Euler beam theory was used in this work, no gyroscopic moments were included in the derived equation. Nelson and McVaugh (1976) adopted the Rayleigh beam theory to take into consideration the rotary inertia and gyroscopic effects in the finite element formulation. Later, Nelson (1980) gave a detailed finite element matrix equation using the rotating Timoshenko beam theory to include shear deformation as well. There were also some publications dealing with finite element formulations for nonuniform cross-sectional rotors based on beam theory (Thomas and Wilson, 1973; Rouch and Kao, 1979; Akella and Craggs, 1986). For a continuum model instead of a beam element, Geradin and Kill (1984), Stephenson et al. (1989), Stephenson and Rouch (1993), and Yu and Craggs (1995b) have used solid finite element approaches in the dynamic analysis of rotors.

---

The FEM solutions can be obtained using modal analysis. If expressed for the whole system, the matrix size of the finite element equation will be quite big, depending on how many elements are used. In order to reduce the size of the overall system matrices, the component mode synthesis method (Nelson and Meacham, 1981; Nelson et al., 1983; Craggs, 1987) is often utilized. In this method, the rotor is partitioned into a set of small substructures in which the modal character is derived. The total system model is then constructed from a reduced number of component modes of each substructure. This procedure is a combination of the FEM and the assumed-mode method. There are also matrix reduction techniques for reducing the size of matrices (Guyan, 1965; Rouch and Kao, 1980). Recently, the continuous coordinate condensation method (Craggs and Eckert, 1992) was proposed for long beams and shafts, so that the natural frequencies can be obtained without any loss of accuracy using only small matrix operations. The TMM based on FEM formulation (Yu and Craggs, 1995a) can be successfully employed to simulate the response of a rotor due to distributed mass imbalance.

### **1.3 Fluid/Shaft Interaction**

Bearings are very important parts in rotating machinery. The role of bearings in rotating systems is not only for locating a rotor and supporting its weight, their dynamic properties and working conditions can also crucially influence the overall dynamic characteristics of the whole system, such as the natural frequencies, the stability and the unbalanced response. There are mainly two types of bearings: rolling-element bearings and fluid-film bearings. The rolling-element bearings are often much stiffer than the rotors they support, and with almost no damping and no cross-coupling, thus having little influence on the dynamic characteristics of the system. For the fluid-film bearings, however, the hydrodynamic behaviour is much more complicated. The motion of the shaft will cause fluid dynamic pressure, which acts on its surface. Therefore, hydrodynamic bearings involve fluid/shaft interaction. But because of their compactness, long life, high load capacity, low

---

power loss, low noise and low cost, they are most commonly used in industry. Many researchers, therefore, have been engaged in the analysis and design of the fluid-film bearings since Osborne Reynolds (1886) derived a differential equation bearing his name about hydrodynamic lubrication theory.

It is clear that the bearings cannot be studied in isolation from the rotor characteristics. Thus, the hydrodynamic forces have been modelled to enable the dynamic analysis of the whole rotor-bearing system. Stodola (1925) first postulated the simplest model by including the flexibility effect of the oil-film. Pastel (1954) evaluated spring and damping coefficients of journal bearings. The properties of these coefficients were found to be related to the rotor stability and oil whip as described by Newkirk (1924; 1925). The linearized coefficient model is still popular today in the dynamic analysis of rotor-bearing systems (Lund, 1987). Some researchers have also considered the fluid inertia forces in journal bearings (Muszynska, 1986; EI-Shafei and Crandall, 1991; EI-Shafei, 1995).

It is clear that the use of dynamic coefficients is an approximation method. In reality, it is the distributed pressure that acts on the rotor surface. Craggs (1993) found that even distributed bearing stiffness along its axial direction can have great effect on the critical speeds of the rotor. It is not appropriate to use eight coefficients in modelling hydrodynamic forces acting on the surface of the three-dimensional elastic rotor model.

There are two reference frames involved in rotor-bearing systems: an inertial or fixed frame and a rotating frame. Conventionally, all variables or coefficients are described in the inertial reference frame. It is easier for design engineers to determine the load capacity of the bearings using this frame. The spring and damping effects of the bearings are evaluated through the displacement and velocity perturbation of the rotor around its equilibrium position in the fixed reference frame. The equations of rotor motion are usually expressed in this frame as well. The equations of the whole system are accordingly given in the fixed reference frame. However, when a three-dimensional elastic rotor model is used and the stresses within the rotor are of interest, one has to choose the rotating reference frame so that rigid rotational motion can be removed. That requires pressure distribution to be expressed

in this frame as well.

The Reynolds equation is a simplified version of the Navier-Stokes (NS) equations based on some physical properties of the oil, the bearing and the journal, and given in the fixed reference frame. For a new problem, the best approach is to derive governing equations from the NS equation, the continuity equation of the oil, and, if needed, the energy equation, the equation of state and other basic equations.

## 1.4 Objective of the Thesis

In the dynamic analysis of rotor-bearing systems, lumped-parameter models have been proven to yield poor results and continuous beam models have been widely used to examine bending vibrations of the shaft. These beam models including the Timoshenko beam are based on an assumption that plane sections remain plane during the deformation. Obviously, this assumption is violated when the rotor has changes in its radial dimension, such as tapered shafts.

A few researchers (Geradin and Kill, 1984; Stephenson et al., 1989; Stephenson and Rouch, 1993; Eckert, 1992) have tried solid finite element approaches instead of beam elements to model rotors. Geradin and Kill (1984) first derived finite element equations for both beam-like and axisymmetric structures. In beam-like structures, an assumption that cross-sections are conserved and remain orthogonal to the neutral axis during deformation is made. Stephenson and Rouch (1989, 1993) utilized axisymmetric elements to analyse bending vibrations of rotors. Since only one symmetric and one anti-symmetric terms are retained to analyse bending behaviour in the displacement functions, some restrictions on displacements still exist beyond finite element modelling. Along any circumferential line of a cross section, radial, axial and circumferential displacements are assumed to vary with  $\sin\theta$  and  $\cos\theta$ , where  $\theta$  is an angle along the centre of the shaft. If only the symmetric components are adopted for a free shaft (Stephenson et al., 1989), transverse displacements on all the points of this circumferential line would be identical and the line would remain



plane after deformation. On the other hand, use of this axisymmetric element modelling may be inefficient when modelling bending, torsional, axial and other possible modes simultaneously. This approach is also inapplicable to non-circular cross sections, distributed density or nonlinear hydrodynamic forces. For whole system analysis, these researchers still used a bearing model with eight dynamic coefficients to simulate fluid/shaft interaction on the shaft surface.

This thesis, therefore, employs a three-dimensional elastic shaft model with a three-dimensional solid finite element technique to examine the dynamic behaviour of rotor-bearing systems. Earlier work (Yu and Craggs, 1995b and 1997) has shown that it is a successful and effective approach. Not only bending, but also torsional and axial vibrations can be analysed simultaneously. Mass imbalance can be consistently modelled without attaching an additional force. The use of the rotating reference frame will reveal, or help one to have a better understanding of, the nature of the shaft whirl, and facilitate the shaft modelling and the stress calculation. Although more degrees of freedom are adopted for the whole shaft using this new approach than in a beam model, some reduction procedures, as mentioned in the preceding discussion, can be implemented for this chain-like structure without any loss of accuracy.

Using a hydrodynamic lubrication equation derived from the NS equations and the continuity equation in the rotating frame, the effect of the distributed oil pressure on the system response can be determined. This approach, instead of using eight dynamic coefficients in the fixed frame, will facilitate the modelling of asymmetric, cracked, or unbalanced rotors. In addition, the weight of a rotor might be regarded as harmonic excitation, and the equilibrium position can be considered to be fixed in the rotating frame.

## **1.5 Scope of the Thesis and Main Contributions**

In the present work, three-dimensional elasticity theory is employed to model rotors with a hollow shaft. A commonly used classical type of elastic continuum is assumed

without involving couple-stresses and volume moments. For each particle of the rotor, the three displacements  $u(x,y,z,t)$ ,  $v(x,y,z,t)$  and  $w(x,y,z,t)$  are expressed in a rotating reference frame. The deformation is assumed to be small. A solid three-dimensional finite element technique along with reduction procedures is used to obtain the convergent solutions effectively. For the modelling of distributed hydrodynamic pressure on the rotor, the NS equations along with finite element techniques are used. The effectiveness of the new approach is confirmed by physical experiments and compared with commercial codes.

The proposed *pure* three-dimensional solid finite element modelling of shafts in this thesis is attempted for the first time. Although some other approaches such as beam-like elements or axisymmetric elements have been used instead of beam elements, restrictions of deformations or displacements still remain beyond finite element modelling. In the new approach, however, three-dimensional characteristics of the elastic shaft can be completely included in the model without any restriction. The allowed modes are only restricted by the prescribed displacement functions used in finite element modelling. The shaft is composed of a series of superelements. Each superelement consists of four basic continuum elements. Any one section of the shaft will then have more pertinent degrees of freedom. Therefore when bending vibration is examined, the related modes are actually bending-like ones in the sense of three-dimensional elastic shafts instead of pure bending modes in one-dimensional models or restricted bending modes in two-dimensional axisymmetric element models. No further assumptions beyond finite element properties are made regarding the displacement or deformation of the shaft. Non-uniform shafts such as tapered ones can be correctly modelled.

Although more degrees of freedom are involved in the three-dimensional solid finite element modelling of the shaft, reduction procedures can be implemented in this chain-like structures without any loss of accuracy. A dynamic reduction method has been proposed which can condense not only dynamic matrices but also dynamic forces. A transfer matrix technique based on finite element models has also been developed. Reduction algorithms greatly reduce computer requirements for this proposed three-dimensional solid finite

element modelling of rotor-bearing systems.

Using the three-dimensional solid finite element modelling, shaft whirl is analysed in the rotating frame of reference. Forward and backward whirl frequencies, critical speeds, and unbalance responses can then be accurately determined. Using three-dimensional solid finite elements permits dynamic stresses to be directly calculated throughout a rotating shaft with complex geometry. Behaviour of forward and backward whirl coexistence in the rotating frame is reported for the first time.

A general lubrication equation is derived, which has one more term than the classical Reynolds equation. Fluid/shaft interaction can be modelled with the introduction of shaft surface forces. Finite element techniques are used in the modelling of fluid/shaft interaction. A distributed fluid/shaft interaction model is then given for the dynamic analysis of a rotor-bearing system in accordance with the three-dimensional solid finite element shaft model.

Damping effects on the peak response frequency are examined. It is found that a forced peak response frequency can be lower or higher than the natural frequency, depending on the point or distributed damping model. What happens in a single degree-of-freedom system cannot be simply applied to other systems.

## **1.6 Subtitles**

The thesis is divided into eight chapters including introduction and conclusion chapters. Results from commercial codes are attached in appendices.

In Chapter 2, a non-rotating shaft is modelled based on three-dimensional elasticity theory with the finite element technique. The selection of coordinate systems, parametric elements, and nodal variables is discussed in detail. A superelement consisting of four basic elements is used to replace a short "beam" element. Results are compared between the Euler beam, the Timoshenko beam, the three-dimensional elasticity approaches and physical experiments.

In Chapter 3, the advantage of solid three-dimensional finite elements is shown. Mass

---

imbalance of rotors is modelled by varying the density within the shaft. Non-circular cross sections of shafts are modelled as well. Coupling behaviour is discussed in detail.

In Chapter 4, a rotating shaft is modelled in the rotating reference frame. The equation is derived using the Hamilton's principle with finite element techniques. Results are compared with the closed form solutions of the Timoshenko beam.

In Chapter 5, the motion of a rotating shaft is discussed in detail. The characteristics of forward and backward whirls are analysed. The advantage of using the rotating frame is shown. Behaviour of forward and backward whirl coexistence is found in the rotating frame.

In Chapter 6, eigenvalue problems and reduction procedures are discussed. Frequency characteristics for different forms are addressed. Two reduction procedures are introduced: transfer matrix method based on finite element formulations and dynamic reduction method.

In Chapter 7, distributed fluid/shaft modelling is developed in accordance with the 3-D solid finite element shaft model. The effect of different damping models on the peak forced response frequency is discussed as well.

Computational results shown in the thesis are obtained through computer programs developed by the author. The programs are briefly introduced in Appendix B. Results using a commercial code - ABAQUS - are also illustrated in Appendix C.

## **Chapter 2**

# **Modelling of Hollow Shafts with 3-D Solid Finite Elements**

In this chapter, a non-rotating hollow shaft is modelled based on 3-D linear elasticity theory with finite element techniques. A superelement consisting of four basic continuum elements is constructed to represent a very short shaft element. The displacement functions for each element are expressed as polynomials, whose coefficients are then determined by nodal variables and their positions. Sometimes the coefficients may depend on the geometry of the shaft. This approach allows one to select displacement polynomials, nodal positions and variables flexibly, so that the concerned behaviour could be best modelled with fewer elements. The resulting unit displacement functions can be different from conventional ones.

The use of cylindrical coordinates in terms of  $r$ ,  $\theta$ ,  $z$  was attempted to model circular cross sectional shafts. Conventional polynomials could not satisfy a basic requirement for allowing rigid body motions of elements. The displacement expressions, in which trigonometric functions must be included, would be more complicated. On the other hand, the bending behaviour, which is of most interest, would not be examined easily in this way. Instead, a Cartesian coordinate system has been employed including orthogonal natural coordinates, so that isoparametric and subparametric element approaches can be easily implemented.

The adopted subparametric element with slope variables along the shaft makes

convergence quicker than the isoparametric element. It is noted that  $C^1$  continuity can be automatically achieved along the axial direction of the shaft. Usually commercial codes or other programs only guarantee  $C^0$  continuity for 3-D solid elements. Having  $C^1$  continuity is beneficial to the modelling of the bending behaviour of the shaft. The obtained results are in good agreement with the measured frequencies.

## 2.1 Finite Element Formulation

### 2.1.1 Superelements and Basic Elements

Let a shaft be divided along its axial line into a series of short shafts that are called *superelements* or substructures. Each superelement consists of four basic continuum elements whose geometry is a quarter-annulus, as shown in Figure 2.1(a). One or more superelements replace a conventional beam or bar element for the shaft modelling. Use of the superelement allows one to treat it as a shaft element, so that some condensation procedures (Craggs and Eckert, 1992; Yu and Craggs, 1995a) can be employed to facilitate computational operations without any loss of accuracy.

For a basic continuum element as shown in Figure 2.1(b), the real coordinates of its geometry can be defined in terms of local coordinates  $(\xi, \eta, \zeta)$  in the following form:

$$\begin{aligned} x &= \{g\}^T [T]^{-1} \{x_i\} \\ y &= \{g\}^T [T]^{-1} \{y_i\} \\ z &= \{g\}^T [T]^{-1} \{z_i\} \end{aligned} \quad (2.1)$$

where

$$\{g\}^T = [\{h\}^T, \zeta \{h\}^T]$$

$$\{h\}^T = [1, \xi, \eta, \xi^2, \xi\eta, \eta^2, \xi^2\eta, \xi\eta^2]$$

$$[T]^T = \begin{bmatrix} \{g^{(1)}\} & \dots & \{g^{(i)}\} & \dots & \{g^{(16)}\} \end{bmatrix}$$

(see Appendix A.1)

$$\{x_i\}, \{y_i\}, \{z_i\} = \text{coordinates at nodes}$$

Note that subscript “ $i$ ” denotes the  $i$ th nodal point. Evaluated at corresponding nodes, the matrix  $[T]$  can be obtained. The product of  $\{g\}^T$  and  $[T]^{-1}$  are also called the geometry shape function. The eight nodes define the mapping and therefore the boundary form of the quarter-annulus cross section. It is found that such an approximation is extremely accurate, and has a maximum error in the radial direction of about 1% (Schwarz, 1988).

The displacement functions are expressed in general as

$$\begin{aligned} u &= \{g_u\}[T_u]^{-1}\{u_i\} \\ v &= \{g_v\}[T_v]^{-1}\{v_i\} \\ w &= \{g_w\}[T_w]^{-1}\{w_i\} \end{aligned} \quad (2.2)$$

where the notations possess the same meaning as those in Eq. (2.1). The product of  $\{g_u\}^T$  and

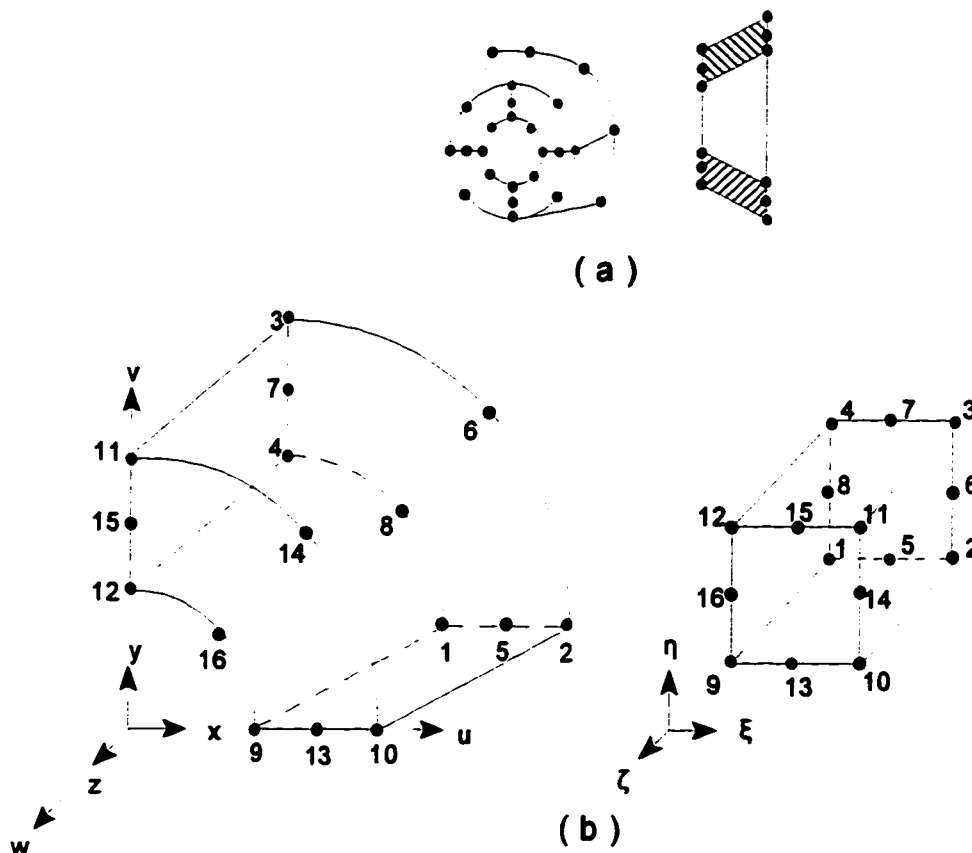


Figure 2.1 Shaft modelling with 3-D solid elements. (a) shaft element or superelement, and (b) basic continuum element

$[T_u]^{-1}$ ,  $\{g_u\}^T$  and  $[T_v]^{-1}$ , or  $\{g_v\}^T$  and  $[T_w]^{-1}$  are also called the displacement shape function. The nodal variables may include slopes if subparametric element formulations are involved. The displacement functions  $u(\xi, \eta, \zeta)$ ,  $v(\xi, \eta, \zeta)$  and  $w(\xi, \eta, \zeta)$  can be interpolated in terms of nodal variables. Note that different polynomials can be chosen in order to simulate the response effectively for a particular problem. Only if isoparametric element formulations are employed, then interpolations of displacements in Eq. (2.2) will be identical to those of coordinates in Eq. (2.1).

As indicated above, the products of first two terms in Eqs. (2.1) and (2.2) are actually the shape functions defining geometry and displacement, respectively. For convenience, usually the tabulated shape functions such as Lagrange and Hermite polynomials are adopted directly. The alternative in this thesis allows one to construct new shape functions based on desired polynomials.

For the three-dimensional elasticity problem, partial differentiation is carried out with respect to global coordinates  $x, y, z$ . Since local coordinates  $\xi, \eta, \zeta$  are utilized in Eq.(2.2), the following Jacobian matrix  $[J]$  is introduced by the usual rules of partial differentiation

$$\{P_l\} = [J] \{P_g\} \tag{2.3}$$

where

$$\{P_l\} = \begin{Bmatrix} \frac{\partial}{\partial \xi} \\ \frac{\partial}{\partial \eta} \\ \frac{\partial}{\partial \zeta} \end{Bmatrix}, \quad \{P_g\} = \begin{Bmatrix} \frac{\partial}{\partial x} \\ \frac{\partial}{\partial y} \\ \frac{\partial}{\partial z} \end{Bmatrix}, \quad [J] = \begin{Bmatrix} \frac{\partial x}{\partial \xi} & \frac{\partial y}{\partial \xi} & \frac{\partial z}{\partial \xi} \\ \frac{\partial x}{\partial \eta} & \frac{\partial y}{\partial \eta} & \frac{\partial z}{\partial \eta} \\ \frac{\partial x}{\partial \zeta} & \frac{\partial y}{\partial \zeta} & \frac{\partial z}{\partial \zeta} \end{Bmatrix}$$

In the above,  $\{P_l\}$  can be evaluated as the functions are specified in local coordinates. From Eq.(2.1), the matrix  $[J]$  can be given explicitly in terms of the local coordinates as



$$[J] = \begin{bmatrix} \frac{\partial \{g\}^T}{\partial \xi} \\ \frac{\partial \{g\}^T}{\partial \eta} \\ \frac{\partial \{g\}^T}{\partial \zeta} \end{bmatrix} [T]^{-1} \begin{bmatrix} \{x_i\} & \{y_i\} & \{z_i\} \end{bmatrix} \quad (2.4)$$

To transform the variables and the region with respect to which the integration is made, a standard process is often employed which involves the determinant of  $[J]$ :

$$\{P_g\} = [J]^{-1} \{P_l\} \quad (2.5a)$$

$$dx \, dy \, dz = \det[J] \, d\xi \, d\eta \, d\zeta \quad (2.5b)$$

### 2.1.2 Potential energy

Six strain components are relevant in full three-dimensional elasticity analysis. The strain matrix is defined as

$$\{\epsilon\} = \begin{Bmatrix} \epsilon_x \\ \epsilon_y \\ \epsilon_z \\ \epsilon_{xy} \\ \epsilon_{yz} \\ \epsilon_{zx} \end{Bmatrix} = \begin{Bmatrix} \frac{\partial u}{\partial x} \\ \frac{\partial v}{\partial y} \\ \frac{\partial w}{\partial z} \\ \frac{\partial u}{\partial y} + \frac{\partial v}{\partial x} \\ \frac{\partial v}{\partial z} + \frac{\partial w}{\partial y} \\ \frac{\partial u}{\partial z} + \frac{\partial w}{\partial x} \end{Bmatrix} = [B] \begin{bmatrix} \{P_g\} & 0 & 0 \\ 0 & \{P_g\} & 0 \\ 0 & 0 & \{P_g\} \end{bmatrix} \quad (2.6)$$

where

$$[B] = \begin{bmatrix} 1 & 0 & 0 & 0 & 0 & 0 & 0 & 0 & 0 \\ 0 & 0 & 0 & 0 & 1 & 0 & 0 & 0 & 0 \\ 0 & 0 & 0 & 0 & 0 & 0 & 0 & 0 & 1 \\ 0 & 1 & 0 & 1 & 0 & 0 & 0 & 0 & 0 \\ 0 & 0 & 0 & 0 & 0 & 1 & 0 & 1 & 0 \\ 0 & 0 & 1 & 0 & 0 & 0 & 1 & 0 & 0 \end{bmatrix}$$

Note that the displacement functions  $u$ ,  $v$  and  $w$  are given explicitly in terms of local coordinates. From Eq. (2.2), it follows

$$\begin{bmatrix} \{P_l\} & 0 & 0 \\ 0 & \{P_l\} & 0 \\ 0 & 0 & \{P_l\} \end{bmatrix} \begin{Bmatrix} u \\ v \\ w \end{Bmatrix} = [G] [T^{-1}] \begin{Bmatrix} \{u_l\} \\ \{v_l\} \\ \{w_l\} \end{Bmatrix} \quad (2.7)$$

where

$$[G] = \begin{bmatrix} \{P_l\} \{g_u\}^T & 0 & 0 \\ 0 & \{P_l\} \{g_v\}^T & 0 \\ 0 & 0 & \{P_l\} \{g_w\}^T \end{bmatrix}, \quad [T^{-1}] = \begin{bmatrix} [T_u]^{-1} & 0 & 0 \\ 0 & [T_v]^{-1} & 0 \\ 0 & 0 & [T_w]^{-1} \end{bmatrix}$$

Eqs. (2.6) and (2.7) can be related by

$$\begin{bmatrix} \{P_g\} & 0 & 0 \\ 0 & \{P_g\} & 0 \\ 0 & 0 & \{P_g\} \end{bmatrix} = [J^{-1}] \begin{bmatrix} \{P_l\} & 0 & 0 \\ 0 & \{P_l\} & 0 \\ 0 & 0 & \{P_l\} \end{bmatrix} \quad (2.8)$$

where

$$[J^{-1}] = \begin{bmatrix} [J]^{-1} & 0 & 0 \\ 0 & [J]^{-1} & 0 \\ 0 & 0 & [J]^{-1} \end{bmatrix}$$

Thus the strain matrix can be given by

$$\{\epsilon\} = [B][J^{-1}][G][T^{-1}] \begin{Bmatrix} \{u_i\} \\ \{v_i\} \\ \{w_i\} \end{Bmatrix} \quad (2.9)$$

In the absence of initial strains, the potential energy or strain energy for an element can be written as

$$V = \frac{1}{2} \iiint_{Vol(e)} \{\epsilon\}^T [D] \{\epsilon\} dx dy dz \quad (2.10)$$

The range of local coordinates is defined as

$$\begin{aligned} -1 &\leq \xi \leq 1 \\ -1 &\leq \eta \leq 1 \\ -1 &\leq \zeta \leq 1 \end{aligned}$$

Substitution of Eqs. (2.5) and (2.9) into Eq. (2.10) yields

$$V = \frac{1}{2} \begin{Bmatrix} \{u_i\} \\ \{v_i\} \\ \{w_i\} \end{Bmatrix}^T [T^{-1}]^T \int_{-1}^1 \int_{-1}^1 \int_{-1}^1 [A]^T [D] [A] \det[J] d\xi d\eta d\zeta [T^{-1}] \begin{Bmatrix} \{u_i\} \\ \{v_i\} \\ \{w_i\} \end{Bmatrix} \quad (2.11)$$

where

$$[A] = [B] [J^{-1}] [G]$$

$$[D] = \text{linear elastic constitutive matrix (See Appendix A.2)}$$

### 2.1.3 Kinetic Energy

For three-dimensional elastic bodies, the kinetic energy can be written as the sum of the translational kinetic energy of all particles. For a particle located at the point (x,y,z), its position after deformation can be given by

$$\mathbf{r} = (x + u)\mathbf{i} + (y + v)\mathbf{j} + (z + w)\mathbf{k} \quad (2.12)$$

where  $\mathbf{i}$ ,  $\mathbf{j}$ , and  $\mathbf{k}$  are unit vectors along x, y, and z axes, respectively. Thus, the kinetic energy of an element can be expressed as

$$\begin{aligned} T &= \frac{1}{2} \iiint_{Vol(e)} \rho \dot{\mathbf{r}} \cdot \dot{\mathbf{r}} dx dy dz \\ &= \frac{1}{2} \iiint_{Vol(e)} \rho (\dot{u}^2 + \dot{v}^2 + \dot{w}^2) dx dy dz \end{aligned} \quad (2.13)$$

where  $\rho$  is the density of the element material. A dot “ $\cdot$ ” denotes the differentiation with respect to the time. Note that unlike a beam or bar model, this three-dimensional model involves only particle kinetic energy.

From Eq. (2.2), the velocity components for each particle can be written as

$$\begin{aligned}\dot{u} &= \{g_u\}[T_u]^{-1}\{\dot{u}_i\} \\ \dot{v} &= \{g_v\}[T_v]^{-1}\{\dot{v}_i\} \\ \dot{w} &= \{g_w\}[T_w]^{-1}\{\dot{w}_i\}\end{aligned}\quad (2.14)$$

Thus Eq. (2.13) becomes

$$T = \frac{1}{2} \begin{Bmatrix} \{\dot{u}_i\} \\ \{\dot{v}_i\} \\ \{\dot{w}_i\} \end{Bmatrix}^T \begin{bmatrix} [m_u] & 0 & 0 \\ 0 & [m_v] & 0 \\ 0 & 0 & [m_w] \end{bmatrix} \begin{Bmatrix} \{\dot{u}_i\} \\ \{\dot{v}_i\} \\ \{\dot{w}_i\} \end{Bmatrix} \quad (2.15)$$

where

$$\begin{aligned}[m_u] &= [T_u]^{-T} \int_{-1}^1 \int_{-1}^1 \int_{-1}^1 \rho \{g_u\} \{g_u\}^T \det[J] d\xi d\eta d\zeta [T_u]^{-1} \\ [m_v] &= [T_v]^{-T} \int_{-1}^1 \int_{-1}^1 \int_{-1}^1 \rho \{g_v\} \{g_v\}^T \det[J] d\xi d\eta d\zeta [T_v]^{-1} \\ [m_w] &= [T_w]^{-T} \int_{-1}^1 \int_{-1}^1 \int_{-1}^1 \rho \{g_w\} \{g_w\}^T \det[J] d\xi d\eta d\zeta [T_w]^{-1}\end{aligned}\quad (2.16)$$

### 2.1.4 Equation of Motion

Once the kinetic and potential energies are obtained, the equation of motion for an element can be easily derived by using either Lagrange equations or Hamilton's principle.

The Lagrange equations can be expressed in the following matrix form:

$$\frac{d}{dt} \left( \frac{\partial L}{\partial \{\dot{U}\}} \right) - \frac{\partial L}{\partial \{U\}} = \{F\} \quad (2.17)$$

where

$$L = T - V$$

$$\{U\} = \left\{ \{u_i\}^T \quad \{v_i\}^T \quad \{w_i\}^T \right\}^T$$

$$\{F\} = \text{generalized nodal forces}$$

and Hamilton's principle can be given by

$$\int_{t_1}^{t_2} (\delta T - \delta V + \delta W) dt = 0 \quad (2.18)$$

where  $\delta W$  is the virtual work done by generalized nodal forces.

Substitution of Eqs. (2.11) and (2.15) into Eq. (2.17) or (2.18) yields the equation of motion for the basic continuum element:

$$[M]\{\ddot{U}\} + [K]\{U\} = \{f\} + \{F\} \quad (2.19)$$

where

$$[M] = \begin{bmatrix} [m_u] & 0 & 0 \\ 0 & [m_v] & 0 \\ 0 & 0 & [m_w] \end{bmatrix}$$

$$[K] = [T]^{-T} \int_{-1}^1 \int_{-1}^1 \int_{-1}^1 [A]^T [D] [A] \det[J] d\xi d\eta d\zeta [T]$$

$\{f\}$  = internal generalized force vector  
 $\{F\}$  = external generalized force vector

A superelement representing a very short shaft is composed of four solid continuum

elements, as shown in Figure 2.1. The mass and stiffness matrices of the superelement can be assembled by direct addition of the basic element matrices, i.e.,

$$[M]^{(sup)} = \sum_i [M]_i^{(e)}, \quad [K]^{(sup)} = \sum_i [K]_i^{(e)} \quad (2.20)$$

where the summation includes the corresponding four annulus elements. To perform the summation, each basic element matrix  $[M]_i^{(e)}$  or  $[K]_i^{(e)}$  is regarded as a matrix  $[M]^{(l)}$  or  $[K]^{(l)}$  of the same order as the superelement matrix  $[M]^{(sup)}$  or  $[K]^{(sup)}$ , where all entries in  $[M]^{(l)}$  or  $[K]^{(l)}$  are zero, except those which correspond to an element degree of freedom. The main purpose for constructing such a superelement is to employ reduction procedures such as continuous coordinate condensation and TMM techniques which can be successfully used in chain-like structures.

## 2.2 Use of Different Interpolations

For the element shown in Figure 2.1, there appear to be three possible types of formulation. Assume that the element geometry is interpolated as given in Eq.(2.1). The displacement functions expressed by Eq.(2.2) can be interpolated differently. If Eq.(2.2) is interpolated using the same polynomials as Eq.(2.1), the elements are called isoparametric elements; and if the polynomial order of Eq.(2.1) is lower (or higher) than that of Eq.(2.2), the elements are named subparametric (or superparametric) elements. Since use of superparametric elements cannot guarantee convergence requirements, only isoparametric and subparametric elements are to be discussed and demonstrated.

### 2.2.1 Isoparametric Elements

The most straightforward formulation is to use isoparametric elements. Thus from Eq.(2.2) to Eq.(2.20) the corresponding polynomial terms and transformation coefficients for displacement functions are all given by

$$\begin{aligned} \{g_u\} &= \{g_v\} = \{g_w\} = \{g\} \\ [T_u] &= [T_v] = [T_w] = [T] \end{aligned} \quad (2.21)$$

There are three nodal variables  $u$ ,  $v$ , and  $w$  at each nodal point. The element can undergo rigid body modes and constant strain states, and satisfy the compatibility requirement. In order to examine the convergence behaviour, different meshes have been made for a free-free steel hollow shaft, as shown in Figure 2.2. Since the dynamic response of the shaft is of interest, comparison is based on its natural frequencies. For consistent modelling, the calculated natural frequencies will converge decreasingly as the discretization of the shaft is increased. Table 2.1 gives the results of bending, torsional and axial modes using 8, 16 and 24 superelements. It can be seen that meshes influence bending frequencies much more than torsional and axial ones. If accurate bending responses are desired, more superelements have to be employed though convergence is guaranteed for this isoparametric element formulation.

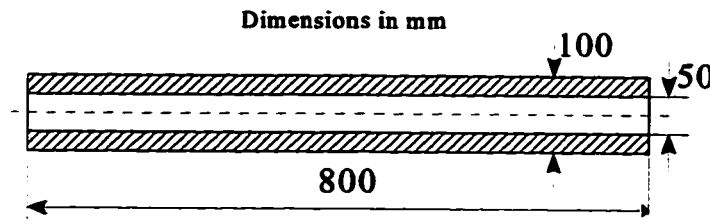


**Figure 2.2 Free-free steel hollow shaft**



**Table 2.1 Convergence of natural frequencies (Hz) using isoparametric elements. Percent deviation from frequencies with 24-superelement in parentheses.**

Modes	24-superelement (1500 d.o.f's)	16-superelement (1020 d.o.f's)	8-superelement (540 d.o.f's)
Bending	763	786(3.0)	902(18)
	1933	2006(3.8)	2387(23)
	3439	3607(4.9)	4495(31)
Torsional	1964	1966(0.1)	1975(0.6)
	3937	3951(0.4)	4027(2.3)
	5926	5974(0.8)	6232(5.7)
Axial	3164	3168(0.1)	3187(0.7)
	6325	6354(0.5)	6513(3.0)
	9469	9570(1.1)	10110(6.8)

### 2.2.2 Subparametric Elements

There are two ways to improve FE solutions, i.e., use of more element meshes or higher polynomial orders of displacement functions. The above computational results show that convergent torsional and axial frequencies can be achieved with only a few elements. However, more element discretization must be used in order to obtain convergent bending frequencies. This behaviour suggests that bending characteristics are not well represented by current polynomials. If proper shape functions which can simulate bending response well are employed, meshes might not be needed to increase in order to obtain accurate results.

It is well known that the transverse displacements  $u$  and  $v$  contribute much more to bending modes than the axial displacement  $w$ . One might notice that the above isoparametric element formulation can only satisfy  $C^0$  continuity along the axial direction. This means that

slopes or deflections may not be continuous. To possess  $C^1$  continuity along the axial direction and high polynomials of  $u$  and  $v$ , Eq.(2.2) is rewritten as

$$\begin{aligned}
 u &= \{g_i\}^T \{\beta_1\} = \{g_i\}^T [T_i]^{-1} \begin{Bmatrix} u_i \\ \frac{\partial u_i}{\partial z} \end{Bmatrix} \\
 v &\equiv \{g_i\}^T \{\beta_2\} = \{g_i\}^T [T_i]^{-1} \begin{Bmatrix} v_i \\ \frac{\partial v_i}{\partial z} \end{Bmatrix} \\
 w &= \{g_i\}^T \{\beta_3\} = \{g_i\}^T [T_i]^{-1} \{w_i\}
 \end{aligned} \tag{2.22}$$

where

$$\{g_i\}^T = [\{h\}^T, \zeta\{h\}^T, \zeta^2\{h\}^T, \zeta^3\{h\}^T]$$

For transverse displacements, the transformation coefficient matrix  $[T_i]$  will be dependent on the real geometry of elements. To evaluate  $[T_i]$ , one has to examine the slope expressions. From Eqs.(2.3) and (2.22), the slope in the x-z plane can be given by

$$\begin{aligned}
 \frac{\partial u}{\partial z} &= J_{31}^* \frac{\partial u}{\partial \xi} + J_{32}^* \frac{\partial u}{\partial \eta} + J_{33}^* \frac{\partial u}{\partial \zeta} \\
 &= \left( J_{31}^* \left\{ \frac{\partial g_i}{\partial \xi} \right\}^T + J_{32}^* \left\{ \frac{\partial g_i}{\partial \eta} \right\}^T + J_{33}^* \left\{ \frac{\partial g_i}{\partial \zeta} \right\}^T \right) \{\beta_1\} \\
 &\triangleq \{g_i^*\}^T \{\beta_1\}
 \end{aligned} \tag{2.23}$$

where  $J_{31}^*$ ,  $J_{32}^*$  and  $J_{33}^*$  are the three elements in the last row of inverse Jacobian matrix  $[J]^{-1}$ .

Thus  $[T_i]$  can be expressed as

$$[T_i] = \begin{bmatrix} \{g_i^{(1)}\}^T \\ \vdots \\ \{g_i^{(i)}\}^T \\ \vdots \\ \{g_i^{(16)}\}^T \\ \{g^*{}^{(1)}\}^T \\ \vdots \\ \{g^*{}^{(i)}\}^T \\ \vdots \\ \{g^*{}^{(16)}\}^T \end{bmatrix} \quad (2.24)$$

where index “(i)” stands for the  $i$ th nodal point.  $\{g^*\}$  is given by

$$\{g^*\} = J_{31}^* \left\{ \frac{\partial g_i}{\partial \xi} \right\} + J_{32}^* \left\{ \frac{\partial g_i}{\partial \eta} \right\} + J_{33}^* \left\{ \frac{\partial g_i}{\partial \zeta} \right\}$$

Evaluated at corresponding nodal points, all elements in  $[T_i]$  can be obtained.

Since the polynomial order used for the coordinates is lower than that for transverse displacements  $u$  and  $v$ , the discussed elements are called subparametric elements. The previously discussed isoparametric elements are well known to satisfy the convergent requirements. It follows that subparametric elements based on convergent isoparametric elements will be guaranteed to be convergent as well (Bathe, 1982).

The convergence of subparametric elements was examined for the same shaft, as shown in Table 2.2. It can be seen that convergent solutions have been quickly acquired. The results show that bending and torsional modes, to which displacements  $u$  and  $v$  mainly contribute, have been better modelled using the proposed  $C^1$  subparametric elements without adding additional nodal points.

**Table 2.2 Convergence of natural frequencies (Hz) using subparametric elements. Percent deviation from frequencies with 16-superelement in parentheses.**

Modes	16-superelement (1700 d.o.f's)	12-superelement (1300 d.o.f's)	8-superelement (900 d.o.f's)
Bending	746	746	750(0.5)
	1886	1890(0.2)	1924(2.0)
	3345	3358(0.4)	3467(3.6)
Torsional	1963	1963	1963
	3925	3925	3925
	5888	5888	5888
Axial	3167	3169(0.1)	3184(0.5)
	6348	6361(0.2)	6481(2.1)
	9546	9592(0.5)	9992(4.7)

### 2.2.3 Comparison

Both isoparametric and subparametric elements will yield convergent solutions as element meshes are increased. The most efficient approach, however, should be the one with less demanding of elements and degrees of freedom and higher accuracy. The comparison between these two approaches was made, as shown in Table 2.3. It was found that for the subparametric element formulation, using only half the amount of discretization that was utilized for the isoparametric element approach could yield more convergent solutions of bending and torsional modes. The axial frequencies were slightly affected, and of course could be improved if a little bit more superelements would be used. Though nodal variables increased to five at each node, element performance has been greatly improved. Slopes become continuous when bending and torsional vibrations are examined. That is why fewer superelements (12) and degrees of freedom (1300) using  $C^1$  subparametric elements give

superior solutions to more superelements (24) and degrees of freedom (1500) using  $C^0$  isoparametric elements. Since consistent finite element modelling is used, solutions should be always above the true values. Lower values then imply better solutions.

**Table 2.3 Comparison of natural frequencies between isoparametric and subparametric element approaches (Hz)**

Modes	Isoparametric element ( 24 superelements, 1500 d.o.f's )	Subparametric element (12 superelements, 1300 d.o.f's)
Bending	763	746
	1933	1890
	3439	3358
Torsional	1964	1963
	3937	3925
	5926	5888
Axial	3164	3169
	6325	6361
	9469	9592

## 2.3 Results

For this 3-D solid finite element approach, Fortran codes were written and run on IBM RISC 6000 Unix machines. Condensation procedures were employed, which will be discussed in the later chapters. Here, computational results are given, and compared with measured ones, Timoshenko beam and rod/bar solutions.

The developed software is discussed in detail in Appendix B. Commercial codes such as ABAQUS have been used as well for non-rotating shafts, as shown in Appendix C. A good agreement is reached between the developed software and ABAQUS results in the case of non-rotating shafts. For rotating shafts, however, where gyroscopic effects and fluid/shaft

interactions need to be included, special software as described in Appendix B has been developed which was used throughout the research. Reduction procedures are also included within the software.

### 2.3.1 Comparison with Beam Solutions

For the uniform shaft as shown in Figure 2.2, *slender* and *short* beam cases were examined. The shaft has an interior diameter of 0.05 m and an exterior diameter of 0.1 m. A *slender* beam defined here is the one with a length of 8 m, and a *short* beam with a length of 0.8 m. Young's modulus is assumed to be  $E = 2.0 \times 10^{11}$  Pa, Poisson's ratio to be  $\nu = 0.3$ , and density to be  $\rho = 7800$  kg/m<sup>3</sup>. Compared with Euler and Timoshenko beam solutions, the results for the two cases are given as shown in Table 2.4 and Table 2.5, respectively.

**Table 2.4 Bending frequencies of *slender* beam (length=8m) using three different approaches (Hz)**

Mode order	Euler beam	Timoshenko beam	3-D solid F.E. (512 superelements)
1	8	8	8
2	22	22	22
3	42	42	42
4	70	70	70
5	105	104	104

**Table 2.5 Bending frequencies (Hz) of *short* beam (length=0.8m) using three different approaches**

Model	Euler beam	Timoshenko beam	3-D solid F.E. (64 superelements)
1	787	744	744
2	2170	1867	1875
3	4255	3281	3307
4	7034	4837	4892
5	10508	6458	6548

It can be seen that for the solutions of the slender beam, there is almost no difference between three different approaches because rotary inertias and shearing effects make less contribution to the bending motion for such a long shaft. However, when the beam becomes short, using the Euler beam theory cannot yield accurate solutions. For this uniform shaft, the computed results are in good agreement with Timoshenko beam solutions.

### 2.3.2 Comparison with Measured Results

For a tapered aluminum shaft as shown in Figure 2.3, the computed results are given in Table 2.6. Its density is  $\rho=2700 \text{ kg/m}^3$ , Young's modulus  $E=10^7 \text{ psi}$  ( $0.689 \times 10^{11} \text{ Pa}$ ), and Poisson's ratio  $\nu=0.34$ . Vest and Darlow (1990) measured its free-free natural bending frequencies and found that tapered shafts cannot be correctly modelled using a standard beam theory. They tried to use some empirical formulas to correct the Young's modulus and therefore gave the corresponding results. This may not be a valid approach for different shafts with different geometry.

Stephenson and Rouch (1993) used an axisymmetric element approach and obtained results as well. For a consistent finite element model, computed natural frequencies should be always above the true values. The solutions they obtained failed to satisfy this criterion.

This may be because only the symmetric components of one Fourier series term were retained. The shortcoming of this axisymmetric element modelling can be analysed in the following.

In this case, radial, circumferential and axial displacements along any circular line of a cross section of the shaft, as shown in Figure 2.4, are expressed as

$$\begin{aligned}u_r &= u_r^{(1)} \cos\theta \\u_\theta &= -u_\theta^{(1)} \sin\theta \\u_z &= u_z^{(1)} \cos\theta\end{aligned}$$

where  $u_r^{(1)}$  and  $u_z^{(1)}$  are the values of  $u_r$  and  $u_z$  at  $\theta = 0$ , and  $u_\theta^{(1)}$  is the value of  $u_\theta$  at  $\theta = -\pi/2$ , respectively. The transverse displacement in x and y directions can be given by

$$\begin{aligned}u_x &= u_r^{(1)} \cos^2\theta + u_\theta^{(1)} \sin^2\theta \\u_y &= \frac{u_r^{(1)} - u_\theta^{(1)}}{2} \sin 2\theta\end{aligned}$$

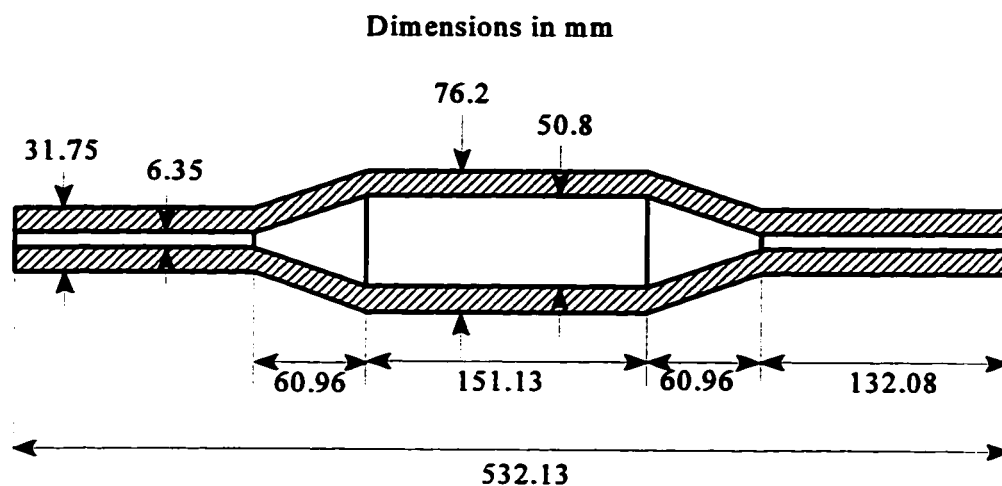


**Figure 2.3 Tapered hollow shaft**



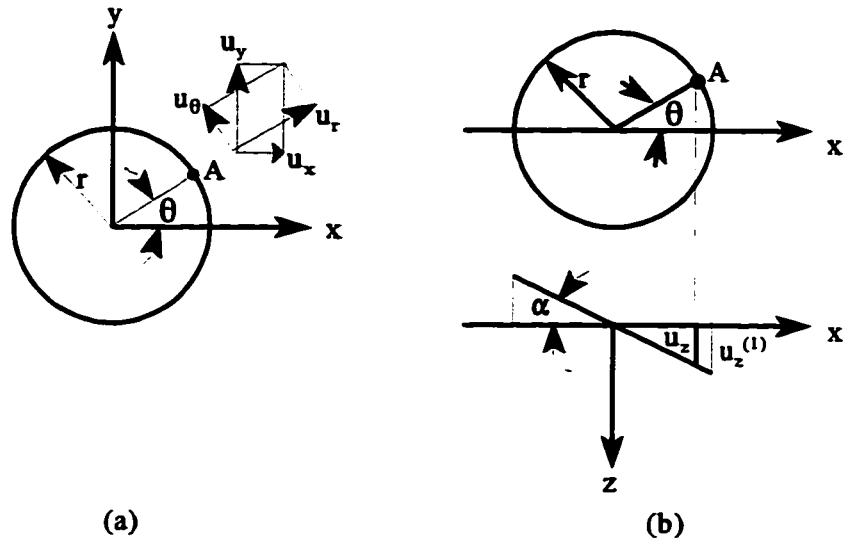


Figure 2.4 Symmetric displacement components in axisymmetric elements. (a) transverse displacements, and (b) axial displacements

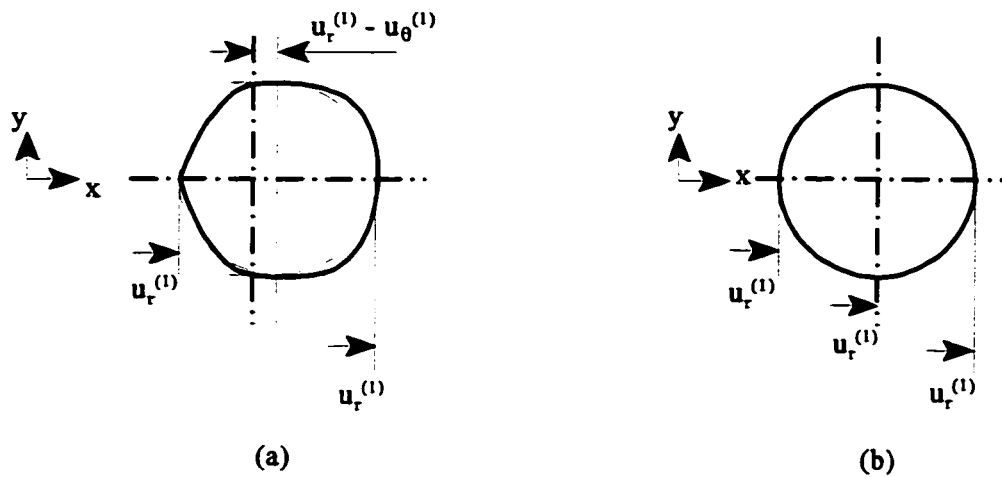


Figure 2.5 Deformed circular line of a cross section. (a)  $u_r^{(1)} \neq u_\theta^{(1)}$ , and (b)  $u_r^{(1)} = u_\theta^{(1)}$

respectively. Obviously the bending direction is in the  $x$ - $z$  plane. No matter how large is the radius  $r$ , the transverse displacements on this circumferential line are restricted by the above expressions. If and only if  $u_r^{(1)}$  is greater (less) than  $u_\theta^{(1)}$ , then the right half of the line would

Table 2.6 Free-free natural bending frequencies (Hz) of tapered shaft with 8 and 12 superelements for a uniform and a tapered section, respectively. Percent error from measured frequencies in parentheses.

Mode	Measured	Vest and Darlow (1990)		Stephenson and Rouch (1993) Axisymmetric FE	Authors 3-D solid FE
		Beam elements	Modulus corrected		
1	1040	1072.1 (3.1)	1043.8 (0.4)	1035.9 (-0.4)	1050 (0.96)
2	1643	1693.6 (3.0)	1658.7 (0.9)	1624.5 (-1.1)	1646 (0.18)
3	4042	4161.3 (2.9)	4123.0 (2.0)	4068.6 (0.7)	4107 (1.61)
4	5886	5970.0 (1.4)	5817.0 (-1.2)	5851.6 (-0.6)	5913 (0.46)
5	7459	7943.0 (6.5)	7867.0 (5.5)	7533.0 (1.0)	7550 (1.22)

Table 2.7 Free-free natural frequencies of tapered shaft for torsional and axial modes with 8 and 12 superelements for a uniform and a tapered section, respectively

Mode	Torsional modes (Hz)	Axial modes (Hz)
1	5098	6216
2	5454	8717
3	8087	13283

be elongated (shortened) and the left would be shortened (elongated), as shown in Figure 2.5(a). If this condition cannot be satisfied, then  $u_y = 0$  and  $u_x = u^{(1)}$  at every point of the circle, as shown in Figure 2.5(b). Regarding axial displacements in this circumferential line, the deformed line will be located in the same plane as shown in Figure 2.4(b) with an angle  $\alpha = \tan^{-1} (u_z^{(1)} / r)$ . Therefore, in the axisymmetric element approach, the transverse displacements along any circumferential line are restricted, and this line will remain in the same plane during deformation.

The proposed 3-D solid finite element approach does not involve any restrictions of displacements or deformations beyond finite element properties. Thus it is believed that this approach will yield most reliable and accurate solutions. The results acquired using 8 and 12 superelements for each uniform and tapered sections, as shown in Table 2.6, are in the best agreement with, and are always slightly above, the measured frequencies.

Other types of vibration modes for this tapered shaft can also be obtained, such as torsional and axial modes, as shown in Table 2.7. Beam models or axisymmetric solid finite elements with one Fourier series term can only yield specific solutions of bending vibration.

## 2.4 Boundary Conditions

For a beam model, there could be up to six different boundary conditions. However, for the 3-D elastic continuum, different boundary condition models might be employed corresponding to these six beam boundary conditions. The simplest boundary condition would be a free surface, which corresponds to a free-free beam model. As it was seen above, solution comparison by using the two different models can be made consistently for this free

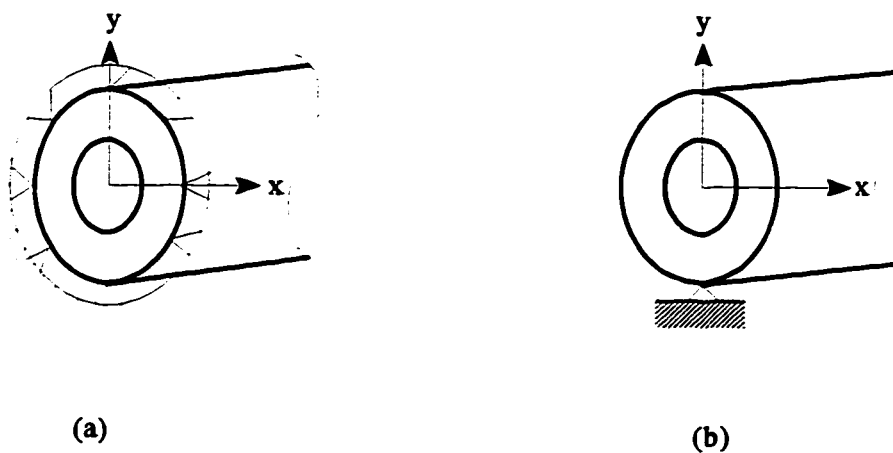


**Figure 2.6 “Simply supported” boundary conditions for 3-D solid continuum shaft model. Zero transverse displacements to (a) all the nodes in x and y directions, and (b) only one node in the bending direction, on the outside surface of the shaft end**

boundary condition. How to define other boundary conditions for the 3-D elastic continuum model corresponding to those for a beam remains a question to researchers.

**Table 2.8 Effects of different “simply supported” models on the natural frequencies for the shaft shown in Figure 2.2 with a length of 0.8 m**

Mode No.	(A) 1st Model (Hz)	(B) 2nd Model (Hz)	(T) Timoshenko beam (Hz)	$\frac{(A)-(B)}{(A)}$	$\frac{(A)-(T)}{(T)}$	$\frac{(B)-(T)}{(T)}$
1	356	348	337	2.2%	5.6%	3.3%
2	1332	1228	1246	8.5%	6.9%	-1.4%
3	2751	2331	2527	18%	8.9%	-7.7%
4	4468	3455	4011	29%	11.4%	-13.9%
5	6406	4670	5598	37%	14.4%	-16.9%

**Table 2.9 Effects of different “simply supported” models on the natural frequencies for the shaft shown in Figure 2.2 with a length of 1.2 m**

Mode No.	(A) 1st Model (Hz)	(B) 2nd Model (Hz)	(T) Timoshenko beam (Hz)	$\frac{(A)-(B)}{(A)}$	$\frac{(A)-(T)}{(T)}$	$\frac{(B)-(T)}{(T)}$
1	160	159	152	0.6%	5.3%	4.6%
2	621	605	586	2.6%	6.0%	3.2%
3	1334	1260	1247	5.5%	7.0%	1.0%
4	2242	2037	2071	9.1%	8.3%	-1.6%
5	3302	2860	3005	13.4%	9.9%	-4.8%

Simply supported boundary conditions are frequently used in beam models. Attempts

were made to simulate this boundary condition in the 3-D continuum model. Two alternatives are illustrated here.

As shown in Figure 2.6, in the first model, both  $x$  and  $y$  directional displacements are set to be zero (i.e.,  $u = v = 0$ ) to all the nodes on the outside diameter of the two shaft ends, and in the second model, only  $y$  directional displacements are set to be zero at the lowest nodes of the two ends. The size of the shaft is illustrated in Figure 2.2. Table 2.8 shows the 3-D model results, the corresponding Timoshenko beam solutions, and the comparisons.

As the shaft length is increased from 0.8 m to 1.2 m, their solution discrepancy using the two different models is reduced and so too their divergence from the Timoshenko beam model. Table 2.9 shows the corresponding solution for the shaft length of 1.2 m.

It can be found that the difference of frequency solutions between the two models of the “simply supported” boundary condition for 3-D continuum modelling is decreased as its length is increased. As it can be seen from Tables 2.8 and 2.9, when the shaft length is increased by 50%, the difference is decreased by nearly 70%. Though the number of support nodes at each end is different between these two models, the resultant forces acting on each end from the fixed reference frame would be the same. Therefore, this effect will be decreased when a shaft length is increased.

One might be able to see that the first model, which restrains all the nodes on the outside surface of the shaft end, is over-constrained, thus yielding higher natural bending frequencies. It is believed that the best model would be based on real contact cases, not necessarily in a good agreement with beam models. For a clamped end, the straightforward approach is to fix all the nodes at the end. However, the author found that this method had yielded quite different stress values near the end from those given by beam formulas.

## 2.5 Discussion

The proposed 3-D subparametric finite elements, which possess  $C^1$  continuity along the axial direction of the shaft, can yield quicker convergent solutions than commonly used

isoparametric elements. Four of these continuum elements construct a very short shaft section, which is defined as a superelement. The whole shaft is modelled by a series of these superelements instead of beam elements.

The computed results are in better agreement with the measured results of a tapered shaft than those using existing axisymmetric elements and beam theory. For a hollow shaft, when its thickness becomes too small or too large, a superelement may need to include more basic continuum elements in order to depict accurate deformation within a cross section of the shaft. Since using the present four basic continuum elements as a superelement of the discussed hollow shaft has yielded accurate convergent solutions for problems of bending, torsional and axial vibrations, a finer mesh within a superelement has not been attempted here.

In the natural frequency computation of 3-D finite element shaft modelling, it was found that high transverse vibration frequencies appeared, which was believed to be shearing modes. Actually, using a simply supported Timoshenko beam approach will also yield shearing modes whose frequencies are relatively higher than bending frequencies.

Free-free end boundary conditions are adopted above. This is convenient to compare with beam solutions directly. For other corresponding boundary conditions used in beam models, it may be hard to define unique equivalent ones for a 3-D elastic body. To simulate a simply supported boundary condition, transverse displacements at one or more nodes may be specified zero on the exterior surface in the two end cross sections. However, it was found that, unlike the solutions for static problems, the natural frequencies varied with how these specified nodes were prescribed. Therefore, to obtain more reliable dynamic solutions, practical contact situations should be better simulated. This behaviour encouraged the author to seek appropriate hydrodynamic modelling for the dynamic analysis of the whole rotor-bearing system.

## Chapter 3

# Modelling of Non-Axisymmetric Shafts

Unlike axisymmetric harmonic finite elements, the proposed three-dimensional (3-D) solid finite elements can be used to model non-axisymmetric shafts which are defined as those having either material or geometry non-symmetry with respect to the axis of the shafts. They also can be successfully employed to model coupled vibrations involving bending, torsional and axial modes.

As is well known, mass imbalance is the main cause of synchronous shaft whirl. To model a shaft with mass imbalance using 3-D solid finite elements, an appropriate approach is to assume distributed material density with respect to the shaft axis. In this way, unbalanced centrifugal forces could be obtained from the kinetic energy in the finite element formulation, while using axisymmetric harmonic elements one must introduce an added unbalance force.

Non-circular cross section shafts are sometimes used in rotating machinery. Here only an elliptic cross section shaft is illustrated to analyse the corresponding dynamic behaviour.

### 3.1 Mass Imbalance Modelling

The mass imbalance is modelled by varying the density distribution. For simplicity, two half sections of a shaft are assumed with density  $\rho + \Delta\rho$  and  $\rho - \Delta\rho$ , as shown in

Figure 3.1. The equivalent eccentricity  $e$  can be related to  $\Delta\rho$  as shown below.

For a half circular ring, its mass centre off the shaft axis can be expressed as

$$l = \frac{4}{3\pi} \frac{R_2^3 - R_1^3}{R_2^2 - R_1^2} \quad (3.1)$$

where

$R_1$  = interior radius of a cross section

$R_2$  = exterior radius of a cross section

$l$  = distance of half ring mass centre measured from the shaft axis

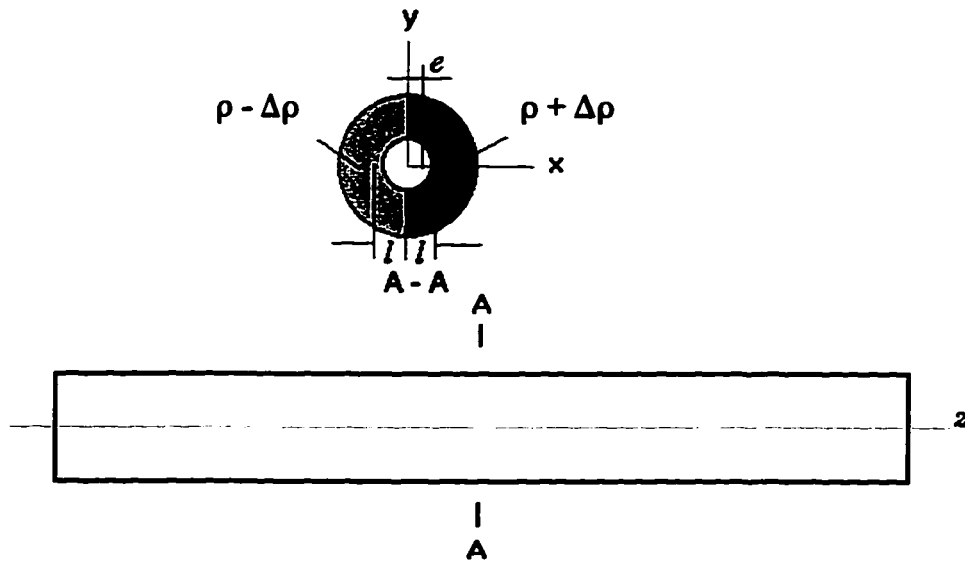


Figure 3.1 Mass imbalance modelled with varying density

A shaft with mass eccentricity  $e$  and average density  $\rho$ , can be modelled by two half rings with density  $\rho + \Delta\rho$  and  $\rho - \Delta\rho$ , respectively. It follows that

$$\begin{aligned} & (\rho + \Delta\rho) \frac{1}{2} \pi (R_2^2 - R_1^2) \Delta h (l - e) \\ & = (\rho - \Delta\rho) \frac{1}{2} \pi (R_2^2 - R_1^2) \Delta h (l + e) \end{aligned} \quad (3.2)$$

where



$\Delta h$  = length of the concerned part of a shaft

Thus, mass density difference  $2\Delta\rho$  between two half rings can be determined by

$$\Delta\rho = \frac{e}{l} \rho \quad (3.3)$$

where

$e$  = mass eccentricity of the concerned shaft

Effects of mass imbalance on natural frequencies and mode shapes were examined based on the variable density model. The shaft, as shown in Figure 3.1, has a modulus of elasticity  $E = 2 \times 10^5$  MPa, density  $\rho = 7800$  kg/m<sup>3</sup>, radii  $R_1 = 25$  mm and  $R_2 = 50$  mm, and length  $L = 800$  mm. For simplicity, a constant mass eccentricity  $e$  is assumed to be in the  $x$ - $z$  plane.

An exciting force parallel to the  $x$ -axis was applied in the  $x$ - $z$  plane to find the corresponding bending modes. For relative eccentricity  $e/R$  ( $R$  is defined as the exterior diameter of the shaft, i.e.,  $R_2$ ) up to 0.10, the first five natural frequencies decrease or increase within 1% of zero-eccentricity frequencies, or even remain unchanged, as shown in Figure 3.2. However, the bending modes are coupled with axial modes when there is any eccentricity. This is because the resultant inertial forces in the axial direction are no longer zero, as shown in Figure 3.6(a), and thus make contributions to the axial vibration. The axial resonant response is not very significant and is very sharp near the coupled frequency. The coupled modes, therefore, are dominated by the bending motion in this case.

To examine the bending modes in the  $y$ - $z$  plane, an exciting force parallel to the  $y$ -axis was used to capture the  $y$ - $z$  bending modes. The natural frequencies decrease slightly, compared with  $\omega_0$ , as shown in Figure 3.3. Since the inertial forces resulting from bending vibrations, whose resultant forces are away from the shaft centre, make contributions to the torsional motion, as shown in Figure 3.6(b), there appear the bending dominant vibrations coupled with the torsional modes.

The torsional frequencies were also examined versus mass imbalance. Since the

---

resultant inertial forces arising from the torsional vibrations are not zero in the  $y$  direction, as shown in Figure 3.6(c), the bending modes are found in the range of the resonant torsional frequencies. The torsional dominant coupled vibration frequencies increase slightly with  $e/R$ , as shown in Figure 3.4.

Scanning forcing frequencies of axial forces yielded the natural frequencies in the axial direction. Since the resultant inertial forces are not located at the centre of the shaft, as shown in Figure 3.6(d), coupled axial-bending vibrations have been found, in which axial modes are dominant. The frequencies decrease slightly with  $e/R$ , as shown in Figure 3.5. The bending motion happens in the  $x$ - $z$  plane.

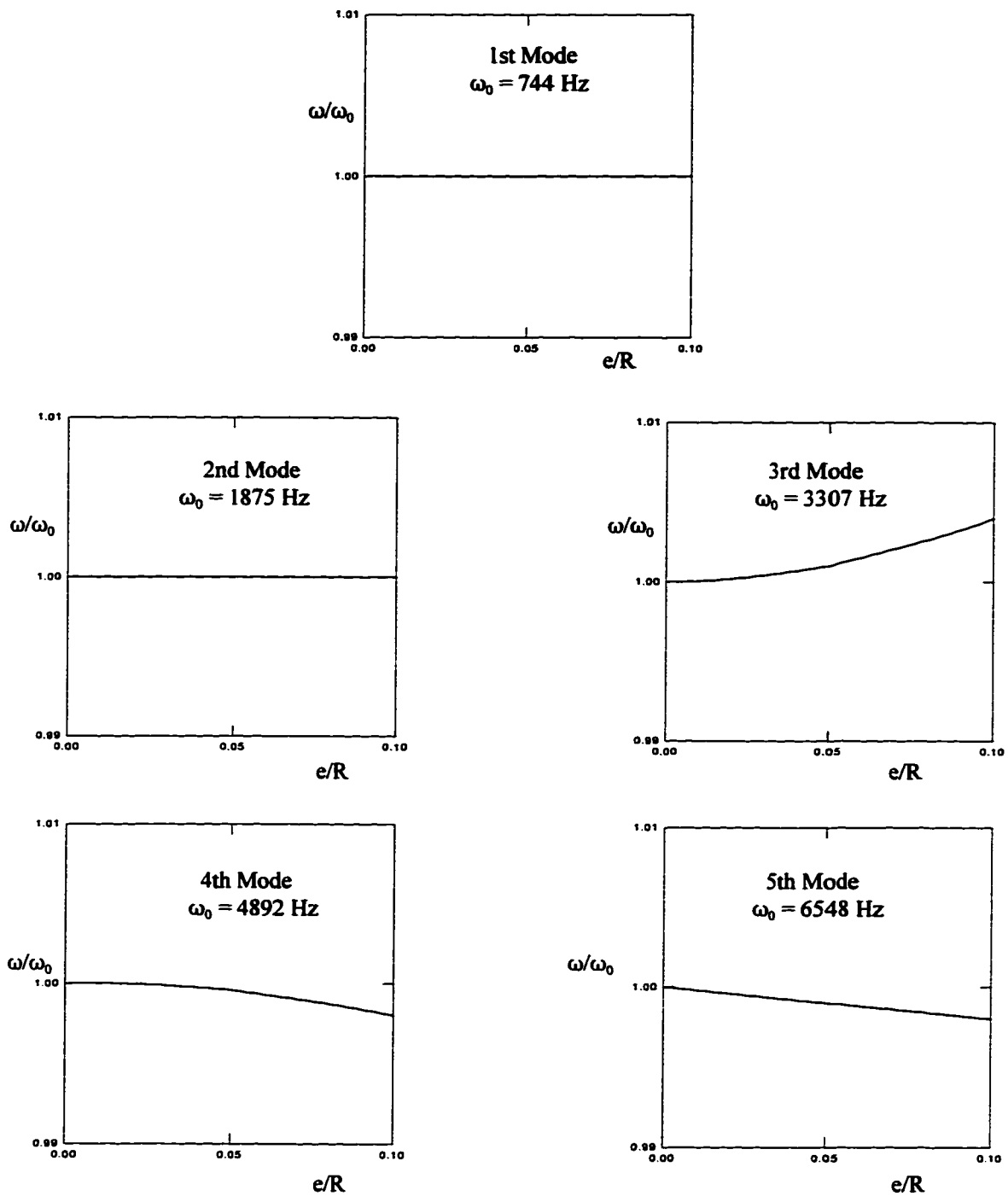


**Figure 3.2** x-z plane bending frequency vs. mass imbalance. Coupled bending-axial modes appear for  $e \neq 0$ .  $\omega_0$  denotes frequency for  $e=0$  and  $R$  stands for the exterior diameter of the shaft.

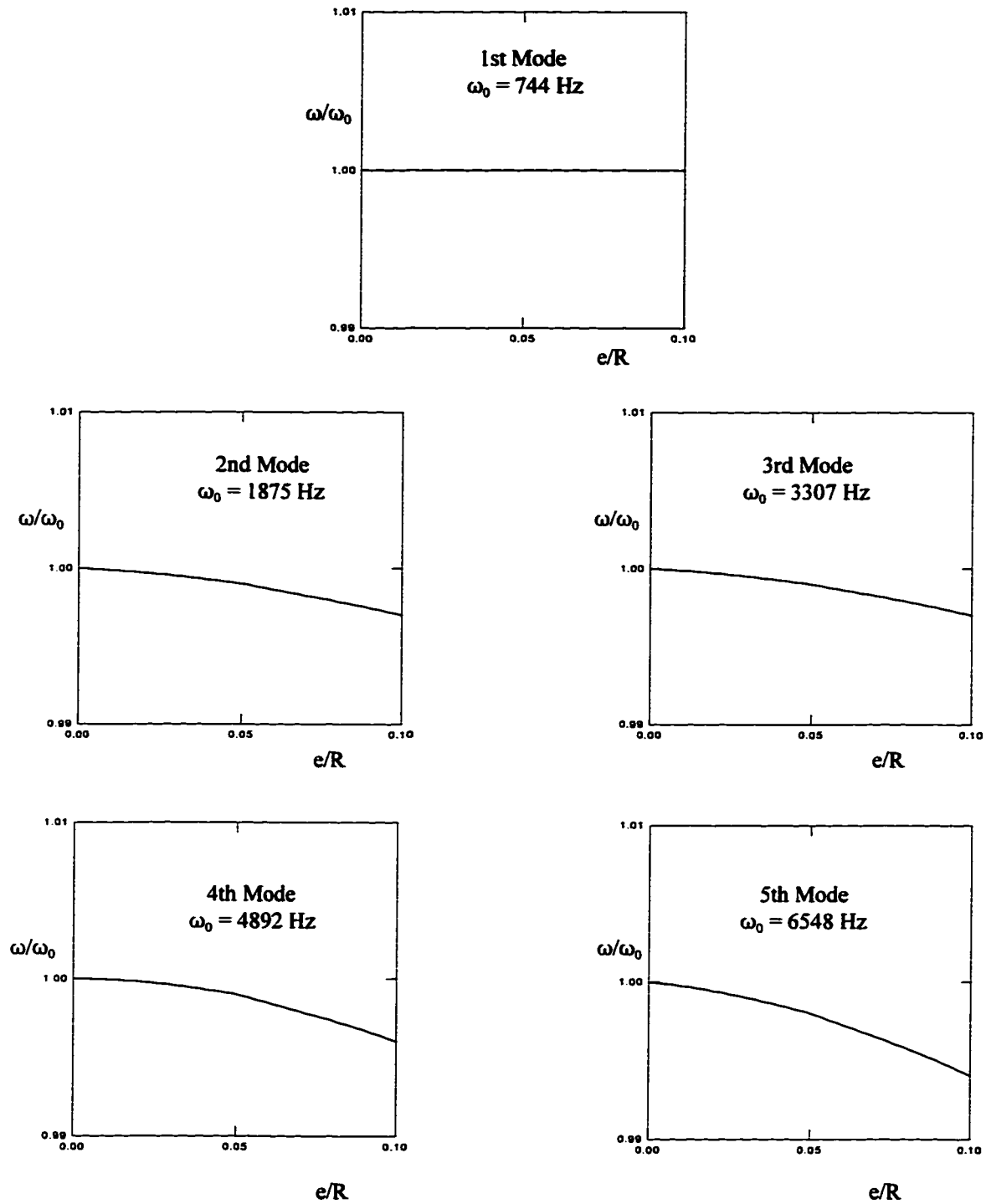


**Figure 3.3**  $y$ - $z$  plane bending frequency vs. mass imbalance. Coupled bending-torsional modes appear for  $e \neq 0$ .  $\omega_0$  denotes frequency for  $e=0$  and  $R$  stands for the exterior diameter of the shaft.

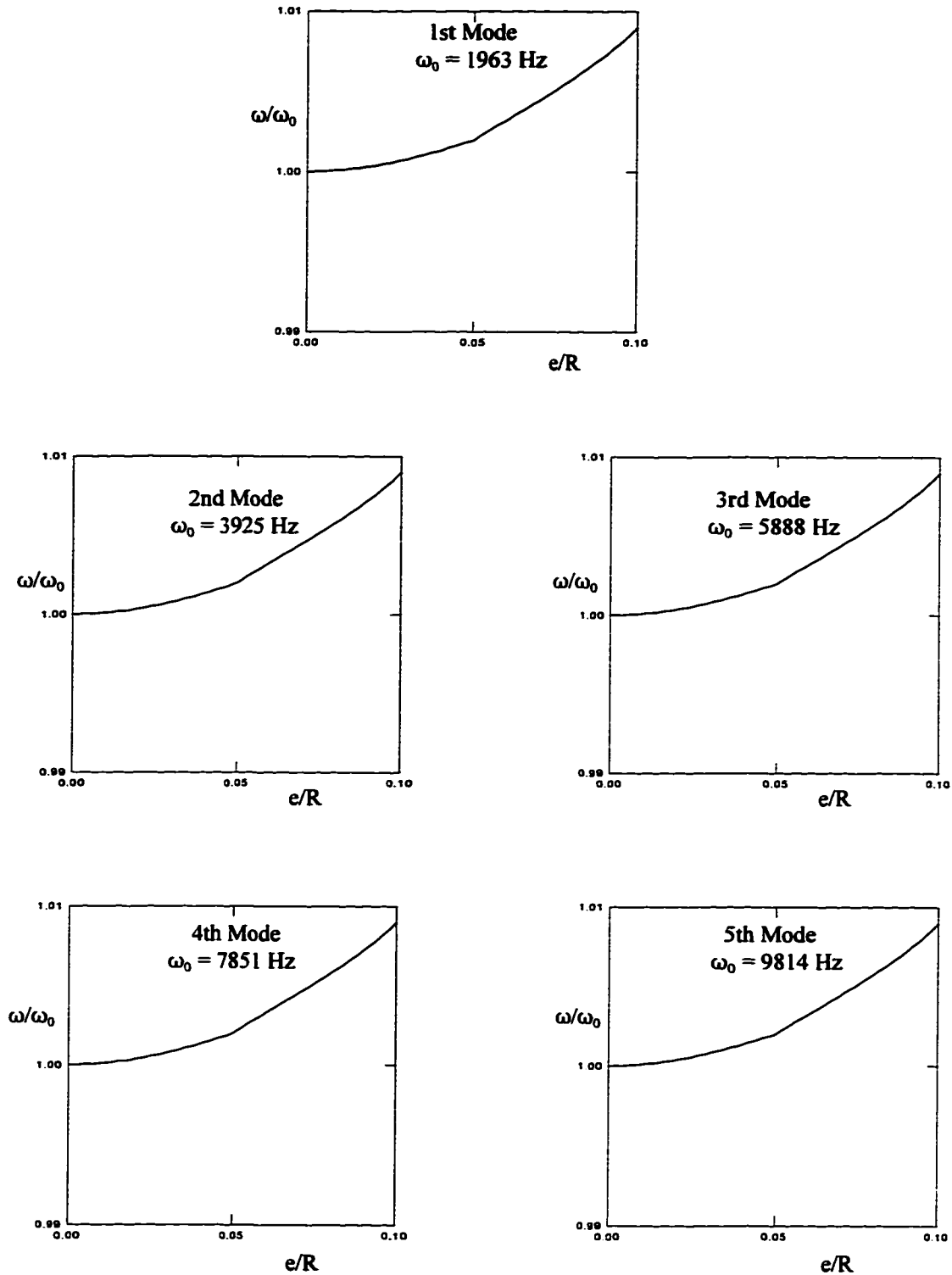


**Figure 3.4** Torsional frequency vs. mass imbalance. Coupled torsional-bending modes appear for  $e \neq 0$ .  $\omega_0$  denotes frequency for  $e=0$  and  $R$  stands for the exterior diameter of the shaft.

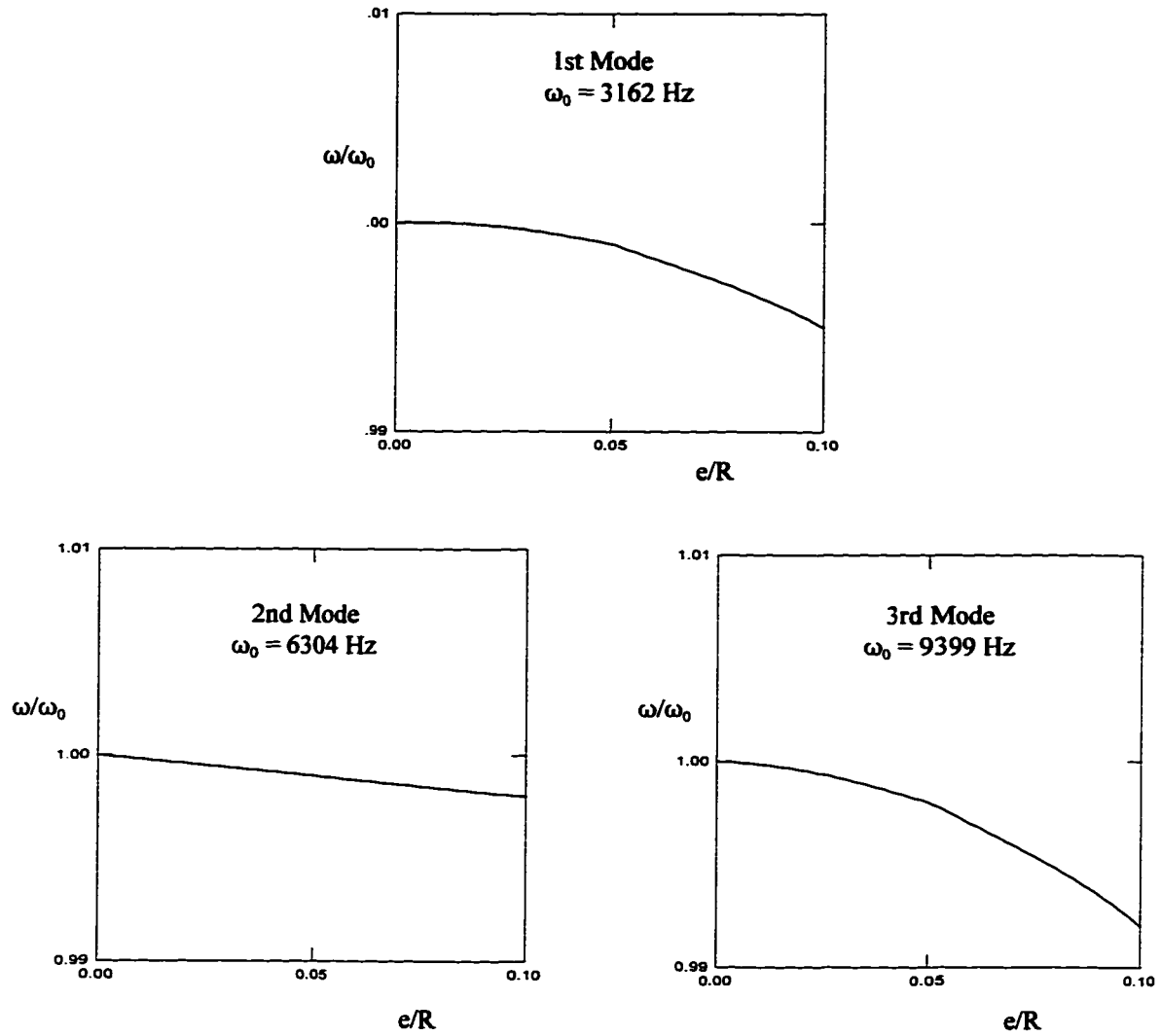


**Figure 3.5** Axial frequency vs. mass imbalance. Coupled axial-bending modes appear for  $e \neq 0$ .  $\omega_0$  denotes frequency for  $e=0$  and  $R$  stands for the exterior diameter of the shaft.

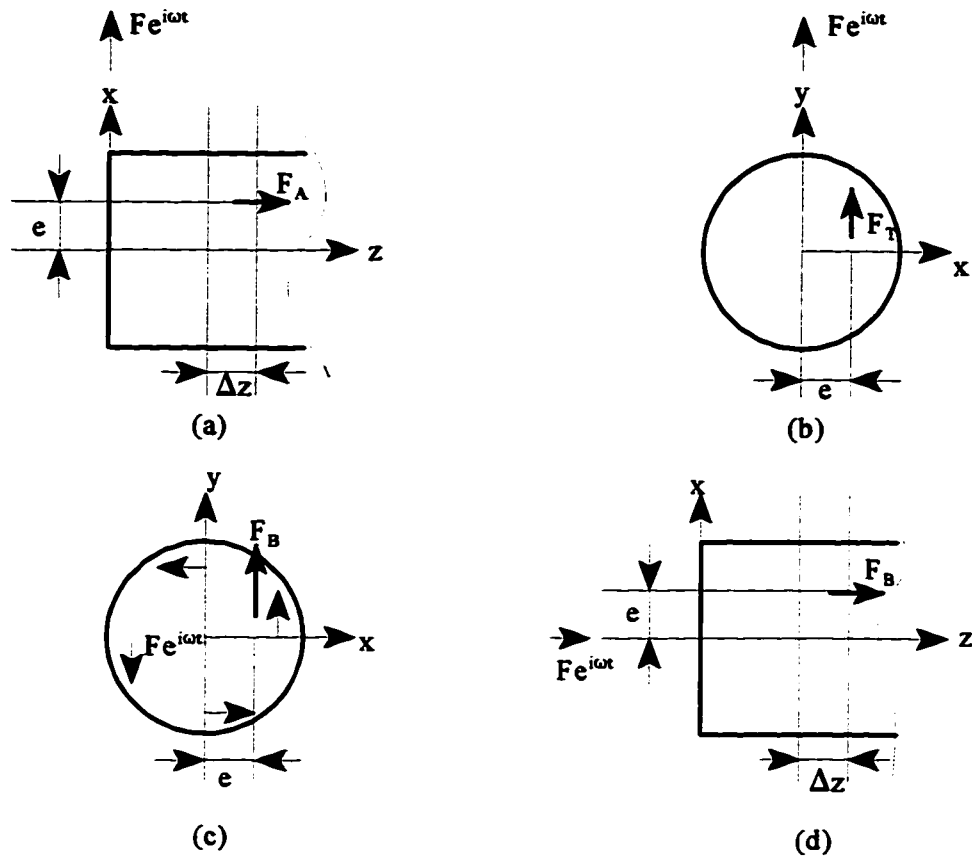
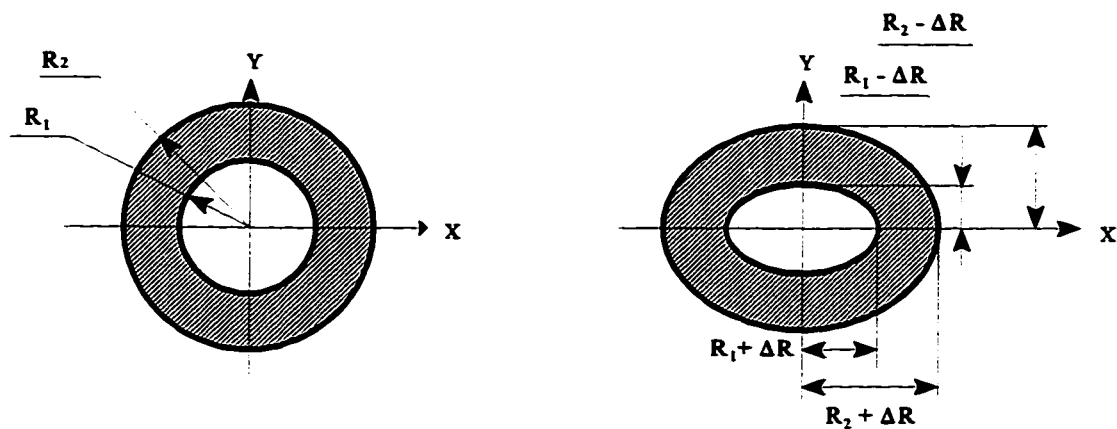


Figure 3.6 Resultant inertial forces in a region over a length  $\Delta z$  where  $e \neq 0$  contributing to another mode type. (a) bending-axial, (b) bending-torsional, (c) torsional-bending, and (d) axial-bending. ( $Fe^{i\omega t}$  stands for exciting forces causing a dominant mode,  $F_A$ ,  $F_T$ , and  $F_B$  denote resultant inertial forces causing a minor axial, torsional, and bending mode, respectively.)

### 3.2 Non-Circular Cross Section Modelling

Using the proposed 3-D solid finite element modelling, the dynamic behaviour of a shaft with non-circular cross sections can be appropriately examined. Here an example of a shaft with an elliptic cross section, as shown in Figure 3.6, is illustrated.

The elliptic cross section was assumed to have the same cross section area of the



**Figure 3.7 Elliptic cross sections compared with circular cross sections**

shaft, thus satisfying

$$\begin{aligned}
 S &= \pi(R_2 + \Delta R)(R_2 - \Delta R) - \pi(R_1 + \Delta R)(R_1 - \Delta R) \\
 &= \pi(R_2^2 - R_1^2)
 \end{aligned}
 \tag{3.4}$$

where

$S$  = cross section area

$R_1$  = interior radius of the circular cross section



$R_2$  = exterior radius of the circular cross section

$\Delta R$  = amount increased and decreased in x and y directions to form an elliptic cross section

For a shaft with radii  $R_1 = 25$  mm and  $R_2 = 50$  mm, and length  $L = 800$  mm, a corresponding elliptic shaft is formed with  $\Delta R = 5$  mm, as shown in Figure 3.7. Compared with the circular shaft, the elliptic one has different natural bending frequencies in x and y directions, as shown in Table 3.1. The results show that the natural frequencies in x direction have been increased due to the greater shaft stiffness, and that those in y direction have been decreased due to the reduced shaft stiffness.

**Table 3.1 Effect of elliptic cross sections on the natural frequencies of bending modes**

<b>Model number</b>	<b>Results for circular cross sections (Hz)</b>	<b>Results in x direction for elliptic cross sections (Hz)</b>	<b>Results in y direction for elliptic cross sections (Hz)</b>
1	744	795	684
2	1875	1994	1732
3	3307	3506	3069
4	4892	5175	4556
5	6548	6916	6115

For the torsional motion, the corresponding vibrational modes have also been examined, as shown in Table 3.2. All the first five natural frequencies have been found to be decreased. This is due to the increased polar moment of inertia. An existing formula for a uniform shaft with circular cross sections can be given by

$$\omega_n = \frac{n\pi}{L} \sqrt{\frac{G}{\rho}}, \quad n = 1, 2, 3, \dots \quad (3.5)$$

For non-uniform cross sections, the above formula cannot be employed due to warping effects.

The axial or longitudinal vibration of the shaft has been analysed as well. The obtained results indicate that there is almost no effect of cross sections on the axial natural frequencies, as shown in Table 3.3.

**Table 3.2 Effect of elliptic cross sections on the natural frequencies of torsional modes, bar theory results in parentheses**

Model number	Results for circular cross sections (Hz)	Results for elliptic cross sections (Hz)
1	1963 (1963)	1934
2	3925 (3926)	3866
3	5888 (5889)	5792
4	7851 (7852)	7707
5	9814 (9815)	9600

**Table 3.3 Effect of elliptic cross sections on the natural frequencies of axial modes, bar theory results in parentheses**

Model number	Results for circular cross sections (Hz)	Results for elliptic cross sections (Hz)
1	3162 (3165)	3162
2	6304 (6330)	6304
3	9399 (9495)	9400

---

### 3.3 Discussion

Since 3-D solid finite elements are employed, shafts with any complex geometry could be appropriately modelled. Here non-axisymmetric shafts have been modelled to reveal or confirm some dynamic behaviour.

To find whether a vibrational mode is coupled with another mode, one only needs to verify whether the inertial forces/moments/torques caused by the former make contributions to the latter. If so, the vibration becomes coupled with these two modes. In this case, an exciting force/moment/torque in one mode will cause the corresponding mode shape which is dominant, and simultaneously the accompanying inertial forces/moments/torque will stimulate the other minor mode, whose amplitude-frequency curve is very sharp.

Non-circular cross section effects on the dynamic response are illustrated through an elliptic shaft. Bending frequencies in the two orthogonal directions are different. A simple formula of torsional frequency using the bar theory agrees with the computed finite element results for circular shafts, but not with elliptic ones. However, there seems almost no effect on axial mode vibrations.

## Chapter 4

# Rotating Shaft Modelling

An analysis of rotating shafts is somewhat more complicated than that of other vibrational systems in that it involves gyroscopic effects, shaft whirls, and mode shapes and natural frequencies which vary with rotational speeds. The simple Jeffcott (1919) model and the Euler beam theory would not yield natural frequency difference between forward and backward whirls in the fixed frame. Although a spinning Timoshenko beam has closed form solutions of free vibration for circular uniform beams (Zhu and Han, 1992), a 3-D solid finite element modelling of rotating shafts is believed to be a more general and rigorous approach for any kind of shafts.

There are two alternatives of coordinate systems: fixed and rotating frames. If the fixed frame is used, each point of the shaft will have both rigid and elastic displacements. Thus unknown displacements would no longer be small (Choi et al, 1992) and the corresponding finite element formulation would be more complicated. The potential energy would involve rigid body motion, thus yielding time-dependent stiffness. However, when the rotating reference frame is introduced, displacement functions will involve only an elastic motion. This allows one to visualize the complicated dynamic behaviour of the rotating shaft as though it were simply oscillating in the rotating frame like a non-rotating shaft.

Lagrangian mechanics has been employed instead of Newtonian mechanics to establish finite element equations of the rotating shaft. Unlike beam approaches, which involve both translational and rotational kinetic energies, the 3-D solid continuum modelling

involves only translational kinetic energy of all particles. Therefore, gyroscopic effects are automatically included in such kinetic energy expressions, which has been confirmed by the difference of forward and backward whirl frequencies expressed in the fixed reference frame.

## 4.1 Dynamic Modelling

A shaft is regarded as an elastic body, which is assumed to be rotating about its undeformed centroidal line with rotational speed  $\Omega$ . The motion of the body is divided into the rigid body motion, which defines the rotating frame, and the small elastic motion relative to this frame. Gyroscopic effects are automatically included with this consistent modelling.

Since displacements are measured relatively to the rotating frame, an assumption of small strains and displacements is valid, which facilitate an elastic dynamic analysis using 3-D solid FE techniques. Huge eigenvalue problems can be avoided when the above-mentioned reduction procedures are implemented to obtain the responses of interest.

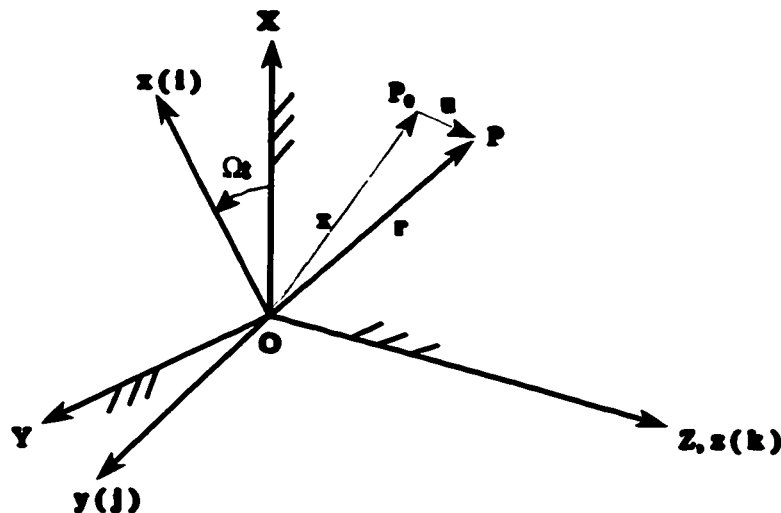


**Figure 4.1 Reference frames and particle positions in shaft**

### 4.1.1 Reference Frames and Kinematics

A particle in the shaft, depicted in Figure 4.1, will have both rigid body and elastic displacements. The frame  $(OXYZ)$  is fixed. The  $Z$ -axis coincides with the undeformed centroidal line of the shaft. The rotating frame  $(Oxyz)$  with unit basis vectors  $i, j$ , and  $k$ , has the rigid body motion of the shaft. It is obtained from the fixed frame by a rotation of angle  $\Omega t$  about the  $Z$ -axis. Only an elastic motion needs to be examined for all particles in the shaft. The material particle position  $P_0$  in the undeformed configuration will move to the position  $P$ , all in the rotating frame.

For the particle with a position vector  $\mathbf{x}$ , its displaced position vector  $\mathbf{r}$  involving a displacement  $\mathbf{u}$  can be given by

$$\mathbf{r} = \mathbf{x} + \mathbf{u} \quad (4.1)$$

where

$$\begin{aligned} \mathbf{x} &= xi + yj + zk \\ \mathbf{u} &= ui + vj + wk \end{aligned} \quad (4.2)$$

The particle velocity can be expressed as

$$\begin{aligned} \dot{\mathbf{r}} &= \left. \frac{\partial}{\partial t} \mathbf{r}(\mathbf{x}, t) \right|_{\mathbf{x}} \\ &= [ \dot{u} - \Omega(y+v) ] i + [ \dot{v} + \Omega(x+u) ] j + \dot{w} k \end{aligned} \quad (4.3)$$

### 4.1.2 Kinetic Energy

If a beam is modelled, its kinetic energy is generally written as the sum of the translational kinetic energy of its centroidal line and the rotational kinetic energy of its cross sections. For the three-dimensional continuum modelled here, however, its kinetic energy

is composed of the sum of only translational energy in terms of each particle.

From Eqs. (4.1 - 4.2), the kinetic energy for any part of the rotating shaft can be given by

$$\begin{aligned}
 T &= \frac{1}{2} \iiint \rho \dot{\mathbf{r}} \cdot \dot{\mathbf{r}} \, dx \, dy \, dz \\
 &= \frac{1}{2} \iiint \rho [(u^2 + v^2 + w^2) + \Omega^2(u^2 + v^2) + \\
 &\quad + 2\Omega^2(yv + xu) + 2\Omega(uv - v\dot{u}) + \\
 &\quad + \Omega^2(x^2 + y^2) + 2\Omega(x\dot{v} - y\dot{u})] \, dx \, dy \, dz
 \end{aligned} \tag{4.4}$$

where  $\rho$  is the density of the concerned part.

It can be seen that the total kinetic energy consists of six terms as shown in Eq.(4.4). However, only the first four terms contribute to the equation of the deformable rotating shaft. This will be discussed later.

### 4.1.3 Potential Energy

Since small displacements are assumed in the rotating reference frame, the potential energy of the concerned part of the shaft can be given by

$$\begin{aligned}
 V &= \frac{E}{2(1+\nu)} \iiint \left[ \frac{\nu}{1-2\nu} \left( \frac{\partial u}{\partial x} + \frac{\partial v}{\partial y} + \frac{\partial w}{\partial z} \right)^2 + \left( \frac{\partial u}{\partial x} \right)^2 + \left( \frac{\partial v}{\partial y} \right)^2 + \left( \frac{\partial w}{\partial z} \right)^2 + \right. \\
 &\quad \left. + \frac{1}{2} \left( \frac{\partial w}{\partial y} + \frac{\partial v}{\partial z} \right)^2 + \frac{1}{2} \left( \frac{\partial u}{\partial z} + \frac{\partial w}{\partial x} \right)^2 + \frac{1}{2} \left( \frac{\partial v}{\partial x} + \frac{\partial u}{\partial y} \right)^2 \right] dx \, dy \, dz
 \end{aligned} \tag{4.5}$$

## 4.2 Finite Element Formulation

As shown in Figure 2.1, a shaft is divided into a series of superelements which consist of four basic continuum elements. The finite element formulation is discussed here with respect to such a continuum element.

The proposed subparametric element approach is employed which has  $C^1$  continuity along the axial direction, as shown in Chapter 2. Eq.(4.4) can be defined as

$$T = T_1 + T_2 + T_3 + T_4 + T_5 + T_6 \quad (4.6)$$

Substitution of Eqs.(2.1) and (2.22) into Eq.(4.6) yields the kinetic energy in the matrix form.

The first term of Eq.(4.6) is given by

$$\begin{aligned} T_1 &= \frac{1}{2} \iiint \rho ( \dot{u}^2 + \dot{v}^2 + \dot{w}^2 ) dx dy dz \\ &= \frac{1}{2} \{ \dot{U} \}^T \begin{bmatrix} [m_u] & 0 & 0 \\ 0 & [m_v] & 0 \\ 0 & 0 & [m_w] \end{bmatrix} \{ \dot{U} \} \end{aligned} \quad (4.7)$$

where

$$\{ U \} = \left[ \{ u_i \}^T, \left\{ \frac{\partial u_i}{\partial z} \right\}^T, \{ v_i \}^T, \left\{ \frac{\partial v_i}{\partial z} \right\}^T, \{ w_i \}^T \right]^T$$

and  $[m_u]$ ,  $[m_v]$ , and  $[m_w]$  can be evaluated in terms of Eq.(2.16). It can be seen that Eq.(4.7) represents the relative kinetic energy in the rotating reference frame. For a non-rotating shaft (i.e.,  $\Omega=0$ ), this would be the total kinetic energy.

The second term is given by

$$\begin{aligned} T_2 &= \frac{1}{2} \iiint \rho \Omega^2 ( u^2 + v^2 ) dx dy dz \\ &= \frac{1}{2} \Omega^2 \{ U \}^T \begin{bmatrix} [m_u] & 0 & 0 \\ 0 & [m_v] & 0 \\ 0 & 0 & 0 \end{bmatrix} \{ U \} \end{aligned} \quad (4.8)$$



which is related to the centrifugal forces due to elastic deformations of the shaft. For a short piece of the shaft over an axial length  $dz$  with a certain cross section, the corresponding equivalent forces can be imagined having not only a resultant inertial force but also a resultant inertial moment if  $u$  and/or  $v$  vary with  $z$ . Such a moment will contribute to the gyroscopic effect of the shaft in the fixed reference frame.

The third term is given by

$$\begin{aligned} T_3 &= \iiint \rho \Omega^2 (xu + yv) \, dx \, dy \, dz \\ &= \Omega^2 \{U\}^T \begin{bmatrix} \{N_x\} \\ \{N_y\} \\ 0 \end{bmatrix} \end{aligned} \quad (4.9)$$

where

$$\begin{aligned} \{N_x\} &= [T_u]^{-T} \int \int \int \rho \{g_u\} \{g\}^T \det[J] \, d\xi \, d\eta \, d\zeta [T]^{-1} \{x\} \\ \{N_y\} &= [T_v]^{-T} \int \int \int \rho \{g_v\} \{g\}^T \det[J] \, d\xi \, d\eta \, d\zeta [T]^{-1} \{y\} \end{aligned}$$

Eq.(4.9) represents centrifugal forces, which are often considered as equivalent external forces when non-vibrational stresses are analysed for rotating bodies. It does not include the centrifugal forces due to elastic displacements.

The fourth term is given by

$$\begin{aligned} T_4 &= \iiint \rho \Omega (\dot{v}u - u\dot{v}) \, dx \, dy \, dz \\ &= \Omega \{\dot{U}\}^T \begin{bmatrix} 0 & -[I]^T & 0 \\ [I] & 0 & 0 \\ 0 & 0 & 0 \end{bmatrix} \{U\} \end{aligned} \quad (4.10)$$

where

$$[J] = [T_v]^{-T} \int_{-1}^1 \int_{-1}^1 \int_{-1}^1 \rho \{g_v\} \{g_v\}^T \det[J] d\xi d\eta d\zeta [T_u]^{-1}$$

Eq.(4.10) involves the inertial forces caused by Coriolis acceleration. This term is introduced due to the use of the rotating reference frame. It will also contribute to the gyroscopic effect of the rotating shaft.

The fifth term is given by

$$\begin{aligned} T_5 &= \frac{1}{2} \iiint \rho \Omega^2 (x^2 + y^2) dx dy dz \\ &= \text{const} \end{aligned} \quad (4.11)$$

which involves the rotational kinetic energy due to the rigid body motion of the rotating shaft. This term obviously makes no contribution to the equation of the motion in the rotating frame.

The last term is given by

$$\begin{aligned} T_6 &= \iiint \rho \Omega (xv - yu) dx dy dz \\ &= \Omega \{ \dot{U} \}^T \begin{bmatrix} \{R_x\} \\ \{R_y\} \\ 0 \end{bmatrix} \end{aligned} \quad (4.12)$$

where

$$\begin{aligned} \{R_x\} &= -[T_u]^{-T} \int_{-1}^1 \int_{-1}^1 \int_{-1}^1 \rho \{g_u\} \{g\}^T \det[J] d\xi d\eta d\zeta [T]^{-1} \{y_i\} \\ \{R_y\} &= [T_v]^{-T} \int_{-1}^1 \int_{-1}^1 \int_{-1}^1 \rho \{g_v\} \{g\}^T \det[J] d\xi d\eta d\zeta [T]^{-1} \{x_i\} \end{aligned}$$

This term also involves the Coriolis component due to the motion of the rotating shaft. However, it can be seen that Eq.(4.12) does not contribute to the equation of the motion if Lagrange's equations of motion are employed (Meirovitch, 1967).

The potential energy in the rotating frame can be rewritten in the matrix form as

$$V = \frac{1}{2} \iiint \{\epsilon\}^T [D] \{\epsilon\} dx dy dz \quad (4.5')$$

where

$$\{\epsilon\} = \left\{ \frac{\partial u}{\partial x}, \frac{\partial v}{\partial y}, \frac{\partial w}{\partial z}, \frac{\partial u}{\partial y} + \frac{\partial v}{\partial x}, \frac{\partial v}{\partial z} + \frac{\partial w}{\partial y}, \frac{\partial u}{\partial z} + \frac{\partial w}{\partial x} \right\}^T$$

[D] = Hooke matrix of elastic coefficients (see Appendix A.2)

Note that Eq.(4.5') can also be expressed in the same form as Eq.(2.11).

### 4.3 Equation of Motion

Since the kinetic and potential energies for each element are expressed in the matrix form in terms of its nodal variables, the finite element equation of the rotating shaft can be obtained using Hamilton's principle

$$\int_{t_1}^{t_2} (\delta T - \delta V + \delta W) dt = 0 \quad (4.13)$$

where  $\delta W$  is the virtual work done by internal and external generalized nodal forces.

Substitution of Eqs.(4.6)-(4.12) and (2.11) into Eq.(4.13) yields the equation of motion for a basic continuum element:

$$[M]\{\ddot{U}\} + [G(\Omega)]\{\dot{U}\} + [K_r(\Omega)]\{U\} = \{N(\Omega)\} + \{f\} + \{F\} \quad (4.14)$$

where

$$\{U\} = \left[ \{u_i\}^T, \left\{ \frac{\partial u_i}{\partial z} \right\}^T, \{v_i\}^T, \left\{ \frac{\partial v_i}{\partial z} \right\}^T, \{w_i\}^T \right]^T$$

$$[M] = \begin{bmatrix} [m_r] & 0 & 0 \\ 0 & [m_r] & 0 \\ 0 & 0 & [m] \end{bmatrix}$$

$$[G(\Omega)] = 2\Omega \begin{bmatrix} 0 & -[m_r] & 0 \\ [m_r] & 0 & 0 \\ 0 & 0 & 0 \end{bmatrix}$$

$$[K_r(\Omega)] = [K] - \Omega^2 \begin{bmatrix} [m_r] & 0 & 0 \\ 0 & [m_r] & 0 \\ 0 & 0 & 0 \end{bmatrix}$$

$$\{N(\Omega)\} = \Omega^2 [\{N_x\}^T, \{N_y\}^T, 0]^T$$

$\{f\}$  = internal generalized force vector

$\{F\}$  = external generalized force vector

To keep  $C^1$  continuity along the shaft  $z$  axis and improve convergence, the above displacements  $u$ ,  $v$ , and  $w$  are defined by Eq.(2.22). Thus five nodal variables including two slopes at each node are involved, and transformation coefficient matrices are given by

$$\begin{aligned} [T_u] &= [T_v] = [T_r] \\ [T_w] &= [T] \end{aligned} \quad (4.15)$$

where  $[T_r]$  and  $[T]$  are given by Eq.(2.24) and Appendix A.1, respectively. Matrices  $[I]$ ,  $[m_u]$  and  $[m_v]$  turn out to be the same, i.e.

$$[I] = [m_u] = [m_v] = [m_r] \quad (4.16)$$

where

$$[m_r] = [T_r]^{-T} \int_{-1}^1 \int_{-1}^1 \int_{-1}^1 \rho \{g_r\} \{g_r\}^T \det[J] d\xi d\eta d\zeta [T_r]^{-1}$$

## 4.4 Discussions

Since the rotating reference frame is introduced, a finite element formulation can be obtained using linear three-dimensional kinematics and elasticity theory. Eq.(4.14) involves both particular and homogeneous solutions.

The particular solution for the whole shaft can be obtained by eliminating the first two terms of Eq.(4.14). It has been found that the resultant force of  $\{N(\Omega)\}$  is just the centrifugal force for each basic element, and that its resultant moment is zero when a uniform shaft is examined.  $[K]$  instead of  $[K_r(\Omega)]$  is often used to calculate stresses of rotating bodies. As seen in Eq.(4.14), this is a very approximate approach and may be only valid for rotating bodies at a low rotational speed. For some mass imbalance distribution along the shaft, the

---

$\Omega^2$  term in  $[K_r(\Omega)]$  mainly contributes to its deformation. At some specific speeds, the deformation can be very large, and the shaft can then be severely bowed. This will be discussed in the next chapter.

The homogeneous solution can be attained by eliminating the right-hand-side terms. This solution will describe the shaft whirling motion, and provide the corresponding natural frequencies of the rotating shaft, i.e., resonant forward and backward whirl frequencies, which will be elucidated in the next chapter.

## **Chapter 5**

# **Motion of Rotating Shaft**

Since a rotating shaft is modelled in the rotating reference frame using three-dimensional solid finite elements, its dynamic behaviour will be analysed based on this frame. As shown in this chapter, the motion of the rotating shaft will be defined or explained in a rotating frame. Shaft whirl, critical speeds and unbalance response will be analysed using three-dimensional solid finite elements.

It can be shown that using the rotating reference frame gives a clear view of the shaft motion. Since the rotating frame is used throughout the analysis, the transverse displacements of the particles within the same cross section are almost the same when bending behaviour is examined. If the fixed frame were employed, the displacements involving rigid and elastic motions would be different even within the same cross section.

Shaft whirl motion has been successfully modelled using the proposed three-dimensional solid finite elements. As rotational speeds increase, the divergence of forward and backward resonant frequencies expressed in the fixed reference frame becomes significant. For a uniform shaft, the computed results have good agreement with the solutions of the spinning Timoshenko beam.

In the rotating frame, an exciting force acting in one direction could lead to forward and backward whirl. These two kinds of whirl could coexist along the shaft. When resonance occurs, the shaft will be totally either forward or backward.

Critical speeds of the rotating shaft are closely related to its unbalance responses,

which present constant magnitudes in the rotating frame if a free-free boundary condition or symmetric bearing supports are used.

When Newton's law is simply applied to a beam or shaft, its rotordynamic analysis is usually carried out in the fixed reference frame. Parameters such as forward and backward whirl frequencies will depend on the reference frame chosen. They can be easily transformed from one to another coordinate system.

## 5.1 Shaft Whirl

Shaft whirl is a unique dynamic phenomenon which does not exist in other non-rotating vibrational systems. The whirl frequencies vary with rotational speeds. There are two kinds of whirl motion: forward and backward whirals. If the whirl is asynchronous with shaft speed, there will be dynamic stresses varying with time.

### 5.1.1 Definition of Whirl in Rotating Frame

Since the rotating frame is used to simulate the shaft motion, its rigid rotation will not be involved. The shaft can only have elastic displacements  $u$ ,  $v$ , and  $w$  in this frame. Due to Coriolis acceleration, there will be both  $x$  and  $y$  directional motions even though excitation or perturbation is only applied in either  $x$  or  $y$  direction.

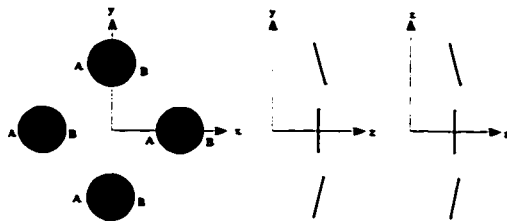


Figure 5.1 Shaft whirl in rotating frame



Figure 5.1 illustrates the whirling motion of a cross section in a symmetric circular shaft. Line AB within this section will not have any rotational motion in the  $xy$  plane. In a one cycle of oscillation, this section has a translational motion along the  $z$  axis although a small relative deformation within the section may be involved. Nevertheless, it undergoes axial vibrations as seen in the  $y-z$  and  $x-z$  planes.

It can be seen that in the reference of the rotating frame, the complicated shaft whirl can be simply viewed as elastic translational motion if deflection is considered, as though the shaft were not rotating. The axial oscillation of the shaft is also involved. Unlike a non-rotating shaft, it has a circular trajectory at resonance. The whirl frequencies at resonance are just natural frequencies, which vary with rotational speed  $\Omega$  when bending vibration is examined. This type of motion is called shaft whirl.

The whirl direction could be the same as or opposite to that of the rotational speed. If the dynamic responses in  $x$  and  $y$  directions of the rotating frame are expressed in the following complex form:

$$\begin{aligned} u &= A e^{i(\omega t + \varphi_u)} \\ v &= B e^{i(\omega t + \varphi_v)} \end{aligned} \quad (5.1)$$

then the whirl angle relative to the  $x$ -axis is given by

$$\theta = \tan^{-1} \left( \frac{Re(v)}{Re(u)} \right) \quad (5.2)$$

where  $Re(v)$  and  $Re(u)$  denote the real part of  $v$  and  $u$ , respectively. It follows that the whirl frequency in the rotating frame can be given by

$$\begin{aligned} \omega_{rot} &= \frac{d\theta}{dt} \\ &= \omega \frac{AB \sin(\varphi_u - \varphi_v)}{A^2 \cos^2(\omega t + \varphi_u) + B^2 \cos^2(\omega t + \varphi_v)} \end{aligned} \quad (5.3)$$

The whirl will be counter clockwise if  $\varphi_u - \varphi_v$  is within  $0 - \pi$ , and otherwise will be clockwise.

There is a special case where  $A=B$  and  $|\varphi_u - \varphi_v| = \pi/2$ . In this case, the whirl frequency  $\omega_{rot}$  will be constant all the time.

It is quite common for rotordynamic analysts to use whirl frequencies in the fixed reference frame. A simple formula can be given by

$$\omega_{fix} = \omega_{rot} + \Omega \quad (5.4)$$

where  $\Omega$  is always defined as positive sign "+".

If  $\omega_{rot}$  has the same rotational direction as  $\Omega$ , then it is said to have forward whirl in the rotating frame; if it has the opposite direction, then it is said to have backward whirl in the rotating frame. The direction and frequency magnitude of the corresponding whirl in the fixed frame is then determined by Eq.(5.4). It can be found that backward whirl in the rotating frame can become forward whirl in the fixed frame.

### 5.1.2 Forced Responses in Rotating Frame

Since the rotating frame is used to simulate the dynamic responses of shafts, excitations are expressed in this frame as well. Gravity is one kind of excitation with a forcing frequency of a rotational speed. Mass imbalance, which can be modelled by a distributed density, can be regarded as a resultant constant force in the rotating frame. Fluid disturbances, forces due to misalignment and other excitations can also be given in the rotating frame.

To examine the dynamic responses, an exciting force has been applied to the different locations with a varying forcing frequency. A simple uniform shaft, as shown in Figure 2.2, is illustrated. Since 3-D solid finite elements are employed, trajectories at different nodal points within one cross section are not the same. However, it was found that transverse displacements within the same cross section are very close in this case regardless of very different axial displacements. Therefore, the average value of the transverse displacements at different nodal points is adopted to represent the trajectory of this cross section.

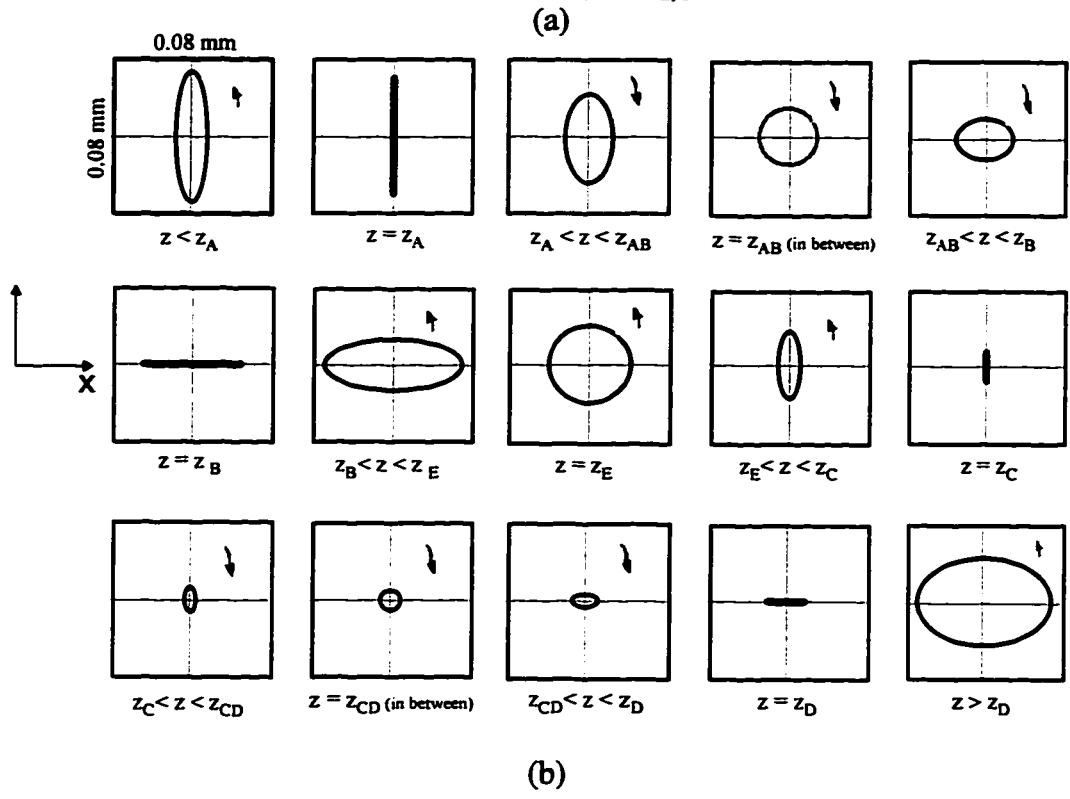
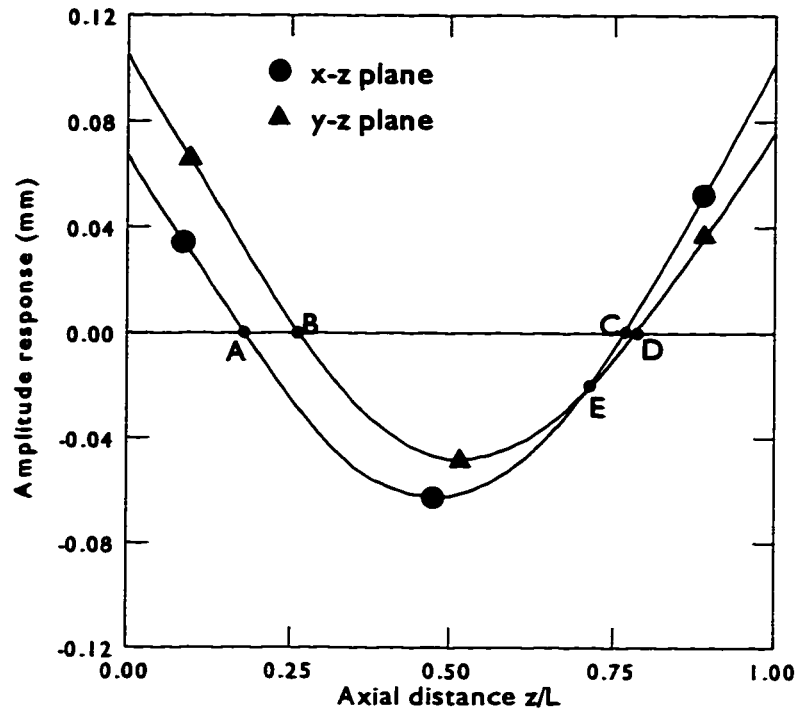


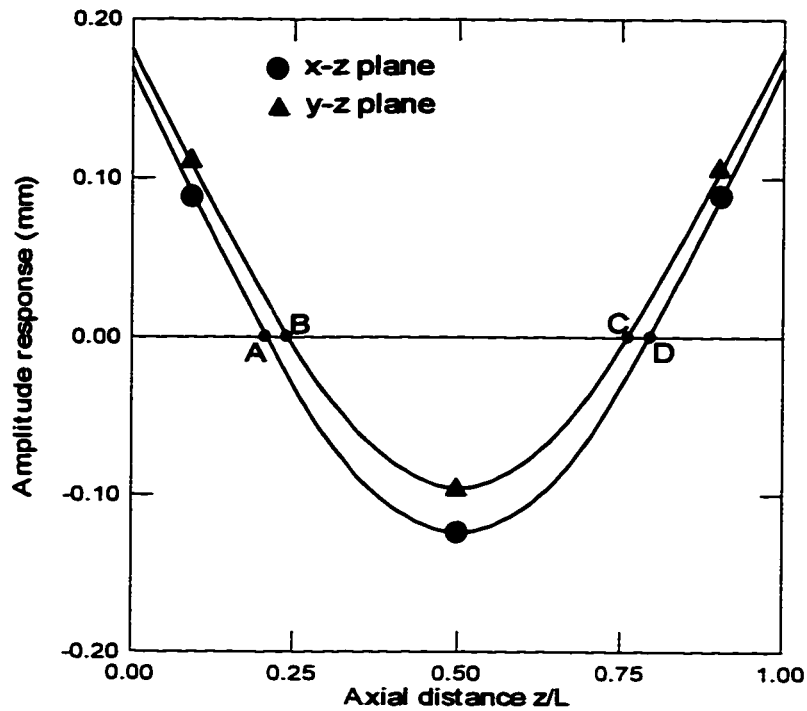
Figure 5.2 Forced response when an exciting force with an amplitude of 1 kN and a frequency of 495 Hz was applied to the left end in x-direction in the rotating frame ( $\Omega = 1570.8$  rad/sec). (a) transverse displacement responses vs. axial distance, and (b) trajectories of transverse displacements for various cross sections from the left to the right end of the shaft.

When an exciting force with an amplitude of 1 kN is exerted to the left end of the shaft with a rotational speed of 1570.8 rad/sec in the  $x$ -direction of the rotating frame, its forced response can be shown in Figure 5.2. Figure 5.2 (a) gives the  $x$  directional and  $y$ -directional responses, which in terms of Eq. (5.1) generally yield elliptic trajectories as shown in Figure 5.2 (b).

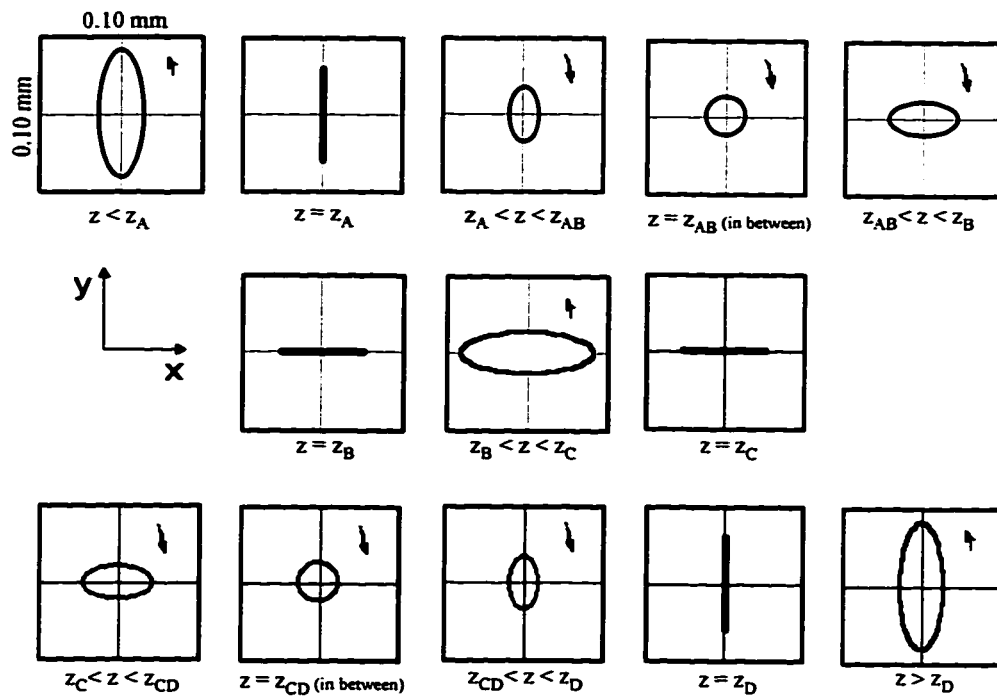
It can be seen that unlike non-rotating bodies, an excitation on the shaft in the  $x$ -direction causes transverse displacements in not only the  $x$ -direction but also the  $y$ -direction. This is due to the rotational speed which leads to the Coriolis acceleration term. In Figure 5.1 (a) the positive amplitude of the  $x$ -directional response corresponds to phase angle  $\varphi_u = 0$ ; that of the  $y$ -directional response corresponds to  $\varphi_v = -\pi/2$ .  $X$ -directional responses have a phase angle of either  $0$  or  $-\pi$ ; and  $y$ -directional responses have a phase angle of either  $-\pi/2$  or  $\pi/2$ .

Near the left end, the trajectories of the shaft can be seen to be elliptic after the superposition of two orthogonal responses, with forward whirl as defined in Eq. (5.3). At the location A, the transverse displacement in the  $x$ - $z$  plane becomes zero, thus the trajectory being a straight line along the  $y$ -direction. Between locations A and B of the shaft, there exists backward whirl in terms of Eq. (5.3). There is a location between A and B where amplitudes of  $x$  and  $y$  directional responses are the same, thus making the backward trajectory circular. At the location B, the trajectory becomes a straight line in the  $x$ -direction. Then after location B, the trajectories become forward again until the location E at which the two amplitude curves intersect. Obviously the trajectory of the location E is circular with forward whirl. The trajectories appear backward between locations C and D. Near the right end of the shaft after the location D, the trajectories become forward.

It can be seen that the response due to the left end excitation is not symmetric with respect to the two ends of the shaft. The shaft whirl can be both forward and backward in a shaft. When the two same exciting forces are applied to the left and right ends, the response becomes symmetric with respect to the two ends of the shaft, but still forward whirl coexists with backward whirl, as shown in Figure 5.3.



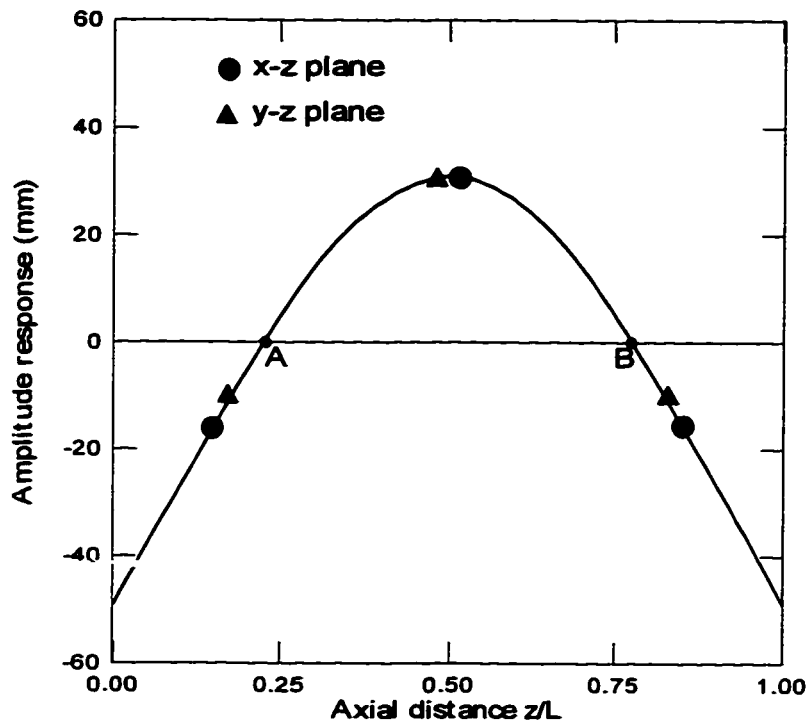
(a)



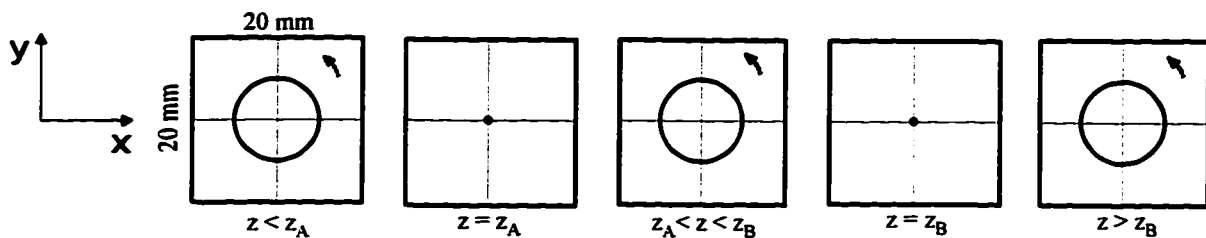
(b)

**Figure 5.3** Forced response when exciting forces with an amplitude of 1 kN and a frequency of 495 Hz were applied to the two ends in x-direction in the rotating frame ( $\Omega = 1570.8$  rad/sec). (a) transverse displacement responses vs. axial distance, and (b) trajectories of transverse displacements for various cross sections from the left to the right end of the shaft.

From Figures 5.2 and 5.3, it can be found that at that forcing frequency for the prescribed rotational speed, the shaft mainly presents forward whirling motion except for the regions between A and B, and between C and D. A, B, C, and D are the critical points where the transition between forward and backward whirls is located. At these points, the whirl becomes a straight line. With the forcing frequency being increased to 505 Hz, the characteristics of the response are totally different, as shown in Figure 5.4.



(a)



(b)

**Figure 5.4** Resonance response when an exciting force with an amplitude of 1 kN and a frequency of 505 Hz was applied to the left end in x-direction in the rotating frame ( $\Omega = 1570.8$  rad/sec). (a) transverse displacement responses vs. axial distance, and (b) trajectories of transverse displacements for various cross sections from the left to the right end of the shaft.

Though only one exciting force is applied to the left end of the shaft, the response is symmetric with respect to the two ends of the shaft for that frequency. There is purely forward whirl with circular trajectories all along the shaft. The amplitude of the response is extremely large, compared with other forcing frequencies. This is believed to be forward whirl at resonance.

With the forcing frequency increased, the trajectories of the response generally become elliptic again. Forward whirl coexists with backward whirl. When a frequency is far away from the previous forward whirl frequency, backward whirl becomes dominant. At the frequency of 930 Hz, the forced response and its trajectories are shown in Figure 5.5.

Similarly, one might be able to envision the response behaviour as discussed above for Figure 5.2. Clearly, backward whirl is dominant along the whole shaft. Forward whirl appears between points A and B, and between points C and D. The intersection points E and F correspond to the circular trajectories.

When the forcing frequency increases to 979.6 Hz, the shaft has pure backward whirl responses along the whole shaft, as shown in Figure 5.6. This is the resonant backward whirl frequency, which corresponds to the peak amplitude responses along the whole shaft.

One can see that the characteristics of the shaft whirling motion depend on the forcing frequency in the rotating frame. There are resonant forward and backward whirl frequencies, i.e., natural frequencies of the rotating shaft. These resonant frequencies correspond to the peak amplitude responses, which could present very large magnitudes. In numerical analysis, large responses will be found when a forcing frequency is almost equal to the resonant frequencies. In this case, even if some excitation is applied into the shaft asymmetrically with respect to the shaft span, the response will still be symmetric with respect to the shaft span and will have either pure forward or pure backward whirl with all the circular trajectories. At other frequencies, forward and backward whirl will coexist along the shaft. Forward/backward whirl will be dominant if a forcing frequency is close to a resonant forward/backward frequency. The trajectories are usually elliptic. A straight line trajectory corresponds to a transition point where the forward whirl region adjoins the backward whirl region.

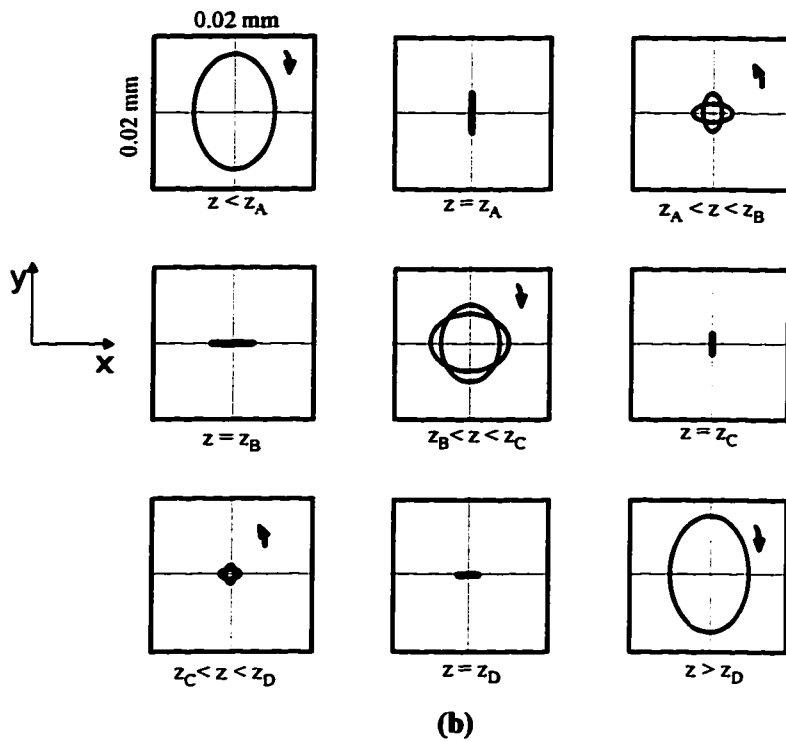
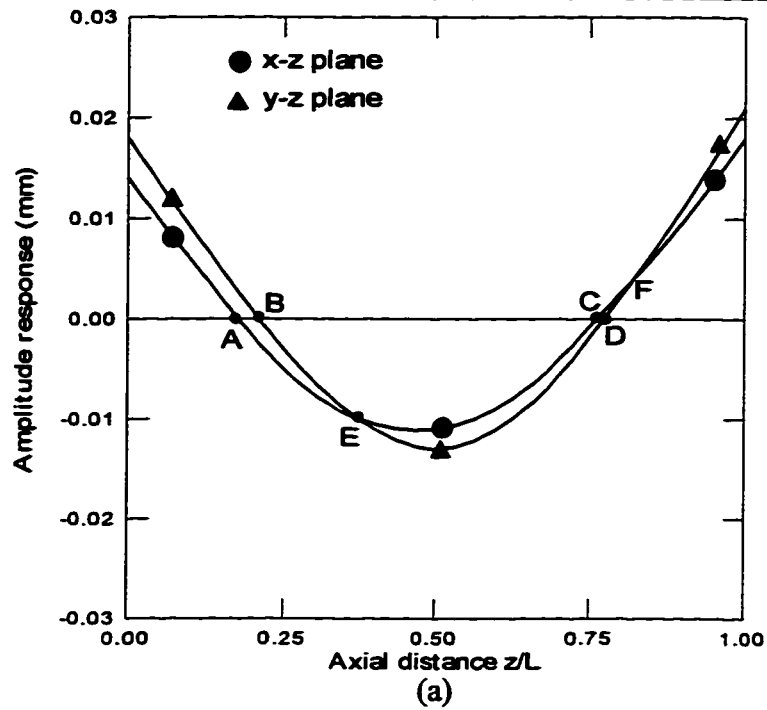
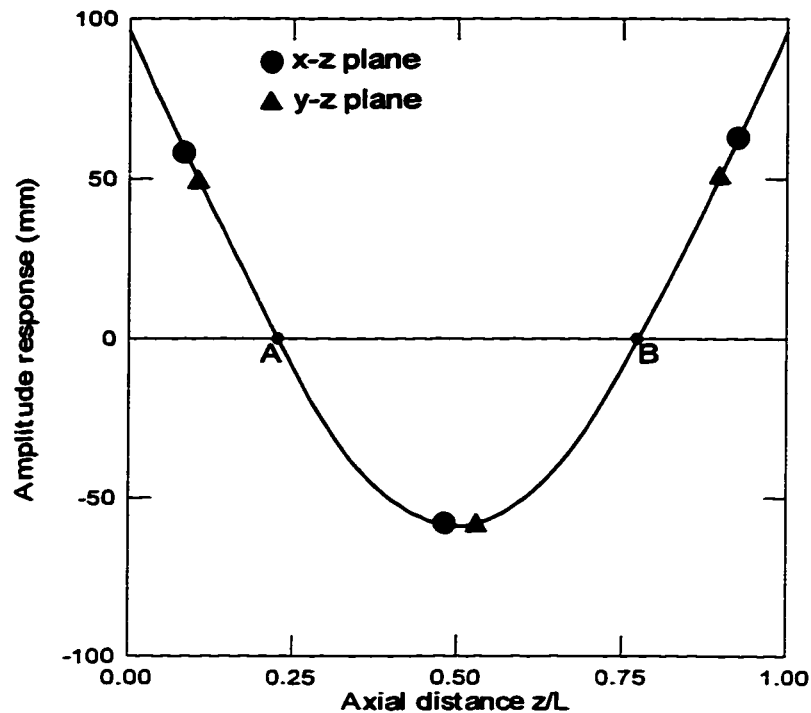
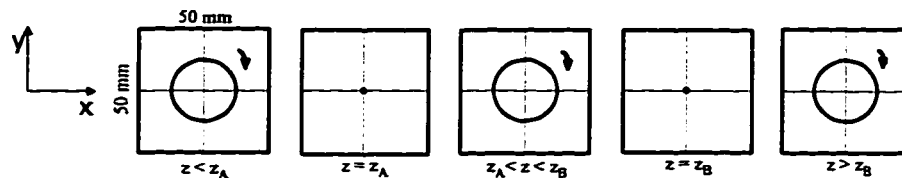


Figure 5.5 Forced response when an exciting force with an amplitude of 1 kN and a frequency of 930 Hz was applied to the left end in x-direction in the rotating frame ( $\Omega = 1570.8$  rad/sec). (a) transverse displacement responses vs. axial distance, and (b) trajectories of transverse displacements for various cross sections from the left to the right end of the shaft.





(a)



(b)

**Figure 5.6 Resonance response when an exciting force with an amplitude of 1 kN and a frequency of 979.6 Hz was applied to the left end in x-direction in the rotating frame ( $\Omega = 1570.8$  rad/sec). (a) transverse displacement responses vs. axial distance, and (b) trajectories of transverse displacements for various cross sections from the left to the right end of the shaft.**

Recently, Muszynska (1996) found the phenomenon of forward and backward whirl coexistence along a rotor in the fixed reference frame. As one can see from the above discussion, forward and backward whirls could exist simultaneously along the shaft in the *rotating frame*. This phenomenon has never been previously indicated. The detailed analysis is shown in a recently accepted paper (Yu et al., 1997) based on the above work.

### 5.1.3 Resonant Whirl Frequencies

Resonant whirl frequencies are defined as the natural frequencies of the rotating shaft. As indicated above, they correspond to infinitely large responses for undamped rotating shafts. In reality, a peak response frequency is considered to be the resonant frequency when a sweeping technique is used with a certain frequency step. At resonance, there is either forward or backward whirl all along the shaft, with the circular trajectories for a uniform shaft, as shown in Figures 5.4 (b) and 5.6 (b).

It is believed that for a uniform shaft, a 3-D solid continuum model will yield results close to solutions for the Timoshenko beam model, as shown in Table 5.1. The shaft size is the same as that in Figure 2.2. When the Timoshenko beam theory is employed, a shear coefficient influences vibration modes to a great extent. Cowper (1966) developed a series of formulas based on the 3-D elasticity theory to calculate these coefficients. Though some terms had to be dropped out to obtain these coefficients in terms of uniform beam models, the author believes that they can yield satisfactory solutions when the beam theory is adopted. In this example, a shear coefficient of 0.6202 was computed.

It can be seen that for an  $i$ th mode, there exist both forward and backward whirl frequencies for the given rotational speed instead of only one frequency for a non-rotating case. This confirms that gyroscopic effects have been consistently included using the proposed 3-D solid finite element modelling. All these values can be determined with computer simulation through the developed code involving reduction procedures, which will be discussed in the next chapter. Whirl directions and frequencies in the fixed frame can also be determined using Eqs.(5.1)-(5.4). As expected, these results are in very good agreement with the Timoshenko beam solutions.

It should be noted that the  $i$ th forward and backward whirl modes represent two different ones. The mode shapes will not be necessarily identical. Figure 5.7 gives their first mode shapes, i.e., relative whirling trajectory radius distribution along the shaft length. Magnitudes of mode shapes are set to be unity (1.00) at  $z = 0$ . It can be seen that if the magnitudes at the mid-span would be set to be the same, then the forward whirling mode

shape would seem to be more flatted.

**Table 5.1 Resonant forward and backward whirl frequencies (Hz) for  $\Omega=15000$  RPM (in parentheses is the percent difference from closed form solutions of rotating Timoshenko beams from Zu and Han (1992) with shear coefficient of 0.6202).**

Mode Type $F_i$ † $B_i$ †	3-D solid F.E. results (in rotating frame)	3-D solid F.E. results (in fixed frame)	Timoshenko beam solutions (in fixed frame)
$F_1$	505	755 (-0.3)	757
$B_1$	980	730 (-0.1)	731
$F_2$	1645	1895 (0.3)	1889
$B_2$	2101	1851 (0.3)	1845
$F_3$	3083	3333 (0.8)	3308
$B_3$	3529	3279 (0.8)	3254
$F_4$	4671	4921 (1.1)	4867
$B_4$	5112	4862 (1.1)	4807
$F_5$	6328	6578 (1.4)	6489
$B_5$	6766	6516 (1.4)	6426

† “F” and “B” are referred to forward and backward whirl, respectively.

Subscript “i” stands for a mode order,  $i=1, 2, 3, \dots$

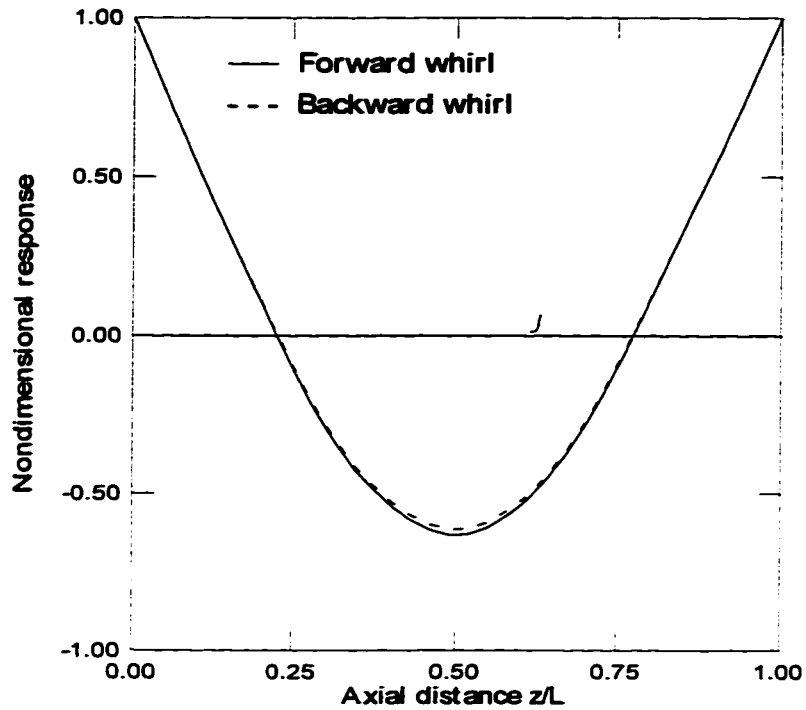


**Figure 5.7 Comparison of transverse mode shapes vs. shaft distance between resonant forward and backward whirling cases ( $\Omega=15000\text{RPM}$ ,  $\omega_f=505\text{ Hz}$  and  $\omega_b=980\text{ Hz}$  in rotating frame)**

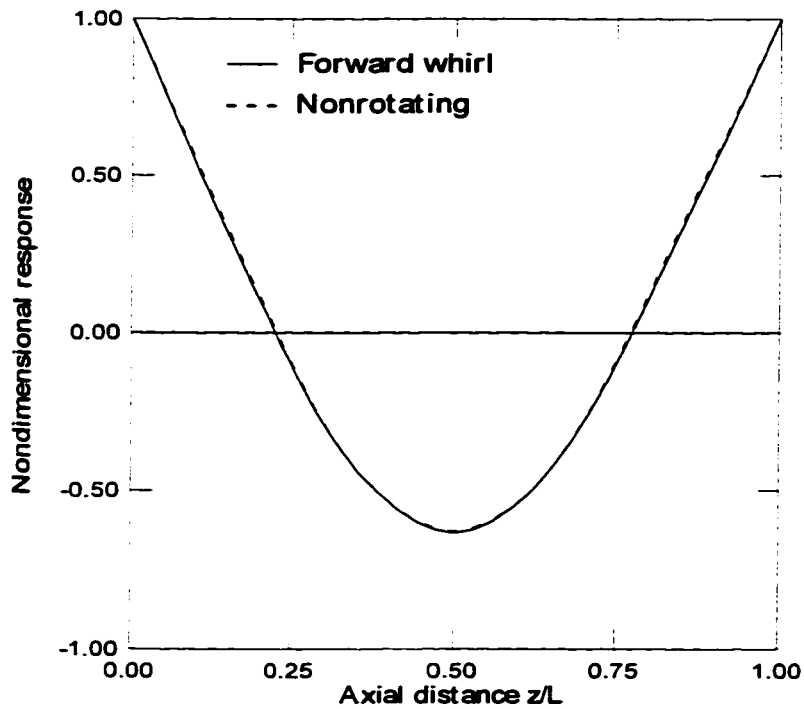


**Figure 5.8 Comparison of transverse mode shapes vs. axial distance between resonant forward whirling and non-rotating cases ( $\Omega=15000\text{ RPM}$ ,  $\omega_f=505\text{ Hz}$  in rotating frame and  $\omega_N=744\text{ Hz}$ )**

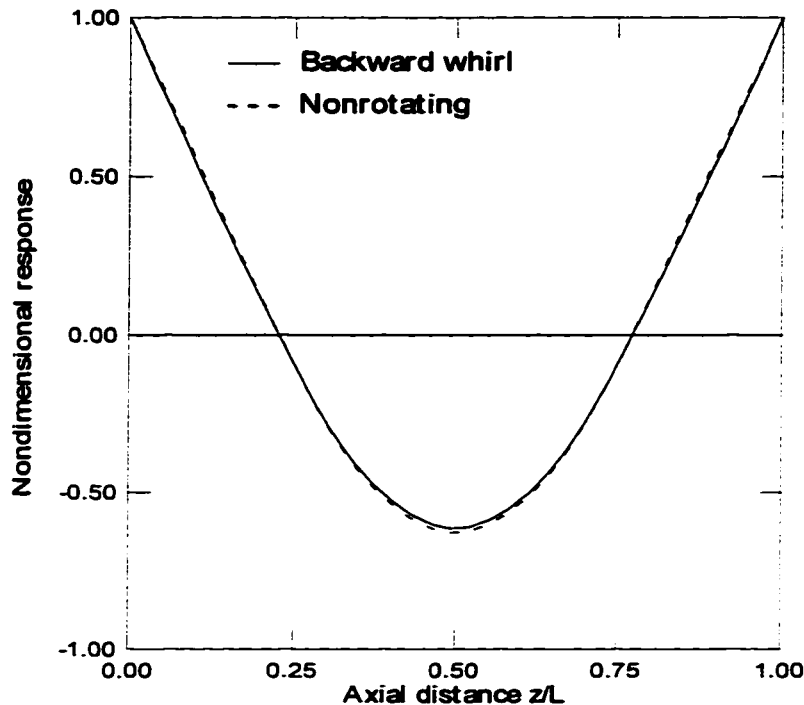


**Figure 5.9 Comparison of transverse mode shapes vs. axial distance between backward whirl and non-rotating case ( $\Omega = 15000$  RPM,  $\omega_b = 980$  Hz in rotating frame and  $\omega_N = 744$  Hz )**

Resonant whirling modes are not identical to non-rotating bending vibration modes either, as shown in Figures 5.8 and 5.9. It can be found that the ratios of end amplitudes to mid-span amplitudes are slightly different among the three mode shapes. The forward and the backward whirling modes have the lowest and highest ratios, respectively, while the non-rotating bending mode has an in-between ratio. It should be noted that whirling mode shapes rotate forward or backward around the shaft axis, while non-rotating mode shapes oscillate in the bending plane around the shaft axis with varying curves. All these properties show that each resonant or natural frequency (755 Hz for forward, 744 Hz for non-rotating, and 730 Hz for backward, if expressed in the fixed frame) corresponds to a unique mode, though there are some similarities among the three modes which are all conventionally called the first order.

The effect of rotational speeds on resonant whirl frequencies has been examined for the same shaft. The frequencies obtained directly from the analysis are expressed in the rotating frame, as shown in Figures 5.10 and 5.11. One can see that both forward and backward whirl frequencies expressed in the rotating frame decrease with rotational speeds. In this frame, as the speed increases, the absolute magnitudes of the resonant forward whirl frequencies decrease until they reach zero, and then increase; those for the backward whirl always increase.

If they are expressed in the fixed frame, the corresponding frequencies can be determined by Eq.(5.4). Conventionally, backward whirl is specified without adding a “-” sign to its frequency. Figure 5.12 shows the first five order whirl frequencies versus rotational speed. As expected, a zero speed corresponding to a non-rotating bending mode is the very special case of resonant whirling motions where the forward and backward whirl modes are degraded to a plane curve with only one frequency for each order. As the shaft speed increases, forward whirl frequencies increase and backward whirl frequencies decrease in the fixed frame. In the figure, the solid line denotes the forward whirl, and the broken line represents the backward whirl. This behaviour gives the information about the change rate of forward and backward whirl frequencies with respect to the rotating frame. From Eq.(5.4), it follows that

$$\frac{d\omega_{fix}}{d\Omega} = \frac{d\omega_{rot}}{d\Omega} + 1 \quad (5.5)$$

Since the left-hand-side will be always greater than zero ( “-” sign for backward frequencies is included), one can have

$$\frac{d\omega_{rot}}{d\Omega} > -1$$

In consideration of the fact that  $\frac{d\omega_{rot}}{d\Omega}$  is always less than zero, one can conclude that the change rate of whirl frequencies as shown in Figures 5.10 and 5.11 in terms of the rotating frame will be

---

$$-1 < \frac{d\omega_{rot}}{d\Omega} < 0 \quad (5.6)$$

The resonant whirl frequencies are also compared with the spinning Timoshenko beam solutions (Zhu and Han, 1992). As shown in Figures 5.13 and 5.14, they are in good agreement with each other for the uniform shaft. It should be noted that this is only used to verify the 3-D solid finite element solutions. In other cases such as tapered shafts and those with more complex geometry, the 3-D solid finite element approach is expected to yield more reliable accurate results than beam theories.

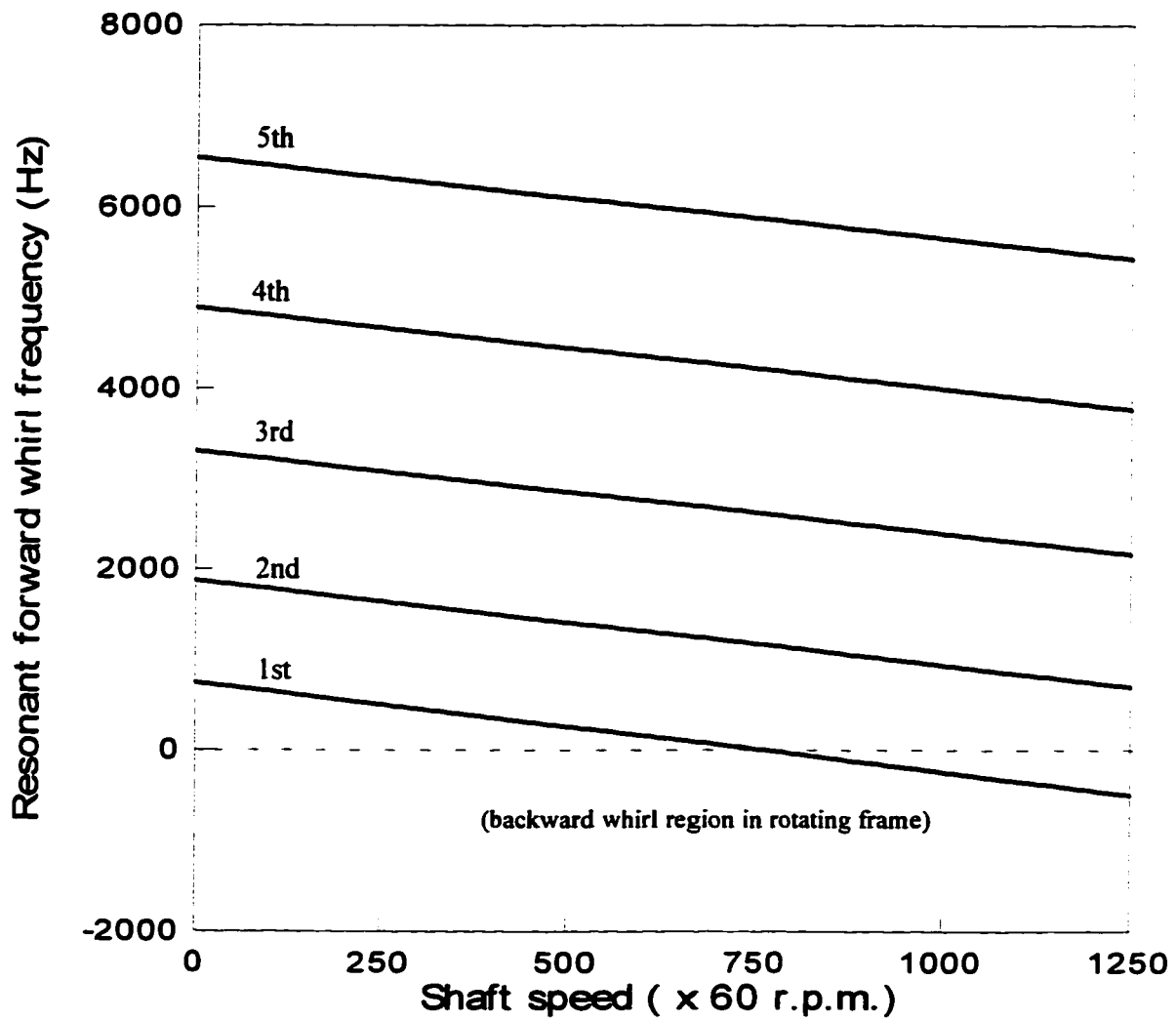


**Figure 5.10** Variation of resonant forward whirl frequencies in rotating frame with shaft speed



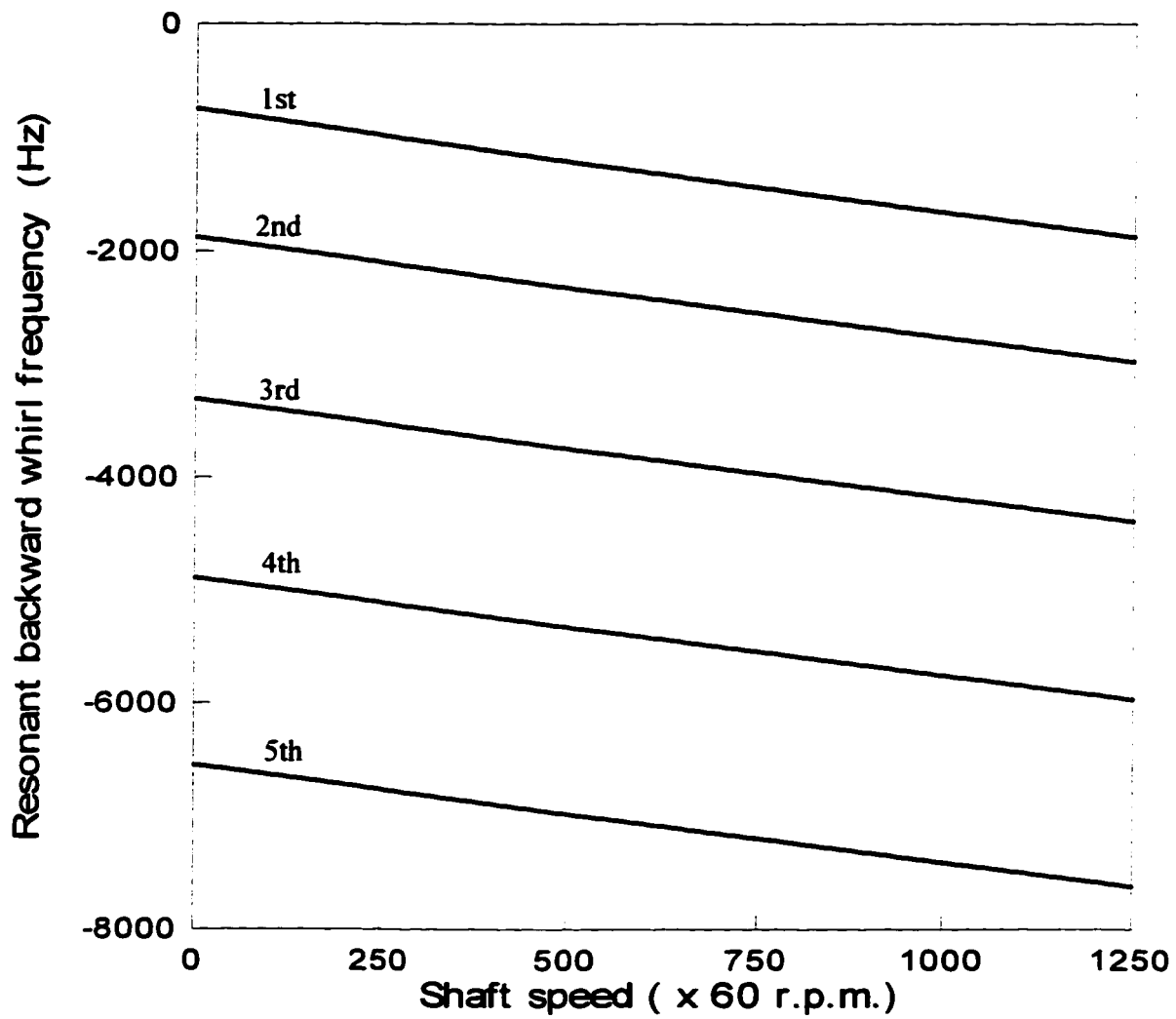


**Figure 5.11** Variation of resonant backward whirl frequencies in rotating frame with shaft speed

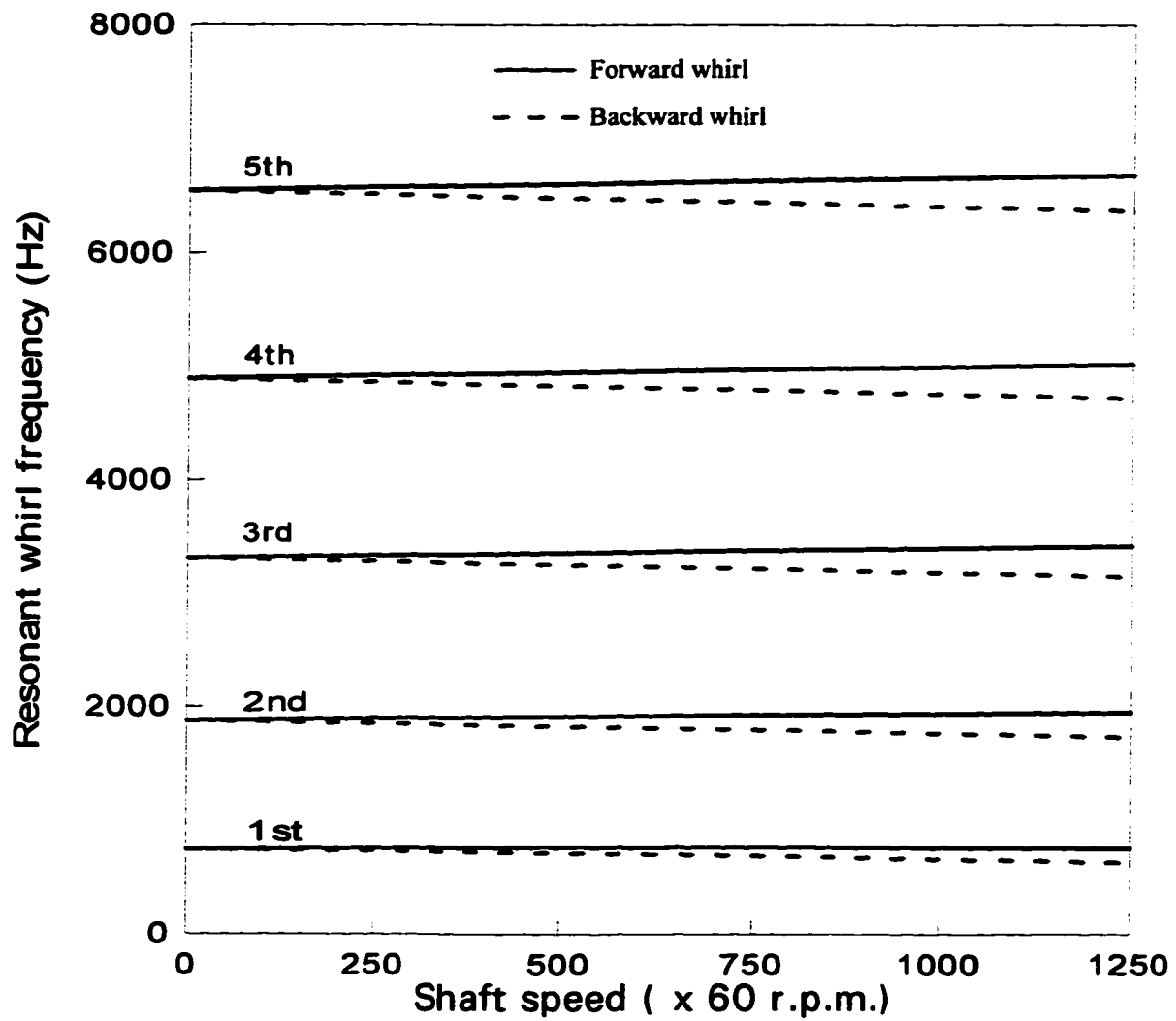


Figure 5.12 Variation of resonant whirl frequencies in fixed frame with shaft speed

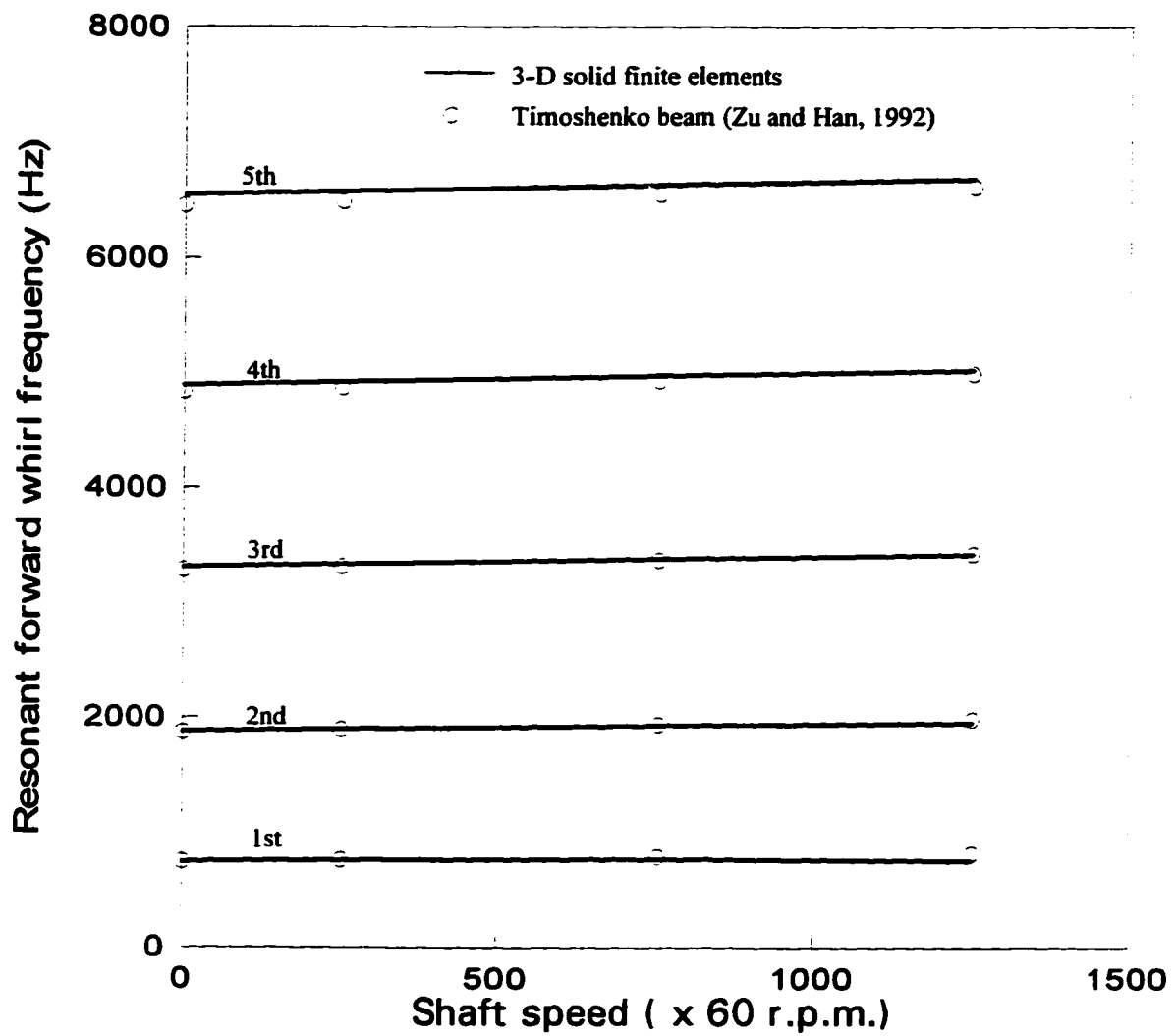


Figure 5.13 Comparison of resonant forward whirl frequencies between 3-D solid finite element and Timoshenko beam approaches

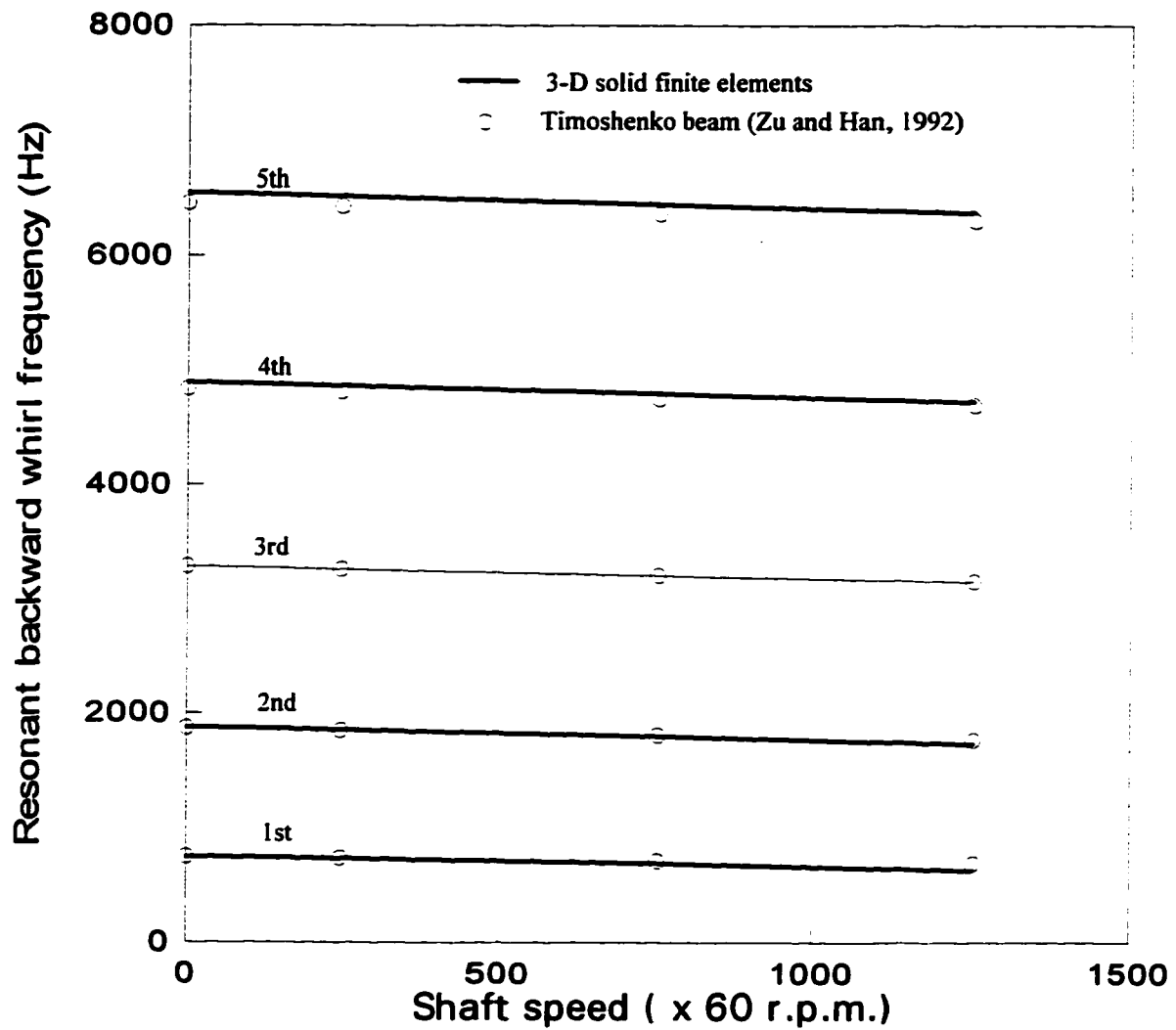


Figure 5.14 Comparison of resonant backward whirl frequencies between 3-D solid finite element and Timoshenko beam approaches

## 5.2 Critical Speeds and Unbalance Response

As one could see from the above, the rotational speed has significant effects on the dynamic response of the shaft. For each rotational speed, there exist resonant forward and backward whirling modes and corresponding frequencies. Critical speeds are often related to the peak system responses. All these are also related to the boundary conditions of the shaft. A simple free surface boundary condition is used here to illustrate their definitions and solution methodology.

### 5.2.1 Definition and Determination of Critical Speeds

Since mass imbalance is considered a major source which causes the unbalance response of the shaft, the flexural critical speed is defined as such a speed which leads to the peak steady-state response of the shaft. This case is also called synchronous whirl with a frequency of zero in the rotating frame or of the shaft speed in the fixed frame.

Mass imbalance rotates with the shaft. Therefore, in the rotating frame, the corresponding distributed centrifugal forces will be constant. If only steady-state unbalance response is concerned, the shaft does not vibrate in the rotating frame. Instead, when a rotational speed reaches the critical values, it *may* be severely bowed into the corresponding mode shape, which is “locked” in the rotating frame. In this case, the equation of motion for each finite element, i.e., Eq.(4.14), can be rewritten as

$$[K_r(\Omega)]\{U\} = \{N(\Omega)\} + \{f\} + \{F\} \quad (5.7)$$

where an external force vector  $\{F\}$  could be set zero when only unbalance response is examined due to shaft centrifugal forces.

To find critical speeds of the shaft, one does not have to know how mass imbalance is exactly distributed. If system matrices were to be assembled, the determinant of the matrix consisting of all elemental stiffness matrices  $[K_r(\Omega)]$  would have to be zero. However, this approach would lead to difficulty in obtaining solutions due to very high order polynomials

of  $\Omega$  being involved. An alternative can be used which involves only small matrix operations as will be discussed in the next chapter. The idea is based on forced vibration response versus frequencies. The corresponding critical speeds of the rotating shaft as shown in Figure 2.2 have been obtained. The results are given in Table 5.2 where the corresponding non-rotating natural bending frequencies are also given. Due to gyroscopic effects, they are higher than the latter, which are sometimes also called at-rest natural frequencies. Therefore, a rotating case should be examined in order to obtain reliable accurate critical speeds.

**Table 5.2 Critical speeds of the rotating shaft**

<b>Order</b>	<b>Critical speeds (cyc/sec)</b>	<b>Non-rotating natural bending frequencies (Hz)</b>
1	764	744
2	1959	1875
3	3491	3307
4	5184	4892
5	6939	6548

One might notice that in Figure 5.10, the curve of the first forward whirl frequency versus rotational speed goes from positive to negative values. Actually, it is found that when the shaft reaches the first critical speed ( $\Omega = 764$  cyc/sec), there is no vibrating mode shape in the rotating frame corresponding to the possible first forward whirl, as shown in Table 5.3. However, when the shaft is kept just below or above the critical speed, there is a vibrating mode, as indicated in Table 5.4. Though defined as backward whirl when “-” sign appears in the rotating frame, the negative frequencies in the figure will turn out to be positive in the fixed frame, which will be considered as the first forward whirl in the fixed frame. Therefore, it can be concluded that the critical speeds can also be determined as such shaft speeds where a zero frequency line ( $\omega(\Omega) = 0$ ) intersects the curves of resonant whirl frequencies versus

shaft speed in the rotating frame.

It is clear that the two approaches mentioned-above are consistently matched with each other. The first method based on Eq.(5.7) may be easier to handle without relevant information about whirling modes.

**Table 5.3 Resonant whirl frequencies corresponding to *vibrating modes* in the rotating frame when the rotational speed reaches  $\Omega = 764$  cyc/sec**

Mode order		Resonant whirl frequencies in the rotating frame $\omega_{rot}$ (Hz)	Resonant whirl frequencies in the fixed frame $\omega_{fix}$ (Hz)
Forward	1		
	2	1164	1928
	3	2616	3380
	4	4211	4975
	5	5872	6636
Backward	1	-1450	-686
	2	-2559	-1795
	3	-3978	-3214
	4	-5557	-4793
	5	-7209	-6445

**Table 5.4 First order resonant whirl frequencies corresponding to *vibrating modes* in the rotating frame for the rotational speed just below and above  $\Omega = 764$  cyc/sec**

Rotational speed $\Omega$ (cyc/sec)	Resonant whirl frequencies in the rotating frame $\omega_{rot}$ (Hz)	Resonant whirl frequencies in the fixed frame $\omega_{fix}$ (Hz)
760	+4	$\approx 764$
768	-4	$\approx 764$

### 5.2.2 Effects of Mass Imbalance on Response

Mass imbalance may cause severe damage to rotating systems. If a shaft were rigid, one would easily balance it using only two planes along its axial distance. However, due to its elasticity, even a well-balanced shaft with a zero resultant centrifugal force and moment may lead to significant unbalance response when it operates at a critical speed.

As indicated before, in this 3-D continuum model mass imbalance at a certain location along the shaft is modelled by varying the density within the corresponding cross section. This is believed to be a consistent modelling of centrifugal forces in accordance with the 3-D continuum shaft model. For a given mass eccentricity  $e(z)$  along the shaft axis, the corresponding density difference  $\Delta\rho(z)$  can be determined as discussed in Chapter 3.

The effects of a few different  $e(z)$ 's on the unbalance response of the whole shaft have been studied. For simplicity, free surface boundary condition is assumed. In reality, the shaft is always attached to fluid-film or rolling element bearings, which will be discussed in Chapter 7. However, it is desired that a shaft be balanced as perfectly as possible. An unbalance force transmitted to the bearings is a source of periodic excitations that can cause vibrations, often very strong, in the non-rotating parts of the machine.

For a uniform shaft as shown in Figure 2.2, an arbitrary distribution  $e(z)$  will usually cause high magnitude of unbalance response when the shaft is running at any speed. However, some particular distributions may not lead to significant responses for all critical speeds. The first and second critical speeds of the shaft, as shown in Table 5.2, are known as 764 Hz and 1959 Hz, respectively. Two different distributed mass imbalance cases were studied to observe their corresponding unbalance responses.

“A” mass imbalance distribution as shown in Figure 5.15, was found to cause an extremely large response when the shaft is kept at the first critical speed of 764 cyc/sec. As expected in Figure 5.16, the deflection curve is very similar to the first non-rotating bending and resonant whirl mode shapes. Obviously, the magnitudes shown in Figure 5.16 would not be reached in real cases because a real system possesses damping and nonlinearity. The purpose is to indicate the severely bowed shape of the shaft caused by this type of imbalance



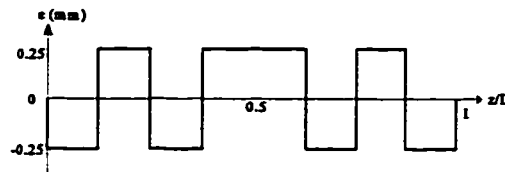


**Figure 5.15 "A" mass imbalance distribution**

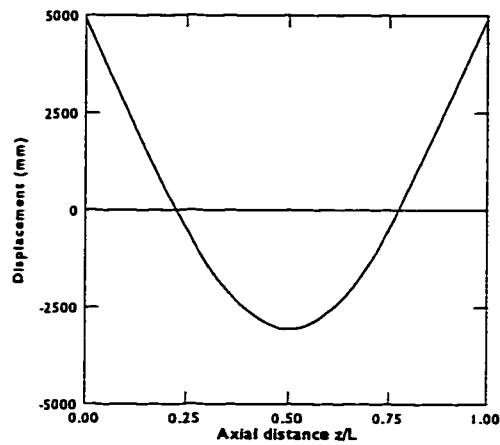


**Figure 5.16 Resonant unbalance response due to  $e(z)$  in Figure 5.15 at 1st critical speed 764 cyc/sec. (Qualitatively showing severely bowed shape being excited, not the case in a real system due to its damping and nonlinearity)**

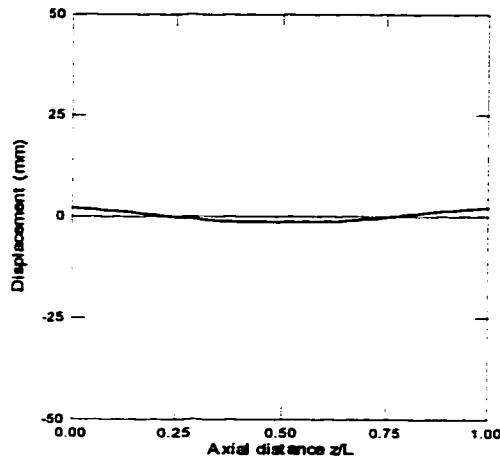


**Figure 5.17 Non - resonant unbalance response due to  $e(z)$  in Figure 5.15 at 2nd critical speed 1959 cyc/sec**

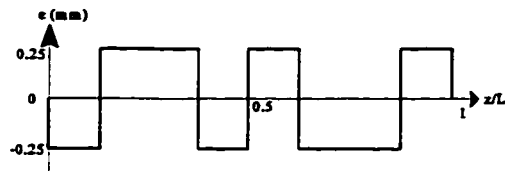


**Figure 5.18 “B” mass imbalance distribution**

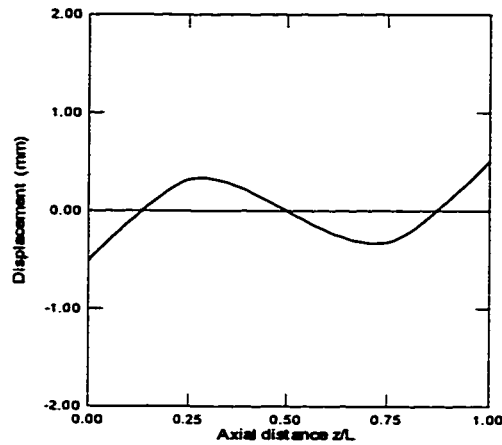


**Figure 5.19 Non-resonant unbalance response due to  $e(z)$  in Figure 5.18 at 1st critical speed 764 cyc/sec**

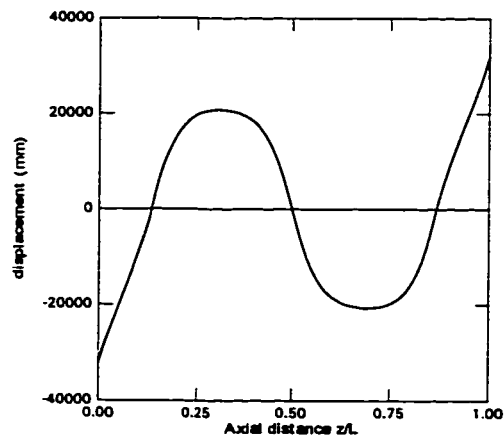


**Figure 5.20 Resonant unbalance response due to  $e(z)$  in Figure 5.18 at 2nd critical speed 1959 cyc/sec. (Qualitatively showing severely bowed shape being excited, not the case in a real system due to its damping and nonlinearity)**

at that shaft speed. However, this type of distribution did not cause a large second mode unbalance response at the second critical speed of 1959 cyc/sec. Instead, the shaft was still slightly bowed in the first mode shape. Therefore, this type “A” distribution will excite the first order mode, but not the second order one.

If a mass imbalance curve  $e(z)$  appears in the form shown in Figure 5.18, named “B” distribution, then the shaft presents totally different unbalance response. The first mode shape does not occur at the critical speed of 764 cyc/sec. Instead, a very small amount of unbalance response in a shape close to the second mode appears at this speed, as shown in Figure 5.19. When the rotational speed reaches the second critical value of 1959 cyc/sec, the shaft presents a huge amount of unbalance response in the second mode, as shown in Figure 5.20. Of course, as indicated above, the large magnitudes shown in Figure 5.20 would not hold in real cases. But a large response is expected at that shaft speed.

Therefore, mass imbalance distribution can have significant effects on unbalance response. The above-mentioned two cases would not cause big problems at very low speeds because no balancing is needed if a rigid rotor model is considered. However, modern rotating machinery tends to work at high speeds. Identification of mass imbalance helps to predict possible dynamic response of the shaft at an operational speed range. This author believes it can be implemented after obtaining reliable data at a few different speeds. Mass imbalance can then be redistributed by choosing appropriate balancing locations so that resonant mode shapes may not be excited at the running speed range.

The mass imbalance distributions in Figures 5.15 and 5.18 are symmetric and anti-symmetric to the midspan of the shaft, respectively. Therefore, they will cause resonant unbalance responses in symmetric and anti-symmetric modes, respectively.

It should be noted that the deflection curve of unbalance response is invariable in the rotating frame at a given speed, as discussed above. If expressed in the fixed reference frame, the shaft would present synchronous motion.

### 5.3 Discussion

The phenomena discussed in this chapter are based on the results with the proposed 3-D solid finite elements. When dynamic stresses due to shaft whirl or bending stresses at critical speeds are evaluated, this approach yields more reliable and accurate results than beam elements.

Shaft whirl has been studied in the rotating frame, thus giving a clear view of its whirling motion. Non-zero frequency excitations in the rotating frame will cause forced vibrations of the shaft in terms of rotating coordinates. This motion is defined as shaft whirl due to the excitations, and the corresponding frequency is called *whirl frequency* in this chapter. Only a frequency that cause resonant response of the shaft will be called a *resonant whirl frequency*, or a *natural frequency* of the rotating shaft. The transverse trajectories all along its axial distance appear in a certain rotating deflection mode shape with very large circular orbits when some excitation is applied at a resonant forward or backward whirl frequency. However, once a forcing frequency deviates from such a resonant forward or backward whirl frequency, forward and backward whirling motion could be found simultaneously at different locations along the shaft axis.

Critical speeds can be determined by the rotating stiffness matrices, or the speeds corresponding to zero resonant whirl frequencies. Mass imbalance distribution may influence unbalance response to a significant extent. A specific distribution can completely eliminate a resonant unbalance response if a shaft operates at the corresponding critical speed!

Mass imbalance, which is modelled by varying the density within the corresponding cross section in this thesis, might also be possibly modelled by varying the geometry while keeping the density constant.

It should be noted that there could be four types of resonant bending modes. Non-rotating bending vibration modes, which are often discussed in many vibration books and references and are easy to understand, corresponds to a non-rotating shaft. For a rotating shaft, there are resonant forward and backward whirling modes which rotate at the whirl frequency with constant radial deflection. In the rotating frame, these whirling modes can

---

be viewed as the superposition of two orthogonal non-rotating bending modes with the whirl frequency. Thus cyclic stresses occur when a shaft undergoes the whirling motion. At critical speeds, a shaft may be bowed to a deflected configuration without any vibratory motion in the rotating frame. Hence the corresponding modes are fixed in the rotating frame, and no cyclic stressing is present. However, the mode shapes are similar to those of the corresponding resonant whirling motion, though not exactly the same. The similarity lies in the fact that they are the natural frequencies and mode shapes for a certain order. The difference is due to the presence of the shaft speed. This author speculates that not only the critical speed mode shape is unique, but also other whirling modes with the same order may be slightly different from each other if the shaft operates at different speeds.

It is found that the rotating shaft modelled as a 3-D continuum in the rotating frame seems to have only a rigid body mode in axial direction. Obviously, non-rotating stiffness has totally six rigid body modes. However, once the shaft rotates at a certain speed, the singularity of the rotating stiffness matrices is changed.

Though only free surface boundary condition is involved here, the analytical and numerical methods for other cases would be the same to that used in this chapter. All the concepts and conclusions might be applied to the shaft with other boundary conditions which have to be established in terms of real contact circumstances.

## **Chapter 6**

# **Eigenvalues and Reduction Procedures**

Rotordynamics differs from general vibration problems in that it often involves a complex eigenvalue analysis of gyroscopic systems. When a rotating frame is employed to analyse the dynamic response of the rotating shaft, Coriolis forces contribute to the gyroscopic terms of the equations of motion. There have been a few approaches developed for the eigenvalue analysis. However, for a very large system involving thousands or more degrees of freedoms, there might be difficulty in solving or obtaining reliable solutions.

Since the 3-D solid finite element approach is used here instead of conventional beam element theories to model the dynamic response of rotor-bearing systems, thousands of degree of freedoms may have to be adopted. Many eigenvalue analysis methods require a change from a second order to a first order system, thus doubling this number. A very high order eigenvalue analysis takes too much computer capacity and cost. On the other hand, though a system involving thousands of degree of freedoms may theoretically have the same number of vibrating modes, higher frequency ranges and related modes are of less interest to engineers. There would not be excitations with such higher frequencies in reality. Moreover, since there must be differences between a computational model and a real system, these computed higher frequency magnitudes are not usually considered to be accurate and reliable. Hence, from the practical point of view, only a few modes within a low frequency range need to be captured.

There have been a few reduction methods, such as Guyan reduction and component mode synthesis, which can be used in the dynamic analysis of structures having a large

number of degrees of freedoms. However, these methods result in lost accuracy to some extent due to mode truncation or neglected inertia terms. Craggs and Eckert (1992) proposed a reduction procedure called the continuous coordinate condensation for beam elements with end nodes.

A transfer matrix technique based on finite element models has been proposed for a chain-like structure (Yu and Craggs, 1995a). It can be used for not only free vibration analysis but also computation of forced response due to any distributed external forces using only small matrix operations. Unlike conventional transfer matrix methods which involve lumped mass matrices, the proposed transfer matrix technique corresponds to the consistent mass, stiffness, gyroscopic terms for the modelled system, thus giving convergent natural frequencies or reliable forced responses.

In this chapter, a dynamic reduction procedure has been developed. Compared with the continuous coordinate condensation method (Craggs and Eckert, 1992), the new developed dynamic reduction method allows one to condense any kind of harmonic excitation in a chain-like structure. This makes it possible for one to know equivalent magnitudes of excitation in terms of a forcing frequency at the two ends of a part where distributed or concentrated excitation exists, thus giving a clue to simulate or reduce the dynamic response by applying equivalent excitation at the two ends. It can also be used to handle elements involving intermediate nodes. This is a very efficient approach for the analysis of unbalance response due to distributed mass imbalance.

## **6.1 General Eigenvalue Analysis**

In rotordynamics, a complex eigenvalue analysis is often involved due to gyroscopic terms in the equation of motion. Knowing the properties of an eigenvalue problem for gyroscopic systems helps to predict and determine the dynamic response to a great extent.

### **6.1.1 Generalized Eigenvalue Problem**

For an autonomous vibrating system, the equation of motion after finite element

discretization can be expressed in the following form:

$$M\ddot{U} + C\dot{U} + KU = 0 \quad (6.1)$$

where  $M$  is an  $n \times n$  mass matrix,  $C$  is an  $n \times n$  gyroscopic/damping matrix,  $K$  is an  $n \times n$  stiffness matrix, and  $U$  is an  $n \times 1$  vector of displacements, or generalized coordinates. The overhead dots denote time derivatives. In order to obtain the corresponding eigenvalues, one usually reconstructs it into the form:

$$A x = \lambda B x \quad (6.2)$$

There have been the QR ( $B=I$ , a unit matrix) and the QZ algorithms for dealing with the above first order eigenvalue problem.  $B$  can be singular in the QZ algorithm.

One might set

$$x = \begin{Bmatrix} \dot{U} \\ U \end{Bmatrix} \quad (6.3)$$

Assuming

$$x = x_0 e^{\lambda t} \quad (6.4)$$

yields

$$\begin{Bmatrix} \dot{U} \\ U \end{Bmatrix} = \begin{Bmatrix} \dot{U}_0 \\ U_0 \end{Bmatrix} e^{\lambda t} \quad (6.5)$$

Eq. (6.1) might be rewritten as the partitioned matrix form in terms of Eq.(6.2)

$$\begin{bmatrix} -C & -K \\ K & 0 \end{bmatrix} \begin{Bmatrix} \dot{U}_0 \\ U_0 \end{Bmatrix} = \lambda \begin{bmatrix} M & 0 \\ 0 & K \end{bmatrix} \begin{Bmatrix} \dot{U}_0 \\ U_0 \end{Bmatrix} \quad (6.6)$$

From Eq.(6.5), it follows



$$\dot{U} = \lambda U_0 e^{\lambda t} \quad (6.7)$$

Comparing Eqs.(6.5) and (6.7) gives

$$\dot{U}_0 = \lambda U_0 \quad (6.8)$$

which is true in any case. However, in the case of singular  $K$ , if using Eq. (6.6), one cannot obtain a correct  $U_0$ .

The reason can be explained as follows. Eq.(6.6) can be expanded into

$$-C\dot{U}_0 - KU_0 = \lambda M\dot{U}_0 \quad (6.9)$$

and

$$K\dot{U}_0 = \lambda KU_0 \quad (6.10)$$

Only if  $K$  is not singular, then one can pre-multiply  $K^{-1}$  and obtain Eq.(6.8). But whether  $K$  is singular or not, one can have from Eqs.(6.9) and (6.10) the following expression

$$(\lambda^2 M + \lambda C + K)\dot{U}_0 = 0 \quad (6.11)$$

The original eigenvalue problem for Eq.(6.1) corresponds to

$$(\lambda^2 M + \lambda C + K)U_0 = 0 \quad (6.12)$$

Therefore, if using Eq.(6.6) in the partitioned matrix form to acquire eigenvectors for the system with a singular  $K$ , one should choose  $\dot{U}_0$  as mode shapes instead of  $U_0$ . This is because the original eigenvalue problem has evolved into Eq.(6.6), i.e., Eqs.(6.9) and (6.10) which are not totally equivalent to the original one.

In the case of  $C = 0$  and  $M$  is non-singular, Eqs. (6.9) and (6.10) can yield

$$\mathbf{K}(\lambda^2 \mathbf{I} + \mathbf{M}^{-1} \mathbf{K}) \mathbf{U}_0 = \mathbf{0} \quad (6.13)$$

which was verified by the author through an example involving a singular  $\mathbf{K}$  matrix. Note this is valid for any  $\mathbf{K}$  matrix. Only if  $\mathbf{K}$  is not singular, then one can have

$$(\lambda^2 \mathbf{M} + \mathbf{K}) \mathbf{U}_0 = \mathbf{0} \quad (6.14)$$

One also could avoid this problem by using a different partitioned matrix from Eq.(6.6) regardless of  $\mathbf{K}$ 's singularity. An alternative can be given by

$$\begin{bmatrix} -\mathbf{M}^{-1} \mathbf{C} & -\mathbf{M}^{-1} \mathbf{K} \\ \mathbf{I} & \mathbf{0} \end{bmatrix} \begin{Bmatrix} \dot{\mathbf{U}}_0 \\ \mathbf{U}_0 \end{Bmatrix} = \lambda \begin{Bmatrix} \dot{\mathbf{U}}_0 \\ \mathbf{U}_0 \end{Bmatrix} \quad (6.15)$$

where a prerequisite of  $\mathbf{M}$ 's non singularity must be guaranteed.

### 6.1.2 Gyroscopic Effects on Stability

For a system with Eq.(6.1), the criterion of stability is to observe the real parts of all complex eigenvalues. If they are all negative, then the system is considered to be stable; if at least one of them is positive, then the system is unstable. There also exists the Routh-Hurwitz criterion which can be found in literature.

The eigenvalue problem for a gyroscopic system can be expressed as

$$[\lambda^2 \mathbf{M} + \lambda \mathbf{G} + \mathbf{K}] \mathbf{U}_0 = \mathbf{0} \quad (6.16)$$

where  $\mathbf{G} (= -\mathbf{G}^T)$  represents a gyroscopic matrix.  $\mathbf{M}$  is assumed to be positive definite. Pre-multiplying Eq.(6.16) by  $\bar{\mathbf{U}}_0^T$  results in

$$m \lambda^2 + i g \lambda + k = 0 \quad (6.17)$$

where

$$\begin{aligned} m &= \bar{U}_0^T M U_0 > 0 \\ k &= \bar{U}_0^T K U_0 \\ ig &= \bar{U}_0^T G U_0 \\ i &= \sqrt{-1} \end{aligned}$$

The solution of Eq.(6.17) can be given by

$$\lambda = i \frac{-g \pm \sqrt{g^2 + 4mk}}{2m} \quad (6.18)$$

If  $K$  is positive definite, then  $k > 0$ , which always yields pure imaginary parts of eigenvalues. If expressed in the rotating frame, however,  $K$  may not be positive definite. In this case, as well known, symmetric rotors remain quite stable. Therefore, it is the gyroscopic effect that contributes to the stabilization of undamped rotor systems. As long as the following condition

$$g^2 + 4mk > 0$$

is satisfied, an eigenvalue  $\lambda$  will be purely imaginary so that the system could be kept stable.

### 6.1.3 Damped Natural Frequencies

For a single-degree-of-freedom (SDOF) system, the corresponding free vibration equation can be given by

$$\ddot{x}(t) + 2\xi\omega_n\dot{x}(t) + \omega_n^2x(t) = 0 \quad (6.19)$$

where  $\xi$  is the damping ratio, and  $\omega_n$  denotes the natural frequency of the system. Its characteristic equation can be given by

$$\lambda^2 + 2\xi\omega_n\lambda + \omega_n^2 = 0 \quad (6.20)$$

Thus one can obtain its solution provided that  $0 < \xi < 1$ :

$$\lambda = (-\xi \pm j\sqrt{1-\xi^2})\omega_n \quad (6.21)$$

where  $j = \sqrt{-1}$ . Sometimes the second term is defined as the damped natural frequency, i.e.,

$$\omega_d = \omega_n \sqrt{1-\xi^2} \quad (6.22)$$

The peak response due to harmonic excitation occurs when the forcing frequency is equal to

$$\omega = \omega_n \sqrt{1-2\xi^2} \quad (6.23)$$

When fluid/shaft interaction is examined, a damped multiple-degree-of-freedom (MDOF) model is often employed. Using Eq.(6.6) or Eq.(6.15), each eigenvalue for an  $n$  DOF system can be expressed as

$$\lambda_i = \alpha_i \pm j\beta_i \quad (6.24)$$

where  $i = 1, 2, \dots, n$ . Eq.(6.24) can be rewritten in a form similar to Eq.(6.21) as

$$\lambda_i = (-\xi_i \pm j\sqrt{1-\xi_i^2})\omega_i \quad (6.25)$$

where

$$\begin{aligned}\omega_i &= \sqrt{\alpha_i^2 + \beta_i^2} \\ \xi_i &= -\frac{\alpha_i}{\sqrt{\alpha_i^2 + \beta_i^2}}\end{aligned}\quad (6.26)$$

It should be noted that in general cases,  $\omega_i$  varies with the damping matrix  $C$ . There is only one exception for proportionally damped systems where a matrix  $CM^{-1}K$  is symmetric so that the vibration equations can completely decouple. As is well known, a system with damping matrix  $C=\alpha M+\beta K$  ( $\alpha, \beta$  constant) satisfies this condition. For most cases, however, there is no such relationship.

An example is given in the following to verify this behaviour. For a system with mass, stiffness and damping matrices assumed as

$$\begin{aligned}M &= \begin{bmatrix} 1 & 0 \\ 0 & 1 \end{bmatrix}, & K &= \begin{bmatrix} 2 & -1 \\ -1 & 2 \end{bmatrix}, \\ C &= 0.01M + 0.01K + \varepsilon \begin{bmatrix} 1 & 0 \\ 2 & 1 \end{bmatrix}\end{aligned}$$

$\varepsilon = 0$  denotes the proportional damping and that  $\varepsilon \neq 0$  indicates a general case. The undamped natural frequencies for  $C=0$  can be easily found to be

$$\omega_{n1} = 1, \quad \omega_{n2} = 1.7321$$

For  $C \neq 0$ , changing parameter  $\varepsilon$  leads to *different* values of  $\omega_i$  and  $\omega_{di}$  ( $=\beta_i$ ). Only when the system has a proportional damping matrix ( $\varepsilon = 0$ ) are values of  $\omega_i$  the same as the above. The detailed values can be seen in Table 6.1.

It is noted that  $\omega_i$  is no longer the undamped natural frequency for  $C=0$ . As  $\varepsilon$  increases, the differences become larger. In general, one could not conclude that damped natural frequencies or resonant frequencies (with respect to forced peak response) will

always be less than the undamped natural frequencies as they are in a proportional damping system. In this example, the damped natural frequency for the first order is less than the first order natural frequency, while that for the second order is greater than the corresponding undamped natural frequency. In forced vibration analysis, the peak response frequencies should be based on frequency response functions (FRF) or modal analysis.

Table 6.1  $\omega_i$  shift from  $\omega_n$  as non-proportional damping increase

$\varepsilon$	$\omega_{1,2}$ in Eq.(6.26)	$\frac{\omega_i - \omega_n}{\omega_n}$	$\xi_i$ in Eq.(6.26)	$\omega_{di}$ (= $\beta_i$ )
0	1.0000	0	0.0100	0.9999
0	1.7321	0	0.0115	1.7319
0.2	0.9912	-0.9%	0.2065	0.9698
0.2	1.7475	0.9%	0.0145	1.7473
0.4	0.9730	-2.7%	0.3898	0.8960
0.4	1.7802	2.8%	0.0285	1.7795
0.6	0.9541	-4.6%	0.5609	0.7899
0.6	1.8154	4.8%	0.0522	1.8129
0.8	0.9373	-6.2%	0.7238	0.6467
0.8	1.8479	6.7%	0.0820	1.8417
1.0	0.9227	-7.7%	0.8812	0.4361
1.0	1.8773	8.4%	0.1155	1.8647

## 6.2 TMM Based on FE Models

For chain-like structures, such as beams and shafts, the two usual numerical approaches of dynamic analysis are the transfer matrix method (TMM) and the finite element method (FEM). Both have been used successfully and extensively.

In the TMM, a relationship is established between a set of unknowns at the two ends of a section of the structure. The equation for the whole system is available by multiplying the successive matrix expressions for connected elements. In the conventional TMM approach, a lumped mass model is often employed, such that both the mass and inertial properties are lumped at discrete points which are considered to be connected by massless elastic members. Although convenient for both modelling and computational processes, this approach is inconsistent and therefore gives poor results. For example, the calculated natural frequencies using a lumped mass approach will not converge as the discretization of the system is increased (Stephenson, et al., 1989).

In the FEM, stiffness, damping and gyroscopic, and mass matrices relate displacements and their first and second time derivatives to a set of nodal forces for each element. The system matrix representation is obtained by assembling element matrices at appropriate entries dictated by the connectivity. Since the individual element matrices reflect the assumptions involved in their formulation, a consistent distributed mass modelling results in better solutions than the lumped mass approach. Obviously, the larger the number of elements that is used, the larger is the system matrix. For this reason, much work [Guyan,1965; Craggs,1987] has been done for reducing the size of a FE model while preserving the lower frequencies and mode shapes of the original FE model. However, these method will certainly lose accuracy to some extent.

An alternative, which employs a transfer matrix technique, therefore is proposed herein: the governing equations are modelled with FEM, rewritten in the form of a dynamic matrix, and then changed into transfer matrix form, so that using only small matrices the finite element solution can be obtained for steady state response caused by harmonic excitations. Note that in the analysis of forced vibration, the external forces must be

included. In a rotor, for example, the distributed centrifugal forces due to mass imbalance are usually regarded as external forces which can be put at the nodal points on the two ends of each element along its axial line through the principle of virtual work. The proposed method can deal with any possible external forces applied in the system.

Considerable computational efficiencies can be attained without any loss of accuracy when dealing with a number of identical elements. Here the chain-like structure just means that the degree of freedom at the left side of an element or substructure is the same as that at the right side.

### 6.2.1 Transfer Matrix Formulation Based on FE Models

In a chain-like structure, the dynamic formulation using finite element method for an  $i$ th element, as shown in Figure 6.1, can be expressed as

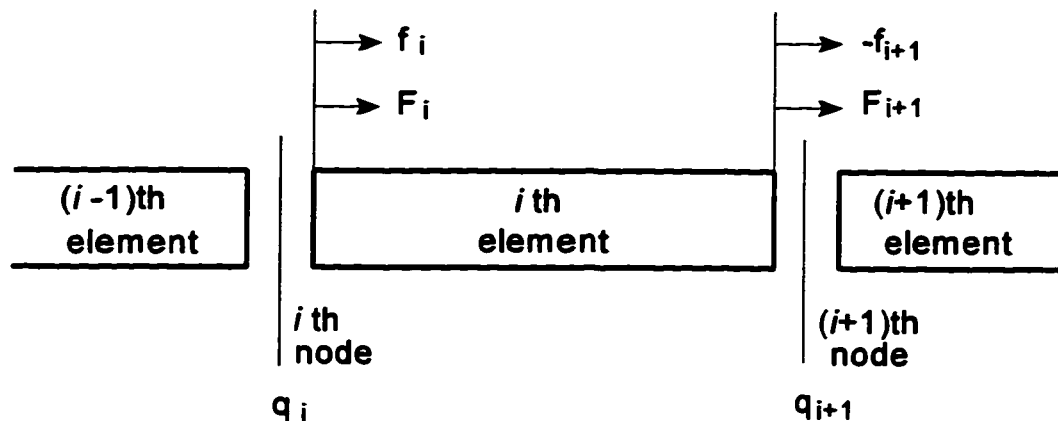


Figure 6.1 The discretized finite element model



$$\begin{aligned}
\begin{bmatrix} m_{11} & m_{12} \\ m_{21} & m_{22} \end{bmatrix} \begin{Bmatrix} \ddot{q}_i \\ \ddot{q}_{i+1} \end{Bmatrix} + \begin{bmatrix} c_{11} & c_{12} \\ c_{21} & c_{22} \end{bmatrix} \begin{Bmatrix} \dot{q}_i \\ \dot{q}_{i+1} \end{Bmatrix} + \begin{bmatrix} k_{11} & k_{12} \\ k_{21} & k_{22} \end{bmatrix} \\
= \begin{Bmatrix} f_i \\ -f_{i+1} \end{Bmatrix} + \begin{Bmatrix} F_i \\ F_{i+1} \end{Bmatrix}
\end{aligned} \tag{6.27}$$

where  $m_{jk}$ ,  $c_{jk}$ , and  $k_{jk}$  represent the sub-matrix of mass, damping and stiffness matrix, respectively, for the  $i$ th element.  $\{q_i\}$  and  $\{q_{i+1}\}$  denote the state vector of displacement.  $f_i$  and  $f_{i+1}$  denote the internal generalized force vectors for the  $i$ th and  $(i+1)$ th nodes due to adjacent elements.  $F_i$  and  $F_{i+1}$  denote the external generalized force vectors equivalently acting on the  $i$ th and  $(i+1)$ th nodes.

For convenience, the following matrix partitions are introduced

$$[M]_i = \begin{bmatrix} m_{11} & m_{12} \\ m_{21} & m_{22} \end{bmatrix}, [C]_i = \begin{bmatrix} c_{11} & c_{12} \\ c_{21} & c_{22} \end{bmatrix}, [K]_i = \begin{bmatrix} k_{11} & k_{12} \\ k_{21} & k_{22} \end{bmatrix} \tag{6.28}$$

The steady state response is assumed corresponding to harmonic excitations. Thus, for an  $i$ th element, the external forces can be expressed as

$$\begin{Bmatrix} F_i \\ F_{i+1} \end{Bmatrix} = \begin{Bmatrix} F_1 \\ F_2 \end{Bmatrix} e^{j\omega t} \tag{6.29}$$

where  $\omega$  represents the harmonic forcing frequency and  $j$  stands for  $\sqrt{-1}$ . The corresponding response can be given by

$$\begin{Bmatrix} q_i \\ q_{i+1} \end{Bmatrix} = \begin{Bmatrix} q_1 \\ q_2 \end{Bmatrix} e^{j\omega t} \tag{6.30}$$

and the internal force vectors can be given by

$$\begin{Bmatrix} f_i \\ -f_{i+1} \end{Bmatrix} = \begin{Bmatrix} f_1 \\ -f_2 \end{Bmatrix} e^{j\omega t} \quad (6.31)$$

Substitution of Eqs. (6.28) - (6.31) into Eq.(6.27) yields

$$[D(\omega)]_i \{q\} = \{f\} + \{F\} \quad (6.32)$$

where

$$[D(\omega)]_i = (-\omega^2[M]_i + j\omega[C]_i + [K]_i),$$

$$\{q\} = \begin{Bmatrix} q_1 \\ q_2 \end{Bmatrix}, \quad \{f\} = \begin{Bmatrix} f_1 \\ -f_2 \end{Bmatrix}, \quad \{F\} = \begin{Bmatrix} F_1 \\ F_2 \end{Bmatrix}$$

Eq.(6.32) can be rewritten as

$$\begin{Bmatrix} q_2 \\ f_2 \\ 1 \end{Bmatrix} = \begin{bmatrix} T_{11} & T_{12} & T_{13} \\ T_{21} & T_{22} & T_{23} \\ 0 & 0 & 1 \end{bmatrix} \begin{Bmatrix} q_1 \\ f_1 \\ 1 \end{Bmatrix} \quad (6.33)$$

where

$$\begin{aligned} T_{11} &= -D_{12}^{-1} D_{11} \\ T_{12} &= D_{12}^{-1} \\ T_{13} &= D_{12}^{-1} F_1 \\ T_{21} &= -D_{21} + D_{22} D_{12}^{-1} D_{11} \\ T_{22} &= -D_{22} D_{12}^{-1} \\ T_{23} &= F_2 - D_{22} D_{12}^{-1} F_1 \end{aligned}$$

It is obvious that the expression

$$[T]_i = \begin{bmatrix} T_{11} & T_{12} & T_{13} \\ T_{21} & T_{22} & T_{23} \\ 0 & 0 & 1 \end{bmatrix}$$

is a  $(2p+1) \times (2p+1)$  transfer matrix, where  $p$  is the degree of freedom at each node. Therefore, the transfer matrix method can be employed to obtain the solution of the finite element formulation for this chain-like structure. In principle, it is believed that the solution using such TMM should be the same as that using the modal superposition method for the global system. However, TMM, takes much less computational time and storage when dealing with a long beam or shaft.

Note that Eq.(6.33) can be in the complex form: whenever  $[C]_i$  is a nonzero matrix, then  $[D(\omega)]_i$  will be complex and so will  $D_{12}$  and  $D_{12}^{-1}$ . In this case, if one cannot obtain  $D_{12}^{-1}$  directly from  $D_{12}$ , one can divide  $D_{12}$  into real and imaginary parts, i.e.

$$D_{12} = A + jB \quad (6.34)$$

Thus its inverse matrix can be given by

$$D_{12}^{-1} = (A + BA^{-1}B)^{-1} - j(B + AB^{-1}A)^{-1} \quad (6.35)$$

Condensation can be made when modelling uniform components of subsystems with a number of identical elements. In this case, two identical elements correspond to the same transfer matrix  $[T]_1$ . Thus the transfer matrix between these two elements is  $[T]_2 = ([T]_1)^2$  and similarly that between these four elements is  $[T]_4 = ([T]_2)^2$ . As shown in Figure 6.2, the corresponding transfer matrix for  $2^n$  identical elements can be formed using only  $n$  times of matrix multiplication rather than  $2^n$ . Therefore, such  $2^n$  elements have been condensed to a superelement relating the variables at two ends without any loss of accuracy. Note that when no external force exists, one only needs to deal with a  $(2p) \times (2p)$  matrix.

Once the model is assembled with suitable condensation to form transfer matrices, the response at the nodes of interest can be easily obtained for any distributed harmonic

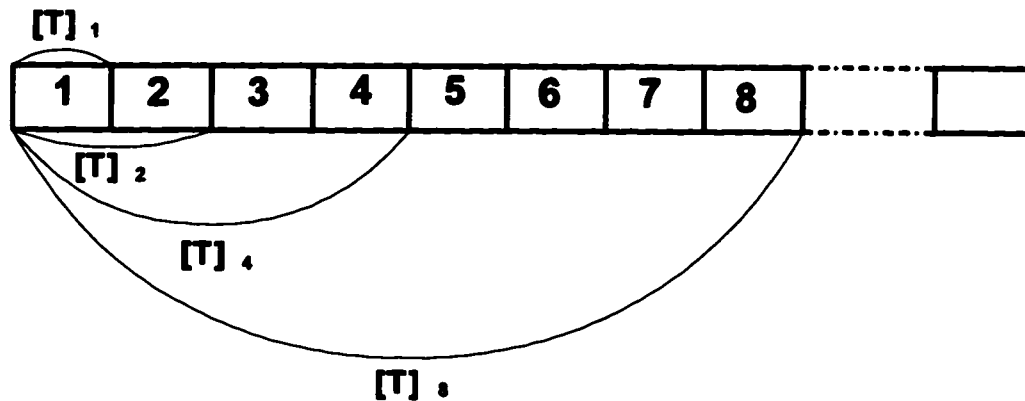


**Figure 6.2 The condensation process for identical elements**

excitation. The computation is performed with a proper frequency step size over the frequency range of interest and the response versus forcing frequency is plotted. The frequencies corresponding to maximum responses can be considered as the natural frequencies of the system if damping effects are negligible.

The proposed transfer matrix method based on finite element formulation is an effective approach. The matrices to be operated are always no bigger than  $(2p+1) \times (2p+1)$ . The computation can be carried out even in a desktop computer for a system with a large number of elements without any loss of accuracy. Forced responses including damping and gyroscopic effects can be obtained without solving eigenvalue problems. This method can be used to handle external forces over the whole system. In a shaft system there usually exists distributed eccentricity of mass, which forms harmonic excitation over the shaft. Using FEM the equivalent loads are assigned to nodal points. Thus, the response on distributed eccentricity of mass can be easily attained.

### 6.2.2 Application and Discussion

Many numerical examples can be given by using the TMM approach based on FEM formulation. In this section, a vibrating Euler beam is first analyzed to obtain its natural frequencies for checking purposes, and then the forced response of a rotating Timoshenko shaft with a distributed unbalance and damping and gyroscopic effects is given to illustrate the validity of the proposed method.

A uniform circular beam with simple supports, as shown in Figure 6.3, was modelled with 4 elements. The beam has a modulus of elasticity  $E = 2 \times 10^5$  MPa, and density  $\rho = 7850$  kg/m<sup>3</sup>. In this example the equations of motion were obtained using a FEM formulation. It is noted that there exist two state variables  $u_i$  and  $(\partial u / \partial x)_i$ , corresponding to each nodal point. Using the proposed TMM approach, the response at the nodes of interest to a forced harmonic input versus forcing frequencies can be easily obtained. The computed results are almost the same as those obtained by using the mode superposition method through finite

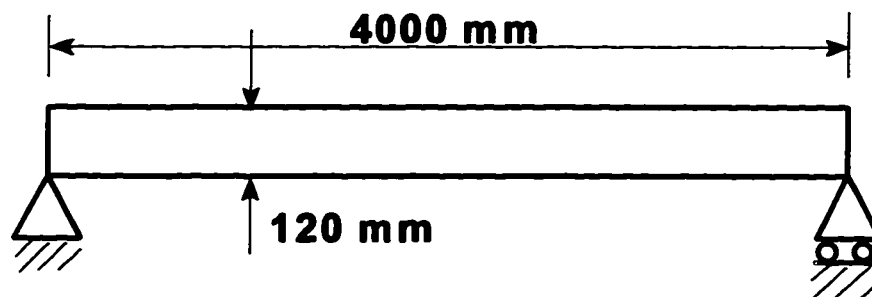


Figure 6.3 A simply supported beam

element modelling.

In Table 6.2 the first three natural frequencies obtained by using power method (Meriovitch, 1975a) for a full eigenvalue problem are compared with the first three peak resonances calculated using the proposed TMM method. There is no difference of results between the two approaches. It is found that the accuracy of peak resonance depends on the frequency step size. In order to save computational time and obtain accurate solution, one can first use a coarse step size to determine the frequency ranges of interest, and then repeat the calculations with a smaller step size near the desired response peaks to obtain more accurate results.

**Table 6.2 Natural Frequencies of Simply Supported Beam**

Peak resonance using TMM based on FEM (rad/sec)	Solution of full eigenvalue problem (rad/sec)
93~94	93.4
375~376	375.1
856~857	856.0

The second example is to obtain the forced response of a rotor-bearing system with distributed unbalance, in which damping and gyroscopic effects are taken into account. The rotating circular shaft supported by isotropic bearings, as shown in Figure 6.4, was modelled with 16 elements using Timoshenko beam theory. The bearing stiffness is  $k = 6\text{MN/m}$  and damping coefficient is  $c = 60\text{kNs/m}$ . Its material properties were set the same as those of the previous case. Moreover, Poisson's ratio is  $\nu = 0.3$ . Each element has 2 deflection and 2 slope nodal variables in two perpendicular planes at either end. Assumed unbalance distribution varying with axial distance  $x$ , can be expressed in  $x$ - $y$  plane as

$$\eta(x) = \begin{cases} -0.2 + 0.8x, & 0 \leq x \leq 500 \\ 0.2 - 0.8(x - 0.5), & 500 < x \leq 1000 \end{cases}$$

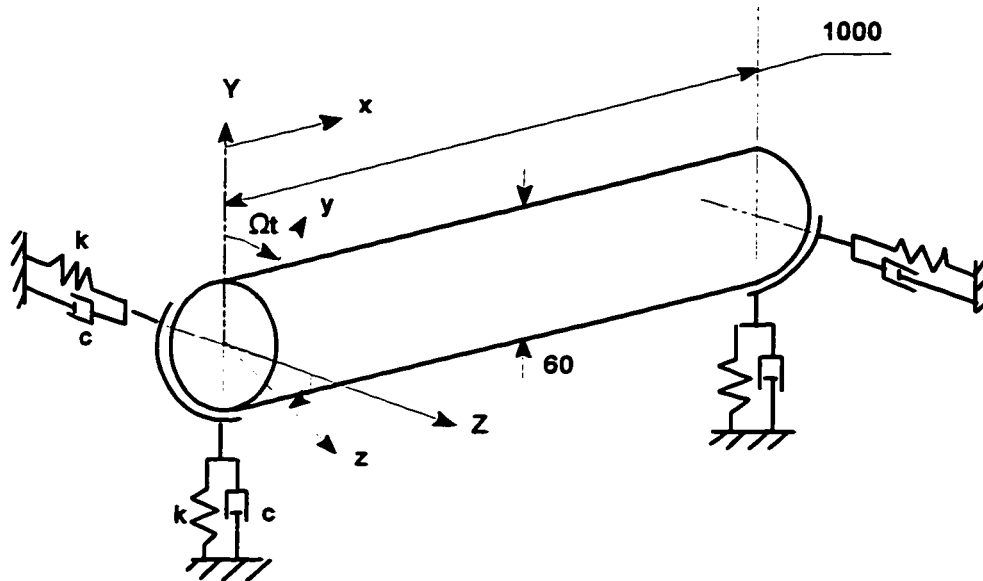


Figure 6.4 The configuration of the rotor-bearing system

and in  $x$ - $z$  plane as

$$\zeta(x) = \begin{cases} -0.1 + 0.4x, & 0 \leq x \leq 500 \\ 0.1 - 0.4(x - 0.5), & 500 < x \leq 1000 \end{cases}$$

As proposed by Nelson (1980), using Hamilton's principle, the finite element equation for a rotating shaft including bearings can be given by

$$([M] + [N])\{\ddot{q}\} + ([C]_b - \Omega[G])\{\dot{q}\} + ([K] + [K]_b)\{q\} = \{Q_c\}\cos\Omega t + \{Q_s\}\sin\Omega t + \{f_r\} \quad (6.36)$$

where  $\{q\} = \{q_1, q_2, \dots, q_8\}^T$  is the displacement vector with respect to  $XY$  and  $XZ$  planes.  $[M]$

and  $[N]$  are the translational and rotatory mass matrix, respectively.  $[G]$  is the gyroscopic matrix which provides coupling between the two planes.  $[K]$  is the shaft stiffness matrix.  $[K_b]$  and  $[C_b]$  are the bearing stiffness and damping matrix, respectively.  $\{Q_c\}$  and  $\{Q_s\}$

are unbalance force vectors, due to distributed mass centre eccentricity  $\eta(x)$  and  $\zeta(x)$ , which can be obtained through variational work expressions.  $\{f_i\}$  stands for internal forces due to adjacent elements.

Note that the right-hand side of Eq.(6.36) can be rewritten as

$$R.H.S. = \{P\} + \{\bar{P}\} + \{f_c\} + \{\bar{f}_c\}$$

where  $\{P\}$  and  $\{\bar{P}\}$  are conjugate pairs of complex vectors with  $\{P\} = 1/2(\{Q_c\} - j\{Q_s\})e^{i\Omega t}$ .

$\{f_c\}$  and  $\{\bar{f}_c\}$  are also conjugate pairs whose real part is equal to  $\{f_r\}$ . Once the complex

response  $\{p\}$  corresponding to excitation  $\{P\}$  has been computed, one can easily obtain the true value of forced responses:

$$\{q\} = \{p\} + j\{\bar{p}\}$$

which is in the form of real numbers.

Since the properties and dimensions of the shaft and bearings are equal in both the orthogonal planes, the deflection trajectory of the shaft will appear in a circle with respect to the inertia frame. Figure 6.5 shows the unbalance response of the shaft at the midspan through the proposed TMM approach. The abscissa is the rotational speed of the shaft, and the ordinate is the corresponding unbalance response orbit radius. At around 4260 rpm, there occurs the peak response with the orbit radius of 0.65 mm. Thus the forced response, based on finite element modelling, of such a damped and gyroscopic system was obtained through only small matrix operations, without solving a complicated eigenvalue problem which is required when the mode superposition method is employed.

From the above examples, it has been shown that a transfer matrix method based on



finite element models can be used for the dynamic analysis of a chain-like structure under harmonic excitations. The given numerical examples have demonstrated its applicability and efficiency. The method allows any possible distributed external forces to be included by transfer matrices, so that the forced response could be successfully simulated. Condensation can be made when dealing with a number of identical elements. It can also be employed in a damped and/or gyroscopic system when the steady state response is examined. This method allows a very large system, with any external forces, to be modelled by finite elements and to be calculated with the transfer matrix technique. The numerical operation can even be implemented on a desktop computer.

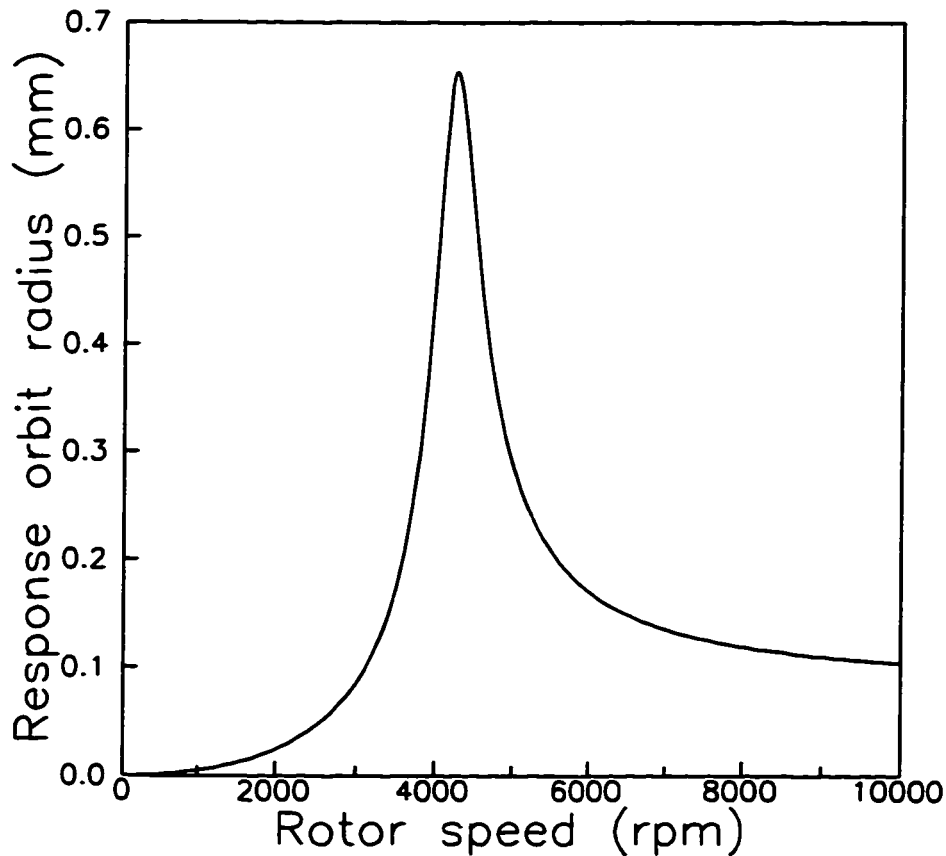


**Figure 6.5** The unbalance response of the rotating shaft with bearings

### 6.3 Dynamic Reduction

It is well known that the finite element method for modelling the dynamics of a large structure often leads to a complicated eigenvalue problem which requires huge working matrices, thus taking much computer memory and long processing time. Since not all these eigenvalues have to be taken into consideration in reality, several reduction methods have been developed. Yu and Craggs (1995a) proposed a transfer matrix technique with finite element modelling. Craggs and Eckert (1992) came up with a reduction procedure called continuous coordinate condensation.

Since transfer matrix techniques are well known to rotordynamic analysts, they can be implemented on a desktop computer. However, it may sometimes cause numerical instability. The previous continuous coordinate condensation method can be used to obtain natural frequencies effectively by using small matrix operations without any loss of accuracy. However, it only involves condensation of dynamic matrices, not of external forces or excitations.

The dynamic reduction condenses not only dynamic matrices but also any distributed forces or excitations. This method allows one to select nodal points of interest, i.e. the remaining degrees of freedom, at which condensed external force or excitation vectors can be equivalently applied. The accuracy of the solution will not be affected due to the use of the dynamic reduction. Thus it gives a relationship between some distributed forces of the system and condensed equivalent forces right at the selected nodes. The magnitudes of these condensed forces are also dependent on the system characteristics and forcing frequencies. It can be inferred that dynamic response due to distributed forces can be simulated by only applying the equivalent forces at the selected nodes. This may help to determine mass imbalance distribution along the shaft through several speeds and balance it in selected planes of interest.

The previous work about coordinate condensation demonstrated that the reduction was applicable to end-node elements which have nodal variables only at left and right ends. In fact, as shown in the following, such restriction is unnecessary and the reduction method

can be employed in all kinds of elements or superelements consisting of a few basic elements. The reduction can be implemented for systems with any boundary conditions, including structures having rigid body motion. The physical meaning of the solution will also be interpreted.

### 6.3.1 Dynamic Matrix and Force Vector Reduction

When the linear vibration behaviour is examined, the equation of motion for each element can be given in the following matrix form:

$$\begin{aligned} [M^{(e)}]\{\ddot{U}^{(e)}\} + ([C^{(e)}] + [G^{(e)}])\{\dot{U}^{(e)}\} + [K^{(e)}]\{U^{(e)}\} \\ = \{F^{(e)}\} + \{f^{(e)}\} \end{aligned} \quad (6.37)$$

Where  $[M^{(e)}]$ ,  $[C^{(e)}]$ ,  $[G^{(e)}]$  and  $[K^{(e)}]$  are the mass, damping, gyroscopic and stiffness matrices of the element, respectively.  $\{U^{(e)}\}$  denotes the displacement vector involving all the degrees of freedom of the element.  $\{F^{(e)}\}$  stands for the generalized force vector due to any distributed external forces or excitations, which can be consistently obtained using the virtual work principle.  $\{f^{(e)}\}$  is the corresponding internal force vector due to adjacent elements.

The dynamic matrix  $[D]$  for the element is defined as

$$[D^{(e)}] = [K^{(e)}] - \omega^2[M^{(e)}] + j\omega([C^{(e)}] + [G^{(e)}]) \quad (6.38)$$

where  $\omega$  is the frequency of harmonic exciting forces exerted somewhere.

Two elements (or superelements composed of several basic elements) undergoing forced vibration, as shown in Figure 6.5, result in the following matrix equations of motion:

$$\begin{bmatrix} D_{11}^{(1)} & D_{12}^{(1)} \\ D_{21}^{(1)} & D_{22}^{(1)} \end{bmatrix} \begin{Bmatrix} U_l \\ U_m \end{Bmatrix} = \begin{Bmatrix} F_l^{(1)} \\ F_m^{(1)} \end{Bmatrix} + \begin{Bmatrix} f_l \\ f_m \end{Bmatrix} \quad (6.39)$$

and

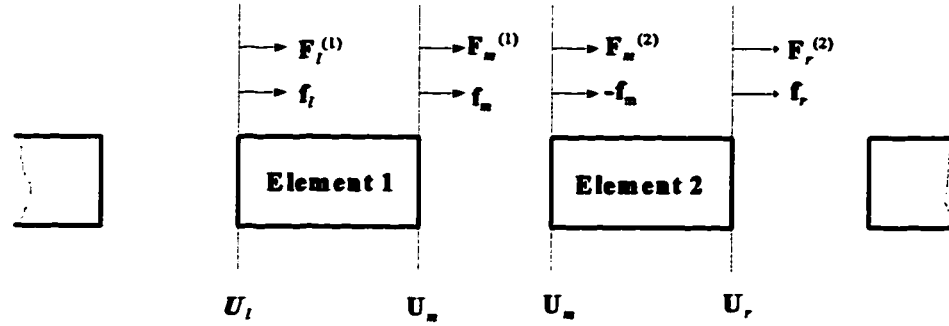


Figure 6.6 Chain assembled elements/superelements

$$\begin{bmatrix} D_{11}^{(2)} & D_{12}^{(2)} \\ D_{21}^{(2)} & D_{22}^{(2)} \end{bmatrix} \begin{Bmatrix} U_m \\ U_r \end{Bmatrix} = \begin{Bmatrix} F_m^{(2)} \\ F_r^{(2)} \end{Bmatrix} + \begin{Bmatrix} -f_m \\ f_r \end{Bmatrix} \quad (6.40)$$

where all displacement and force vectors are expressed in the form of complex amplitudes.

Eqs.(6.39) and (6.40) can be combined into the following matrix equation:

$$\begin{bmatrix} D_{ll} & D_{lm} & 0 \\ D_{ml} & D_{mm} & D_{mr} \\ 0 & D_{rm} & D_{rr} \end{bmatrix} \begin{Bmatrix} U_l \\ U_m \\ U_r \end{Bmatrix} = \begin{Bmatrix} F_l^{(1)} \\ F_m^{(1)} + F_m^{(2)} \\ F_r^{(2)} \end{Bmatrix} + \begin{Bmatrix} f_l \\ 0 \\ f_r \end{Bmatrix} \quad (6.41)$$

where the left-hand side square matrix is defined as

$$\begin{bmatrix} D_{ll} & D_{lm} & 0 \\ D_{ml} & D_{mm} & D_{mr} \\ 0 & D_{rm} & D_{rr} \end{bmatrix} = \begin{bmatrix} D_{ll}^{(1)} & D_{lr}^{(1)} & 0 \\ D_{rl}^{(1)} & D_{rr}^{(1)} + D_{ll}^{(2)} & D_{lr}^{(2)} \\ 0 & D_{rl}^{(2)} & D_{rr}^{(2)} \end{bmatrix}$$

Note that the displacement vector  $U_m$  can be expressed as

$$\begin{aligned}
 U_m = & -D_{mm}^{-1}D_{ml}U_l - D_{mm}^{-1}D_{mr}U_r + \\
 & + D_{mm}^{-1}(F_m^{(1)} + F_m^{(2)})
 \end{aligned}
 \tag{6.42}$$

Eliminating  $U_m$  in Eq. (6.41), a condensed form of the forced vibration problem due to any distributed harmonic excitations can be written as

$$\begin{aligned}
 & \begin{bmatrix} D_{ll} - D_{lm}D_{mm}^{-1}D_{ml} & -D_{lm}D_{mm}^{-1}D_{mr} \\ -D_{rm}D_{mm}^{-1}D_{ml} & D_{rr} - D_{rm}D_{mm}^{-1}D_{mr} \end{bmatrix} \begin{Bmatrix} U_l \\ U_r \end{Bmatrix} \\
 & = \begin{Bmatrix} F_l^{(1)} - D_{lm}D_{mm}^{-1}(F_m^{(1)} + F_m^{(2)}) \\ F_r^{(2)} - D_{rm}D_{mm}^{-1}(F_m^{(1)} + F_m^{(2)}) \end{Bmatrix} + \begin{Bmatrix} f_l \\ f_r \end{Bmatrix}
 \end{aligned}
 \tag{6.43}$$

Thus, the new reduced matrix form, i.e., Eq.(6.43) represents a substructure or superelement consisting of the two chained elements or superelements. Not only can the two dynamic matrices be condensed into the new one with the same size of one element or superelement, but also the distributed excitation can be equivalently condensed into concentrated nodal forces at the two ends of the new reduced subsystem. This process can be repeated as many other subsequent elements or superelements are added to the model being condensed, as shown in Figure 6.6 and expressed by

$$[D^*] \begin{Bmatrix} U_l \\ U_k \end{Bmatrix} = \begin{Bmatrix} F_l^* \\ F_k^* \end{Bmatrix} + \begin{Bmatrix} f_l \\ f_k \end{Bmatrix}
 \tag{6.44}$$

where  $D^*$  denotes the dynamic matrix of the new reduced system.  $U_l$  and  $U_k$  are the displacement amplitude vectors at the two ends, and could have more than one variable depending on the chosen elements or superelements.  $F_l^*$  and  $F_k^*$  represent the condensed force or excitation vectors equivalently acting at the two ends, due to any distributed force or excitation within the subsystem being reduced.  $f_l$  and  $f_k$  are just internal force vectors

produced by unreduced adjacent elements or superelements.

Sometimes more than one element must be discretized along the direction perpendicular to the chain line when using continuum elements instead of beam elements (Yu and Craggs, 1995b and 1997). In this case, one can form a *superelement* consisting of several basic elements. This superelement can be regarded as a short shaft element. Then the reduction procedure can still be utilized to obtain dynamic response due to any distributed loads.

It can be noticed that considerable computational efficiencies are achieved when one models uniform systems with a number of identical elements or superelements. Two identical elements can be condensed to a new superelement consisting of both elements. Then the two new superelements can be restructured to form another new superelement representing the four elements. In this way, after  $n$  times of condensation,  $2^n$  elements can be condensed into the reduced system without an increase of matrix and vector size.

It can be seen that distributed forces or excitations are modelled with two condensed vectors as they were applied at the two ends of the condensed system. The distributed forces within a basic element can first be consistently transformed into nodal forces such as the first term of the right-hand side of Eqs. (6.39) and (6.40). Then using the proposed reduction method for the condensed part of the system results in the equivalent force vectors such as

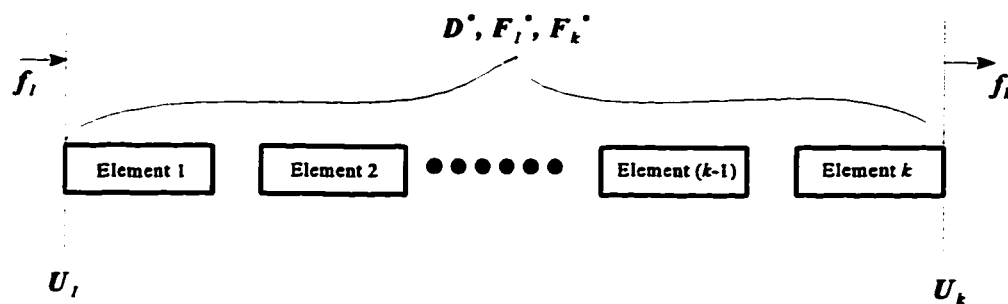


**Figure 6.7** New reduced system consisting of  $k$  elements/superelements

that in Eqs.(6.43)or (6.44). There could be more than one variable at each node, and more than one node at each end of the condensed part of the system. Therefore,  $F_i^*$  or  $F_k^*$  in Eq.(6.44) may have more than one variable depending on the chosen elements. This force condensation process results in no accuracy loss in the sense of consistent finite element modelling. Note that values of forces vary with dynamic stiffness matrices of the condensed part of the system. Therefore, even a constant concentrated force or distributed forces acting at some locations will be equivalent to *forcing frequency dependent* generalized nodal forces acting at both ends of the condensed part of the system. For the same reason, to a constant mass imbalance distribution, the equivalent nodal forces and moments are not simply proportional to the square of the shaft speed  $\Omega^2$ .

### 6.3.2 Condensation of Elements Having Intermediate Nodes

It has been shown in the above that the dynamic reduction method can be implemented in chain assembled finite elements having nodes only at both ends. Many elements, however, have nodal variables at intermediate nodes, as shown in Figure 6.7.

Through finite element modelling, the equation of motion for such an element as shown in Figure 6.7 (c), can be given in the following matrix form:

$$[M]\{\ddot{x}\} + ([C] + [G])\{\dot{x}\} + [K]\{x\} = \{F\} + \{f\} \quad (6.45)$$

Where  $[M]$ ,  $[C]$ ,  $[G]$  and  $[K]$  are the mass, damping, gyroscopic and stiffness matrices, respectively.  $\{x\}^T = \{x_l^T, x_m^T, x_r^T\}$  is the displacement vector in the order of left, middle and right end nodal variables.  $\{F\}$  is the generalized nodal force vector due to distributed external loads.  $\{f\}$  is the corresponding internal force vector.

The dynamic matrix  $[D]$  for the element is defined as

$$[D] = [K] - \omega^2[M] + j\omega([C] + [G]) \quad (6.46)$$

where  $\omega$  is the forcing frequency. The corresponding amplitude response  $\{X\}^T = \{X_l^T, X_m^T, X_r^T\}$  for this element can be expressed as

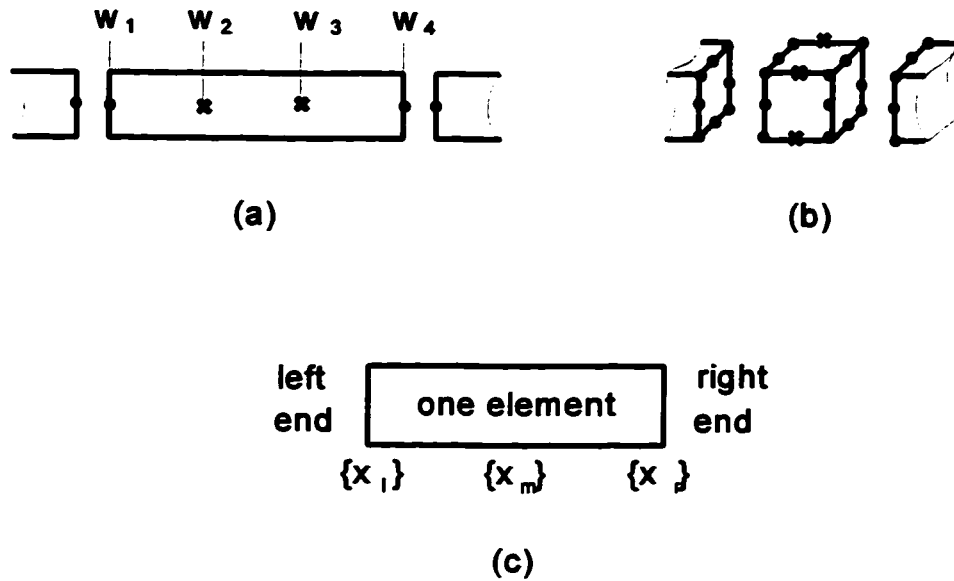


**Figure 6.8 Elements having intermediate nodal variables. (a) beams element with intermediate nodes “\*\*”, (b) continuum elements with intermediate nodes “\*\*”, and (c) general elements with intermediate nodal variables**

$$\begin{bmatrix} D_{ll} & D_{lm} & D_{lr} \\ D_{ml} & D_{mm} & D_{mr} \\ D_{rl} & D_{rm} & D_{rr} \end{bmatrix} \begin{Bmatrix} X_l^{(e)} \\ X_m^{(e)} \\ X_r^{(e)} \end{Bmatrix} = \begin{Bmatrix} F_l^{(e)} \\ F_m^{(e)} \\ F_r^{(e)} \end{Bmatrix} + \begin{Bmatrix} f_l^{(e)} \\ 0 \\ f_r^{(e)} \end{Bmatrix} \quad (6.47)$$

where  $F_l^{(e)}$ ,  $F_m^{(e)}$ , and  $F_r^{(e)}$  are generalized external force amplitudes.  $f_l^{(e)}$  and  $f_r^{(e)}$  are the corresponding internal force amplitudes due to adjacent left and right elements. Since the number of intermediate nodal variables can be different from that of left and right nodal variables,  $D_{lm}$ ,  $D_{ml}$ ,  $D_{mr}$  and  $D_{rm}$  may *not* be square matrices. This does not hinder one from



using the reduction method. It can be seen that Eq.(6.47) can be reduced to the following form:

$$\begin{bmatrix} D_{ll} - D_{lm}D_{mm}^{-1}D_{ml} & D_{lr} - D_{lm}D_{mm}^{-1}D_{mr} \\ D_{rl} - D_{rm}D_{mm}^{-1}D_{ml} & D_{rr} - D_{rm}D_{mm}^{-1}D_{mr} \end{bmatrix} \begin{Bmatrix} X_l^{(e)} \\ X_r^{(e)} \end{Bmatrix} = \begin{Bmatrix} F_l^{(e)} - D_{lm}D_{mm}^{-1}F_m^{(e)} \\ F_r^{(e)} - D_{rm}D_{mm}^{-1}F_m^{(e)} \end{Bmatrix} \quad (6.48)$$

Note that the above process is the reduction procedure within only one element involving intermediate nodal variables. Eq. (6.48) now has the same form as Eq.(6.39) or (6.40). Thus following the reduction procedure described in 6.3.1, one can condense more of such elements, so that the actual size of the working matrices remain the same as that in Eq. (6.48) and considerable computational efficiencies can be achieved when modelling uniform chain-like structure with many identical elements.

### 6.3.3 Boundary Conditions

Eigenvalues or forced responses of a structure vary with boundary conditions. Previous work (Craggs and Eckert, 1992) demonstrated a few examples where boundary conditions were set to guarantee no rigid body motion. However, not only elastic but also rigid body motions do occur in some cases such as rotating shafts and free-free beams. Can the dynamic reduction method still be employed to obtain convergent eigenvalues?

Usually what interests engineers is the pure elastic motion although the rigid body motion may exist for the structure. To obtain eigenvalues or forced responses corresponding to elastic modes, one does not have to evaluate rigid body modes. In fact, a particular distributed excitation at a forcing frequency can only excite a mode which has a natural frequency close to it. Similarly, the rigid body modes will not occur when forcing frequencies are greater than zero. Therefore, the eigenvalues corresponding to elastic modes within the frequency range of interest can be easily obtained without any additional

processing.

When constraints such as clamped and hinged beams appear, one needs to handle them by eliminating corresponding displacements and rows and columns in dynamic matrices or adding appropriate stiffness at these points; when no constraints appear or constraints still allow rigid body motions, one can find out elastic modes and corresponding natural frequencies by sweeping harmonic forcing frequencies of interest without removing rigid body modes.

### 6.3.4 Implication of Solution

The dynamic reduction method is based on the steady state forced responses to harmonic excitations. From the theory of vibration, it is known that if the exciting force coincides with one of the natural frequencies of the system, a condition known as resonance occurs, and the system undergoes large oscillations. When a mass matrix is real symmetric positive definite and a stiffness matrix is real symmetric and positive semidefinite or positive definite, the resonance information reveals the corresponding natural frequencies and mode shapes under the assumption of no damping. If damping is considered, the resonance will approximately give the imaginary part of the corresponding complex eigenvalues of the system.

For rotating shafts, gyroscopic terms are included in the equation of motion. If properties of mass and stiffness matrices remain the same as above, the resonance can still accurately lead to the resolution of real eigenvalue problems for the system. In this case, a resonance frequency or natural frequency corresponds to the pure imaginary eigenvalue, and the eigenvector is complex (Meirovitch, 1974). However, when the stiffness matrix is negative definite, it will be hard to determine *priori* the nature of eigenvalues. If the gyroscopic force is substantial to stabilize the system so that all the eigenvalues remain purely imaginary, then the continuous coordinate condensation method can still be adopted to attain true solutions.

It is noted that when external excitations are applied to a stable system, the dynamic

---

reduction method yields the accurate forced response. When damping and/or gyroscopic terms are included, the operation can be in the form of complex matrices. If the eigenvalues of the system are purely imaginary, this procedure reveals accurate eigenvalues and eigenvectors. If the eigenvalues of the system are complex with small negative real parts which often results from damping, the solution can still be approximately regarded as natural frequencies and mode shapes. However, this reduction method ceases to determine the stability of the system because all real parts of the eigenvalues cannot be given simultaneously. Fortunately, for many vibrating systems stabilities are guaranteed and only natural frequencies and forced response are of interest to engineers.

The dynamic response will be based on types of excitations for a given system. When bending modes are examined, for example, one should apply certain bending excitations to the system. Thus in case there is more than one mode corresponding to the same natural frequency, these modes can be easily captured by applying appropriate excitations. Of course, coupling behaviour can be observed by looking at response due to another mode type of excitations, as discussed in Chapter 3.

## **Chapter 7**

# **Fluid/Shaft Interaction**

In many rotating machines, the shaft is supported by fluid-film bearings instead of rolling-element bearings. The latter can be easily modelled by a linear or nonlinear bidirectional spring with little or no damping and no cross-coupling. Even though rolling-element bearings are used in aircraft turbine engines due to easy maintenance, fluid-film bearings are still attached to ensure high damping. Fluid-film bearings have a long life, high load capacity and low power loss.

Since beam elements are usually employed to model a shaft, eight dynamic coefficients ( four stiffness and four damping coefficients ) are often added to the shaft, as a bearing effect, to conduct the dynamic analysis of the whole system. For the shaft modelled with 3-D solid finite elements, however, it is believed that a corresponding distributed pressure model should be employed in accordance with the shaft model, to obtain system response accurately.

There are many types of fluid-film bearings including seals. In addition to plain journal bearings, tilting pad bearings are sometimes used to provide stable working conditions despite low load capacity. Seals are more complicated to model than ordinary bearings. Since the plain journal bearing is the simplest of all hydrodynamic bearings, all the discussion in this chapter will be referred to this type of bearing.

In this chapter, a lubrication equation in the rotating frame is derived and then applied

to practical bearing problems. Pressure distribution calculation is carried out using finite element techniques. A distributed shaft surface force model due to dynamic pressure of the fluid is established in accordance with the previously discussed 3-D solid finite element shaft model. Comparison of distributed and concentrated damping force models shows the necessity of using the former model. Forced responses due to mass imbalance are also computed for a rotor-bearing system.

## 7.1 Relationship of Dynamic Coefficients between Fixed and Rotating Frames

When beam elements are employed in the rotordynamic analysis, the fixed frame is often involved in which eight dynamic coefficients are evaluated. One can also model a rotor-bearing system in the rotating frame which corresponds to different dynamic coefficients. The relationship of dynamic coefficients in fixed and rotating frames is given in the following.

Assume there is a bearing force which can be expressed in the fixed reference frame as

$$\begin{Bmatrix} F_x \\ F_y \end{Bmatrix} = [K] \begin{Bmatrix} x \\ y \end{Bmatrix} + [C] \begin{Bmatrix} \dot{x} \\ \dot{y} \end{Bmatrix} \quad (7.1)$$

where  $[K]$  and  $[C]$  are defined as so called stiffness and damping matrices of the bearing. The eight dynamic coefficients are assumed as

$$[K] = \begin{bmatrix} k_{11} & k_{12} \\ k_{21} & k_{22} \end{bmatrix}, \quad [C] = \begin{bmatrix} c_{11} & c_{12} \\ c_{21} & c_{22} \end{bmatrix} \quad (7.2)$$

This bearing force can also be expressed in the rotating reference frame, as shown in

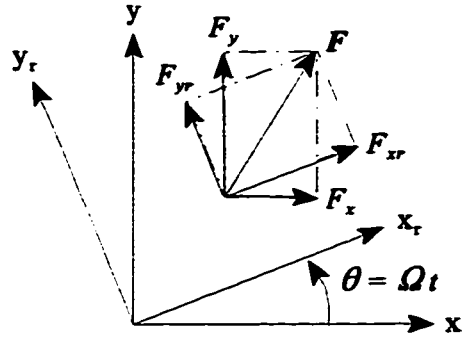


**Figure 7.1 Bearing force in the fixed and rotating reference frames**

Figure 7.1. It follows that

$$\begin{Bmatrix} F_{xr} \\ F_{yr} \end{Bmatrix} = [T] \begin{Bmatrix} F_x \\ F_y \end{Bmatrix} \quad (7.3)$$

where the left-hand side denotes the components of the bearing force in the rotating reference frame.  $[T]$  is the coordinate transfer matrix, which can be given by

$$[T] = \begin{bmatrix} \cos\theta & \sin\theta \\ -\sin\theta & \cos\theta \end{bmatrix} \quad (7.4)$$

where  $\theta = \Omega t$ . It can be seen that  $[T]^{-1} = [T]^T$ .

The displacements in the two reference frames can be related by

$$\begin{Bmatrix} x \\ y \end{Bmatrix} = [T]^{-1} \begin{Bmatrix} x_r \\ y_r \end{Bmatrix} \quad (7.5)$$

Differentiating Eq.(7.5) with respect to the time results in

$$\begin{Bmatrix} \dot{x} \\ \dot{y} \end{Bmatrix} = \frac{d}{dt}([T]^{-1}) \begin{Bmatrix} x_r \\ y_r \end{Bmatrix} + [T]^{-1} \begin{Bmatrix} \dot{x}_r \\ \dot{y}_r \end{Bmatrix} \quad (7.6)$$

Substituting Eqs.(7.1), (7.2), (7.4), (7.5), (7.6) into Eq.(7.3) yields

$$\begin{Bmatrix} F_{xr} \\ F_{yr} \end{Bmatrix} = [K_r] \begin{Bmatrix} x_r \\ y_r \end{Bmatrix} + [C_r] \begin{Bmatrix} \dot{x}_r \\ \dot{y}_r \end{Bmatrix} \quad (7.7)$$

where

$$[K_r] = \begin{bmatrix} k_{11}^{(r)} & k_{12}^{(r)} \\ k_{21}^{(r)} & k_{22}^{(r)} \end{bmatrix} + \Omega \begin{bmatrix} k_{11}^{(c)} & k_{12}^{(c)} \\ k_{21}^{(c)} & k_{22}^{(c)} \end{bmatrix} \quad (7.8)$$

$$[C_r] = \begin{bmatrix} c_{11}^{(r)} & c_{12}^{(r)} \\ c_{21}^{(r)} & c_{22}^{(r)} \end{bmatrix} \quad (7.9)$$

in which

$$\begin{aligned} k_{11}^{(r)} &= k_{11} \cos^2\theta + (k_{21} + k_{12}) \sin\theta \cos\theta + k_{22} \sin^2\theta \\ k_{12}^{(r)} &= k_{12} \cos^2\theta - (k_{11} - k_{22}) \sin\theta \cos\theta - k_{21} \sin^2\theta \\ k_{21}^{(r)} &= k_{21} \cos^2\theta - (k_{11} - k_{22}) \sin\theta \cos\theta - k_{12} \sin^2\theta \\ k_{22}^{(r)} &= k_{22} \cos^2\theta - (k_{21} + k_{12}) \sin\theta \cos\theta + k_{11} \sin^2\theta \end{aligned} \quad (7.10)$$

$$\begin{aligned}
k_{11}^{(e)} &= c_{12} \cos^2 \theta - (c_{11} - c_{22}) \sin \theta \cos \theta - c_{21} \sin^2 \theta \\
k_{12}^{(e)} &= -c_{11} \cos^2 \theta - (c_{12} + c_{21}) \sin \theta \cos \theta - c_{22} \sin^2 \theta \\
k_{21}^{(e)} &= c_{22} \cos^2 \theta - (c_{12} + c_{21}) \sin \theta \cos \theta + c_{11} \sin^2 \theta \\
k_{22}^{(e)} &= -c_{21} \cos^2 \theta + (c_{11} - c_{22}) \sin \theta \cos \theta + c_{12} \sin^2 \theta
\end{aligned} \tag{7.11}$$

and

$$\begin{aligned}
c_{11}^{(r)} &= c_{11} \cos^2 \theta + (c_{21} + c_{12}) \sin \theta \cos \theta + c_{22} \sin^2 \theta \\
c_{12}^{(r)} &= c_{12} \cos^2 \theta - (c_{11} - c_{22}) \sin \theta \cos \theta - c_{21} \sin^2 \theta \\
c_{21}^{(r)} &= c_{21} \cos^2 \theta - (c_{11} - c_{22}) \sin \theta \cos \theta - c_{12} \sin^2 \theta \\
c_{22}^{(r)} &= c_{22} \cos^2 \theta - (c_{21} + c_{12}) \sin \theta \cos \theta + c_{11} \sin^2 \theta
\end{aligned} \tag{7.12}$$

It can be seen that in general, the dynamic coefficients, i.e., stiffness and damping matrices of the bearings, are not the same in the two reference frames. If they are constant in one reference frame, they will generally become time-dependent in the other frame provided the two frames are rotating with respect to each other. It should be noticed that damping coefficients will contribute to the stiffness matrix in the other rotating frame.

There is one exception when  $k_{11} = k_{22} = k_1$ ,  $k_{12} = -k_{21} = k_2$  and  $c_{11} = c_{22} = c_1$ ,  $c_{12} = -c_{21} = c_2$ , i.e.,

$$[K] = \begin{bmatrix} k_1 & k_2 \\ -k_2 & k_1 \end{bmatrix}, \quad [C] = \begin{bmatrix} c_1 & c_2 \\ -c_2 & c_1 \end{bmatrix} \tag{7.13}$$

In this case, the corresponding stiffness and damping matrices can be given by



$$[K_r] = \begin{bmatrix} k_1 & k_2 \\ -k_2 & k_1 \end{bmatrix} + \Omega \begin{bmatrix} c_2 & -c_1 \\ c_1 & c_2 \end{bmatrix}, \quad [C_r] = \begin{bmatrix} c_1 & c_2 \\ -c_2 & c_1 \end{bmatrix} \quad (7.14)$$

If an inertial force generated in one reference frame needs to be expressed in the other frame, one could use the relation

$$\begin{Bmatrix} \ddot{\bar{x}} \\ \ddot{\bar{y}} \end{Bmatrix} = \Omega^2 \begin{bmatrix} -c & s \\ -s & -c \end{bmatrix} \begin{Bmatrix} x_r \\ y_r \end{Bmatrix} + 2\Omega \begin{bmatrix} -s & -c \\ c & -s \end{bmatrix} \begin{Bmatrix} \dot{x}_r \\ \dot{y}_r \end{Bmatrix} + \begin{bmatrix} c & -s \\ s & c \end{bmatrix} \begin{Bmatrix} \ddot{x}_r \\ \ddot{y}_r \end{Bmatrix} \quad (7.15)$$

where

$$c = \cos(\Omega t), \quad s = \sin(\Omega t)$$

to obtain the corresponding expressions

## 7.2 Lubrication Equations in Rotating Frame

Rotordynamics involves both rotating shaft dynamics and bearing hydrodynamics. The latter can also be called a shaft/fluid interaction problem. Baskharone and Hensel (1991a, 1991b) dealt with seals using three-dimensional fluid finite elements. They gave four dynamic coefficients in the form of Eq.(7.13). Since the fluid-film of journal bearings is relatively thin, a simpler lubrication equation might be more appropriate and economical. The Reynolds equation (Reynolds, 1886; Childs, 1993) was established in the fixed frame of reference. If the rotating frame is selected, the distributed pressure can be straightforwardly expressed on the surface of the shaft.

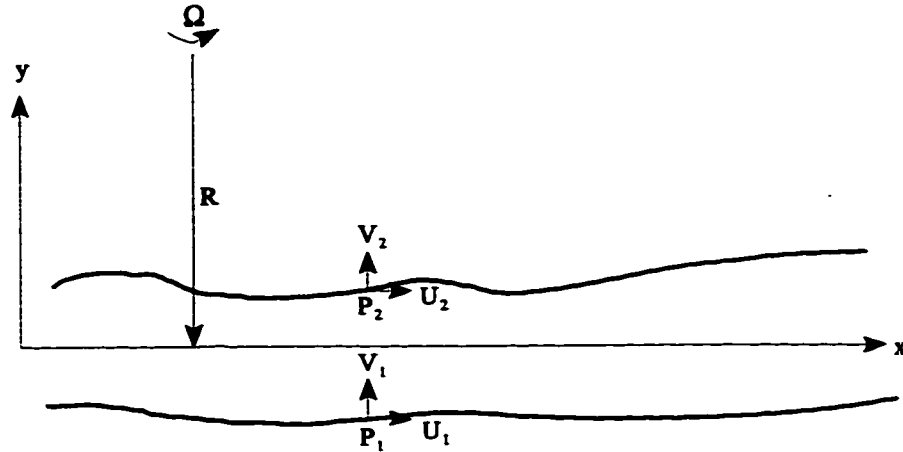


Figure 7.2 Fluid-film in a rotating frame

### 7.2.1 General Equations

In the rotating frame as shown in Figure 7.1, the  $xy$  plane rotates at a constant angular speed  $\Omega$  around  $z$ -axis. The two solid surfaces are filled with fluid, thus producing a very small thickness of the fluid-film. At an arbitrary location  $(x, z)$  of the film, there are two points  $P_1(x, y_1, z)$  and  $P_2(x, y_2, z)$  on the two surfaces, respectively. The corresponding velocities on these surface points (boundary conditions for fluid) are assumed to be  $U_1, V_1$  and  $U_2, V_2$  in  $x$  and  $y$  directions.

The Navier-Stokes equation for an incompressible Newtonian fluid in a non-inertial reference frame can be expressed as

$$\frac{DV}{Dt} = -\frac{1}{\rho}\nabla p + \nu\Delta V - a_e - 2(\omega \times V) \quad (7.16)$$

where

$V = ui + vj + wk$  ( velocity relative to the rotating frame)

$\omega = \Omega k$  (angular velocity of the rotating frame relative to the inertial frame)

$a_e = (R - y)\Omega^2 j$  (absolute acceleration at the point  $(x, y, z)$  when there is no relative motion in fluid)

$$2(\omega \times V) = 2\Omega u j - 2\Omega v i$$

$p$  = pressure

$\rho$  = fluid density

$\nu$  = fluid kinetic viscosity, which is assumed to be constant.

$$\nabla = \frac{\partial}{\partial x} i + \frac{\partial}{\partial y} j + \frac{\partial}{\partial z} k$$

$$\Delta = \frac{\partial^2}{\partial x^2} + \frac{\partial^2}{\partial y^2} + \frac{\partial^2}{\partial z^2}$$

Eq.(7.16) can be further expressed in x, y, and z directions as

$$\begin{aligned} \frac{\partial u}{\partial t} + u \frac{\partial u}{\partial x} + v \frac{\partial u}{\partial y} + w \frac{\partial u}{\partial z} &= -\frac{1}{\rho} \frac{\partial p}{\partial x} + \nu \left( \frac{\partial^2 u}{\partial x^2} + \frac{\partial^2 u}{\partial y^2} + \frac{\partial^2 u}{\partial z^2} \right) + 2\Omega v \\ \frac{\partial v}{\partial t} + u \frac{\partial v}{\partial x} + v \frac{\partial v}{\partial y} + w \frac{\partial v}{\partial z} &= -\frac{1}{\rho} \frac{\partial p}{\partial y} + \nu \left( \frac{\partial^2 v}{\partial x^2} + \frac{\partial^2 v}{\partial y^2} + \frac{\partial^2 v}{\partial z^2} \right) - 2\Omega u - (R-y)\Omega^2 \\ \frac{\partial w}{\partial t} + u \frac{\partial w}{\partial x} + v \frac{\partial w}{\partial y} + w \frac{\partial w}{\partial z} &= -\frac{1}{\rho} \frac{\partial p}{\partial z} + \nu \left( \frac{\partial^2 w}{\partial x^2} + \frac{\partial^2 w}{\partial y^2} + \frac{\partial^2 w}{\partial z^2} \right) \end{aligned} \quad (7.17)$$

Continuity equation for the incompressible-fluid can be given by

$$\frac{\partial u}{\partial x} + \frac{\partial v}{\partial y} + \frac{\partial w}{\partial z} = 0 \quad (7.18)$$

Nondimensionalization is made in order to yield simplified equations of the motion. The spatial coordinates are set to be

$$\bar{x} = \frac{x}{R}, \quad \bar{y} = \frac{y}{C_r}, \quad \bar{z} = \frac{z}{R}, \quad (7.19)$$

where  $C_r$  denotes the radial clearance between the bearing and the shaft. Velocity

components in the xz plane are nondimensionalized in terms of the shaft surface velocity  $R\Omega$ , i.e.,

$$\bar{u} = \frac{u}{R\Omega}, \quad \bar{w} = \frac{w}{R\Omega} \quad (7.20)$$

It follows that according to the continuity equation Eq.(7.18) the nondimensionalized velocity component perpendicular to the fluid-film has to be in the following form:

$$\bar{v} = \left( \frac{R}{C_r} \right) \frac{v}{R\Omega} \quad (7.21)$$

The Reynolds number is defined as

$$Re = \frac{C_r(R\Omega)}{v} \quad (7.22)$$

The pressure is nondimensionalized as

$$\bar{p} = Re \left( \frac{C_r}{R} \right) \frac{p}{\rho(R\Omega)^2} \quad (7.23)$$

Time is nondimensionalized as

$$\bar{t} = \Omega t \quad (7.24)$$

Substitution of Eqs.(7.19)-(7.24) into Eq.(7.17) yields

$$\begin{aligned} & Re \frac{C_r}{R} \left[ \frac{\partial \bar{u}}{\partial \bar{t}} + (\bar{u} \frac{\partial \bar{u}}{\partial \bar{x}} + \bar{v} \frac{\partial \bar{u}}{\partial \bar{y}} + \bar{w} \frac{\partial \bar{u}}{\partial \bar{z}}) \right] \\ & = -\frac{\partial \bar{p}}{\partial \bar{x}} + \frac{\partial^2 \bar{u}}{\partial \bar{y}^2} + \left( \frac{C_r}{R} \right)^2 \left( \frac{\partial^2 \bar{u}}{\partial \bar{x}^2} + \frac{\partial^2 \bar{u}}{\partial \bar{z}^2} \right) + 2 Re \left( \frac{C_r}{R} \right)^2 \bar{v} \end{aligned} \quad (7.25a)$$

$$\left(\frac{C_r}{R}\right)^2 \left[ \frac{C_r^2 \Omega}{\nu} \frac{\partial \bar{v}}{\partial t} + Re \frac{C_r}{R} \left( \bar{u} \frac{\partial \bar{v}}{\partial x} + \bar{v} \frac{\partial \bar{v}}{\partial y} + \bar{w} \frac{\partial \bar{v}}{\partial z} \right) \right]$$

$$= -\frac{\partial \bar{p}}{\partial y} + \frac{\partial^2 \bar{v}}{\partial y^2} + \left(\frac{C_r}{R}\right)^2 \left( \frac{\partial^2 \bar{v}}{\partial x^2} + \frac{\partial^2 \bar{v}}{\partial z^2} \right) - 2 Re \left(\frac{C_r}{R}\right)^2 \bar{u} - Re \left(\frac{C_r}{R}\right)^2 \left( 1 - \frac{C_r \bar{y}}{R} \right)$$
(7.25b)

$$Re \frac{C_r}{R} \left[ \frac{\partial \bar{w}}{\partial t} + \left( \bar{u} \frac{\partial \bar{w}}{\partial x} + \bar{v} \frac{\partial \bar{w}}{\partial y} + \bar{w} \frac{\partial \bar{w}}{\partial z} \right) \right]$$

$$= -\frac{\partial \bar{p}}{\partial z} + \frac{\partial^2 \bar{w}}{\partial y^2} + \left(\frac{C_r}{R}\right)^2 \left( \frac{\partial^2 \bar{w}}{\partial x^2} + \frac{\partial^2 \bar{w}}{\partial z^2} \right)$$
(7.25c)

Since  $C_r/R$  and  $Re$  are assumed to be very small, Eqs.(7.25a)-(7.25c) can be simplified as

$$\frac{\partial^2 u}{\partial y^2} = \frac{1}{\mu} \frac{\partial p}{\partial x}, \quad \frac{\partial^2 w}{\partial y^2} = \frac{1}{\mu} \frac{\partial p}{\partial z}, \quad \frac{\partial p}{\partial y} = 0$$
(7.26)

where  $\mu$  ( $= \nu\rho$ ) represents absolute viscosity. Using the boundary conditions as shown in Figure 7.1, it follows that

$$y = y_1(x, z): \quad u = U_1, \quad v = V_1, \quad w = 0$$

$$y = y_2(x, z): \quad u = U_2, \quad v = V_2, \quad w = 0$$
(7.27)

Thus, from Eqs.(7.26) - (7.27) the fluid velocity within this thin film can be given by

$$u = \frac{1}{2\mu} \frac{\partial p}{\partial x} (y - y_1)(y - y_2) + \frac{1}{y_2 - y_1} [U_1(y_2 - y) + U_2(y - y_1)]$$

$$w = \frac{1}{2\mu} \frac{\partial p}{\partial z} (y - y_1)(y - y_2)$$
(7.28)

Substitution of Eq.(7.28) into the continuity equation, i.e., Eq.(7.18), one has

$$\begin{aligned} \frac{\partial v}{\partial y} = & -\frac{\partial}{\partial x} \left[ \frac{1}{2\mu} \frac{\partial p}{\partial x} (y-y_1)(y-y_2) \right] - \frac{\partial}{\partial z} \left[ \frac{1}{2\mu} \frac{\partial p}{\partial z} (y-y_1)(y-y_2) \right] \\ & - \frac{\partial}{\partial x} \left\{ \frac{1}{y_2-y} [U_1(y_2-y) + U_2(y-y_1)] \right\} \end{aligned} \quad (7.29)$$

Note that for integrating  $f(x,t)$  with respect to  $x$  from  $x=a(t)$  to  $x=b(t)$ , the following relationship holds

$$\frac{d}{dt} \int_{a(t)}^{b(t)} f(x,t) dx = \int_{a(t)}^{b(t)} \frac{\partial}{\partial t} f(x,t) dx + f[b(t),t] \frac{d}{dt} b(t) - f[a(t),t] \frac{d}{dt} a(t)$$

Integrating Eq.(7.29) plus the above expression yields

$$\begin{aligned} V_2 - V_1 = & \int_{y_1}^{y_2} \frac{\partial v}{\partial y} dy = -\frac{\partial}{\partial x} \int_{y_1}^{y_2} \left[ \frac{1}{2\mu} \frac{\partial p}{\partial x} (y-y_1)(y-y_2) \right] dy - \frac{\partial}{\partial z} \int_{y_1}^{y_2} \left[ \frac{1}{2\mu} \frac{\partial p}{\partial z} (y-y_1)(y-y_2) \right] dy - \\ & - \frac{\partial}{\partial x} \int_{y_1}^{y_2} \left\{ \frac{1}{y_2-y} [U_1(y_2-y) + U_2(y-y_1)] \right\} dy + U_2 \frac{\partial y_2}{\partial x} - U_1 \frac{\partial y_1}{\partial x} \end{aligned} \quad (7.30)$$

Since the fluid-film thickness can be given by

$$H(x,z) = y_2(x,z) - y_1(x,z) \quad (7.31)$$

Eq.(7.30) can be rewritten as

$$\begin{aligned} \frac{\partial}{\partial x} \left[ \frac{H^3}{\mu} \frac{\partial p}{\partial x} \right] + \frac{\partial}{\partial z} \left[ \frac{H^3}{\mu} \frac{\partial p}{\partial z} \right] = & 12(V_2 - V_1) + 6(U_1 + U_2) \frac{\partial H}{\partial x} + 6H \frac{\partial}{\partial x} (U_1 + U_2) \\ & - 12U_2 \frac{\partial y_2}{\partial x} + 12U_1 \frac{\partial y_1}{\partial x} \end{aligned} \quad (7.32)$$

This is a simplified lubrication equation similar to the laminar-flow Reynolds equation (Childs, 1993). However, it appears that in general  $y_1(x,z)$  and  $y_2(x,z)$  cannot be completely substituted by  $H(x,z)$ .

If  $y_1(x,z)$  is assumed to be zero or constant, then Eq.(7.32) becomes

$$\frac{\partial}{\partial x} \left[ \frac{H^3}{\mu} \frac{\partial p}{\partial x} \right] + \frac{\partial}{\partial z} \left[ \frac{H^3}{\mu} \frac{\partial p}{\partial z} \right] = 12(V_2 - V_1) + 6(U_1 - U_2) \frac{\partial H}{\partial x} + 6H \frac{\partial}{\partial x} (U_1 + U_2) \quad (7.33)$$

which is often seen in books and papers. Another extreme situation is in the case where  $y_2(x,z)$  is assumed to be zero or constant. Then Eq.(7.32) becomes

$$\frac{\partial}{\partial x} \left[ \frac{H^3}{\mu} \frac{\partial p}{\partial x} \right] + \frac{\partial}{\partial z} \left[ \frac{H^3}{\mu} \frac{\partial p}{\partial z} \right] = 12(V_2 - V_1) + 6(U_2 - U_1) \frac{\partial H}{\partial x} + 6H \frac{\partial}{\partial x} (U_1 + U_2) \quad (7.34)$$

The correctness of Eq.(7.32) can be shown herein. To establish a lubrication equation along the thin film  $x$ , as shown in Figure 7.3 (a), two alternatives can be used. In Figure 7.3 (b),  $y_1$  is prescribed to be zero. It follows that

$$\begin{aligned} y_2(x,z) &= H(x,z); \\ U_1 &= U_A, \quad V_1 = V_A; \\ U_2 &= U_B, \quad V_2 = V_B. \end{aligned}$$

Thus

$$\begin{aligned} & \text{R.H.S. of Eq.(7.32) or Eq.(7.33)} \\ &= 12(V_B - V_A) + 6(U_A - U_B) \frac{\partial H}{\partial x} + 6H \frac{\partial}{\partial x} (U_A + U_B) \end{aligned}$$

However, if  $y_2$  is prescribed to be zero as shown in Figure 7.3 (c), then

$$\begin{aligned} y_1(x,z) &= -H(x,z); \\ U_1 &= U_B, \quad V_1 = -V_B; \\ U_2 &= U_A, \quad V_2 = -V_A. \end{aligned}$$

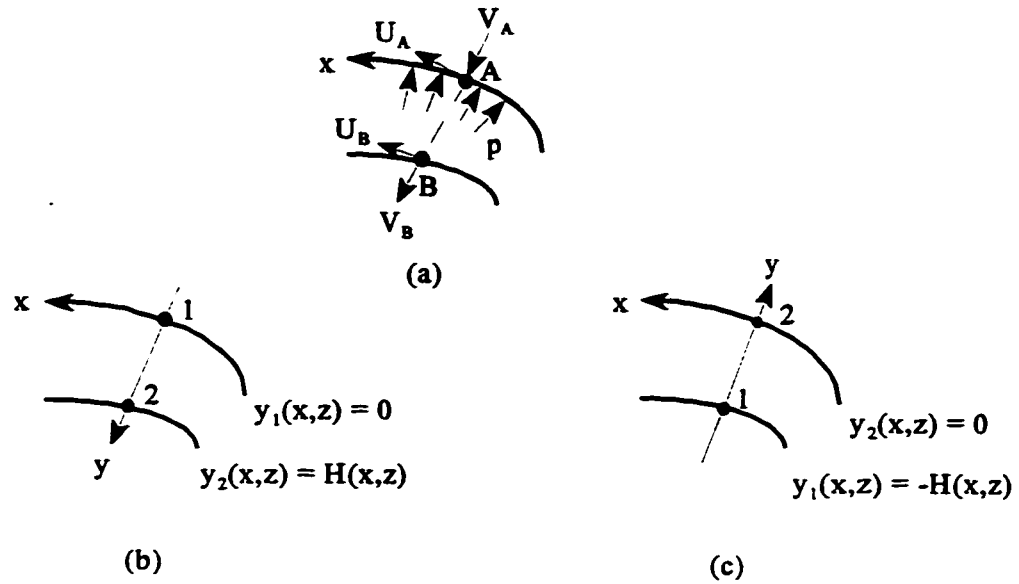


**Figure 7.3 Application of Eq.(7.32) in prescribed coordinates**

The right-hand-side of the corresponding equation can be written as

$$\begin{aligned}
 & \text{R.H.S. of Eq.(7.32) or Eq.(7.34)} \\
 & = 12 [(-V_A) - (-V_B)] + 6(U_A - U_B) \frac{\partial H}{\partial x} + 6H \frac{\partial}{\partial x} (U_A + U_B) \\
 & = 12(V_B - V_A) + 6(U_A - U_B) \frac{\partial H}{\partial x} + 6H \frac{\partial}{\partial x} (U_A + U_B)
 \end{aligned}$$

The two different prescribed coordinates with respect to  $y$  yield exactly the same partial differential equation as shown above. The two identical equations also show that a lubrication equation along the thin film  $x$  can be established by prescribing either  $y_1=0$  or  $y_2=0$  on the surface where an evaluation of pressure distribution is desired.

The author believes that Eq.(7.32) can be used more effectively in the two defect surfaces where both  $y_1$  and  $y_2$  vary with the film length  $x$ . It should be noted that viscous forces along the surfaces are often neglected. It seems that  $x$  axis should be prescribed along the surface upon which pressure distribution is examined.



The lubrication equation can be used in rotating or non-rotating reference frames. This is due to an assumed low Reynolds number  $Re$  and a short film clearance-to-radius ratio  $C/R$ , which allow one to neglect higher order terms such as inertia forces of the fluid.

## 7.2.2 Application of the Lubrication Equation

The purpose of the present development is to show how to apply the lubrication equation Eq.(7.32) in the rotor-fluid-bearing interaction. The effect of chosen circumferential coordinates and reference frames on the final equation will be examined. The relative elastic deformation within the rotor is considered to be small enough to be negligible, compared to the motion in the fluid. Note that the *circumferential variable*  $x$  as defined in Figure 7.2 is replaced by  $R\theta$ .  $R$  is the radius of the rotor (To be precisely,  $R + C$ , instead of  $R$  needs to be used for the bearing surface. This difference, however, makes no contribution to the final simplified equation).  $\theta$  is a counterclockwise rotation originating at the line of bearing or rotor centre. The perturbation of the rotor is assumed to be around the centre of the bearing. The rotor is assumed to be rotating counterclockwise at a rotational speed  $\Omega$ .

### Circumferential coordinates parallel to the bearing surface

The pressure is evaluated upon a circumferential coordinate parallel to the bearing surface. As shown in Figure 7.4, a circumferential film line is assumed to be a circle, parallel or attached to the bearing surface between the rotor and the bearing. Therefore,  $\theta$  corresponds to rotation about the centre of the bearing. Rotor displacement and velocity perturbations

$$\Delta x, \Delta y; \quad \Delta \dot{x}, \Delta \dot{y}$$

correspond to a film thickness  $H$  and fluid/rotor and fluid/bearing interface velocity components  $U_1, V_1$ , and  $U_2, V_2$ .

One can see that in the triangle  $\Delta OAC$ , the following relation holds:

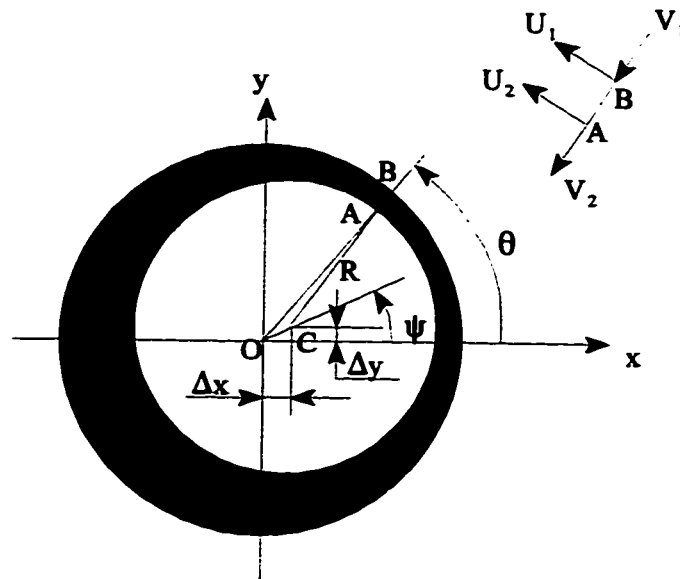


**Figure 7.4 Circumferential coordinate parallel to the bearing surface**

$$(\overline{OA})^2 = (\overline{AC})^2 + (\overline{OC})^2 + 2\overline{AC} \overline{OC} \cos(\psi - \theta)$$

where

$$\overline{OA} = \overline{OB} - \overline{AB} = (R + C_r) - H, \quad \overline{AC} = R, \quad \overline{OC} = e$$

Thus the film thickness  $H$  can be given by

$$H = R + C_r - \sqrt{R^2 + e^2 + 2Re \cos(\psi - \theta)}$$

Neglecting higher order terms than  $e/R$  after expanding  $H$  in terms of Taylor series results

in

$$H = C_r - e \cos(\psi - \theta) = C_r - \Delta x \cos \theta - \Delta y \sin \theta \quad (7.35)$$

In Eq.(7.32), the change rates of two surface edges to the film circumferential variable can be given by

$$\frac{\partial y_1}{\partial x} = 0, \quad \frac{\partial y_2}{\partial x} = \frac{\partial H}{\partial x} \quad (7.36)$$

### 1. In fixed frame

Evaluation of pressure distribution on the bearing surface in the fixed or inertial reference frame is the most common method in the hydrodynamic bearing analysis. Velocity components can be given by

$$\begin{aligned} U_1 = V_1 = 0; \\ U_2 = -\Delta \dot{x} \sin \theta + \Delta \dot{y} \cos \theta + R\Omega, \quad V_2 = -\Delta \dot{x} \cos \theta - \Delta \dot{y} \sin \theta \end{aligned} \quad (7.37)$$

Substitution of Eqs.(7.35) -(7.37) into Eq.(7.32) yields the following equation after neglecting second order terms:

$$\begin{aligned} \frac{1}{R^2} \frac{\partial}{\partial \theta} \left( \frac{H^3}{\mu} \frac{\partial p}{\partial \theta} \right) + \frac{\partial}{\partial z} \left( \frac{H^3}{\mu} \frac{\partial p}{\partial z} \right) \\ = -12 \Delta \dot{x} \cos \theta - 12 \Delta \dot{y} \sin \theta + 6 \Omega \Delta x \sin \theta - 6 \Omega \Delta y \cos \theta \end{aligned} \quad (7.38)$$

### 2. In rotating frame

In this frame, the bearing will be observed to be rotating clockwise at the speed  $\Omega$ . The origin of the rotating frame is set to be in the bearing centre. Thus the effect of a displaced rotor configuration is neglected if the pressure is considered to be acting on the rotor surface. Velocity components in this rotating frame are expressed as

$$\begin{aligned}
 U_1 &= -(R + C_r)\Omega, & V_1 &= 0; \\
 U_2 &= -\Delta x \sin\theta + \Delta y \cos\theta, & V_2 &= -\Delta x \cos\theta - \Delta y \sin\theta
 \end{aligned}
 \tag{7.39}$$

Using Eq.(7.32) along with Eqs.(7.35), (7.36) and (7.39) yields

$$\begin{aligned}
 &\frac{1}{R^2} \frac{\partial}{\partial \theta} \left( \frac{H^3}{\mu} \frac{\partial p}{\partial \theta} \right) + \frac{\partial}{\partial z} \left( \frac{H^3}{\mu} \frac{\partial p}{\partial z} \right) \\
 &= -12 \Delta x \cos\theta - 12 \Delta y \sin\theta - 6 \Omega \Delta x \sin\theta + 6 \Omega \Delta y \cos\theta
 \end{aligned}
 \tag{7.40}$$

#### Circumferential coordinates parallel to the rotor surface

It seems that pressure calculated directly on the rotor surface will yield more accurate solutions in the rotordynamic analysis. In this circumferential coordinate parallel or attached to the rotor surface,  $\theta$  is measured from the centre of the rotor. The simple diagram can be shown in Figure 7.5. In the triangle  $\Delta OBC$

$$(\overline{OB})^2 = (\overline{BC})^2 + (\overline{OC})^2 + 2 \overline{BC} \overline{OC} \cos(\psi - \theta)$$

where

$$\overline{OB} = R + C_r, \quad \overline{BC} = \overline{AC} + \overline{AB} = R + H, \quad \overline{OC} = e$$

It follows

$$H = C_r - \Delta x \cos\theta - \Delta y \sin\theta \tag{7.41}$$

$$\frac{\partial y_1}{\partial x} = -\frac{\partial H}{\partial x}, \quad \frac{\partial y_2}{\partial x} = 0 \tag{7.42}$$

Now the direction of film thickness  $H$  is perpendicular to the rotor surface. Thus the pressure is evaluated on the rotor surface as it is desired.

### 1. In fixed frame

An expression of pressure distribution on the rotor surface in the fixed frame is attempted. Velocity components can be given by

$$\begin{aligned} U_1 = V_1 = 0; \\ U_2 = -\Delta x \sin \theta + \Delta y \cos \theta + R\Omega, \quad V_2 = -\Delta x \cos \theta - \Delta y \sin \theta \end{aligned} \quad (7.43)$$

Use of Eq.(7.32) yields the following equation after neglecting second order terms:

$$\begin{aligned} \frac{1}{R^2} \frac{\partial}{\partial \theta} \left( \frac{H^3}{\mu} \frac{\partial p}{\partial \theta} \right) + \frac{\partial}{\partial z} \left( \frac{H^3}{\mu} \frac{\partial p}{\partial z} \right) \\ = -12 \Delta x \cos \theta - 12 \Delta y \sin \theta + 6 \Omega \Delta x \sin \theta - 6 \Omega \Delta y \cos \theta \end{aligned} \quad (7.44)$$

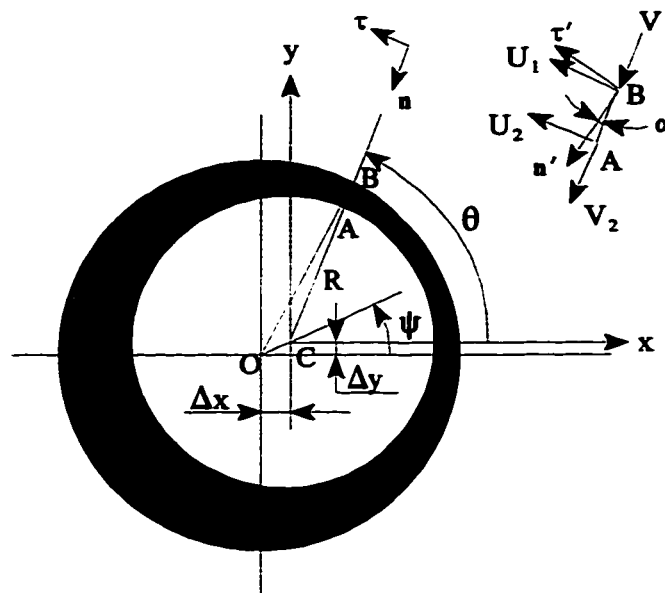


Figure 7.5 Circumferential coordinate parallel to the rotor surface

## 2. In rotating frame

In this frame, the bearing will be observed to be rotating clockwise at the speed  $\Omega$ . The origin of the rotating frame is set to be in the rotor centre. The relative motion is considered by fixing the rotor. As shown in Figure 7.5, point B on the bearing surface has a relative position

$$\mathbf{r} = -\Delta x \mathbf{i} - \Delta y \mathbf{j} - (R + C_r) \mathbf{n} \quad (7.45)$$

where  $\mathbf{i}$  and  $\mathbf{j}$  are the unit vectors of rotating coordinates  $x$  and  $y$ , and  $\mathbf{n}$  is the normal direction of the bearing surface. Note that

$$\frac{d\mathbf{i}}{dt} = \Omega \mathbf{j}, \quad \frac{d\mathbf{j}}{dt} = -\Omega \mathbf{i}, \quad \frac{d\mathbf{n}}{dt} = -\Omega \boldsymbol{\tau}'$$

Thus the velocity at point B with respect to the rotating frame can be given by

$$\begin{aligned} \frac{d\mathbf{r}}{dt} = & [\Delta \dot{x} \cos \theta - \Omega \Delta y \cos \theta + \Delta \dot{y} \sin \theta + \Omega \Delta x \sin \theta] \mathbf{n} + \\ & + [\Delta \dot{x} \sin \theta - \Omega \Delta y \sin \theta - \Delta \dot{y} \cos \theta - \Omega \Delta x \cos \theta] \boldsymbol{\tau}' - \Omega (R + C_r) \boldsymbol{\tau}' \end{aligned}$$

Since the angle  $\alpha$  in Figure 7.5 can be given by

$$\begin{aligned} \cos \alpha &= \frac{(R + C_r)^2 + (R + H_r)^2 - e^2}{2(R + C_r)(R + H_r)} \\ &= 1 + \frac{\left(\frac{C_r}{R} - \frac{H_r}{R}\right)^2 - \left(\frac{e}{R}\right)^2}{2\left(1 + \frac{C_r}{R}\right)\left(1 + \frac{H_r}{R}\right)} \\ &\approx 1 \end{aligned}$$

It follows that velocity components in this rotating frame, as shown in Figure 7.5, can be expressed as

$$\begin{aligned}
 U_1 &= \Delta \dot{x} \sin \theta - \Omega \Delta y \sin \theta - \Delta \dot{y} \cos \theta - \Omega \Delta x \cos \theta - \Omega(R + C_r), \\
 V_1 &= \Delta \dot{x} \cos \theta - \Omega \Delta y \cos \theta + \Delta \dot{y} \sin \theta + \Omega \Delta x \sin \theta; \\
 U_2 &= 0, \quad V_2 = 0.
 \end{aligned} \tag{7.46}$$

Substitution of Eqs.(7.41), (7.42) and (7.46) into Eq.(7.32) yields

$$\begin{aligned}
 &\frac{1}{R^2} \frac{\partial}{\partial \theta} \left( \frac{H^3}{\mu} \frac{\partial p}{\partial \theta} \right) + \frac{\partial}{\partial z} \left( \frac{H^3}{\mu} \frac{\partial p}{\partial z} \right) \\
 &= -12 \Delta \dot{x} \cos \theta - 12 \Delta \dot{y} \sin \theta - 6 \Omega \Delta x \sin \theta + 6 \Omega \Delta y \cos \theta
 \end{aligned} \tag{7.47}$$

From the above case studies, one could see that

1. For a plain journal bearing, the lubrication equation, i.e., Eq.(7.32), will yield different forms in the fixed and rotating frames. This change can be simply made by replacing “ $\Omega$ ” with “ $-\Omega$ ”.

2. A circumferential coordinate can be chosen to be parallel to (or directly on) either the bearing or the rotor surface. The results seem to be no difference for a small perturbation around the bearing centre.

3. For small perturbation, the circumferential coordinate can be established parallel to (or directly on) either the original or the displaced surface. The final equation will still be the same.

## 7.3 Pressure Distribution Calculation Using FEA

### 7.3.1 Equation in Rotating Frame for Eccentric Rotor

In the above discussion, the position of the rotor is situated in the centre of the

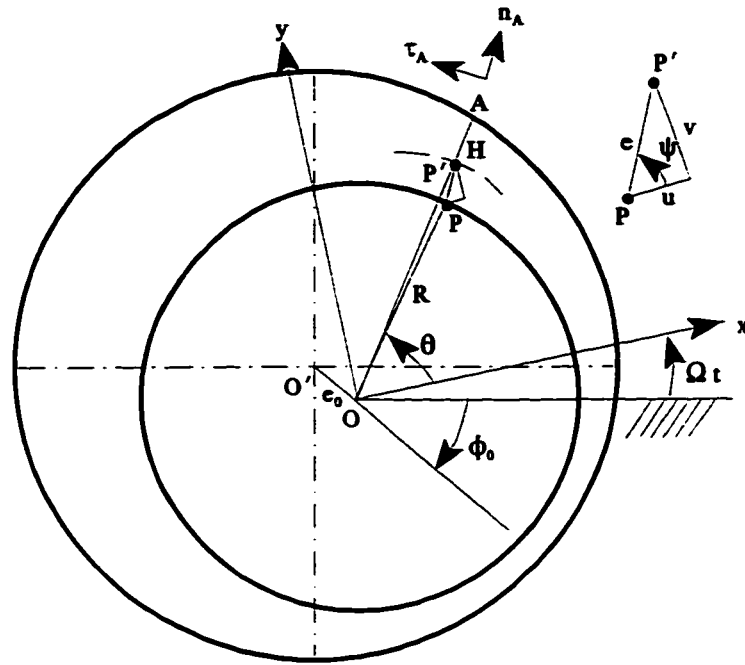


**Figure 7.6 Perturbation in rotating frame around eccentric rotor centre O**

bearing. Then hydrodynamic pressure is evaluated based on some small perturbation. For a light rotor or a rotor placed vertically, this procedure is considered to be very effective.

There are many situations where a rotor is located eccentrically relative to the bearing centre, due to the weight of the rotor. In this case, the rotor may be considered to be perturbed around its eccentric steady-state position, as shown in Figure 7.6.  $O'$  is the centre of the bearing,  $O$  is the centre of the rotor under steady-state condition due to its weight or other external non-rotating forces. The eccentricity  $e_0$  and the angle  $\phi_0$  can be determined from the lubrication equation Eq.(7.42) by prescribing zero velocity perturbation, plus boundary conditions.

Note that in the  $\Delta OO'A$ , one can obtain

$$(R + C_r)^2 = e_0^2 + \overline{OA}^2 + 2e_0 \overline{OA} \cos(\phi_0 + \Omega t + \theta)$$



After neglecting a second order term  $(e_0/R+C_r)^2$ , one may have

$$\overline{OA} = R + C_r - e_0 \cos(\phi_0 + \Omega t + \theta) \quad (7.48)$$

One may also be able to see that in  $\Delta OP'P$ ,

$$(\overline{OA} - H)^2 = e^2 + R^2 + 2Re \cos(\psi - \theta) \quad (7.49)$$

Note that the following relation

$$e \cos(\psi - \theta) = u \cos \theta + v \sin \theta \quad (7.50)$$

holds.

From Eqs.(7.48)-(7.50), one can obtain the film thickness

$$H = H_0 - u \cos \theta - v \sin \theta \quad (7.51)$$

where

$$H_0 = C_r - e_0 \cos(\phi_0 + \Omega t + \theta) \quad (7.52)$$

is steady state film thickness when there is no perturbation of  $u$  and  $v$ .

Let the circumferential coordinate be attached on the rotor of rotation. Thus,  $y_1$  and  $y_2$  presented in Eq.(7.32), are assumed as

$$\begin{aligned} y_1 &= 0 && \text{(on the rotor surface);} \\ y_2 &= H && \text{(on the bearing surface).} \end{aligned}$$

Since the circumferential coordinate is fixed on the rotating rotor surface, a perturbation  $u$  and  $v$  will make contributions to the velocity (expressed in this rotating circumferential coordinate) at the point A on the bearing surface. In the other words, the rotor is considered to be “motionless” as long as the relative motion between the bearing and the

rotor is correctly taken into account.

In this circumferential coordinate, therefore, the rotor surface velocity components are given by

$$U_1 = V_1 = 0$$

and the velocity at the point A on the bearing can be given by

$$\begin{aligned} V_A &= -\Omega \overline{OA} \tau_A - \dot{u}i - \dot{v}j + \Omega(i \times j) \times (-ui - vj) \\ &= U_2 \tau_A + V_2 n_A \end{aligned} \quad (7.53)$$

where

$$\begin{aligned} U_2 &= \dot{u} \sin \theta - \Omega v \sin \theta - \dot{v} \cos \theta - \Omega u \cos \theta - \Omega \overline{OA} \\ V_2 &= -\dot{u} \cos \theta + \Omega v \cos \theta - \dot{v} \sin \theta - \Omega u \sin \theta \end{aligned}$$

Assume that fluid film pressure is composed of steady state magnitude  $p_0$  and dynamic magnitude  $p$ . Thus, variable  $p$  in Eq. (7.32) is replaced by  $p_0$  and  $p$ . The variable  $p_0$  corresponds to  $H = H_0$  and no perturbation of rotor displacement and velocity. For a horizontal heavy rotor,  $H_0$  will vary with angle  $\theta$ , and a resultant value of  $p_0$  on the rotor surface will balance external forces such as the weight of gravity.

Substitution of  $y_1, y_2, H_0, p, p_0, U_1, V_1, U_2,$  and  $V_2$  into Eq.(7.32)

yields a general lubrication equation, which even could be applied to very flexible rotors. After dropping off second order terms, the left-hand side of the equation can be given by

$$\begin{aligned}
L.H.S. = & \frac{\partial}{\partial \theta} \left[ \frac{H_0^2(H_0 - u \cos \theta - v \sin \theta)}{R^2 \mu} \frac{\partial p}{\partial \theta} \right] + \frac{\partial}{\partial z} \left[ \frac{H_0^2(H_0 - u \cos \theta - v \sin \theta)}{\mu} \frac{\partial p}{\partial \theta} \right] \\
& - \frac{\partial}{\partial \theta} \left[ \frac{3H_0^2(u \cos \theta + v \sin \theta)}{R^2 \mu} \frac{\partial p_0}{\partial \theta} \right] - \frac{\partial}{\partial z} \left[ \frac{3H_0^2(u \cos \theta + v \sin \theta)}{\mu} \frac{\partial p_0}{\partial \theta} \right] \\
& + \frac{\partial}{\partial \theta} \left[ \frac{H_0^3}{R^2 \mu} \frac{\partial p_0}{\partial \theta} \right] + \frac{\partial}{\partial z} \left[ \frac{H_0^3}{\mu} \frac{\partial p_0}{\partial \theta} \right]
\end{aligned} \tag{7.54a}$$

and the right-hand side can be given by

$$R.H.S. = A_1 \dot{u} + A_2 \dot{v} + A_3 u + A_4 v + A_5 \frac{\partial \dot{u}}{\partial \theta} + A_6 \frac{\partial \dot{v}}{\partial \theta} + A_7 \frac{\partial u}{\partial \theta} + A_8 \frac{\partial v}{\partial \theta} + A_9 \tag{7.54b}$$

where

$$\begin{aligned}
A_1 &= -12 \cos \theta - 6 \frac{\sin \theta}{R} \frac{\partial H_0}{\partial \theta} + 6 \frac{H_0}{R} \cos \theta \\
A_2 &= -12 \sin \theta + 6 \frac{\cos \theta}{R} \frac{\partial H_0}{\partial \theta} + 6 \frac{H_0}{R} \sin \theta \\
A_3 &= -6 \Omega \sin \theta + 6 \Omega \frac{H_0}{R} \sin \theta + 12 \Omega \frac{\cos \theta}{R} \frac{\partial H_0}{\partial \theta} \\
A_4 &= 6 \Omega \cos \theta - 6 \Omega \frac{H_0}{R} \cos \theta + 12 \Omega \frac{\sin \theta}{R} \frac{\partial H_0}{\partial \theta} \\
A_5 &= 6 \frac{H_0}{R} \sin \theta \\
A_6 &= -6 \frac{H_0}{R} \cos \theta \\
A_7 &= -6 \Omega \cos \theta - 12 \Omega \frac{H_0}{R} \cos \theta \\
A_8 &= -6 \Omega \sin \theta - 12 \Omega \frac{H_0}{R} \sin \theta \\
A_9 &= 6 \Omega \frac{\partial H_0}{\partial \theta}
\end{aligned}$$

Note that the last two terms in Eq.(7.54a) and  $A_0$  in Eq.(7.54b) can be cancelled with each other. It means that when no perturbation of rotor displacements and velocities, the following relation

$$\frac{\partial}{\partial \theta} \left[ \frac{H_0^3}{R^2 \mu} \frac{\partial p_0}{\partial \theta} \right] + \frac{\partial}{\partial z} \left[ \frac{H_0^3}{\mu} \frac{\partial p_0}{\partial \theta} \right] = 6\Omega \frac{\partial H_0}{\partial \theta} \quad (7.55)$$

holds. Eq. (7.55) represents the steady state pressure which supports the rotor under external forces such as gravity. The equation can be formed to be time independent by replacing  $\Omega t + \theta$  with a new variable.

It can be seen that Eq.(7.54) is a time dependent equation in general due to the combination of rotor eccentricity  $e_0$  and perturbation  $u$  and  $v$  in the rotating frame. Therefore, displacements  $u$  and  $v$ , and dynamic pressure  $p$  will involve terms containing  $\sin(\Omega t)$  and  $\cos(\Omega t)$ . This will add difficulties in obtaining the response of the whole rotor-bearing system.

### 7.3.2 Equation in Rotating Frame for Centered Rotor

For vertical rotor-bearing systems or light rotors,  $e_0$  can be considered to be zero. One may also be able to make an assumption that the steady state position of the rotor is originally at the centre of the bearing. Thus, the dynamic response is calculated by summing all perturbations due to any possible dynamic force expressed in the rotating frame. For

further simplicity, terms involving  $\frac{H_0}{R}$  and  $\frac{1}{R} \frac{\partial H_0}{\partial \theta}$  are neglected when they are

compared with unity. Thus, one may obtain

$$\begin{aligned} & \frac{\partial}{\partial \theta} \left[ \frac{C_r^2}{R^2 \mu} (C_r - 3u \cos \theta - 3v \sin \theta) \frac{\partial p}{\partial \theta} \right] + \frac{\partial}{\partial z} \left[ \frac{C_r^2}{\mu} (C_r - 3u \cos \theta - 3v \sin \theta) \frac{\partial p}{\partial z} \right] \\ & = -12 \dot{u} \cos \theta - 12 \dot{v} \sin \theta - 6 \Omega u \sin \theta + 6 \Omega v \cos \theta - 6 \Omega \frac{\partial u}{\partial \theta} \cos \theta - 6 \Omega \frac{\partial v}{\partial \theta} \sin \theta \end{aligned} \quad (7.56)$$

One might need to have an insight of possible steps toward the solution of Eq.(7.56) and alternatives before conducting detailed numerical analysis. Finite element analysis is employed on the interface between the rotating shaft surface and the fluid film. If a linear analysis is desired, terms  $u \frac{\partial p}{\partial \theta}$  and  $v \frac{\partial p}{\partial \theta}$  may have to be dropped out.  $p$ ,  $u$  and  $v$  can

be substituted by

$$p = [N_e]^T \{p_e\}, \quad u = [N_e]^T \{u_e\}, \quad v = [N_e]^T \{v_e\} \quad (7.57)$$

where  $[N_e]$  is the shape function related to the element geometry, and  $\{p_e\}$ ,  $\{u_e\}$  and  $\{v_e\}$  are the nodal variables. Applying the Galerkin method to Eq.(7.56) for an arbitrary element yields

$$[H] \{p_e\} = [A] \{U_e\} + [B] \{\dot{U}_e\} \quad (7.58)$$

where  $\{U_e\}$  represents all the nodal displacement variables including slopes if any. Note that since  $[H]$  could be singular,  $[H]^{-1}$  may not be available. It is required that the whole interface equation has to be formed. Then after using boundary conditions to make the system matrix  $[H_s]$  non-singular, the pressure all over the interface  $\{p_s\}$  can be expressed as (not the final magnitude):

$$[H_s] \{p_s\} = [A_s] \{U_s\} + [B_s] \{\dot{U}_s\} \quad (7.59)$$

On the shaft, virtual work done by pressure is

$$\delta W = \{\delta U_s\}^T [Q] \{p_s\} \quad (7.60)$$

where  $[Q]$  involves an area integral over the elemental range. Therefore, the corresponding equivalent nodal force vector can be given by

$$\{F_s\} = [Q_s] \{p_s\} \quad (7.61)$$

Thus,  $\{p_s\}$  can be substituted in terms of  $\{U_s\}$  and  $\{\dot{U}_s\}$ . Using Boolean transformation matrix can make it match solid element nodal variables.

Reduction procedures, however, may not be able to be implemented within the shaft/fluid interface. To achieve high accuracy, many elements have to be adopted over the interface. Therefore, an alternative, which will be discussed next, is used to allow the application of reduction procedures for even the shaft section surrounded by the fluid film.

### 7.3.3 Perturbation Equations for Centered Rotor

Assume that dynamic pressure  $p$  can be expressed as

$$p = p_{,u} u + p_{,v} v + p_{,\dot{u}} \dot{u} + p_{,\dot{v}} \dot{v} + \dots \quad (7.62)$$

where

$$p_{,u} = \frac{\partial p}{\partial u}, \quad p_{,v} = \frac{\partial p}{\partial v}, \quad p_{,\dot{u}} = \frac{\partial p}{\partial \dot{u}}, \quad p_{,\dot{v}} = \frac{\partial p}{\partial \dot{v}}$$

represent the change rate of dynamic pressure over displacement/velocity. Substitution of Eq.(7.62) into Eq.(7.56), in which  $\partial u/\partial \theta$  and  $\partial v/\partial \theta$  are considered to be zero, yields

$$Au + Bv + C\dot{u} + D\dot{v} + \dots = 0 \quad (7.63)$$

Neglecting terms of second order or higher, one has

$$\begin{aligned} \frac{1}{R^2} \frac{\partial}{\partial \theta} \left( \frac{C_r^3}{\mu} \frac{\partial p_{,x}}{\partial \theta} \right) + \frac{\partial}{\partial z} \left( \frac{C_r^3}{\mu} \frac{\partial p_{,x}}{\partial z} \right) &= -6\Omega \sin \theta \\ \frac{1}{R^2} \frac{\partial}{\partial \theta} \left( \frac{C_r^3}{\mu} \frac{\partial p_{,y}}{\partial \theta} \right) + \frac{\partial}{\partial z} \left( \frac{C_r^3}{\mu} \frac{\partial p_{,y}}{\partial z} \right) &= 6\Omega \cos \theta \\ \frac{1}{R^2} \frac{\partial}{\partial \theta} \left( \frac{C_r^3}{\mu} \frac{\partial p_{,x}}{\partial \theta} \right) + \frac{\partial}{\partial z} \left( \frac{C_r^3}{\mu} \frac{\partial p_{,x}}{\partial z} \right) &= -12 \cos \theta \\ \frac{1}{R^2} \frac{\partial}{\partial \theta} \left( \frac{C_r^3}{\mu} \frac{\partial p_{,y}}{\partial \theta} \right) + \frac{\partial}{\partial z} \left( \frac{C_r^3}{\mu} \frac{\partial p_{,y}}{\partial z} \right) &= -12 \sin \theta \end{aligned} \quad (7.64)$$

Eq.(7.64) can be solved using FEA plus prescribed boundary conditions. Set

$$s = R\theta$$

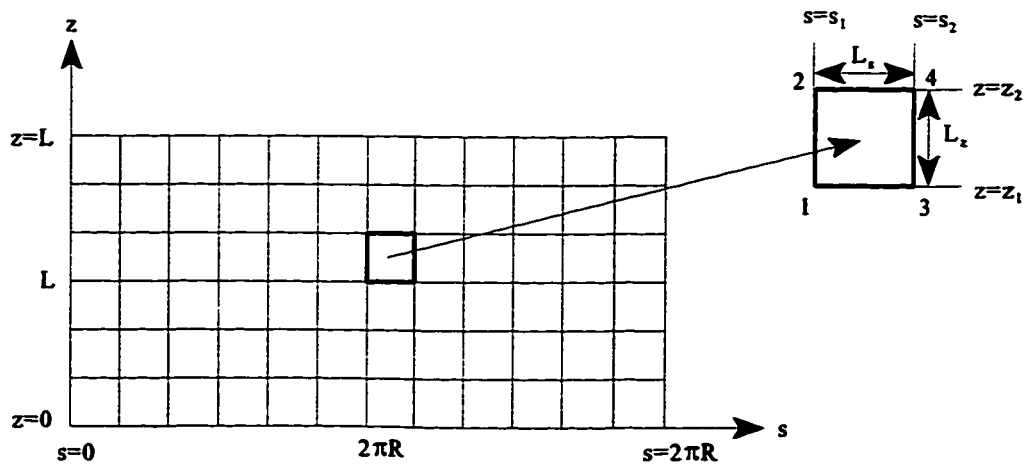


Figure 7.7 Diagram of finite element meshes for solving Eq.(7.65)

Let  $\phi$  stands for  $p_w, p_v, p_u, p_y$ , and  $E(s)$  for the remaining term. It follows that

$$\frac{\partial^2 \phi}{\partial s^2} + \frac{\partial^2 \phi}{\partial z^2} + E(s) = 0 \quad (7.65)$$

Assume that the bearing length is equal to  $L$ . Therefore, finite element discretization is made on the surface  $L \times 2\pi R$ . The steady state pressure, as indicated before, is  $p_0$ . At both axial ends of the bearing, the pressure is always kept as  $p_0$ , without additional dynamic pressure due to the rotor displacement or velocity perturbation. A continuous flow is assumed over the circumferential surface. Thus, the corresponding boundary conditions can be given by

$$\begin{aligned} \phi|_{z=0} &= \phi|_{z=L} = 0, \\ \phi|_{s=0} &= \phi|_{s=2\pi R} = 0 \end{aligned} \quad (7.66)$$

For an arbitrary element, as marked in Figure 7.5, the function  $\phi$  can be written as

$$\begin{aligned} \phi &= [N(s,z)]^T \{ \phi_e \} \\ &= \sum_{i=1}^4 N_i(s,z) \phi_i \end{aligned} \quad (7.67)$$

where



$$\begin{aligned}
 N_1 &= 1 - \frac{s-s_1}{L_s} - \frac{z-z_1}{L_z} + \frac{s-s_1}{L_s} \frac{z-z_1}{L_z} \\
 N_2 &= \frac{z-z_1}{L_z} - \frac{s-s_1}{L_s} \frac{z-z_1}{L_z} \\
 N_3 &= \frac{s-s_1}{L_s} - \frac{s-s_1}{L_s} \frac{z-z_1}{L_z} \\
 N_4 &= \frac{s-s_1}{L_s} \frac{z-z_1}{L_z}
 \end{aligned} \tag{7.68}$$

are shape functions with

$$N_i(s_j, z_j) = \delta_{ij}$$

Inserting Eq.(7.67) into Eq.(7.65) leads to the residual

$$Res = \left( \frac{\partial^2 [N]^T}{\partial s^2} + \frac{\partial^2 [N]^T}{\partial z^2} \right) \{\phi_e\} + E(s) \tag{7.69}$$

where

$$E(s) = \begin{cases} \frac{6\mu\Omega}{C_r^3} \sin\left(\frac{s}{R}\right), & \text{for } \phi = p_u ; \\ \frac{-6\mu\Omega}{C_r^3} \cos\left(\frac{s}{R}\right), & \text{for } \phi = p_v ; \\ \frac{12\mu}{C_r^3} \cos\left(\frac{s}{R}\right), & \text{for } \phi = p_w ; \\ \frac{12\mu}{C_r^3} \sin\left(\frac{s}{R}\right), & \text{for } \phi = p_v . \end{cases} \tag{7.70}$$

The Galerkin method yields the following equation:

$$\int_{z_1}^{z_2} \int_{s_1}^{s_2} \{N\} \text{Res} \, ds \, dz = 0 \quad (7.71)$$

i.e.,

$$\left[ \int_{z_1}^{z_2} \int_{s_1}^{s_2} \{N\} \frac{\partial^2 \{N\}^T}{\partial s^2} \, ds \, dz + \int_{z_1}^{z_2} \int_{s_1}^{s_2} \{N\} \frac{\partial^2 \{N\}^T}{\partial z^2} \, ds \, dz \right] \{\Phi\} + \int_{z_1}^{z_2} \int_{s_1}^{s_2} \{N\} E(s) \, ds \, dz = 0 \quad (7.72)$$

Note that the first term in Eq.(7.72) can be integrated by parts:

$$\int_{z_1}^{z_2} \int_{s_1}^{s_2} \{N\} \frac{\partial^2 \{N\}^T}{\partial s^2} \, ds \, dz \{\Phi_e\} = \int_{z_1}^{z_2} \left[ \{N\} \frac{\partial \{N\}^T}{\partial s} \{\Phi_e\} \right]_{s_1}^{s_2} dz - \int_{z_1}^{z_2} \int_{s_1}^{s_2} \frac{\partial \{N\}}{\partial s} \frac{\partial \{N\}^T}{\partial s} \, ds \, dz \{\Phi_e\}$$

where the first term will yield four values corresponding to the four nodes of an element. When assembled into global equations, they will be cancelled between element interfaces. While on the boundary, even if nonzero, they do not need to be evaluated since  $\phi$  is set to be zero along the boundary  $z = 0$  and  $z = L$ . Thus, only the last term remains in the above expression. Similar results can be obtained for the second term of Eq.(7.72). Finally, Eq.(7.72) can be rewritten as

$$\int_{z_1}^{z_2} \int_{s_1}^{s_2} \left( \frac{\partial \{N\}}{\partial s} \frac{\partial \{N\}^T}{\partial s} + \frac{\partial \{N\}}{\partial z} \frac{\partial \{N\}^T}{\partial z} \right) \, ds \, dz \{\Phi_e\} = \int_{z_1}^{z_2} \int_{s_1}^{s_2} \{N\} E(s) \, ds \, dz \quad (7.73)$$

Substitution of Eqs.(7.68) and (7.70) into Eq.(7.73) yields

$$[H_e]\{\Phi_e\} = \{Q\} \quad (7.74)$$

where

$$[H_e] = \frac{L_s L_z}{6} \left( \frac{1}{L_s^2} \begin{bmatrix} 2 & 1 & -2 & -1 \\ 1 & 2 & -1 & -2 \\ -2 & -1 & 2 & 1 \\ -1 & -2 & 1 & 2 \end{bmatrix} + \frac{1}{L_z^2} \begin{bmatrix} 2 & -2 & 1 & -1 \\ -2 & 2 & -1 & 1 \\ 1 & -1 & 2 & -2 \\ -1 & 1 & -2 & 2 \end{bmatrix} \right) \quad (7.65)$$

$$\{Q\} = \frac{3\mu\Omega L_s L_z}{C_r^3} \left\{ \begin{array}{l} \frac{R}{L_s} \cos\left(\frac{s_1}{R}\right) + \frac{R^2}{L_s^2} \left[ \sin\left(\frac{s_1}{R}\right) - \sin\left(\frac{L_s+s_1}{R}\right) \right] \\ \frac{R}{L_s} \cos\left(\frac{s_1}{R}\right) + \frac{R^2}{L_s^2} \left[ \sin\left(\frac{s_1}{R}\right) - \sin\left(\frac{L_s+s_1}{R}\right) \right] \\ -\frac{R}{L_s} \cos\left(\frac{L_s+s_1}{R}\right) + \frac{R^2}{L_s^2} \left[ \sin\left(\frac{L_s+s_1}{R}\right) - \sin\left(\frac{s_1}{R}\right) \right] \\ -\frac{R}{L_s} \cos\left(\frac{L_s+s_1}{R}\right) + \frac{R^2}{L_s^2} \left[ \sin\left(\frac{L_s+s_1}{R}\right) - \sin\left(\frac{s_1}{R}\right) \right] \end{array} \right\}, \text{ for } \phi = p_u \quad (7.66a)$$

$$\{Q\} = \frac{3\mu\Omega L_s L_z}{C_r^3} \left\{ \begin{array}{l} \frac{R}{L_s} \sin\left(\frac{s_1}{R}\right) - \frac{R^2}{L_s^2} \left[ \cos\left(\frac{s_1}{R}\right) - \cos\left(\frac{L_s+s_1}{R}\right) \right] \\ \frac{R}{L_s} \sin\left(\frac{s_1}{R}\right) - \frac{R^2}{L_s^2} \left[ \cos\left(\frac{s_1}{R}\right) - \cos\left(\frac{L_s+s_1}{R}\right) \right] \\ -\frac{R}{L_s} \sin\left(\frac{L_s+s_1}{R}\right) - \frac{R^2}{L_s^2} \left[ \cos\left(\frac{L_s+s_1}{R}\right) - \cos\left(\frac{s_1}{R}\right) \right] \\ -\frac{R}{L_s} \sin\left(\frac{L_s+s_1}{R}\right) - \frac{R^2}{L_s^2} \left[ \cos\left(\frac{L_s+s_1}{R}\right) - \cos\left(\frac{s_1}{R}\right) \right] \end{array} \right\}, \text{ for } \phi = p_v \quad (7.66b)$$

$$\{Q\} = \frac{6\mu L_s L_z}{C_r^3} \left\{ \begin{array}{l} -\frac{R}{L_s} \sin\left(\frac{s_1}{R}\right) + \frac{R^2}{L_s^2} \left[ \cos\left(\frac{s_1}{R}\right) - \cos\left(\frac{L_s + s_1}{R}\right) \right] \\ -\frac{R}{L_s} \sin\left(\frac{s_1}{R}\right) + \frac{R^2}{L_s^2} \left[ \cos\left(\frac{s_1}{R}\right) - \cos\left(\frac{L_s + s_1}{R}\right) \right] \\ \frac{R}{L_s} \sin\left(\frac{L_s + s_1}{R}\right) + \frac{R^2}{L_s^2} \left[ \cos\left(\frac{L_s + s_1}{R}\right) - \cos\left(\frac{s_1}{R}\right) \right] \\ \frac{R}{L_s} \sin\left(\frac{L_s + s_1}{R}\right) + \frac{R^2}{L_s^2} \left[ \cos\left(\frac{L_s + s_1}{R}\right) - \cos\left(\frac{s_1}{R}\right) \right] \end{array} \right\}, \text{ for } \phi = p, i \quad (7.66c)$$

$$\{Q\} = \frac{6\mu L_s L_z}{C_r^3} \left\{ \begin{array}{l} \frac{R}{L_s} \cos\left(\frac{s_1}{R}\right) + \frac{R^2}{L_s^2} \left[ \sin\left(\frac{s_1}{R}\right) - \sin\left(\frac{L_s + s_1}{R}\right) \right] \\ \frac{R}{L_s} \cos\left(\frac{s_1}{R}\right) + \frac{R^2}{L_s^2} \left[ \sin\left(\frac{s_1}{R}\right) - \sin\left(\frac{L_s + s_1}{R}\right) \right] \\ -\frac{R}{L_s} \cos\left(\frac{L_s + s_1}{R}\right) + \frac{R^2}{L_s^2} \left[ \sin\left(\frac{L_s + s_1}{R}\right) - \sin\left(\frac{s_1}{R}\right) \right] \\ -\frac{R}{L_s} \cos\left(\frac{L_s + s_1}{R}\right) + \frac{R^2}{L_s^2} \left[ \sin\left(\frac{L_s + s_1}{R}\right) - \sin\left(\frac{s_1}{R}\right) \right] \end{array} \right\}, \text{ for } \phi = p, j \quad (7.66d)$$

Note that no numerical integration is needed. The only approximation regarding the solution of Eq.(7.65) comes from shape functions which must be employed for the FEA computational technique. If a fine mesh is used over the interface between the fluid film and the rotating shaft, accurate solutions can be reached.

**Numerical Results** The rate of dynamic pressure due to the perturbation of a rotating shaft with a radius  $R = 0.05\text{m}$  surrounded by a fluid film is evaluated on the shaft

surface. The bearing length, i.e., axial distance of fluid/shaft interaction, is assumed to be  $L = 0.1\text{m}$  with the clearance  $C_r = 0.075\text{ mm}$ . The fluid viscosity is assumed to be  $\mu = 0.035\text{ N}\cdot\text{s}/\text{m}^2$ . As shown in Figure (7.7), on the surface  $L \times 2\pi R$  a mesh of  $8 \times 24$  elements is used.

The computed results are shown in Figures (7.8)~(7.11). To verify the limiting case of results, a close form solution for “short bearing” (Vance, 1988) is used as listed below for comparison:

$$p(\theta) = p_a + \frac{3\mu\Omega}{C_r^3} \left( \frac{L^2}{4} - z^2 \right) \frac{u \sin\theta}{\left( 1 + \frac{u}{C_r} \cos\theta \right)^3}, \quad -\frac{L}{2} \leq z \leq \frac{L}{2}$$

where  $u$  is the distance of the rotor relative to the centre of the bearing. Therefore, the rate of dynamic pressure due to the perturbation  $u$  can be given by

$$p_{,u} = \left. \frac{\partial p}{\partial u} \right|_{u=0} = \frac{3\mu\Omega}{C_r^3} \left( \frac{L^2}{4} - z^2 \right) \sin\theta$$

The distribution is similar to the FE solutions, as shown in Figure 7.8. The maximum value is  $p_{,u} = 0.75 \mu\Omega L^2/C_r^3$  around  $\theta = \pi/2$ . Though the corresponding value in Figure 7.8 ( $L/D = 1$ ) is lower, it approaches this value using FEA when  $L/D$  is decreased to become a very “short bearing”, as shown in Table 7.1.

**Table 7.1 Maximum values of  $p_{,u}$  with  $L/D$  using FEA**

L/D	1	1/4	1/8	1/16
$(p_{,u} _{\max})/(\mu\Omega L^2/C_r^3)$	0.53	0.68	0.70	0.75

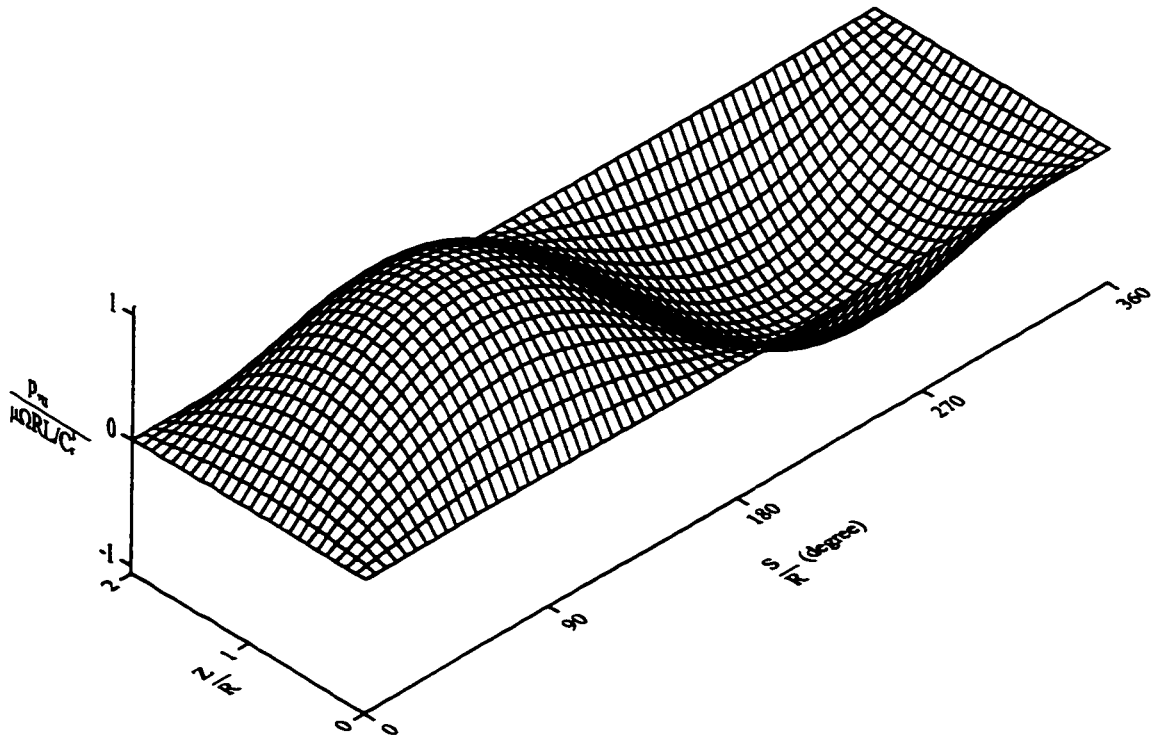


Figure 7.8 Distribution of  $p_u (= \frac{\partial p}{\partial u})$  over the rotating shaft surface with fluid

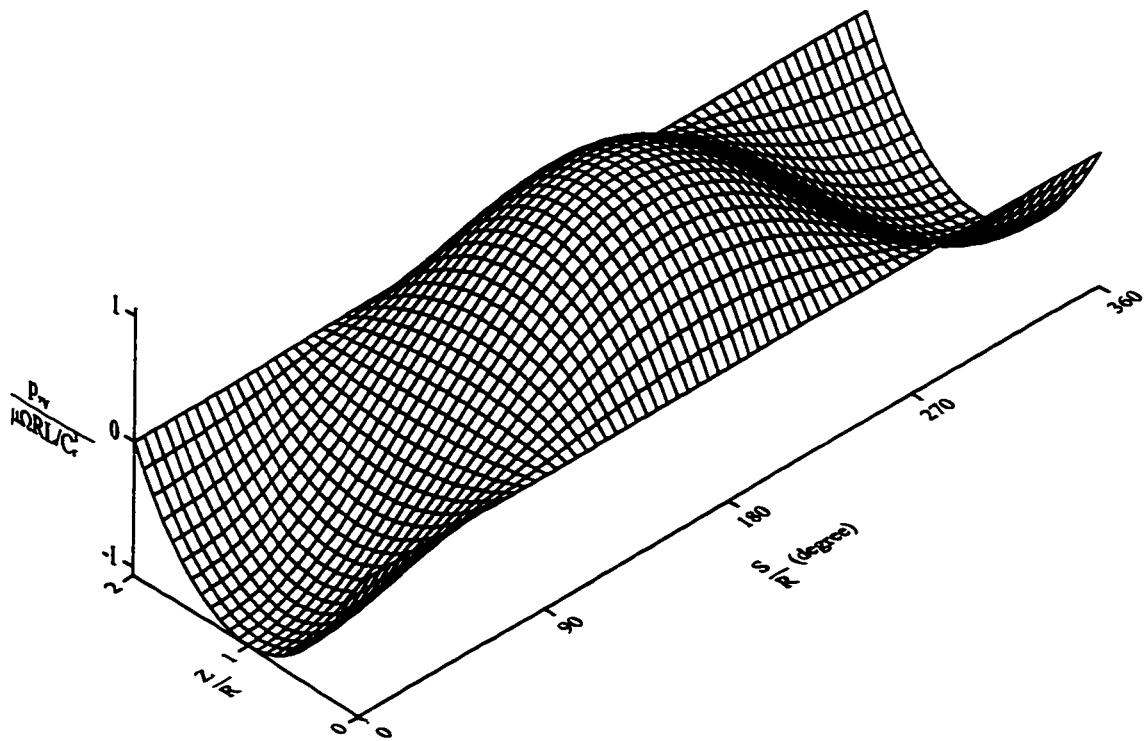
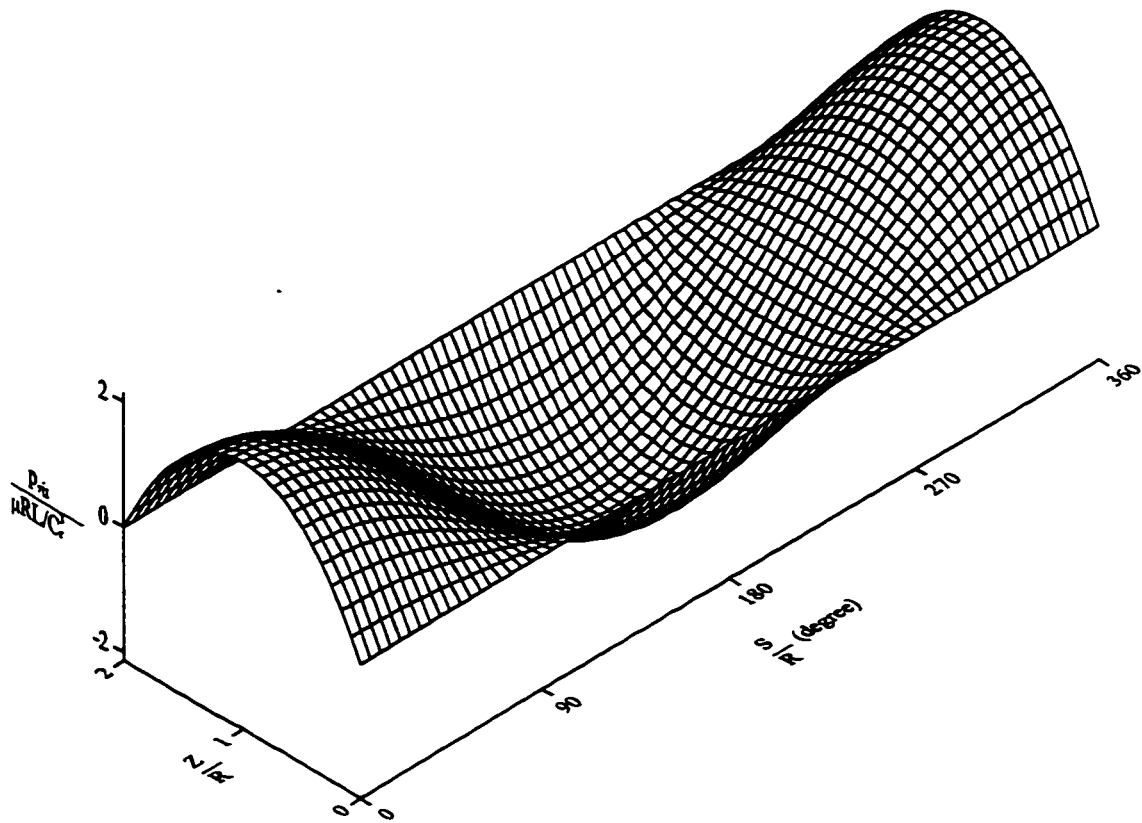
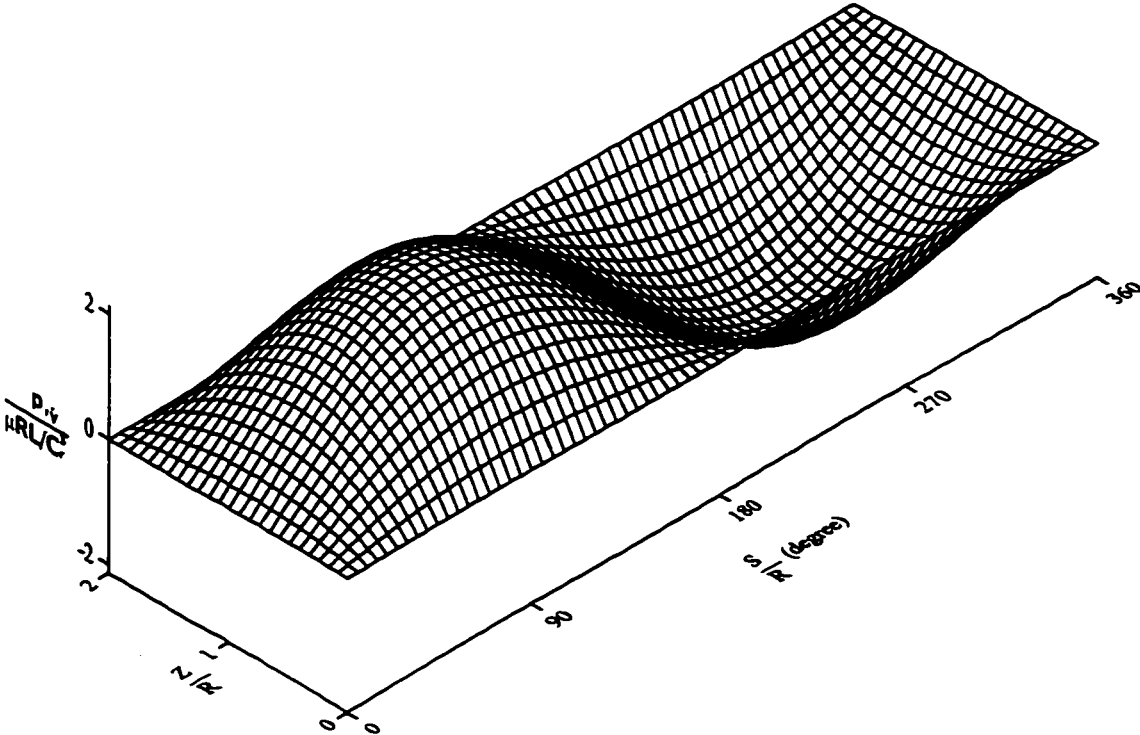


Figure 7.9 Distribution of  $p_w (= \frac{\partial p}{\partial v})$  over the rotating shaft surface with fluid



**Figure 7.10** Distribution of  $p_{st} (= \frac{\partial p}{\partial u})$  over the rotating shaft surface with fluid





**Figure 7.11** Distribution of  $p_v (= \frac{\partial p}{\partial v})$  over the rotating shaft surface with fluid

## 7.4 Distributed Shaft Surface Forces in Accordance With 3-D FE Model

Once the change rate of dynamic pressure over rotating shaft surface perturbation has been determined as is discussed above, the value of dynamic pressure on the shaft surface, as shown in Figure 7.12, can be given by

$$\begin{aligned} -p\mathbf{n} = & -(p_{,u}u + p_{,v}v)\cos\theta\mathbf{i} - (p_{,u}u + p_{,v}v)\sin\theta\mathbf{j} - \\ & -(p_{,\dot{u}}\dot{u} + p_{,\dot{v}}\dot{v})\cos\theta\mathbf{i} - (p_{,\dot{u}}\dot{u} + p_{,\dot{v}}\dot{v})\sin\theta\mathbf{j} \end{aligned} \quad (7.67)$$

on the outside surface of each shaft solid element, the virtual work due to the dynamic pressure  $p$  can be written as

$$\delta W = \int \int_e \delta \mathbf{u} \cdot (-p\mathbf{n}) dA \quad (7.68)$$

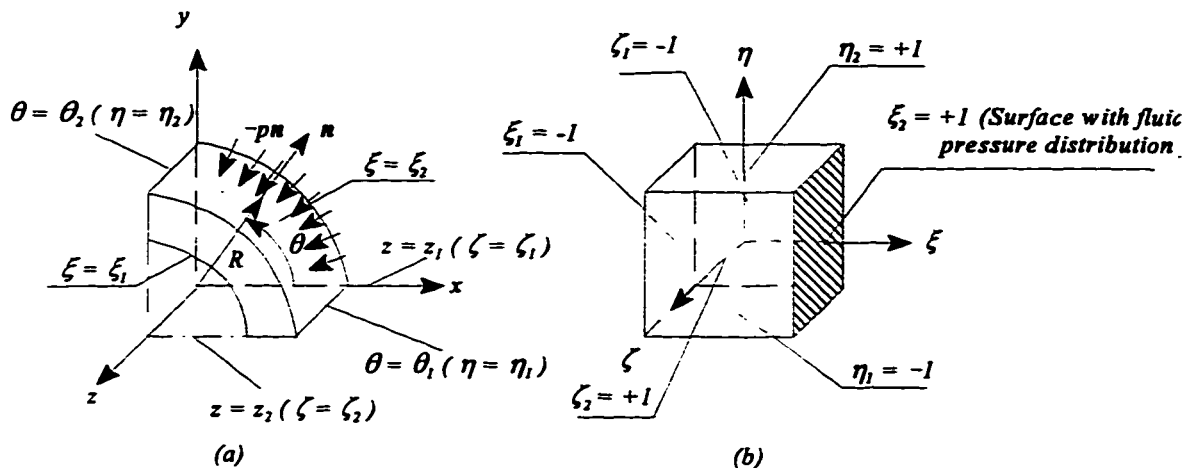


Figure 7.12 Fluid pressure acting on the surface of a shaft solid element. (a) in the global coordinate, and (b) in the local coordinate

where

$$\mathbf{u} = u\mathbf{i} + v\mathbf{j} + w\mathbf{k}$$

Substitution of Eqs.(2.22) and (7.67) into Eq.(7.68) yields

$$\begin{aligned} \delta W = & -\{\delta U_e\}^T [T']^T \left( \iint_c [G] \begin{Bmatrix} \cos\theta \\ \sin\theta \\ 0 \end{Bmatrix} \begin{bmatrix} p_x & p_y & 0 \end{bmatrix} [G]^T dA \right) [T'] \{U_e\} - \\ & -\{\delta U_e\}^T [T']^T \left( \iint_c [G] \begin{Bmatrix} \cos\theta \\ \sin\theta \\ 0 \end{Bmatrix} \begin{bmatrix} p_{,i} & p_{,j} & 0 \end{bmatrix} [G]^T dA \right) [T'] \{\dot{U}_e\} \end{aligned} \quad (7.69)$$

where

$$\{U_e\} = \left[ \{u_i\}^T, \left\{ \frac{\partial u_i}{\partial z} \right\}^T, \{v_i\}^T, \left\{ \frac{\partial v_i}{\partial z} \right\}^T, \{w_i\}^T \right]^T$$

$$[T'] = \begin{bmatrix} [T_i]^{-1} & & \\ & [T_i]^{-1} & \\ & & [T]^{-1} \end{bmatrix}$$

where  $[T_i]$ ,  $[T]$ ,  $\{g_i\}$ , and  $\{g\}$  can be found in Chapter 2.

$$[G] = \begin{bmatrix} \{g_i\} & & \\ & \{g_i\} & \\ & & \{g\} \end{bmatrix}$$

Regarding  $\cos\theta$ ,  $\sin\theta$  and  $dA$ , their general expressions can be given by

$$\cos\theta = \frac{x}{R} = \frac{1}{R} \{g\}^T [T]^{-1} \{x_i\}, \quad \sin\theta = \frac{y}{R} = \frac{1}{R} \{g\}^T [T]^{-1} \{y_i\}$$

and

$$dA = \left[ \left( \frac{\partial y}{\partial \eta} \frac{\partial z}{\partial \zeta} - \frac{\partial z}{\partial \eta} \frac{\partial y}{\partial \zeta} \right)^2 + \left( \frac{\partial z}{\partial \eta} \frac{\partial x}{\partial \zeta} - \frac{\partial x}{\partial \eta} \frac{\partial z}{\partial \zeta} \right)^2 + \left( \frac{\partial x}{\partial \eta} \frac{\partial y}{\partial \zeta} - \frac{\partial y}{\partial \eta} \frac{\partial x}{\partial \zeta} \right)^2 \right] d\eta d\zeta$$

Note that since the concerned surface is circular and uniform, the straightforward expressions can be used instead of the above general forms. As shown in Figure 7.12,  $\theta$  is linearly proportional to  $\eta$  alone, and  $z$  depends linearly on  $\zeta$ . Thus, one can have

$$\theta = \frac{\theta_2 - \theta_1}{\eta_2 - \eta_1} (\eta - \eta_1) + \theta_1 \quad (7.70)$$

and

$$dA = R d\theta dz = R \frac{\theta_2 - \theta_1}{\eta_2 - \eta_1} \frac{z_2 - z_1}{\zeta_2 - \zeta_1} d\eta d\zeta \quad (7.71)$$

Note that on the interface between the fluid and the shaft, element discretization is not set to be the same here. The local coordinates for fluid film elements need to be transformed to solid element coordinates. For the example shown in 7.3.3, six fluid film elements are attached to the surface of one solid shaft element. As shown in Figure 7.13, local coordinates of the attached solid element must be adopted in shape functions for each fluid film element. Thus, the shape functions for each fluid film element in terms of local coordinates of the solid shaft element can be given by



Table 7.2 Fluid film elemental local coordinates matching shaft solid elemental local coordinate

$\eta$ range	Element	$\eta_1$
$-1 \leq \eta \leq -2/3$	#1	-1
$-2/3 \leq \eta \leq -1/3$	#2	-2/3
$-1/3 \leq \eta \leq 0$	#3	-1/3
$0 \leq \eta \leq 1/3$	#4	0
$1/3 \leq \eta \leq 2/3$	#5	1/3
$2/3 \leq \eta \leq 1$	#6	2/3

$$\{F_s\} = -[K_f]\{U_s\} - [C_f]\{\dot{U}_s\} \quad (7.73)$$

where

$$[K_f] = [T^{-1}]^T \left( \iint_e [G] \begin{Bmatrix} \cos\theta \\ \sin\theta \\ 0 \end{Bmatrix} [p_{,u} \ p_{,v} \ 0] [G]^T dA \right) [T^{-1}] \quad (7.74)$$

$$[C_f] = [T^{-1}]^T \left( \iint_e [G] \begin{Bmatrix} \cos\theta \\ \sin\theta \\ 0 \end{Bmatrix} [p_{,u} \ p_{,v} \ 0] [G]^T dA \right) [T^{-1}]$$

which correspond to the 3-D solid finite element modelling of the shaft. Unlike eight dynamic coefficients used for beam models, Eq.(7.73) gives *distributed* fluid/shaft interaction forces in terms of solid shaft element displacement and velocity magnitudes. If dynamic pressure  $p$  is of interest, its magnitude can be estimated using Eq.(7.62).

Reduction procedures such as continuous coordinate condensation or transfer matrix method based on FE model, can be successfully implemented along the axial distance of the shaft. If Eq.(7.59) were used to model the fluid/shaft interaction, such reduction procedures

would not be able to be implemented because the dynamic pressure cannot be worked out in terms of displacement and velocity components in the same fluid film element.

## 7.5 Numerical Examples

Using the developed fluid/shaft interaction model, the dynamic response of a hollow shaft as described in Figure 2.2 is examined here. It is being supported by two bearings at the two ends as shown in Figure 7.14. Numerical solutions of the unbalance response are given with the rotational speed of the shaft. Damping effects, especially distribution extents, on the dynamic response are studied by letting the rotational speed equal to zero.

### 7.5.1 Unbalance Response of the Rotor-Bearing System

The shaft is supposed to have a distributed mass imbalance, as shown in Figure 5.15. As mentioned earlier, for 3-D solid finite element modelling, mass imbalance is modelled by distributed mass distribution instead of concentrated eccentric masses used in lumped-parameter or beam models. This mass imbalance modelling technique has been successfully employed in Chapter 5 where free-free surface boundary conditions are applied on the shaft. Recall that the natural frequency is 744 Hz and the critical speed is 764 rev./sec (Equivalent of Hz).

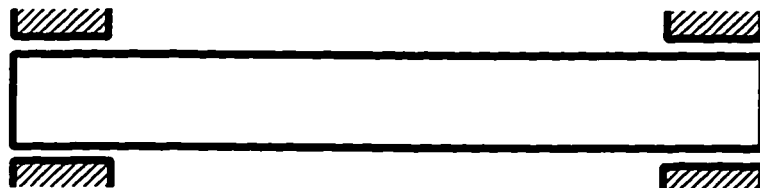


**Figure 7.14** A shaft supported by bearings

Here the dynamic response of a rotor-bearing system is being calculated using the developed fluid/shaft interaction model as indicated in 7.4. All the parameters of the fluid film bearings are the same as those in 7.3. The responses are depicted in the rotating frame at a rotational speed of the shaft, namely,  $\Omega$ . Figure 7.15 shows the response at the mid-span where transverse displacements within the cross section are almost the same. Thus, the deflection at any one of the nodal points or their average value represents the system response at the mid-span. The abscissa is the x-directional displacement  $u$ , and the ordinate is the y-directional displacement  $v$  in the rotating frame. Mass imbalance varying with the axial distance is located in the x-direction. One may have noticed that this type of imbalance will cause high value responses similar to the first mode shape when the rotational speed is close to the first critical speed.

As one can see from Figure 7.15, phases of the responses (combination of  $u$  and  $v$  displacements) are always behind that of the mass imbalance plane (x-z plane). The phase difference is between  $0 \sim \pi$ , varying with the shaft speed. As the shaft speed increases, the deflection at the mid-span increases. A lag of  $\pi/2$  corresponds approximately to the value of natural frequency (744 Hz), but not to the maximum value of the response. When the rotational speed reaches 900 rev./sec (Hz), the system presents the peak response measured from the centre of the bearings, with a phase lag of  $124^\circ$  from the imbalance plane. As the speed continues to increase, the response radius decreases, with a phase lag close to  $\pi$ .

Therefore, 900 rev./sec instead of 764 rev./sec will be called the critical speed of the rotor-bearing system, which leads to the maximum response radius. It can be seen that the introduction of bearings raises the critical speeds. Note that the motion in the x-direction will cause the motion in the y-direction by two sources. One is from the Coriolis acceleration in the shaft, and the other is from the hydrodynamic pressure of the fluid-film. It is believed that the corresponding dynamic stresses can be more accurately evaluated based on 3-D data than those with beam models.



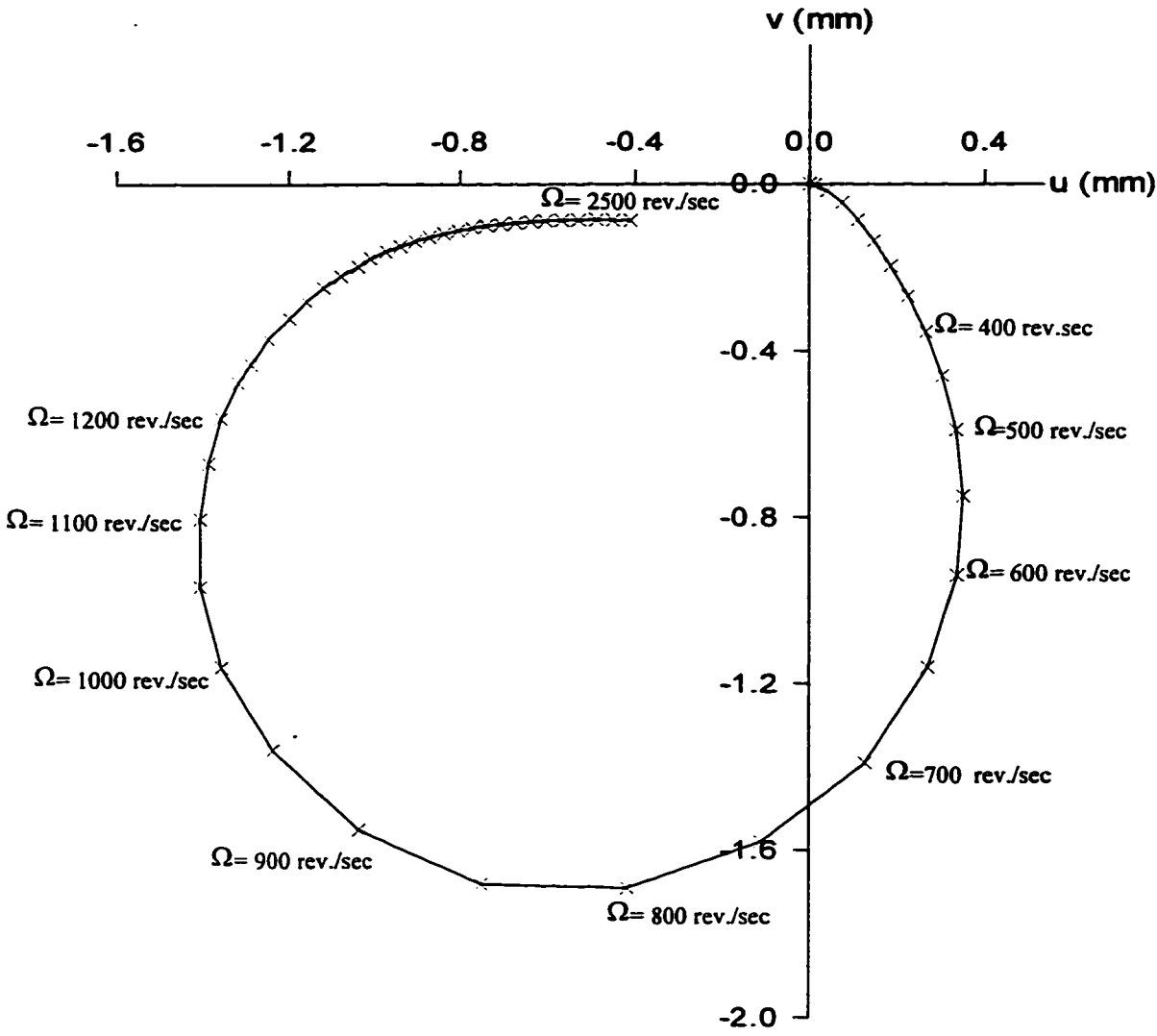


Figure 7.15 Unbalance response varying with shaft speed  $\Omega$  in rotating frame

### 7.5.2. Damping Effects on the Rotor-Bearing System

Damping takes an important role in the vibration response of the rotor-bearing system. Shaft perturbation relative to the bearing through the fluid film will equivalently produce a damping force. Many rotordynamists use concentrated force models in consideration of this damping effect, namely, four damping coefficients for each bearing. Craggs (1993) examined the effect of distributed bearing stiffness on the system response, and found out the great difference between a point support and distributed models under certain circumstances. Here damping effects of the bearing using the developed shaft/fluid interaction model are presented, and then the difference between one-point and multiple-point (equivalent of distributed model) models is examined.

To study the damping effects of the bearing on the response of the rotor-bearing system as shown in Figure 7.14, the shaft speed  $\Omega$  is prescribed to be zero. Thus, no gyroscopic and bearing stiffness effects will be involved. An exciting force with amplitude of 2kN is applied to the mid-span of the shaft. Amplitude-frequency and Phase-frequency curves are shown in Figures 7.16 and 7.17. When a forcing frequency reaches 810 Hz, a peak response arises. Meanwhile, the corresponding phase angle is behind that of the exciting force with a lag of approximately  $\pi/2$ .

For this free-free shaft without bearing supports, the first natural frequency is known as 744 Hz. Using the developed shaft/fluid interaction model, the peak response frequency is found to be around 810 Hz, higher than the natural frequency. For a *single-degree-of-freedom* (SDOF) system, however, it is concluded that the peak response frequency will be *decreased* from the natural frequency. What conclusions can be drawn for a *multiple-degree-of-freedom* (MDOF) or continuous system?

A one-point damping model is used first to find the peak response frequencies. The damping coefficients are obtained by integrating the values in Figures 7.10 and 7.11 in x and y directions over the fluid film, as shown in the following:

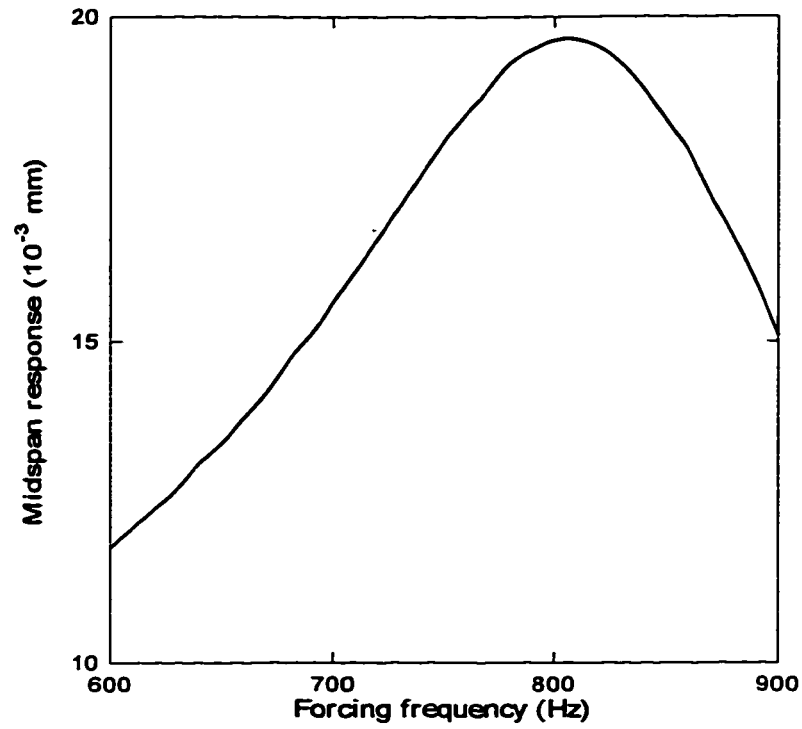


Figure 7.16. Amplitude-frequency response

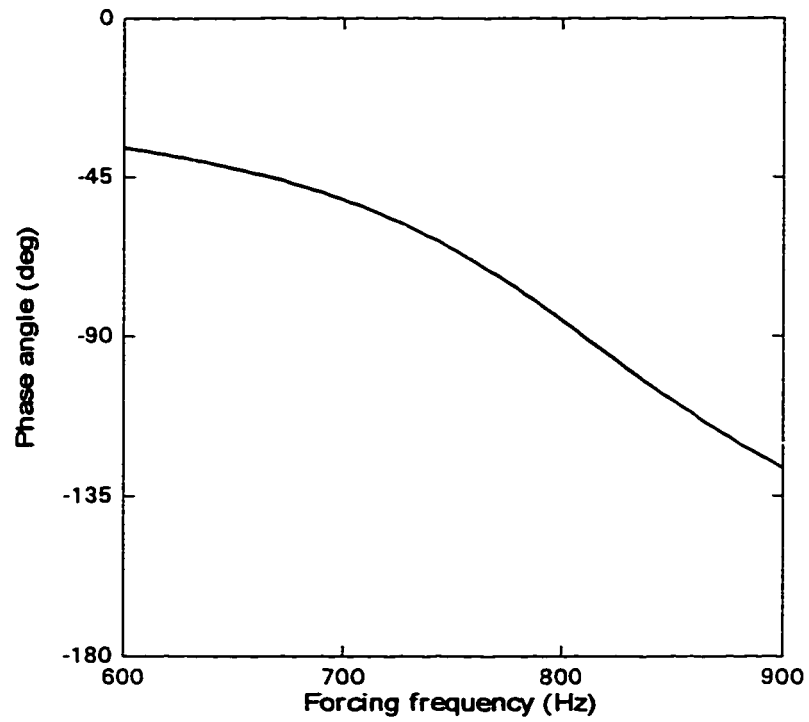


Figure 7.17 Phase-frequency response

$$C_{xx} = C_{yy} = 2C = 9.197 \times 10^6 \text{ N/s},$$

$$C_{xy} = C_{yx} = 0$$

An exciting force is applied to the one quarter of the shaft axial distance in order to avoid being located right in a node of the first few mode shapes, as shown in Figure 7.18 (a). The obtained first three peak response frequencies, as shown in Table 7.3, are below the corresponding natural frequencies, which seems to yield the same conclusion drawn from the SDOF system.

However, if damping becomes slightly distributed using the three-point model as shown in Figure 7.18 (b), the peak response frequencies have been increased to the values greater than the natural frequencies. When the nine-point model, as shown in Figure 7.18 (c), is used to model more distributed damping effects, the peak response frequencies are found to be increased more.

For a shaft, therefore, if a damped region is modelled using dampers only within one cross section, the peak response frequencies will be lower than the corresponding natural frequencies. If the damped region is modelled using multiple dampers or distributed damping forces along the axial distance of the shaft, the peak response frequencies will be greater than the natural frequencies.

**Table 7.3 One-point and multiple-point damping effects on the forced response**

Order	<i>natural frequency</i> (Hz)	One-point damping model (Hz)	three-point damping model (Hz)	nine-point damping model (Hz)
1	744	432	806	825
2	1875	1538	2121	2177
3	3307	3007	3782	3882

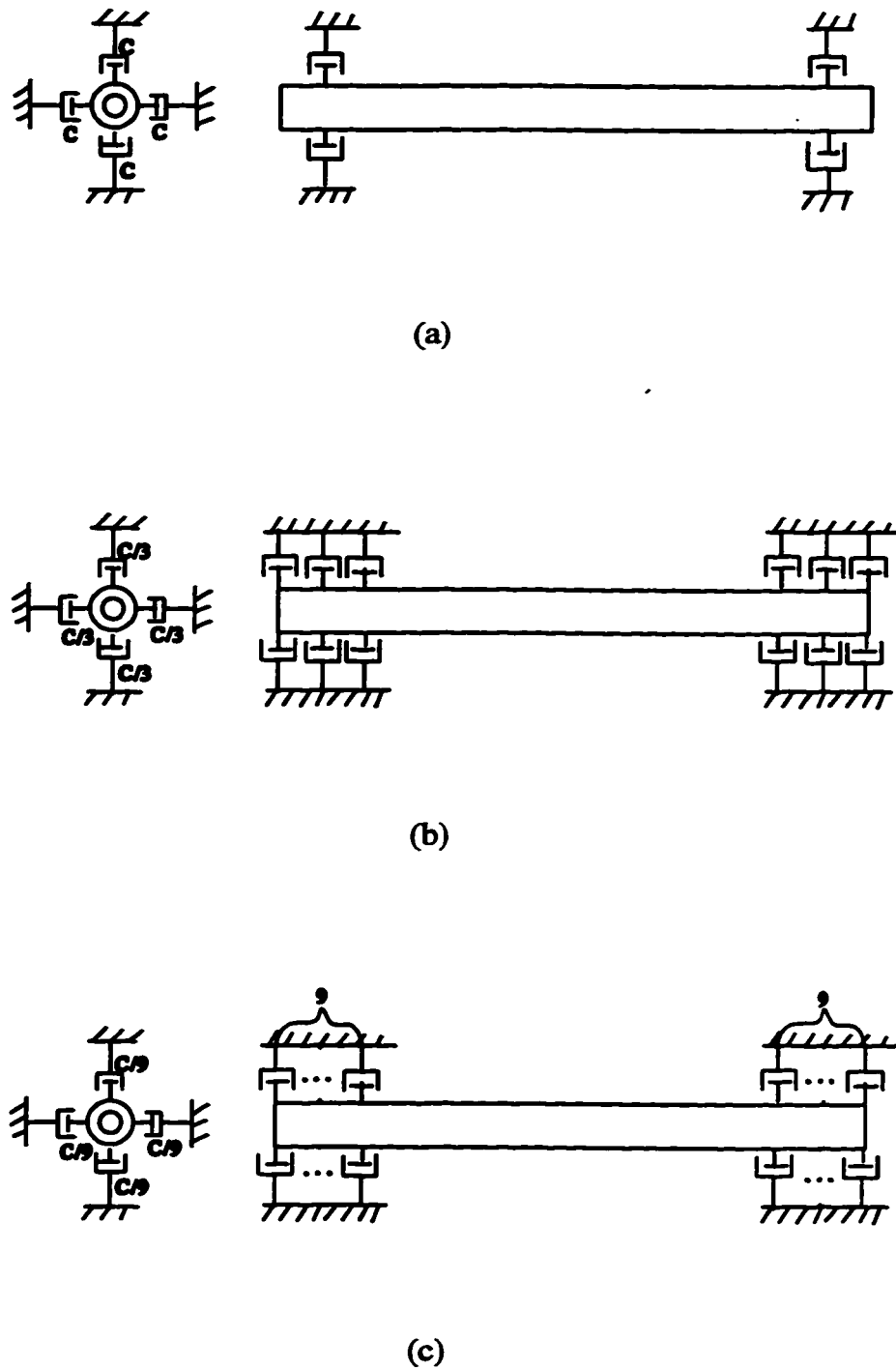


Figure 7.18 One-point and multiple-point (equivalent of distributed one) damping models. (a) one-point, (b) three-point, and (c) nine-point

This suggests that when dealing with heavy damping systems, care should be taken regarding the difference between the natural frequencies and the corresponding peak response frequencies due to some excitations. Distributed and lumped damping models could yield quite different forced responses. The conclusion drawn from SDOF may not be consistent with that from MDOF or continuous systems. The peak response frequencies could be higher than the corresponding natural frequencies.

The reason is that a general damped system is not of proportional damping, thus not being able to be transformed to a set of uncoupled individual SDOF systems. Complex mode theory may have to be involved if one wishes to obtain the solution using the modal analysis technique in terms of analytical or experimental approaches. This topic will not be discussed in detail here.

It is noted that the distributed damping is simulated by attaching several dampers evenly over a short length near the two ends. The distance over this length may somewhat shorten the effective length of the shaft, though there is no spring force involved on the shaft.

## 7.6 Discussion

Since simple beam models are often employed in the rotordynamic analysis, eight dynamic coefficients are conventionally used to model fluid/shaft interaction. Most of the fluid/shaft interaction research focuses on the fluid behaviour, or computational fluid dynamics (CFD). When 3-D solid finite elements are adopted to model rotating shafts, the corresponding distributed fluid/shaft interaction model should be developed to match the solid shaft modelling.

The simplified lubrication equation as developed in this chapter can be used in both the rotating and fixed frame. Compared with the traditional Reynolds equation, an additional term has been found in more general boundary conditions, which may aid the fluid/shaft interaction analysis, especially for defect surfaces. The circumferential coordinate can be chosen to be attached to the rotating shaft. The corresponding velocity components at the

surface boundary should be evaluated in terms of this coordinate. Otherwise, a totally erroneous equation may result.

Even using the simplified lubrication equation, the dynamic pressure will not be linearly proportional to the shaft displacement components. For an eccentric rotor, the dynamic pressure on the rotating shaft surface will be time-dependent. If the steady-state position of the shaft center is assumed to be in the bearing center, a time-independent lubrication equation can be formed. The linearized finite element equation for each fluid film element has to be assembled over the whole fluid film surface plus certain boundary conditions, thus yielding a totally coupled fluid/shaft equation. Since reduction procedures cannot be used with small matrix operations within that region, instead a perturbation method is adopted to obtain the ratio of dynamic pressure over shaft displacement and velocity components. Finally shaft surface forces due to dynamic pressure can be expressed in terms of the solid finite element displacement and velocity nodal variables.

The unbalance response of a rotor-bearing system can be given using the 3-D solid finite element model along with the corresponding distributed fluid/shaft interaction model. The lumped and distributed damping effects on the forced peak response frequencies suggest that one should not simply apply a conclusion drawn from SDOF systems to a damped MDOF or continuous systems.

It should be noted that the above fluid/shaft interaction model is applied to a rotor-bearing system where the steady-state position of the shaft centre is assumed to be in the bearing centre. This is the case when a rotor is located in the vertical position. A very light rotor in the horizontal position may also belong to this case.

If this fluid/shaft interaction model is omitted, an alternative which uses simple concentrated spring and damper models may also be employed to obtain dynamic responses. If results with high accuracy are desired, however, a fluid/shaft interaction model should be included in the whole system analysis.

## **Chapter 8**

# **Conclusions and Suggestions for Further Research**

Three dimensional (3-D) solid finite element modelling of rotating shafts, without making any restrictions on the motion to beam-like behaviour or prescribed axisymmetric bending modes, is reported for the first time. The modelling procedures have been given in all the previous chapters, and some important conclusions have been made which will be discussed in the following.

### **8.1 Conclusions**

The major contributions of the thesis include the establishment of 3-D solid FE model for rotating shafts, the discovery of the nature of shaft whirls, the development of the TMM technique based on FE models, and the dynamic reduction procedure, modelling of fluid/shaft interaction in accordance with the 3-D solid finite element shaft model. In this thesis, the following main conclusions can be reached:

The proposed 3-D solid finite element model automatically includes all the possible modes which cover bending, torsional, axial and any other modes. A 1-D shaft model such as a beam has only one or two degrees of freedom in cross sections of shafts, and thus cannot completely reflect the behaviour of deformation for shafts with complex geometry. A 2-D



axisymmetric finite element model still has restrictions of displacements in any circumferential line of a shaft. It can be shown that this circumferential line remains plane during deformation in axisymmetric element bending modes. The proposed new model has no restrictions of displacements or deformations beyond 3-D solid finite element properties. Therefore, the allowed modes are only restricted by the prescribed displacement functions used in setting up the individual finite elements, which are then assembled together across a shaft section into a superelement. Any one section of a shaft will have more pertinent degrees of freedom. Moreover, the proposed 3-D subparametric finite elements possess  $C^1$  continuity along the axial direction of the shaft, and give quicker convergent solutions than commonly used isoparametric elements. When bending vibration is analysed with the 3-D solid finite element approach, one examines bending-like modes in a 3-D domain instead of *pure* bending modes in 1-D beam models or restricted bending modes in 2-D axisymmetric element models.

In the special restricted cases of a slender or stubby uniform shaft, this model shows good agreement with the Euler and/or Timoshenko beam theories when bending frequencies are examined. However, when the shaft has a non-uniform cross section varying with its length, a basic beam assumption that plane sections remain plane is violated. A 2-D axisymmetric finite element model with one Fourier series term cannot completely break through the plane assumption of cross sections. In this case, the 3-D solid finite element model should be used to depict accurate deformations of the shaft. It is shown that the computed results for a tapered shaft are in very good agreement with the measured data.

Mass imbalance can be consistently modelled by varying the density in a cross section in this 3-D solid finite element model. It should be noted that due to its non-symmetric properties, mass imbalance is difficult to model in an axisymmetric finite element model. Coupled modes between bending and torsional actions, and between bending and axial actions are found in the case of mass imbalance. When a harmonic exciting force, moment or torque is applied to a shaft with a frequency close to a resonant frequency of bending, torsional or axial mode, it will cause inertia forces, moments, or torques in another

mode direction due to mass imbalance and thus excite the latter mode. The coupled frequencies change very slightly from the natural frequencies of the dominant mode. Non-circular cross sections yield different natural bending frequencies in two orthogonal directions, and lower torsional frequencies, although they have almost no effect on axial frequencies.

The free surface boundary conditions are adopted to compare with free-free beam solutions and measured results without introducing other errors caused by boundary constraint modelling. For other corresponding boundary conditions used in beam modes, it may be hard to define equivalent ones for a 3-D elastic shaft. To simulate a simply supported boundary condition, transverse displacements at one or more nodes may be specified zero on the exterior surface in the two ends. The corresponding natural frequency values, however, depend greatly on how these nodes are determined, especially for short shafts. To reach reliable dynamic solutions, therefore, practical contact situations should be simulated.

When dealing with a rotating shaft, the rotating frame is used which facilitates the FE modelling and gives a clear view of the shaft whirl of bending vibration. In the rotating frame, it can be seen that the complicated shaft whirl can be simply viewed as elastic translational motion if deflection is considered, as though the shaft were not rotating. Non-rotating bending modes mainly involve the motion in one plane along the shaft axis, although there are small displacements or deformations in the direction perpendicular to this plane with 3-D solid finite element elements. Rotating bending modes or whirling modes can be viewed in the rotating frame as the superposition of two orthogonal non-rotating bending modes with the whirl frequency. It is found that  $i$ th mode shapes of non-rotating, resonant forward and backward whirling cases are very close, though they are totally different in the physical meaning. Using 3-D solid finite elements would allow the cyclic stresses to be directly calculated throughout a rotating shaft with complex geometry.

The whirling behaviour has been examined under harmonic excitations in the rotating frame. Forward and backward whirls could coexist along the shaft if observed in the rotating frame. When forcing frequencies reach resonant whirl frequencies, or natural

frequencies of the rotating shaft, the whirl becomes either purely forward or purely backward. This whirling nature in the rotating frame, which may aid rotordynamic analysis, is believed to be reported for the first time, although there were some discussions about it in a fixed frame (Muszynska, 1996). This author views this peculiar phenomenon as the consequence of the combination of two different deflection curves in the two orthogonal bending planes.

Resonant whirl frequencies, i.e., natural frequencies of rotating shafts, can be determined in terms of the rotating or fixed frame. It can be seen that for an  $i$ th mode, there exist both forward and backward whirl frequencies for the given rotational speed instead of only one frequency for a non-rotating case. The difference of forward and backward frequencies in the fixed frame, confirms that gyroscopic effects have been consistently included using the proposed 3-D solid finite element modelling. Forward whirl in the fixed frame may correspond to backward whirl in the rotating frame at high shaft speed, while backward whirl in the fixed frame is always backward in the rotating frame. In the fixed frame, forward whirl frequencies increase and backward whirl frequencies decrease with shaft speed. A low backward whirl frequency in the fixed frame may correspond to a high frequency backward whirl at high shaft speed, thus yielding high frequency cyclic stresses within the shaft. As expected, forward and backward whirl frequencies for uniform shafts using 3-D solid finite elements are in good agreement with those using the Timoshenko beam theory. In the cases of shafts with complex geometry, the 3-D solid finite element approach will yield more accurate results than other methods.

Critical speeds can be determined by the rotating stiffness matrices or zero resonant whirl frequencies. Mass imbalance distribution along the shaft may influence unbalance response significantly. A specific distribution can avoid resonant unbalance response at some critical speeds. Synchronous whirl corresponding to zero whirl frequency in the rotating frame without relative oscillation within the shaft, is often caused by mass imbalance. However, the shaft can be bowed severely at critical speeds, with high non-cyclic stresses within the shaft.

For general eigenvalue analysis of damping and/or gyroscopic systems involving rigid body modes, care should be taken when an original equation is reconstructed into a standard form. Gyroscopic effects can contribute to the stabilization of undamped rotor systems. In a non-proportional damped multiple-degree-of-freedom system, items in a damped natural frequency expression no longer have the same meaning as that in a one-degree-of-freedom system.

A transfer matrix method based on finite element models has been presented for the dynamic analysis of a chain-like structure under harmonic excitations. The given numerical examples have demonstrated its applicability and efficiency. The method allows any possible distributed external forces to be included by transfer matrices, so that the forced response could be successfully simulated. Condensation can be made when dealing with a number of identical elements. It can also be employed in a damped and/or gyroscopic system when the steady state response is examined. The principal advantage of the method is that it allows a very large system with any external forces to be modelled with the powerful finite element formulation and calculated with the transfer matrix technique, so that numerical operation could be implemented on desktop computers. Examples show that it can be used to obtain natural frequencies and forced responses.

A dynamic reduction method can be used to condense not only dynamic matrices but also force or excitation vectors. This method allows one to handle elements even with intermediate nodal variables and boundary conditions with rigid body motion. For a particular region in a chain-like structure, the nodal points of interest, or the remaining degrees of freedom, can be chosen in which a condensed dynamic matrix and an external force or excitation vector can be equivalently applied without any loss of accuracy. Thus, a relationship is established between some distributed/concentrated external forces of the concerned region and condensed equivalent forces at the nodal points of interest. The magnitudes of condensed forces rely on the inherent characteristics of the region and the forcing frequency. It can be inferred that the harmonic forced responses at the nodal points of interest can even be reduced to zero by applying these equivalent concentrated forces at

the same frequency to these nodal points. The effect of these equivalent dynamic forces within the concerned part on the responses will be the same. This procedure can help to determine mass imbalance distribution along the shaft at several speeds and balance is achieved by applying the equivalent forces at preselected planes.

The above two reduction methods can be implemented for a dynamic analysis of a chain-like structure without any loss of accuracy. A popular TMM can easily be employed by engineers, and can also yield internal forces along the chain line. The dynamic reduction method can be used to deal with elements having intermediate nodal variables and to give accurate results without involving any numerical instability problems. Mainly dynamic reduction was used to obtain 3-D solid finite element results. The reduction algorithm substantially reduces computer code requirements for the 3-D solid finite element modelling of rotor-bearing systems. Another advantage is that for any kind of excitation within the concerned part of a chain-like system, equivalent magnitudes at the input and output ends can be determined at a forcing frequency based on a consistent finite element model and the dynamic reduction procedure, without any loss of accuracy, thus giving a clue to simulate or reduce the dynamic response by applying only equivalent harmonic excitation at the two ends.

A simplified lubrication equation has been developed, which can be used in either the rotating or the fixed frame. Compared with the classical Reynolds equation, an additional term has been found in more general boundary conditions, which may aid the fluid/shaft interaction analysis, especially for defect surfaces. For a small perturbation around the bearing centre, a lubrication equation in the rotating frame differs from that in the fixed frame in the sign of shaft speed, and a circumferential coordinate can be chosen on either the bearing or shaft surface without any difference. For an eccentric rotor where a steady-state position of the shaft centre differs from the bearing centre, a lubrication equation in the rotating frame around the steady-state position will be time-dependent.

It can be seen that dynamic pressure is not linearly proportional to shaft displacement and velocity components. The pressure distribution without perturbation in terms of these

components has been shown using finite element techniques. Coupled fluid/shaft interaction can be formed with the introduction of shaft surface forces. Since reduction procedures may not be easily implemented within the fluid/shaft interface, a perturbation method is adopted to account for this interaction in a rotor-bearing system. Using finite element techniques, the ratio of dynamic pressure over shaft displacement and velocity components in the rotating frame can be given. Then distributed shaft surface forces in accordance with the 3-D solid finite element model can be included in the dynamic analysis of rotor-bearing systems. Reduction procedures can be successfully implemented within the fluid film region along the shaft axial direction. The unbalance response of a rotor-bearing system for a centered rotor-bearing system is shown using the 3-D solid finite element modelling along with the corresponding distributed fluid/shaft interaction model in a 3-D domain.

Case studies of damping effects on a rotor-bearing system show an interesting characteristic of peaked response frequencies below, which can be used in other vibration systems as well. For a shaft supported by two dampers, a forced peak response frequency will be lower than the corresponding natural frequency if the dampers are modelled with point models, and higher with distributed models. Therefore, care should be taken when dealing with high damped continuous or multiple degrees-of-freedom systems. Conclusions drawn from a single degree-of-freedom system cannot be simply applied to the other systems.

## 8.2 Further Work

The following further studies are suggested to continue and extend the present work:

The present modelling procedure can be extended to include solid shafts. Although more nodal variables would be involved, reduction procedures can greatly reduce computational operations. The 3-D solid FE model is also expected to be able to link very stiff disks as rigid bodies. Dynamic stresses can be evaluated based on the displacement distribution.

The refinement of 3-D shaft model to include second and higher order terms in kinematics can be considered. Comparison of results with the present model can be made to see whether there is any improvement.

Fluid/shaft interaction modelling can be improved by solving nonlinear coupled equations. Modelling of horizontal rotor-bearing systems in the rotating frame should be further investigated.

## References

Akella, S., and Craggs, A., 1986, "Modifications to a Timoshenko Beam-Shaft Finite Element to Include Internal Disks and Changes in Cross-Section," *Journal of Sound and Vibration*, Vol. 106, pp. 227-239.

Baskharone, E. A., and Hense, S. J., 1991a, "A Finite-Element Perturbation Approach to Fluid/Rotor Interaction in Turbomachinery Elements. Part 1: Theory," *ASME Journal of Fluids Engineering*, Vol. 113, pp. 351-361.

Bathe, K.J., 1982, *Finite Element Procedures in Engineering Analysis*, Prentice Hall.

Baskharone, E. A., and Hense, S. J., 1991b, "A Finite-Element Perturbation Approach to Fluid/Rotor Interaction in Turbomachinery Elements. Part 2: Application," *ASME Journal of Fluids Engineering*, Vol. 113, pp. 362-367.

Bently, D.E., 1986, "Vibration Analysis Techniques for Detecting and Diagnosing Shaft Cracks," *Orbit*, Vol. 1(7), pp. 18-21.

Bogacz, R., Szolc, T. and Irretier, H., 1992, "An Application of Torsional Wave Analysis to Turbogenerator Rotor Shaft Response," *ASME Journal of Vibration and Acoustics*, Vol. 114, pp. 149-153.

Childs, D., 1993, *Turbomachinery Rotordynamics--Phenomena, Modeling, and*



---

*Analysis*, John Wiley & Sons, New York.

Choi, S. H., Pierre, C., and Ulsoy, A. G., 1992, "Consistent Modeling of Rotating Timoshenko Shafts Subject to Axial Loads," *ASME Journal of Vibration and Acoustics*, Vol. 114, pp. 249-259.

Cowper, G.R., 1966, "The Shear Coefficient in Timoshenko's Beam Theory," *ASME Journal of Applied Mechanics*, Vol. 33, pp. 335-340.

Craggs, A., 1986, "A Procedure for Balancing Large Turbo-Generator Sets via a Finite Element Model," *Journal of Sound and Vibration*, Vol. 108, pp. 349-352.

Craggs, A., 1987, "A Component Mode Method for Modeling the Dynamics of Turbo-Generator Sets," *Journal of Sound and Vibration*, Vol. 117, pp. 277-288.

Craggs, A., 1989, "The Application of the Transfer Matrix and Matrix Condensation Methods with Finite Element Elements to Duct Acoustics," *Journal of Sound and Vibration*, Vol. 132, pp. 393-402.

Craggs, A., and Eckert, W.F., 1992, "A Reduction Procedure for Finite Element Models of Beams and Shafts," *Journal of Sound and Vibrations*, Vol. 156, pp. 559-570.

Craggs, A., 1993, "Effect of Distributed Bearing Stiffness on the Critical Speeds of Shafts," *Journal of Sound and Vibration*, Vol. 163, pp. 559-565.

Diken, H., and Tadjbakhsh, I.G., 1989, "Unbalance Response of Flexible Rotors Coupled With Torsion," *ASME Journal of Vibration, Acoustics, Stress, and Reliability in Design*, Vol. 111, pp. 179-186.

Dimarogonas, A.D., and Paipetis, S.A., 1983, *Analytical Methods in Rotor Dynamics*,

---

Applied Science Publishers, London.

Dimentberg, F.M., 1961, *Flexural Vibrations of Rotating Shafts*, Butter-Worths, London.

Eckert, W.F., 1992, "The Application of Finite Element Models to the Analysis and System Identification of Flexible Rotors," Ph.D. Thesis, University of Alberta.

Ehrich, F.F., 1990, "Pseudo-High-Speed Balancing," *ASME Journal of Vibration and Acoustics*, Vol. 112, pp. 418-425.

Ehrich, F.F., 1991, "Some Observations of Chaotic Vibration Phenomena in High-Speed Rotordynamics," *ASME Journal of Vibration and Acoustics*, Vol. 113, pp. 50-57.

EI-Shafei, A., and Crandall, S.H., 1991, "Fluid Inertia Forces in Squeeze Film Dampers," *Rotating Machinery and Vehicle Dynamics*, ASME DE-Vol. 35, pp. 219-228.

EI-Shafei, A., 1995, "Modeling Fluid Inertia Forces of Short Journal Bearings for Rotordynamic Applications," *ASME Journal of Vibration and Acoustics*, Vol. 117, pp. 462-469.

Eshleman, R.L., 1984, "Some Recent Advances in Rotor Dynamics," *IMEchE International Conference on Vibrations in Rotating machinery*, York, pp. xi-xx.

Eshleman, R. L., and Eubanks, R. A., 1969, "On the Critical Speeds of continuous Motors," *ASME Journal of Engineering for Industry*, Vol. 91, pp. 1180-1188.

Geradin, M., and Kill, N., 1984, "A New Approach to Finite Element Modeling of Flexible Rotors," *Engineering Computations*, Vol. 1, pp. 52-64.

---

Gmur, T.C., and Rodrigues, J.D., 1991, "Shaft Finite Elements for Rotor Dynamics Analysis." *ASME Journal of Vibration and Acoustics*, Vol. 113, pp. 482-492.

Goodwin, M.J., 1989, *Dynamics of Rotor-Bearing Systems*, Unwin-Hyman, London.

Goodwin, M.J., 1991, "Dynamics of Rotor-Bearing Systems -- An Overview," *The Shock and Vibration Digest*, Vol. 23, pp. 3-14.

Green, R., 1948, "Gyroscopic Effects of the Critical Speeds of Flexible Rotors," *Journal of Applied Mechanics*, Vol. 15, pp. 369-376.

Gupta, K., Gupta, K.D., and Athre, K., 1993, "Unbalance Response of a Dual Rotor System: Theory and Experiment," *ASME Journal of Vibration and Acoustics*, Vol. 115, pp. 427-435.

Guyan, R.J., 1965, "Reduction of Stiffness and Mass Matrices," *American Institute of Aeronautics and Astronautics Journal*, Vol. 3, p.380.

Hablani, M.B., and Shrivastava, S.K., 1977, "A Modal Analysis for the Damped Linear Gyroscopic Systems," *ASME Journal of Applied Mechanics*, Vol. 44, pp. 250-254.

Huang, T.C., 1961, "The Effect of Rotatory Inertia and of Shear Deformation on the Frequency and Normal Mode Equations of Uniform Beams With Simple End Conditions," *ASME Journal of Applied Mechanics*, Vol. 28, pp. 579-584.

Inagaki, T., 1987, "Numerical Computational Method for Rotor-Foundation," *The 1987 ASME Design Technical Conference-11th Biennial Conference on Mechanical Vibration and Noise, Rotating Machinery Dynamics*, Boston, Vol. 2, pp. 383-390.

---

Jeffcott, H.H., 1919, "The Lateral Vibration of Loaded Shafts in the Neighbourhood of a Whirling Speed: The Effect of Want of Balance," *Philosophical Magazine*, Ser.6, 37, pp. 304.

Laws, W.C., and Muszynska, A., 1987, "Periodic and Continuous Vibration Monitoring for Preventive/Predictive Maintenance of Rotating Machinery," *ASME Journal of Engineering for Turbines and Power*, Vol. 109, pp. 159-167.

Loewy, R.G., and Piarulli, V.J., 1969, *Dynamics of Rotating Shafts*, The Shock and Vibration Information Center, Naval Research Laboratory, Washington, D.C.

Love, A.E.H., 1927, *A Treatise on the Mathematical Theory of Elasticity*, 4th edition, Dover Publications, New York.

Lund, J.W., and Orcutt, F.K., 1967, "Calculation and experiments on the unbalance response of a flexible rotor", ASME, *Journal of Engineering for Industry*, Vol. 89, pp. 785-796.

Lund, J.W., 1987, "Review of the Concept of Dynamic Coefficients for Fluid Film Journal Bearings," *ASME Journal of Tribology*, Vol. 109, pp. 37-41.

Meirovitch, L., 1967, *Analytical Methods in Vibration*, Macmillan, New York.

Meirovitch, L., 1974, "A New Method of Solution of the Eigenvalue Problem for Gyroscopic Systems," *AIAA Journal*, Vol. 12, pp. 1337-1342.

Meirovitch, L., 1975a, *Elements of Vibration Analysis*, McGraw-Hill, New York.

Meirovitch, L., 1975b, "A Modal Analysis for the Response of Linear Gyroscopic

---

Systems,” *ASME Journal of Applied Mechanics*, Vol. 42, pp. 446-450.

Mioduchowski, A., and Faulkner, M.G., 1986, “Analysis of Single Rotor Turbines by Means of Torsional Waves,” *Proceedings of the International Conference on Rotordynamics*, Tokyo, Japan, pp. 345-348.

Mioduchowski, A., 1990, “On Dynamics of Nonhomogeneous Multi Mass Drive Systems,” *Ingenieur-Archiv*, Vol. 60, pp. 303-310.

Mioduchowski, A., 1995, “Analysis of Stepped Shafts with Undercut by Means of Torsional Waves,” *Proceedings of the Ninth World Congress on the Theory of Machines and Mechanisms*, Politecnico di Milano, Italy, pp. 924-928.

Muszynska, A., 1986, “Modal testing of Rotor/Bearing Systems,” *International Journal of Analytical and Experimental Modal Analysis*, Vol. 1, pp. 15-34.

Muszynska, A., Bently, D.E., Franklin, W.D., Grant, J.W., and Goldman, P., 1993, “Applications of Sweep Frequency Rotating Force Perturbation Methodology in Rotating Machinery For Dynamics Stiffness Identification,” *ASME Journal of Engineering for Gas Turbines and Power*, Vol. 115, pp. 266-271.

Muszynska, A., and Grant, J.W., 1991, “Stability and Instability of a Two-Mode Rotor Supported by Two Fluid-Lubricated Bearings,” *ASME Journal of Vibration and Acoustics*, Vol. 113, pp. 316-324.

Muszynska, A., 1996, “Forward and Backward Precession of a Vertical Anisotropically Supported Rotor,” *Journal of Sound and Vibration*, Vol. 192, pp. 207-222.

Muszynska, A., Hatch, C.T., and Bently, D.E., 1996, “Dynamics of Anisotropically

---

Supported Rotors," *Proceedings of ISROMAC-6*, pp. 1-10.

Myklestad, N., 1944, "A New Method for Calculating Natural Modes of Uncoupled Bending Vibration of Airplane Wings and Other Types of Beams," *Journal of Aeronautical Society*, Vol. 11, pp. 153-162.

Nelson, H.D., and McVaugh, J.M., 1976, "The Dynamics of Rotor-Bearing Systems Using Finite Elements," *ASME Journal of Engineering for Industry*, Vol. 98, pp. 593-600.

Nelson, H.D., 1980, "A Finite Rotating Shaft Element Using Timoshenko Beam Theory," *ASME Journal of Mechanical Design*, Vol. 102, 793-803.

Nelson, H.D., and Meacham, W.L., 1981, "Transient Analysis of Rotor Bearing Systems Using Component Mode Synthesis," *ASME Gas Turbine Conference*, Houston, Paper No. 81-GT-110.

Nelson, H.D., Meacham, W.L., Fleming, D.P., and Kascak, A.F. 1983, "Nonlinear Analysis of Rotor-Bearing Systems Using Component Mode Synthesis," *ASME Journal of Engineering for Power*, Vol. 105, pp. 606-614.

Nelson, H.D., and Nataraj, C., 1986, "The Dynamics of a Rotor System with a Cracked Shaft," *ASME Journal of Vibration, Acoustics, Stress, and Reliability in Design*, Vol. 108, pp. 189-196.

Newkirk, B.L., 1924, "Shaft Whipping," *General Electric Review*, p.169.

Newkirk, B.L., and Taylor, H.D., 1925, "Shaft Whipping due to Oil Action in Journal Bearings," *General Electric Review*, pp. 559-568.

---

Papadopoulos, C.A., and Dimarogonas, A.D., 1992, "Coupled Vibration of Cracked Shafts," *ASME Journal of Vibration and Acoustics*, Vol. 114, pp. 461-467.

Pastel, E., 1954, "Beitrag zur Ermittlung der Hydrodynamischen Dämpfung und Federeigenschaften von Gleitlagren," *Ingenieur-Archiv*, Vol. XXII, pp. 147-155.

Prohl, M., 1945, "A General method for Calculating Critical Speeds of Flexible Rotors," *ASME Journal of Applied Mechanics*, Vol. 12, pp. 142-148.

Rankine, W.J.Mc.Q., 1869, "Centrifugal Whirling of Shafts," *Engineer*, XXVI.

Rao, J.S., 1983, *Rotor Dynamics*, Wiley Eastern, New Delhi.

Rao, J.S., Sarma, K.V.B., and Gupta, K., 1987, "Transient Analysis of Rotors by Transfer Matrix Method," *Proceedings of 11th Biennial ASME Conference on Vibration and Noise, Rotating Machinery Dynamics*, Vol. 2, pp. 545-552.

Reynolds, O., 1886, "On the Theory of Lubrication and Its Application to Mr. beauchamp Tower's experiments Including an Experimental Determination of the Viscosity of olive Oil," *Phi. Trans.*, Vol. 177(i), pp. 157-234.

Rouch, K. and Kao, J.S., 1979, "A Tapered Beam Finite Element for Rotordynamics Analysis," *Journal of Sound and Vibration*, Vol. 66, pp. 119-140.

Rouch, K. and Kao, J.S., 1980, "Dynamic reduction of rotor dynamics by the finite element method," *ASME Journal of Mechanical Design*, Vol. 102, pp. 360-368.

Rouvas, C., and Childs, D.W., 1993, "A Parameter Identification Method for the Rotordynamic Coefficients of a High Reynolds Number Hydrostatic Bearing," *ASME*

---

*Journal of Vibration and Acoustics*, Vol. 115, pp. 264-270.

Ruhl, R.L. and Booker, J.F., 1972, "A Finite Element Model for Distributed Parameter Turborotor Systems," *ASME Journal of Engineering for Industry*, pp. 126-132.

Stephenson, R.W., Rouch, K.E., and Arora, R., 1989, "Modeling of Rotors with Axisymmetric Solid Harmonic Elements," *Journal of Sound and Vibration*, Vol. 131, pp. 431-443.

Stephenson, R.W., and Rouch, K.E., 1993, "Modeling Rotating Shafts Using Axisymmetric Solid Finite Elements with Matrix Reduction," *ASME Journal of Vibration and Acoustics*, Vol. 115, pp. 484-489.

Sankar, T.S., 1991, "Rotor Dynamics: A State-of-the-Art," *Transactions of the CSME*, Vol. 15, pp. 1-42.

Schwarz, H.R., 1988, "Finite Element Methods", Academic Press.

Schwibinger, P. and Nordmann, R., 1990, "Torsional Vibrations in Turbogenerators Due to Network Disturbances," *ASME Journal of Vibration and Acoustics*, Vol. 112, pp. 312-320.

Senthilnathan, N.R. and Lee, K.H., 1992, "Some Remarks on Timoshenko Beam Theory," *ASME Journal of Vibration and Acoustics*, Vol. 114, pp. 495-497.

Shiau, T.N. and Hwang, J.L., 1989, "A New Approach to the Dynamic Characteristic of Undamped Rotor-Bearing systems," *ASME Journal of Vibration, Acoustics, Stress, and Reliability in Design*, Vol. 111, pp. 379-385.



---

Shiau, T.N. and Hwang, J.L., 1993, "Generalized polynomial Expansion Method for the Dynamics Analysis of Rotor-Bearing systems," *ASME Journal of Engineering for Gas Turbines and Power*, Vol. 115, pp. 209-217.

Stodola, A., 1925, "Kristische Wellenstörung infolge der Nachgiebigkeit des Oelpolsters im Lager," *Schweizerische Bauzeitung*, Vol. 85, pp. 265-266.

Stodola, A., 1927, *Steam and Gas Turbine*, McGraw-Hill, New York.

Taylor, A. G., 1993, "A Finite Element Analysis of the Instability Mechanisms in Non-Axisymmetric Rotor Systems," Ph.D. Thesis, University of Alberta.

Teodorescu, P.P., 1975, *Dynamics of Linear Elastic Bodies*, Abacus Press, England.

Thomas, D.J. and Wilson, R.R., 1973, "Timoshenko Beam Finite Elements," *Journal of Sound and Vibration*, Vol. 31, pp. 315-330.

Timoshenko, S.P. 1921, "On the Correction for Shear of the Differential Equation for Transverse Vibrations of Prismatic Bars," *Philosophical Magazine*, Vol. 41, pp. 744-746.

Timoshenko, S.P., 1922, "On the Transverse Vibrations of Bars of Uniform Cross-Section," *Philosophical Magazine*, Vol. 43, pp. 125-131.

Timoshenko, S.P., and Goodier, J.N., 1951, *Theory of Elasticity*, 2nd edition, McGraw-Hill, New York.

Timoshenko, S.P., 1955, *Vibration Problems in Engineering*, 3rd edition, Van Nostrand, Princeton, N.J.

Uhrig, R., 1966, "The transfer matrix seen as one method of structural analysis among others," *Journal of Sound and Vibration*, Vol. 4, pp. 136-148.

---

Vance, J.M., 1988, *Rotor Dynamics of Turbomachinery*, John Wiley & Sons, New York.

Vest, T.A. and Darlow, M.S., 1990, "A Modified Conical Beam Element Based on Finite Element Analysis: Experimental Correlations," *ASME Journal of Vibration and Acoustics*, Vol. 112, pp. 350-354.

Yu, J., 1991, "Use of a New Formula in the Analysis of Torsional Harmonic Excitations for IC Engines," *SAE Proceedings of the 1991 Noise and Vibration Conference*, Traverse City, Michigan, pp. 209-214.

Yu, J., 1994, "Relationship between Mean Value and Fourier Coefficients of a Time-Varying Function with Half-Period Rests: Theory and Application," *ASME Journal of Vibration and Acoustics*, Vol. 116, pp. 26-30.

Yu, J., and Craggs, A., 1995a, "Transfer Matrix Method for Finite Element Models of a Chain-Like Structure Under Harmonic Excitations," *Journal of Sound and Vibration*, Vol. 187, pp. 169-175.

Yu, J., and Craggs, A., 1995b, "Dynamic Analysis of Hollow Shafts with 3-D Solid Finite Elements," *Proceedings of the 15th Canadian Congress of Applied Mechanics*, Victoria, British Columbia, pp. 358-359.

Yu, J., and Craggs, A., 1997, "3-D Solid Finite Element Modelling of Rotating Shafts," *Proceedings of the 15th International Modal Analysis Conference*, Orlando, Florida, pp. 1488-1494.

Yu, J., Craggs, A., and Mioduchowski, A., 1997, "Modelling of Shaft Whirl With 3-D Solid Finite Elements," accepted by *the 7th International Symposium on Transport*

---

*Phenomena and Dynamics of Rotating Machinery (ISROMAC-7).*

Zienkiewicz, O.C., 1971, *The Finite Element Method In engineering Science*, McGraw-Hill, New York.

Zu, Jean W.Z. and Han, Ray P.S., 1992, "Natural frequencies and Normal Modes of a Spinning Timoshenko Beam with General boundary Conditions," *ASME Journal of Applied Mechanics*, Vol. 59, pp. S197-S204.

# Appendix A

## Matrix Coefficients

### A.1 Coefficients of Transformation

In the order of node number as shown in Figure 2.1 (b) where the local coordinates are defined within

$$-1 \leq \xi \leq 1, \quad -1 \leq \eta \leq 1, \quad -1 \leq \zeta \leq 1$$

coefficients of transformation can be evaluated as

$$[T] = \begin{bmatrix} 1 & -1 & -1 & 1 & 1 & 1 & -1 & -1 & -1 & 1 & 1 & -1 & -1 & -1 & 1 & 1 \\ 1 & 1 & -1 & 1 & -1 & 1 & -1 & 1 & -1 & -1 & 1 & -1 & 1 & -1 & 1 & -1 \\ 1 & 1 & 1 & 1 & 1 & 1 & 1 & 1 & -1 & -1 & -1 & -1 & -1 & -1 & -1 & -1 \\ 1 & -1 & 1 & 1 & -1 & 1 & 1 & -1 & -1 & 1 & -1 & -1 & 1 & -1 & -1 & 1 \\ 1 & 0 & -1 & 0 & 0 & 1 & 0 & 0 & -1 & 0 & 1 & 0 & 0 & -1 & 0 & 0 \\ 1 & 1 & 0 & 1 & 0 & 0 & 0 & 0 & -1 & -1 & 0 & -1 & 0 & 0 & 0 & 0 \\ 1 & 0 & 1 & 0 & 0 & 1 & 0 & 0 & -1 & 0 & -1 & 0 & 0 & -1 & 0 & 0 \\ 1 & -1 & 0 & 1 & 0 & 0 & 0 & 0 & -1 & 1 & 0 & -1 & 0 & 0 & 0 & 0 \\ 1 & -1 & -1 & 1 & 1 & 1 & -1 & -1 & 1 & -1 & -1 & 1 & 1 & 1 & -1 & -1 \\ 1 & 1 & -1 & 1 & -1 & 1 & -1 & 1 & 1 & 1 & -1 & 1 & -1 & 1 & -1 & 1 \\ 1 & 1 & 1 & 1 & 1 & 1 & 1 & 1 & 1 & 1 & 1 & 1 & 1 & 1 & 1 & 1 \\ 1 & -1 & 1 & 1 & -1 & 1 & 1 & -1 & 1 & -1 & 1 & 1 & -1 & 1 & 1 & -1 \\ 1 & 0 & -1 & 0 & 0 & 1 & 0 & 0 & 1 & 0 & -1 & 0 & 0 & 1 & 0 & 0 \\ 1 & 1 & 0 & 1 & 0 & 0 & 0 & 0 & 1 & 1 & 0 & 1 & 0 & 0 & 0 & 0 \\ 1 & 0 & 1 & 0 & 0 & 1 & 0 & 0 & 1 & 0 & 1 & 0 & 0 & 1 & 0 & 0 \\ 1 & -1 & 0 & 1 & 0 & 0 & 0 & 0 & 1 & -1 & 0 & 1 & 0 & 0 & 0 & 0 \end{bmatrix}$$

## A.2 Constitutive Matrix

For isotropic materials, the constitutive matrix is given in terms of Lamé's constant by

$$[D] = \begin{bmatrix} \lambda + 2G & \lambda & \lambda & 0 & 0 & 0 \\ \lambda & \lambda + 2G & \lambda & 0 & 0 & 0 \\ \lambda & \lambda & \lambda + 2G & 0 & 0 & 0 \\ 0 & 0 & 0 & G & 0 & 0 \\ 0 & 0 & 0 & 0 & G & 0 \\ 0 & 0 & 0 & 0 & 0 & G \end{bmatrix}$$

in which

$$\lambda = \frac{E\nu}{(1+\nu)(1-2\nu)}$$

$$G = \frac{E}{2(1+\nu)}$$

where  $E$  is the Young's modulus and  $\nu$  is the Poisson's ratio.

# **Appendix B**

## **Synopsis of Developed Software**

All the results shown in the previous chapters were obtained using the software developed by the author. Fortran has been mainly used on the UNIX machines at the Department. The software includes 3-D solid FE modelling, dynamic matrix and force vector reduction (development of the continuous coordinate condensation), TMM based on FE models, shaft/fluid interaction modelling, etc.

A circular or elliptical hollow shaft with uniform or tapered cross sections can be successfully modelled using 3-D solid finite elements. Given geometrical and material parameters, the code can automatically form grids which specify elements and nodal points.  $C^1$  continuity is guaranteed along the shaft axis. Shape functions, in terms of local coordinates, are formed based on real geometry of the concerned element. Gauss quadrature is used when integration is involved. Superelements are employed to make possible the dynamic matrix and force vector reduction along the shaft axis. Both rotating and non-rotating shafts can be analyzed to obtain the dynamic responses of bending, torsion, axial and other possible modes.

The dynamic matrix and force vector reduction allows one to obtain both a condensed dynamic matrix and a condensed dynamic force vector. Therefore, it involves only a small matrix operation even for a very long shaft. Many numerical examples used by the author show that numerical stability can be guaranteed to ensure accurate results. Forced and free vibration responses, or steady-state displacements can be obtained using this reduction method. It allows one to calculate the unbalance response due to distributed mass imbalance along the shaft axis, while the previous continuous condensation coordinate procedure may not be able to handle. It can be employed in structures other than shafts. Moreover, use of

---

the dynamic force vector reduction can yield the relationship between the equivalent dynamic forces and the original dynamic forces for the condensed part of the system.

The transfer matrix method (TMM) is considered to be a convenient tool in beam-like structures. Even before the finite element analysis was available, TMM had been very popular in the dynamic analysis of beam-like structures. The new developed TMM technique is based on FE models rather than lumped mass models. Therefore, results of FEA can be achieved by using a simple TMM approach. Moreover, forces within the shaft cross section can be obtained. Reduction can be further made for a series of identical shaft elements. As shown in Chapter 6, this method has been employed in the rotating Timoshenko beam with a finite element model.

Fluid/shaft interaction is modelled using FEA. Ratios of dynamic pressure to shaft perturbation can be evaluated for the given fluid film surface. The corresponding shaft surface forces can be automatically modelled in accordance with 3-D solid shaft finite elements. The response of a rotor-bearing system can be given.

There are some other programs which have been used throughout the research project. All these programs can yield satisfactory results.

# Appendix C

## Use of ABAQUS Code

There are many general purpose finite element commercial codes available today. ABAQUS is the one of them, which can be used in stress, vibration, acoustic and heat transfer analysis, especially good for nonlinear analysis. The purpose for using ABAQUS is to verify capabilities of the author's code and to use its postprocessing to observe 3-D mode shapes in a desired view direction.

Natural frequencies and mode shapes of a non-rotating shaft as shown in Figure 2.2 are given with the ABAQUS code. Free surface boundary conditions are assumed for the whole shaft. Elements of type C3D20 (20-node quadratic bricks) are employed with a regular mesh.

An input file is listed in Appendix C.1. The corresponding results are shown in Appendix C.2 along with 3-D mode shapes.

### C.1 ABAQUS Input File

An ABAQUS input file **shaft.inp** is listed in the following:

```
*HEADING
3-D UNIFORM SHAFT
*NODE, SYSTEM=C
1, 0., 0., 0.
2, 0., 0., 0.8
11000, 0.025, 0., 0.
51000, 0.05, 0., 0.
18000, 0.025, 315., 0.
58000, 0.05, 315., 0.
```



---

```
11128, 0.025, 0., 0.8
51128, 0.05, 0., 0.8
18128, 0.025, 315., 0.8
58128, 0.05, 315., 0.8
*NGEN, LINE=C, NSET=INSIDEA
11000, 18000, 1000, 1, 0., 0., 0., 0., 0., 1.
*NGEN, LINE=C, NSET=OUTSIDEA
51000, 58000, 1000, 1, 0., 0., 0., 0., 0., 1.
*NGEN, LINE=C, NSET=INSIDEB
11128, 18128, 1000, 2, 0., 0., 0.8, 0., 0., 1.
*NGEN, LINE=C, NSET=OUTSIDEB
51128, 58128, 1000, 2, 0., 0., 0.8, 0., 0., 1.
*NFILL, NSET=A
INSIDEA, OUTSIDEA, 2, 20000
*NFILL, NSET=B
INSIDEB, OUTSIDEB, 2, 20000
*NFILL
A, B, 128, 1
*NSET, NSET=AB
A, B
*ELEMENT, TYPE=C3D20
11001,
11000, 51000, 53000, 13000,
11002, 51002, 53002, 13002,
31000, 52000, 33000, 12000,
31002, 52002, 33002, 12002,
11001, 51001, 53001, 13001
14001,
17000, 57000, 51000, 11000,
```

---

```
17002, 57002, 51002, 11002,  
37000, 58000, 31000, 18000,  
37002, 58002, 31002, 18002,  
17001, 57001, 51001, 11001  
*ELGEN, ELSET=ALL  
11001, 3, 2000, 1000, 1, 0, 0, 64, 2, 1  
14001, 1, 0, 0, 1, 0, 0, 64, 2, 1  
*SOLID SECTION, MATERIAL=STEEL, ELSET=ALL  
*MATERIAL, NAME=STEEL  
*ELASTIC  
2.E11, 0.3  
*DENSITY  
7800.  
*RESTART, WRITE  
*STEP  
EIGENVALUE ANALYSIS  
*FREQUENCY  
20, 12000., 1.0  
*NODE PRINT, FREQUENCY=0, NSET=AB  
U  
*NODE FILE, FREQUENCY=0, NSET=AB  
U  
*END STEP
```

---

## **C.2 Results and 3-D Mode Shapes**

Using postprocessing yields 3-D mode shapes, which are shown in Figures C.1 - C.10 along with the corresponding natural frequencies.

Figures C.1 - C.5 show the first five bending modes, Figures C.6 - C.8 demonstrate the first three torsional modes, and Figures C.9 and C.10 display the first two axial modes. Comparison of results shows good agreement between the author's and the ABAQUS codes.

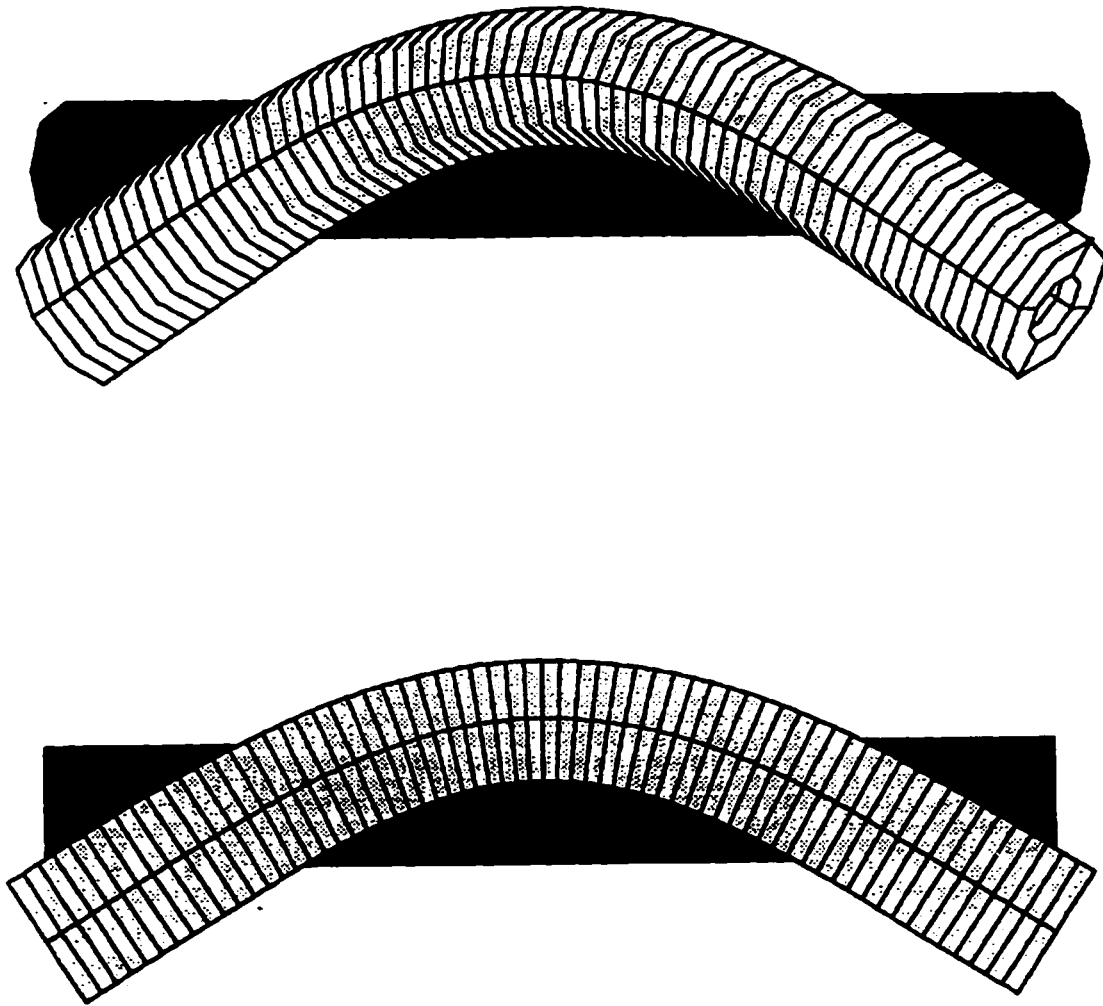


**Figure C.1 1st bending mode with natural frequency 744 Hz  
(744 Hz using the author's code)**

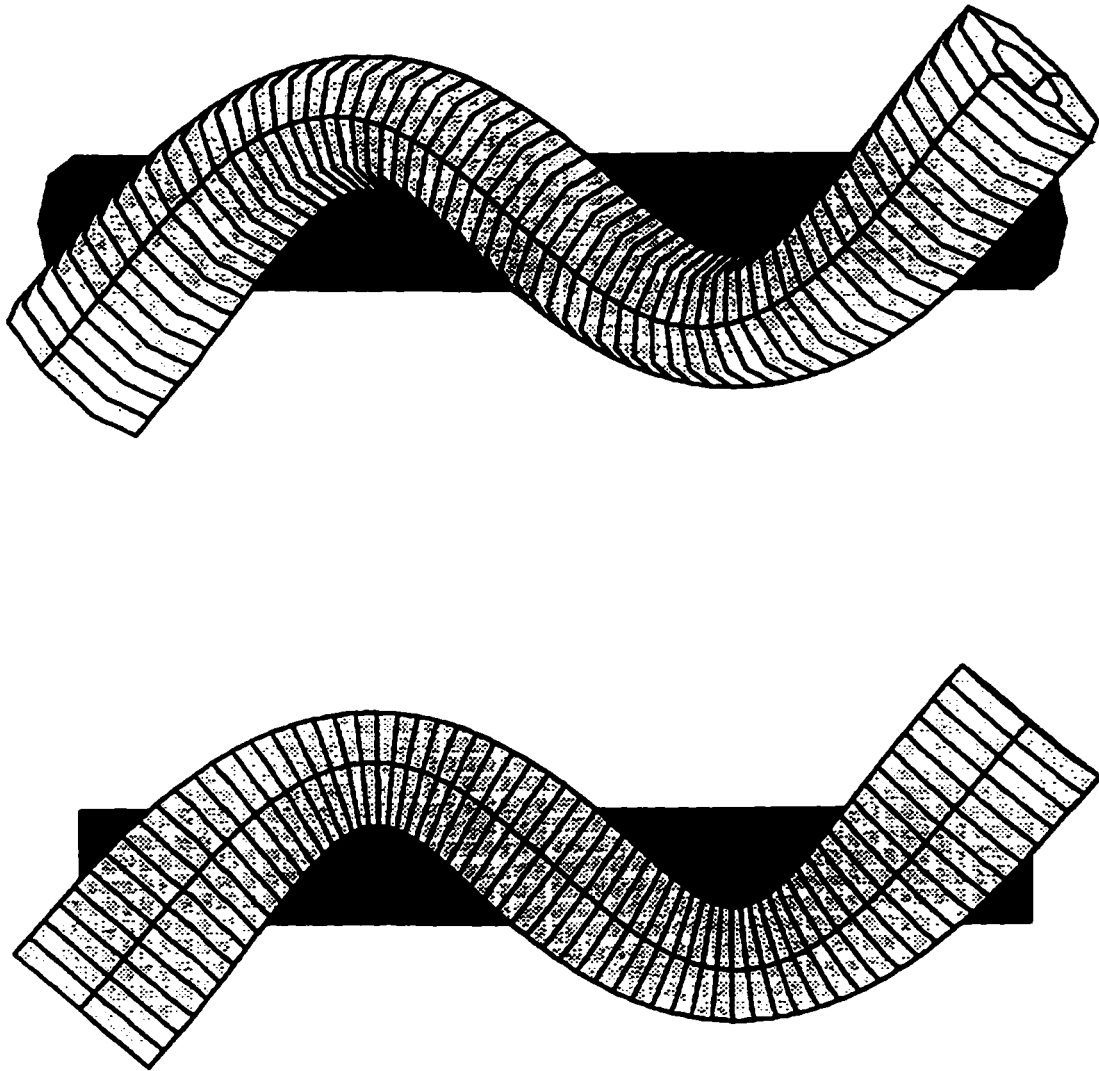


**Figure C.2 2nd bending mode with natural frequency 1874 Hz  
(1875 Hz using the author's code)**

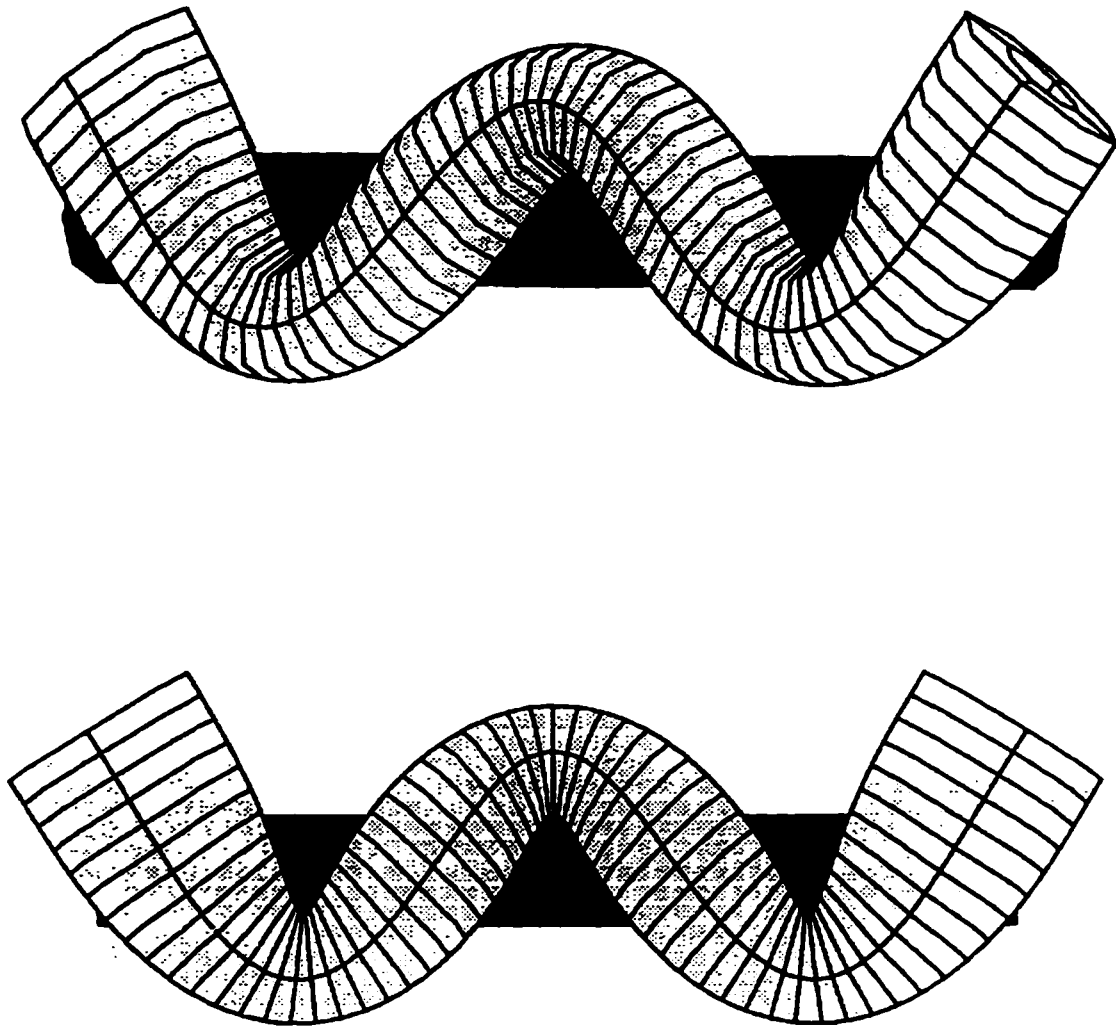


**Figure C.3 3rd bending mode with natural frequency 3304 Hz  
(3307 Hz using the author's code)**

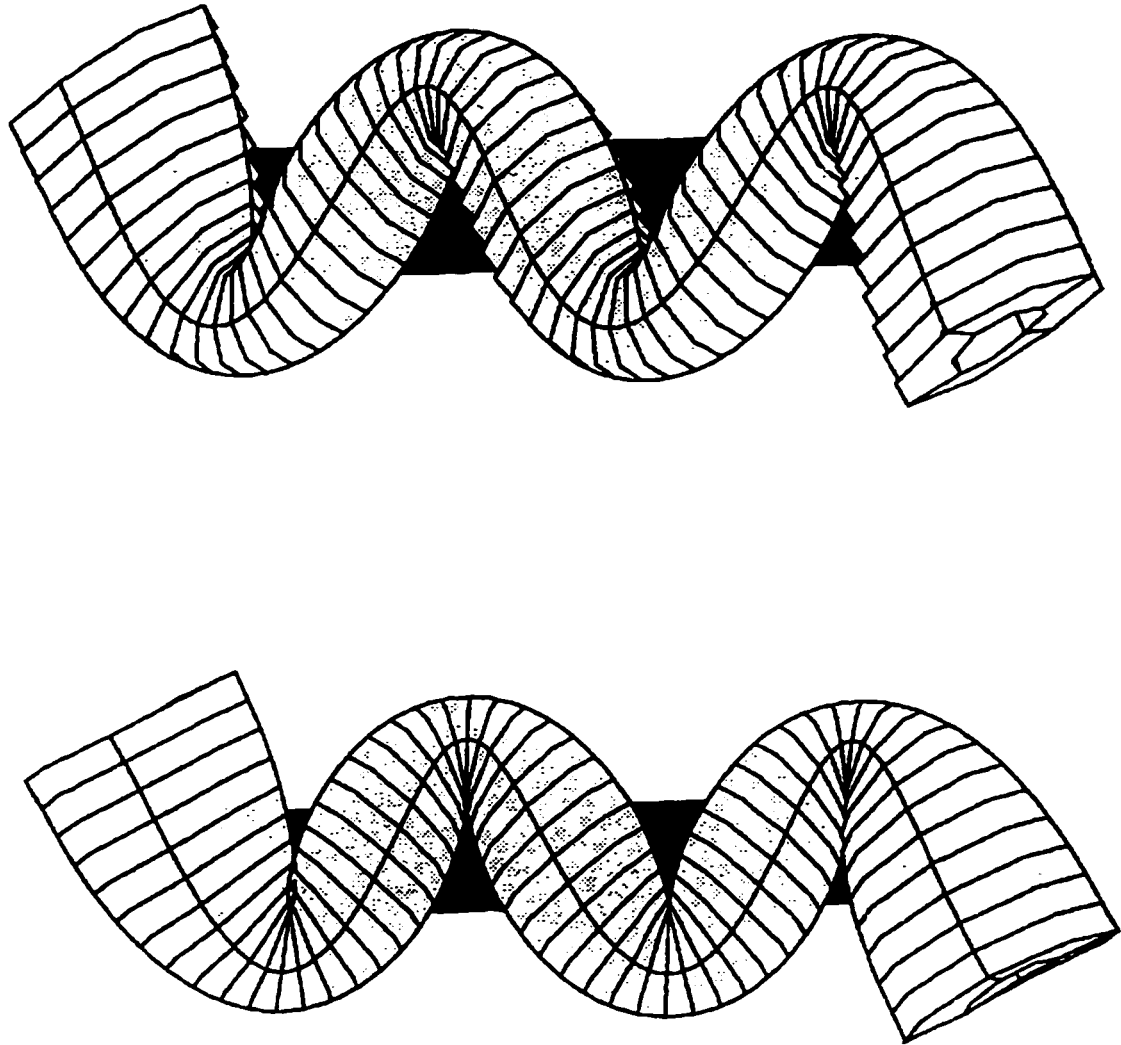


**Figure C.4 4th bending mode with natural frequency 4887 Hz  
(4892 Hz using the author's code)**

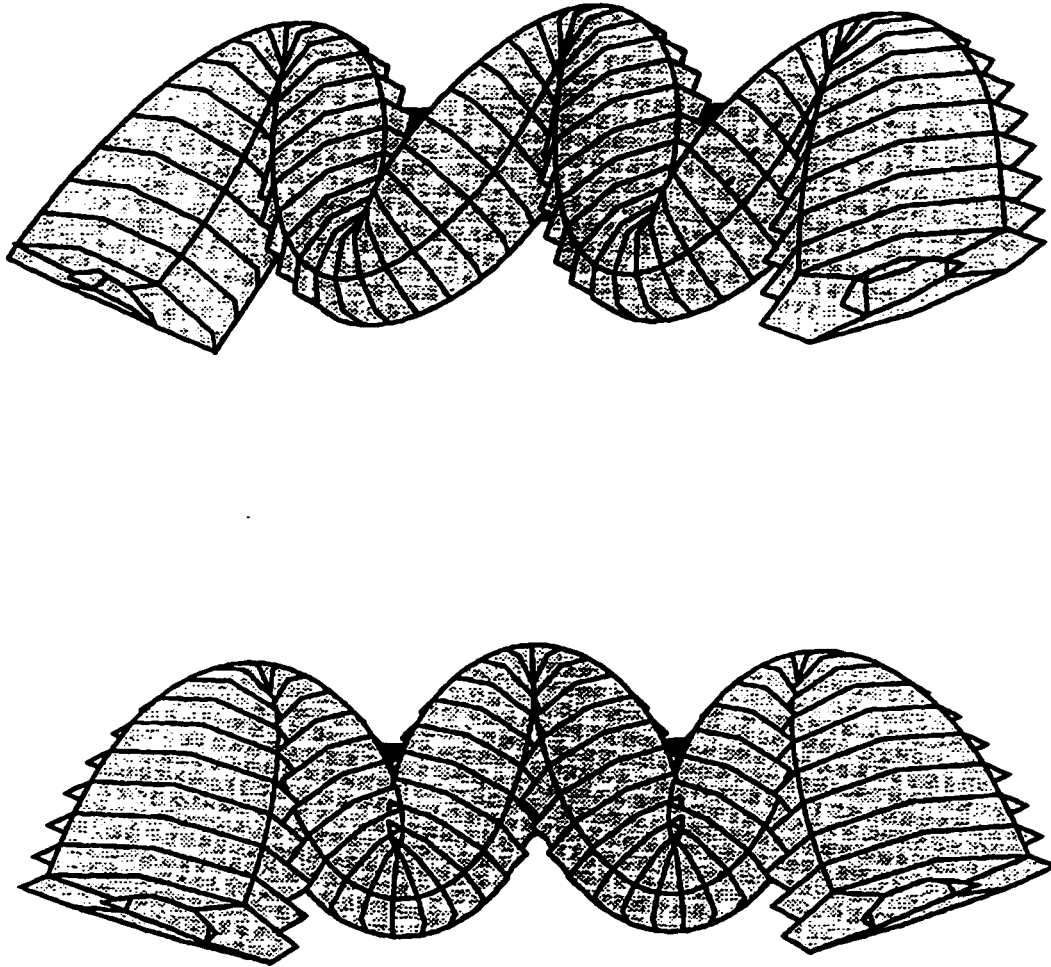


**Figure C.5 5th bending mode with natural frequency 6538 Hz  
(6548 Hz using the author's code)**





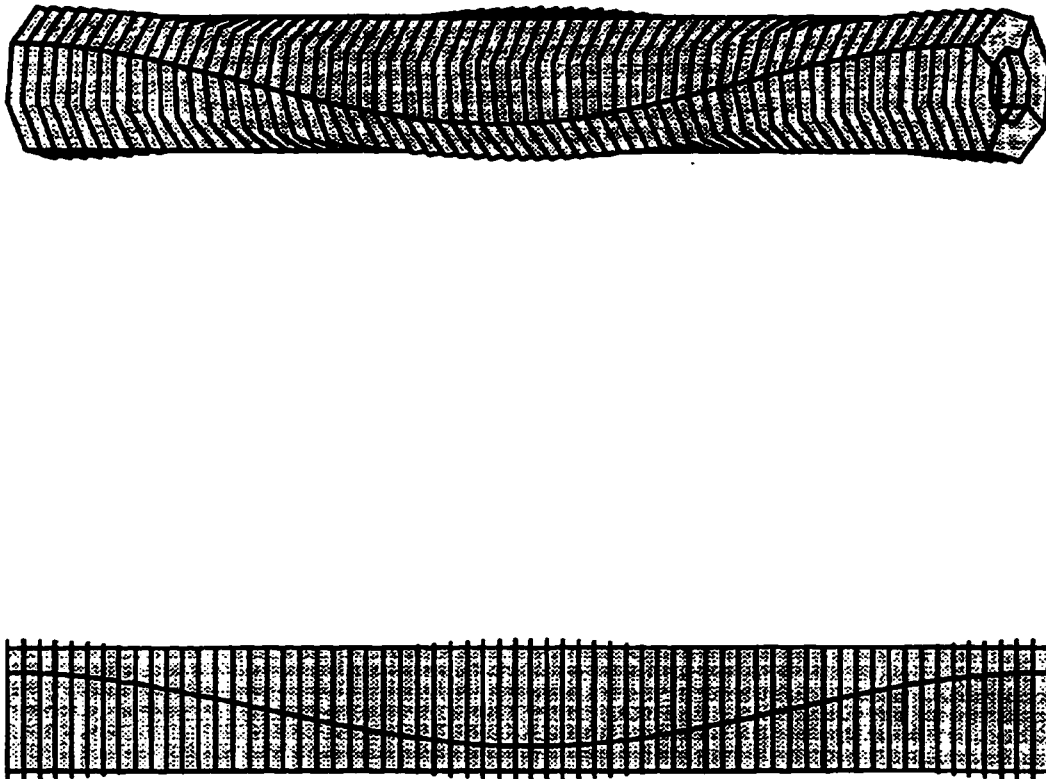


**Figure C.7 2nd torsional mode with natural frequency 3926 Hz  
(3925 Hz using the author's code)**

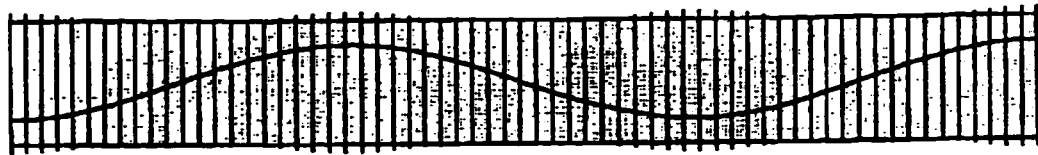
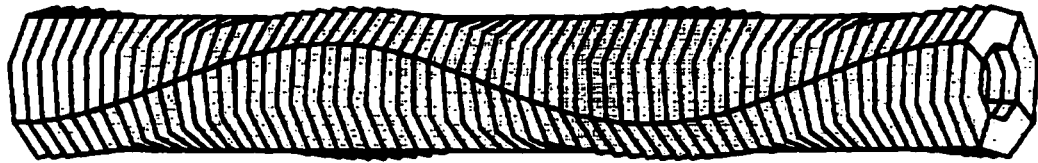


**Figure C.8 3rd torsional mode with natural frequency 5888 Hz  
(5888 Hz using the author's code)**

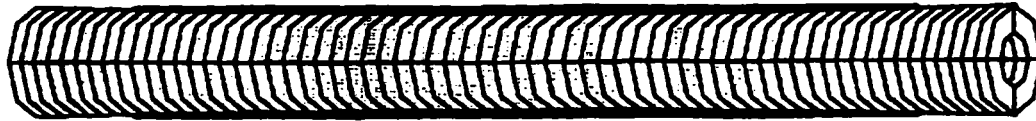


**Figure C.9 1st axial mode with natural frequency 3161 Hz  
(3162 Hz using the author's code)**

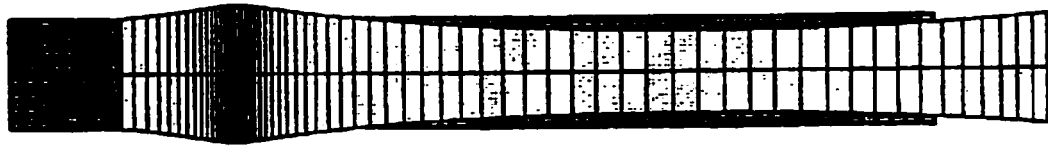
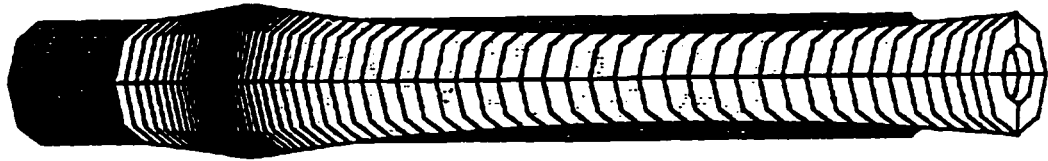


**Figure C.10 2nd axial mode with natural frequency 6301 Hz  
(6304 Hz using the author's code)**